Heliospheric Propagation of Solar Wind and Coronal Mass Ejections

A thesis submitted in partial fulfilment of

the requirements for the degree of

Doctor of Philosophy

by

Sandeep Kumar

(Roll No. 20330016)

Under the guidance of

Prof. Nandita Srivastava

Udaipur Solar Observatory

Physical Research Laboratory, Ahmedabad, India

Department of Physics

Indian Institute of Technology Gandhinagar, India

2025

Dedicated to

my family

Declaration

I hereby declare that this thesis is a result of my own original work and reflects my personal understanding and ideas. Where the ideas or words of others have been used, appropriate citations and references have been provided to acknowledge the original sources. I affirm that I have complied with the principles of academic honesty and integrity, and I have not engaged in any form of misrepresentation, fabrication, or falsification of data, facts, sources, or content. I fully understand that any breach of these principles may result in disciplinary action by the Institute and may also lead to legal consequences from the original content creators, in cases where proper citation or required permissions have not been obtained.

Sandeep Kumar

(Roll No: 20330016)

Certificate

I feel very happy to certify that the thesis entitled "**Heliospheric Propagation of Solar Wind and Coronal Mass Ejections**" by **Mr. Sandeep Kumar** has been carried out under my supervision and this work has not been submitted anywhere else for any degree or diploma.

Prof. Nandita Srivastava
(Thesis supervisor)
Udaipur Solar Observatory
Physical Research Laboratory
Ahmedabad-380009, Gujarat, India

Acknowledgements

First and foremost, I would like to express my sincere and heartfelt gratitude to my advisor, Prof. Nandita Srivastava, for her unwavering support and guidance throughout my Ph.D. journey. Her patience, motivation, enthusiasm, and profound knowledge have been invaluable in helping me navigate the many challenges and milestones of this research. Her constant academic support, encouragement, and insightful feedback at every stage of my work have played a pivotal role in shaping both my research and writing. I am deeply indebted to her for her exceptional mentorship, which has not only enriched my scientific approach but also emphasized the importance of clear and effective communication of research. Her visionary perspective and dedication have been a continuous source of inspiration.

I am also extremely grateful to the members of my Doctoral Studies Committee (DSC): Prof. Dibyendu Chakrabarty, Prof. Shibu K. Mathew, and Dr. Rohan Eugene Louis. Their thought-provoking questions, constructive suggestions, and consistent support have significantly contributed to deepening my understanding of the subject. The engaging discussions and their invaluable insights have had a lasting impact on my research. I extend my heartfelt thanks especially to Prof. Dibyendu Chakrabarty for his continuous encouragement and thoughtful guidance throughout my doctoral work.

I am thankful for the fruitful scientific interactions I have had with Prof. Nat Gopalswamy and Dr. Seiji Yashiro from NASA GSFC, and Prof. Nikolai Pogorelov from the University of Alabama in Huntsville. Their expertise, generous feedback, and valuable suggestions have made a meaningful contribution to the advancement of my research.

I also extend my sincere thanks to Dr. Dana Camelia Talpeanu, Dr. Marilena Mierla, Dr. Elke D'Huys, and Dr. Marie Dominique from the Royal Observatory of Belgium for their helpful advice and guidance. I am grateful for the support received through the PROBA2 Guest Investigator Program and would like to thank the PROBA2 operational team for their cooperation. I also appreciate the support of the SWAP project, a joint initiative by the Centre Spatial de Liège and the Royal Observatory of Belgium, funded by the Belgian Federal Science Policy

Office (BELSPO).

I am deeply grateful to the developers and contributors of all the Python libraries used to carry out my this thesis work for making their tools openly available and for maintaining high standards of documentation and usability. Their efforts have greatly advanced the accessibility of computational tools in solar physics and have been fundamental to the progress of this work. I also thank and acknowledge K. Marubashi for providing the flux rope fitting code in IDL. I would also like to acknowledge the use of Grammarly which proved to be a helpful tools in refining the presentation of my thoughts and enhancing the clarity and precision of my written expression throughout the preparation of this thesis. While all ideas and interpretations remain my own, the assistance in improving word choice, structure, and coherence contributed to more effective communication of the work.

I would like to express my deep appreciation to the Director, Dean, Registrar, Head of Academic Services, and the Academic Committee of PRL for their continuous support and guidance throughout my doctoral journey. I am also thankful to all the faculty members of PRL for their valuable perspectives and encouragement.

I extend my thanks to the medical team of PRL, especially Dr. Samir Dani, Dr. Sheetal Patel, and Dr. V. Bhandari, for their care and support whenever needed. Their assistance has been crucial during my time at PRL. I am also grateful to the academic and administrative personnel of IITGN for their help and efficiency in managing official procedures, which greatly facilitated the smooth progress of my research.

I would like to express my heartfelt gratitude to all the teachers (my father Shree Sajjan Kumar and my mother Shrimati Santro Devi, Mr. Sunil, Mr. Surender Sharma, Ms. Salini, Mr. Ranbir and Dr. Vijay Goyal) who have guided and shaped my academic journey from its very beginning. I am also deeply grateful to my college professors, Ms Malika, Ms Rashim and Mr. Ishwar Mawlia for nurturing my interest in science and helping me develop a deeper understanding of the subject.

I would also like to extend my heartfelt gratitude to the teachers and mentors at

IIT Indore who guided me during my master's studies. In particular, I am deeply thankful to Dr. Bhargav Vaidya and Prof. Subhendu Rakshit, whose passionate teaching and dedicated efforts left a lasting impact on me.

In summary, I am grateful to my every teacher who, at various stages of my academic journey, taught with effort and passion. Their contributions have shaped my growth and inspired my pursuit of knowledge.

I am deeply grateful to Dinesh V. Hegde for his invaluable support during my visit to the University of Alabama in Huntsville. The time I spent working with him was among the most enriching and rewarding experiences of this journey. In addition, I would like to thank Ashutosh, Shanmugha Balan, Shweta and Parthibh. Though the time I spent with them was brief, it was truly enriching and memorable. Working and learning alongside them was a valuable experience that I will always cherish.

I am deeply thankful to my family for their unwavering support. In particular, I would like to express my heartfelt gratitude to my father, my mother and my sisters, Pooja and Priyanka, and my friend Jagjeet, for their unconditional love and constant encouragement. I feel deeply grateful to have Jyoti in my life as a true friend and a wonderfully supportive life-partner. Her constant encouragement carried me through the final phase of my PhD. I am also grateful to my PRL batchmates Dharmendra, Kamarn, Debashish, and Gurucharan for their camaraderie and support, as well as to my seniors, Yogesh and Bijoy, for their valuable guidance and friendship. Finally, I extend my sincere thanks to everyone who has supported me both directly and indirectly throughout this journey. Their kindness, motivation, and belief in me have been instrumental in the successful completion of this research work.

Sandeep Kumar

Abstract

Coronal mass ejections (CMEs) are expansive bursts of kinetic and magnetic energy in the heliosphere originating from the Sun. An important area of space weather study revolves around understanding the trajectory of CMEs through the heliosphere and their interaction with the surrounding solar wind environment. The ambient solar wind, being the medium in which the CMEs propagate, plays a significant role in influencing space weather. This is because CMEs interact with the ambient solar wind and other large-scale magnetic field structures. CMEs are subject to changes in their direction of propagation and orientation as they propagate through the heliosphere. Therefore, the study of the heliospheric propagation of the CMEs should be complemented with the study of the ambient medium, i.e., the magnetic field and solar wind. The thesis work is divided into two parts. 1) Ambient solar wind modeling and optimization. 2) Studying the impact of the ambient solar wind on heliospheric propagation of CMEs.

State-of-the-art magnetohydrodynamics (MHD) space weather forecasting frameworks are based upon the Potential Field Source Surface (PFSS) and Schatten Current Sheet (SCS) extrapolation models for the magnetic field using synoptic magnetograms. These models create a solar wind background for the simulations using empirical relations of Wang, Sheeley, and Arge (WSA), at the inner boundary of the heliosphere and have been used to simulate CMEs. In our approach we combine coronal models (PFSS+WSA or PFSS+SCS+WSA) to Heliospheric Upwind extrapolation (HUX) model which is a simplistic solar wind velocity extrapolation model in the heliosphere, to estimate solar wind velocity at L1.

We implemented the solar wind velocity prediction framework (PFSS+WSA+HUX and PFSS+SCS+WSA+HUX) on 60 Carrington Rotations (CRs) from CR2047 to CR2107 during 2006–2011, covering the descending and deep minimum phase of the solar cycle (SC) 23 and the ascending phase of SC24. Our framework performed well over the descending phase of SC23 and ascending phase of SC24 (average cc=0.65). We noticed unexpected decrease in the performance of the framework during the deep minimum phase of the SC23, which is attributed to the decrease in the observed coronal hole area.

In the next part of the study, we explore the effects and necessity of optimizing the source surface height (R_{ss}) in PFSS model in the context of its use in solar wind velocity forecasting model, i.e., the WSA model, taking into account different types of magnetograms from the GONG network. Our findings suggest a need for optimization of R_{ss} in PFSS in the WSA model with the phases of the SC, particularly using a lower value R_{ss} (2.0 $R_{\odot}$) near the solar maximum and a higher value of R_{ss} (3.0 $R_{\odot}$) at minimum as compared to the standard value of R_{ss} (2.5 $R_{\odot}$). Based on a detailed study of 16 CRs selected at different phases of SC24 and SC25 using different magnetograms, we found that the performance of the solar wind velocity framework (PFSS+WSA+HUX) is improved by 40% with zero-point corrected (ZPC) maps, as compared to the standard full Carrington maps from GONG. This improvement is attributed to its capability to capture the global magnetic field. This was further confirmed by comparing the extrapolated global magnetic field structures with the large-scale coronal features observed in the 174 $\mathring{A}$ channel using extended field-of-view images from the PROBA2/SWAP instrument. Our extended analysis for two solar cycles (SC24 and SC25) using full CR ZPC maps suggests that for $\approx$ 60% of the CRs during ascending, declining, and minimum phases of SC24 and SC25, the framework with higher R_{ss} ($\geq$ 2.75) performed better as compared to lower R_{ss} ($\leq$ 2.5 $R_{\odot}$). Whereas during the maximum phase, the framework with lower R_{ss} ($\leq$ 2.5 $R_{\odot}$) performed better for $\approx$ 72% of the CRs as compared to higher R_{ss} ($\geq$2.5 $R_{\odot}$).

To study the role of the solar wind in heliospheric propagation of the CMEs, we investigated the heliospheric propagation of 15 Earth-impacting CMEs observed during April 2010 to August 2018 in the field of view (FOV) of the COR2 to Heliospheric Imager (HI) onboard the STEREO spacecraft. About half of the 15 events followed self-similar expansion up to 40 $R_{\odot}$. The remaining events showed deflection either in latitude, longitude and tilt. We found clear evidence of continuous rotation of two CMEs observed on 5 October 2012 and 23 May 2017, i.e., an increase in the tilt angle, estimated using the graduated cylindrical shell (GCS) reconstruction model at different heliocentric distances. We also used toroidal and cylindrical flux rope fitting on the in situ observations of interplanetary mag-

netic field (IMF) and solar wind parameters to estimate the tilt at L1 for these two events. Our study shows that CME rotation is a rare phenomenon observable in HI images. This rarity can be partially attributed to the special conditions of the ambient magnetic field and solar wind required for CME rotation. Although CME rotation appears to be more commonly observed in the lower corona, where the ambient magnetic field dominates, it requires conducive conditions of both the magnetic field and the solar wind to favor a persistent rotation of the CME throughout the heliosphere. This particular study highlights the role of HI observations to connect observations near the Sun and near Earth, improving our understanding of how CMEs move through the heliosphere.

To investigate the impact of CME deflection in the heliosphere on its arrival time prediction at L1, we conducted a case study of the 21 April 2023 CME, which triggered a major geomagnetic storm (Dst = –213 nT). This study underscores the critical importance of multi-viewpoint imaging for accurate arrival time forecasts. It also highlights the benefit of employing multiple modeling approaches to reduce uncertainties in the propagation direction of the CME in the heliosphere. With an aim to incorporate the effects of some of the physical aspects in solar wind extrapolation, next we developed a heliospheric solar wind model to simulate the ambient solar wind and incorporated an elliptical cone model of the CME into hydrodynamic (HD) simulations. Using this framework, we simulated the 21 April 2023 CME event. The resulting solar wind velocity and density profiles showed good agreement with in situ observations at L1, successfully replicating the CME arrival in the density and velocity profile.

To incorporate the internal magnetic field structure of a CME with a better geometrical shape, we implemented a geometrical and magnetic field flux rope model based on Flux Rope in 3D (FRi3D) model by Isavnin (2016). This implementation enabled us to track CME evolution from near the Sun to up to 80 $R_{\odot}$ using coronagraphic and heliospheric images and also to model observed IMF at L1. Our analysis for 5 October 2012 CME by comparing flux rope parameters near the Sun and at L1 revealed signatures of CME rotation and compression in the heliosphere.

In short, in this thesis, we have shown that solar wind velocity forecasting improves with the optimization of source surface height and the use of zero-point corrected maps from GONG. Further, our findings contribute to our understanding of the complex dynamics involved in CME propagation and highlight the need for comprehensive modeling and observational studies to improve space weather prediction.

Keywords: Solar wind, corona, PFSS, WSA, coronal holes, solar cycle, coronal mass ejections (CMEs), interplanetary coronal mass ejections (ICMEs), heliosphere.

List of Abbreviations and Acronyms

Abbreviation	Definition
ACE	Advanced Composition Explorer
PSP	Parker Solar Probe
SWAP	Sun Watcher using Active Pixel System detector and Image Processing
AR	Active Regions
CH	Coronal Holes
HCS	Heliospheric Current Sheet
SCS	Schatten Current Sheet
L1	First Lagrangian Point of Sun-Earth System
$R_\odot$	Radius of the Sun
CME	Coronal Mass Ejection
ICME	Interplanetary Coronal Mass Ejection
MC	Magnetic Cloud
CIR	Co-rotating Interaction Region
SIR	Stream Interaction Region
IMF	Interplanetary Magnetic Field
MHD	Magnetohydrodynamic
PFSS	Potential Field Source Surface
WS	Wang–Sheeley
WSA	Wang–Sheeley–Arge
DBM	Drag-Based Model
ADBM	Advanced Drag-Based Model
HUX	Heliospheric Upwind eXtrapolation
GONG	Global Oscillation Network Group
CR	Carrington Rotation
SSN	Sunspot Number
DCHB	Distance from Coronal Hole Boundary
ZPC	Zero-Point-Corrected

STD	Standard
GSE	Geocentric Solar Ecliptic
HEEQ	Heliocentric Earth Equatorial
SC	Solar Cycle

Contents

List of Figures

List of Tables

Chapter 1

Introduction

1.1 Sun and Heliosphere

1.1.1 Sun and Solar Structure

Our Sun is an ordinary star from an astronomical point of view (G2V spectral class), and it illuminates our planet with light. Table 1.1 lists some of the properties of the Sun. It is a magnetically active star, which makes it interesting and sometimes dangerous from the human point of view. The presence of the magnetic field in the Sun makes it a center of many exotic phenomena, such as a million-degree atmosphere (corona) on a cool photosphere (5778° K), solar flares, supersonic solar wind and giant magnetic eruptions called coronal mass ejections. The Sun has the following layers constituting its internal structure and its atmosphere.

Core

The **core** is the innermost region of the solar interior, where energy is generated through nuclear fusion. It contains about 10% of the total mass of the Sun. Due to the high gravitational pressure at the center, this region reaches temperatures of approximately 15 MK and has a density of around $1.5 \times 10^5 \mathrm{kg/m^3}$ (Lang, 2006). These extreme conditions make it ideal for the fusion of hydrogen into helium, which is the primary nuclear reaction powering the Sun. The conditions

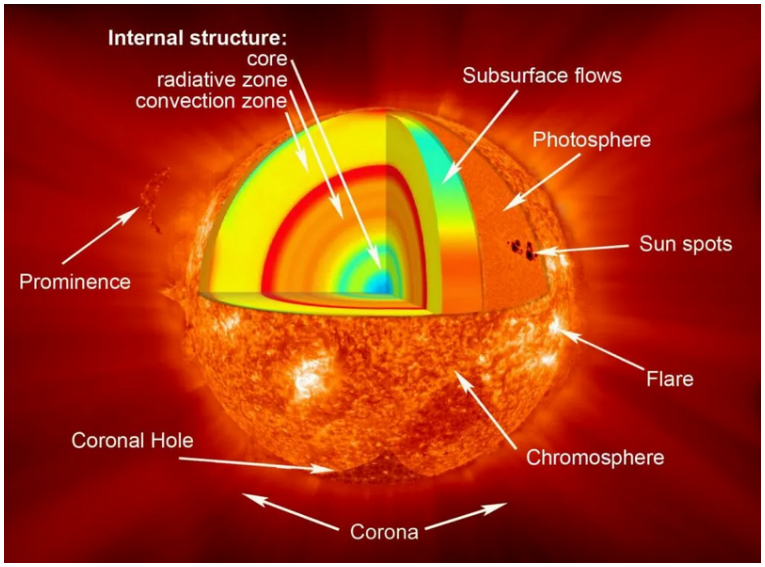

Figure 1.1: Different layers of the Sun. Picture credit: NASA

necessary for sustained nuclear fusion exist up to about $0.3\,R_\odot$, beyond which the temperature and density drop, and the density falls to around $2.0 \times 10^4 \mathrm{kg/m^3}$. Outside this boundary, the **radiative zone** begins.

Radiative Zone

The **radiative zone** is a region in the solar interior composed of highly ionised gases. It derives its name from the dominant energy transport mechanism in this region, i.e., radiative transfer. This zone extends from the outer edge of the core to about 0.75 $R_\odot$. In this region, gamma-ray photons produced in the core are repeatedly absorbed and re-emitted by particles. As a result, the energy of the photons gradually decreases as they propagate outward. The movement of photons in the radiative zone resembles a random walk, making the energy transfer process extremely slow. The density in the radiative zone decreases from approximately $2.0 \times 10^4 \mathrm{kg/m^3}$ at its base to about $2.0 \times 10^2 \mathrm{kg/m^3}$ at its outer boundary. Similarly, the temperature drops from roughly 7 MK to 2 MK from the bottom to the top of the zone. Owing to the high density in the radiative zone (approximately 2×10^4 kg/m^3), the mean free path of photons is extremely short, about 9.0×10^{-2} cm. As a result, photons require tens to hundreds of thousands of years to diffuse through this layer (Mitalas and Sills, 1992).

Convective Zone

The **convective zone** is the outermost layer of the solar interior. It is named after its primary energy transport mechanism, convection, which dominates in this region due to the steep temperature gradient and the opacity of the plasma (Foukal, 2004).

In this zone, the temperature decreases from about 2 MK at the bottom to approximately 5800 K at the surface. The density is significantly lower than in the inner regions, dropping to around 2×10^{-4} kg/m^3. The convective zone spans the outermost 15% of the Sun's radius.

Because of the comparatively lower temperatures, the gases in this region are not fully ionized, unlike those in the core and radiative zone. The base of the convective zone or the tachocline is also believed to be the site of the solar dynamo, which is responsible for generating the magnetic field of the Sun. The tachocline is a narrow transition layer between the radiative and convective zones of the Sun, characterized by strong rotational shear. In this region, the sound speed and density profiles show a distinct sudden 'bump' (Spiegel and Zahn, 1992).

Photosphere

The **photosphere** is the layer of the Sun, from which photons finally escape into space and reach our eyes. It is the only part of the Sun visible to the human eye. The photosphere is about 500 km thick and exhibits a variety of dynamic features, such as:

1. **Sunspots**: These are dark, cooler regions on the solar surface caused by intense magnetic field concentrations. They typically appear in pairs (with opposite magnetic polarity) or in groups. The temperature of sunspots is approximately 1000–1500 K lower than the surrounding photosphere, making them appear darker (Figure 1.2).

2. **Granulation**: This refers to the small, grain-like cellular patterns covering the photosphere. They are caused by convective currents in the center

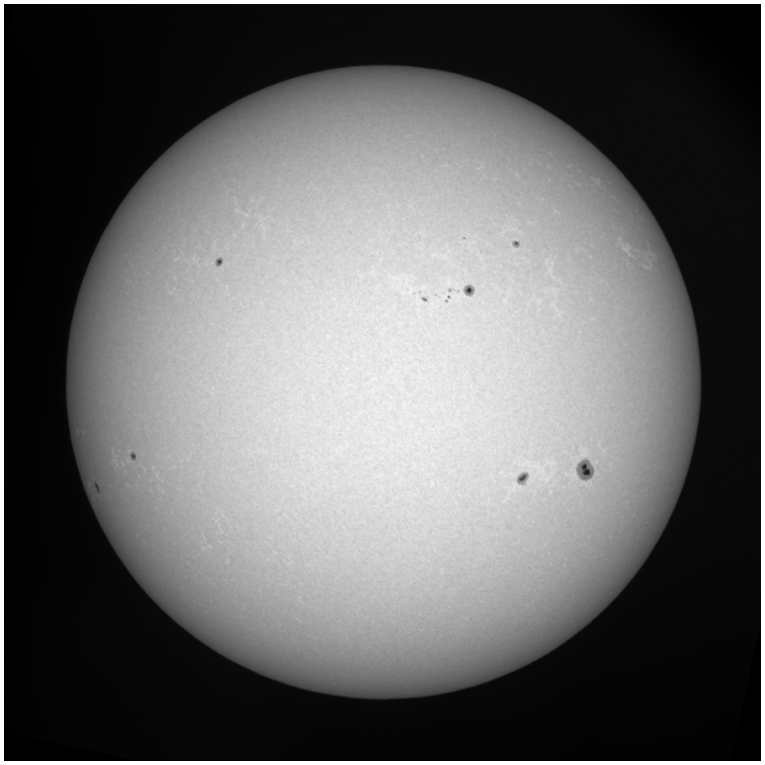

Figure 1.2: Image of the photosphere of the Sun on 10 December 2022. Taken by solar Spar telescope at Udaipur Solar Observatory.

of granules (appearing brighter), while cooler plasma sinks at the edges (appearing darker). Each granule spans roughly 1000 km and lasts for 10–20 minutes. Apart from granulation, there is supergranulation, which is a large-scale version of granules, often associated with concentrations of magnetic fields.

3. **Faculae**: These are bright, thread-like structures, specifically near the solar limb. Faculae are hotter than the surrounding regions and are often linked to areas with stronger magnetic fields.

Chromosphere

The **chromosphere** is a thin layer of the solar atmosphere, approximately 2500 km thick, located just above the photosphere. Within this layer, the temperature increases from about 6000°K at the base to roughly 20000°K at the top. At these temperatures, hydrogen atoms emit radiation in the Balmer series (specif-

ically transitions from $n = 3$ to $n = 2$), producing the characteristic H_α line at 656.28 nm, which gives the chromosphere its distinctive reddish color. The **chromosphere** is not visible to the naked eye under normal conditions; it can be seen during a total solar eclipse, appearing as a narrow red ring around the Sun when the Moon blocks the bright photosphere. Several different features can be observed in the chromosphere, such as:

- **Spicules**: These are thin, jet-like structures of plasma that rise from the lower chromosphere to its upper boundary and fall back within about 10 minutes. They are the most common and recognizable features in this region.
- **Filaments/Prominences**: These are large, relatively cool gaseous structures suspended in the hotter solar atmosphere by magnetic fields (Figure 1.3). When seen against the bright solar disk, they appear dark and are called filaments. When observed at the solar limb, they are referred to as prominences.
- **Plages**: These are bright, hair-like features often found near active regions. They are associated with enhanced magnetic activity.

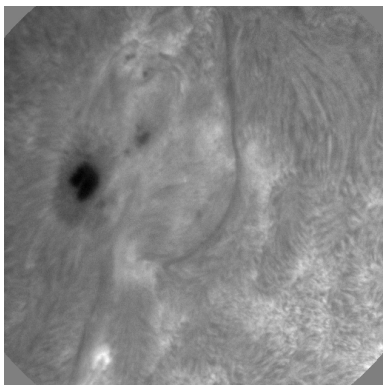

Figure 1.3: Filament structure observed on the Sun on 22 December 2022 in H_α. Credit: Multi-Application Solar Telescope (MAST), Udaipur Solar Observatory.

Corona

The **corona** is the outermost layer of the atmosphere of the Sun. It is a highly rarefied plasma with extremely low density (1000 particles/cc), yet it reaches astonishing temperatures of about 1–2 MK. Despite its high temperature, the total thermal energy (or heat content) is relatively low due to the low particle density. Because of all these reasons, it is only visible when the bright light from the solar disk is blocked, such as during a total solar eclipse or with the use of an artificial occulter. During these conditions, the corona appears as a faint, pearly-white halo surrounding the Sun. One of the most long-standing questions in solar physics is the million-degree temperature of the corona, which is above the much cooler photosphere, which has a temperature of only about 5778° K. The coronal temperature is inferred from the presence of highly ionized atoms, which require such extreme temperatures to form. For example, the detection of calcium ions that have been ionized 14 times (Ca XV) indicates the presence of million-degree plasma. To achieve such a high degree of ionization, significant energy is required to remove so many electrons from neutral atoms. Due to the extremely high temperatures in the solar corona, most coronal features are best observed in high-energy wavelengths such as extreme ultraviolet (EUV) and X-rays. The corona is composed of various structures, including bright closed coronal loops, streamers, active regions, sheared arcades, and open or closed magnetic loops.

The corona is not in hydrostatic equilibrium. Its material continuously escapes into space in the form of the solar wind, which fills the heliosphere. This wind primarily consists of electrons and protons. The heliosphere is the region of influence of the solar magnetic field and solar wind. It is filled with magnetic plasma carried by the solar wind, which flows outward in all directions from the rotating Sun. Due to the motion of the Sun around the Milky Way galaxy, it has different extensions in the direction of the motion and opposite to it. Its extension is only known in the direction of the motion of the Sun, which is about 100 AU, where the bow shock forms between the interstellar medium and the solar wind.

In the solar corona, β , which is the ratio of the thermal pressure to the mag-

netic pressure, plays a crucial role in determining the dynamics and structure of the plasma. In most of the coronal regions (up to $\approx 2.5\ R_\odot$), $\beta \ll 1$ indicates that magnetic pressure dominates over thermal pressure. This means the magnetic field largely governs the behaviour of the plasma. The low β condition in the corona explains why coronal features such as loops and arcades closely trace magnetic field lines. The plasma is effectively "frozen in" in the field. As coronal plasma expands into the heliosphere, β increases. In the outer corona ($\beta \geq 1$) and beyond, plasma and magnetic pressures become comparable, where the dynamics is dominated by the flow pressure and thermal pressure.

Table 1.1: Basic Physical Properties of the Sun (Adapted from Yoder (1995)).

Parameter	**Value**
Mass	1.988×10^{33} g
Mean Radius	6.960×10^{10} cm
Surface Gravity	27400 cm s^{-2}
Escape Velocity	6.175×10^{7} cm s^{-1}
Average Density	1.408 g cm^{-3}
Adopted Sidereal Period	25.38 days
Obliquity to the Ecliptic	$7^\circ\ 15'$
Luminosity	3.846×10^{33} erg s^{-1}
Solar Constant	1.367×10^{6} erg cm^{-2} s^{-1}
Effective Temperature	5778 K
Absolute Visual Magnitude	4.83
Spectral Type	G2V

1.1.2 Carrington Rotation (CR)

The Carrington Rotation is a method used to track the rotation of the Sun relative to the Earth. It was introduced by British astronomer Richard Christopher Carrington in the mid-19th century, based on his observations of sunspots. The Carrington rotation period is based on observations of sunspots at a latitude of approximately 26° north and south of the solar equator. He determined that the

average rotation period of sunspots at around ±26° latitude was about 27.2753 days, which he adopted as the standard solar rotation period for his coordinate system. Carrington defined a fixed solar rotation period of approximately 27.2753 days, which corresponds to the sidereal rotation period of the Sun as seen from Earth. The system also introduced Carrington longitude, a fixed coordinate system on the Sun where longitude is anchored to the original observations made by Carrington on 9 November 1853, which marks the beginning of the first Carrington rotation. Since then, each full rotation has been sequentially numbered, and this framework is now widely used for organizing solar observations, such as tracking sunspots, active regions, and coronal holes. Despite the differential rotation of the Sun, where different latitudes rotate at different speeds, the Carrington system provides a consistent and standardized reference frame for long-term solar studies.

1.1.3 MHD Equations Governing Solar Plasma

A wide variety of interplanetary structures and processes, on scales ranging from 50 km to more than 50 AU (Burlaga, 1995), can be derived from the equations of magnetohydrodynamics (MHD). The MHD equations are a combination of the Navier-Stokes equations for fluid dynamics and Maxwell's equations for electromagnetism. These equations govern the behaviour of astrophysical plasmas, fusion devices, and various geophysical flows. The fundamental MHD equations consist of the following: **Continuity Equation**

$$\frac{\partial \rho}{\partial t} + \nabla \cdot (\rho \mathbf{v}) = 0 \tag{1.1}$$

This equation expresses the conservation of mass, where:

- ρ is the mass density,
- $\mathbf{v}$ is the velocity field.

Momentum Equation

$$\rho \left(\frac{\partial \mathbf{v}}{\partial t} + \mathbf{v} \cdot \nabla \mathbf{v} \right) = -\nabla p + \mathbf{J} \times \mathbf{B} + \rho \mathbf{g} + \nabla \cdot \mathbf{T} \tag{1.2}$$

This equation describes the conservation of momentum, where:

- p is the fluid pressure,
- $\mathbf{B}$ is the magnetic field,
- $\mathbf{J} = \frac{1}{\mu_0}\nabla \times \mathbf{B}$ is the current density,
- $\mathbf{g}$ is the gravitational acceleration,
- $\mathbf{T}$ is the viscous stress tensor.

Induction Equation

$$\frac{\partial \mathbf{B}}{\partial t} = \nabla \times (\mathbf{v} \times \mathbf{B}) - \nabla \times (\eta \nabla \times \mathbf{B}) \tag{1.3}$$

This equation governs the evolution of the magnetic field, where:

- $\eta = \frac{1}{\sigma \mu_0}$ is the magnetic diffusivity,
- σ is the electrical conductivity.

Energy Equation

$$\frac{\partial e}{\partial t} + \nabla \cdot [(e + p)\mathbf{v} - \eta \mathbf{J} \times \mathbf{B} + \mathbf{q}] = \rho \mathbf{v} \cdot \mathbf{g} + Q_{visc} \tag{1.4}$$

This equation represents the conservation of energy, where:

- e is the total energy density,
- $\mathbf{q}$ is the heat flux,
- Q_{visc} is the viscous dissipation.

Gauss's Law for Magnetism

$$\nabla \cdot \mathbf{B} = 0 \tag{1.5}$$

This equation states that no magnetic monopoles exist, ensuring that the magnetic field lines form closed loops. In an ideal case, the conductivity is infinite, and there is no viscous dissipation; terms $\mathbf{T}$, η and Q_{visc} are zero.

1.1.4 Introduction to Solar Wind

The pressure profile of the heliosphere/extended corona, according to Chapman, is as follows:

$$p = p_0 \exp\left\{\frac{7GM_\odot\rho_0}{5p_0R_\odot}\left[\left(\frac{R_\odot}{r}\right)^{5/7} - 1\right]\right\} \tag{1.6}$$

where p_0 and ρ_0 are the values of the pressure and density at the solar surface, it is clear that the pressure tends to a constant value as r tends to infinity (Choudhuri, 1998). Parker (1958) in 1958, based on his hydrodynamic calculations (on Chapman's extended corona), first inferred that the solar corona could not be in hydrostatic equilibrium. This is not physically possible because as r tends to infinity from the Sun, the pressure should continue to drop down to the value of the interstellar pressure. This interstellar pressure value is much smaller than the value inferred from Chapman's theory, i.e., according to Eq: 1.6). It suggests that the hydrostatic model of the solar corona is not physical. Therefore, the corona must be expanding outwards, giving rise to the idea of a dynamic outflow of plasma filling up the whole interplanetary region. This continuous outflow is termed as the solar wind.

For a purely radial, steady-state, isothermal coronal outflow, the radial velocity profile is given by the simple hydrodynamical equation for the radial flow of solar wind, which can be written as:

$$\left(\frac{u}{u_s}\right)^2 - \ln\left(\frac{u}{u_s}\right)^2 = 4\ln\left(\frac{r}{r_c}\right) + 4\frac{r_c}{r} + C,$$

Here, u, u_s and r are the outflow speed of solar wind, isothermal sound speed and radial distance from the Sun, respectively. r_c is the heliocentric distance at which flow turns from subsonic to supersonic, and C is a constant based on the value for which there are different solutions as shown in Figure 1.4.

1. Class *II* and Class *I* are nonphysical representing two velocities at single r.
2. Class *III*b solution starts at supersonic speeds and turns to subsonic values at $r = \infty$.
3. Class *III*a solution starts at supersonic speeds and remains supersonic throughout the domain.

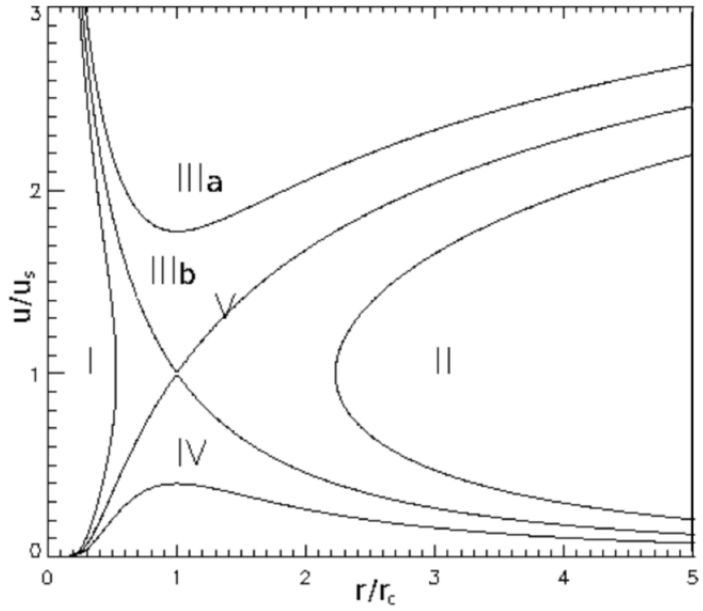

Figure 1.4: Parker solution for solar wind outflow (Adapted from Krista (2012)).

4. In the Class IV solution u is sub-sonic throughout the domain $a < r < \infty$ and is called "subsonic breeze".

5. Class V is the solar wind solution for which u increases monotonically from subsonic values and turns supersonic at $r = r_c$.

Class IIIa and Class IIIb solutions are not physical for the solar corona because they predict super-sonic flow at the base of the corona, which is not observed and is also not consistent with a static picture of the solar photosphere. Therefore, Class V solution corresponds to the realistic solar wind solution in the heliosphere. It is also important to note that the actual solar wind profile is neither isothermal nor adiabatic. The actual solar wind is multi-fluid in nature and approximated using the polytropic equation with an index of 5/3 (Choudhuri, 1998).

1.1.5 Parker Spiral

In a highly conducting plasma environment, the solar wind plasma parcels and solar magnetic field are tangled together in a condition called "frozen-in". After certain heliocentric distances (r_0), plasma parcels drag the solar magnetic field in

the heliosphere, and due to the rotation of the Sun, the magnetic field follows the path of the plasma parcels known as the Parker spiral solution, as given below.

$$B_r(r,\theta,\phi) = B(r_0,\theta,\phi_0)\left(\frac{r_0}{r}\right)^2, \tag{1.7}$$

$$B_\theta(r,\theta,\phi) = 0, \tag{1.8}$$

$$B_\phi(r,\theta,\phi) = -B(r_0,\theta,\phi_0)\,\frac{\Omega\, r_0}{u_s}\,\frac{r_0}{r}\,\sin\theta. \tag{1.9}$$

Here r, θ and ϕ define any location in the heliosphere, r_0, θ_0 and ϕ_0 are the initial position of the plasma parcels. B_r, B_θ and B_ϕ are the radial, latitudinal and longitudinal components of the magnetic field. These equations give rise to spiral magnetic field lines in the heliosphere, as shown in Figure 1.5 in the ecliptic plane.

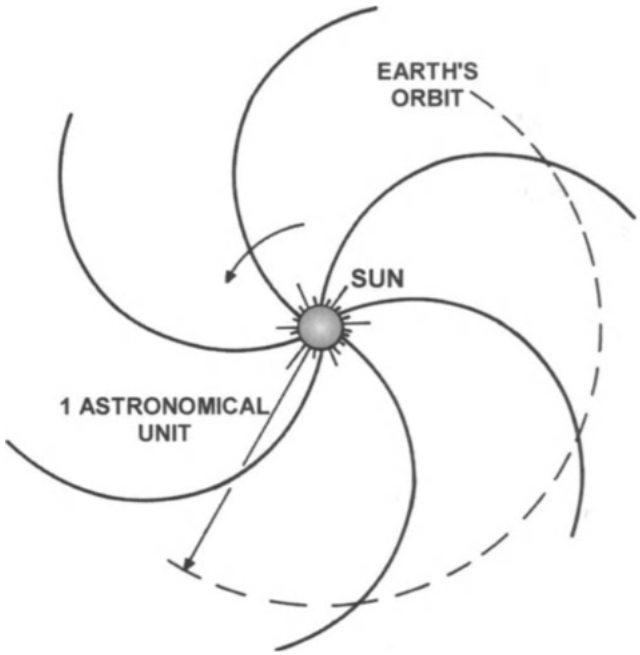

Figure 1.5: Parker spiral in the heliosphere (Adapted from Bittencourt (2004)).

The above treatment of solar wind by Parker involved a simplistic picture applicable only on the larger length scales in the heliosphere, where the MHD /HD approach is valid ($\geq$ 150 km). However, in reality, the solar wind is quite complex.

It consists of electrons, protons, alpha particles and a tiny fraction of heavier ions. Further, solar wind varies in density, speed and temperature over time, and solar latitude and longitude depend on the nature of the source regions. The general properties of the solar wind are captured by a few parameters measured at the first Lagrangian point (L1 point) of the Sun-Earth system and shown in Table 1.2. In general, the solar wind exhibits a bimodal nature and is typically categorized

Table 1.2: Solar Wind Parameters at L1 (Adapted from Zhou et al. (2020)).

Solar Wind Parameters	**Minimum Values**	**Maximum Values**	**Mean Values**
Number density	0.04 cm^{-3}	8 cm^{-3}	5 cm^{-3}
Bulk velocity	200 km/s	900 km/s	400–500 km/s
Proton temperature	5×10^3 K	1×10^5 K	2×10^5 K
Magnetic field	0.25 nT	40 nT	6 nT

into two distinct types: slow solar wind and fast solar wind. These types differ significantly in their speeds as well as in their physical characteristics, such as temperature and composition. Measurements near the L1 point indicate that the slow solar wind travels at speeds of 300–500 km/s, has a temperature of approximately 0.1 MK, and possesses a composition that closely resembles the solar corona. In contrast, the fast solar wind travels at speeds around 750 km/s (ranging from 600 to 900 km/s), has a higher temperature of about 0.8 MK, and its elemental composition is more similar to that of the photosphere (Geiss et al., 1995). Moreover, the slow solar wind tends to be denser—about twice as dense as the fast wind—and exhibits greater variability. The slow solar wind is believed to originate from multiple regions, including the streamer belt, the quiet Sun, and active regions. However, its exact sources remain a topic of ongoing debate (Fisk, 2003). As illustrated in Figure 1.6, adapted from McComas et al. (2003), the slow solar wind is emitted primarily from low latitudes (up to approximately 30°–35°) observed during solar minimum (during 1992 to 1998). During periods of increased solar activity (1998–2003), the slow wind extends to higher latitudes. In contrast, the fast solar wind originates predominantly from coronal holes (Zirker, 1977), which are characterised by the footpoints of the open magnetic field lines

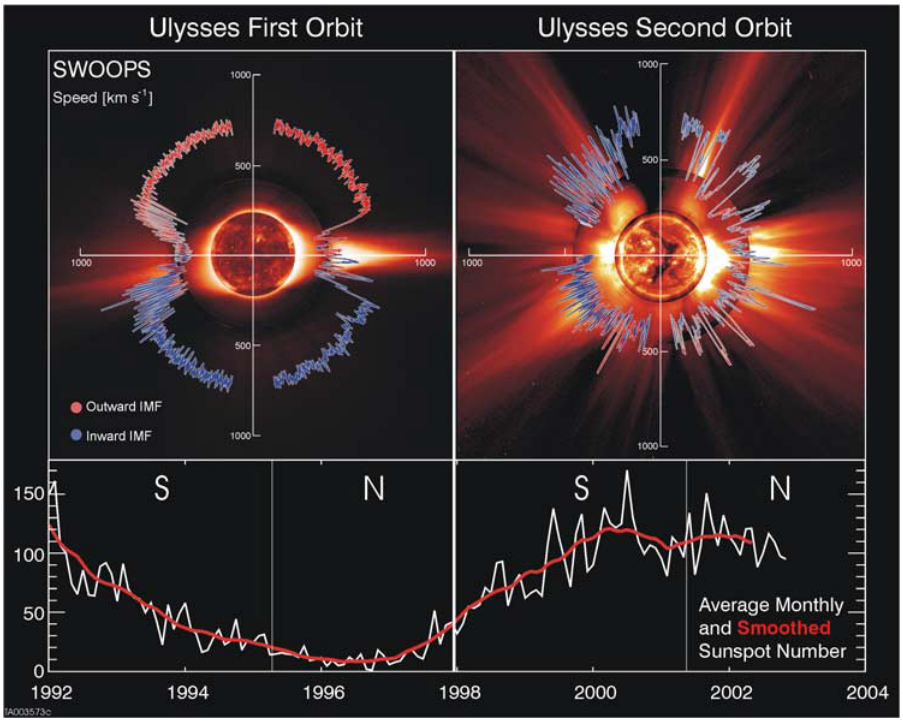

Figure 1.6: The top left and right panels show solar wind velocity (distance from the centre of the Sun) as a function of helio-latitudes during SC minimum and maximum for the first and second orbits of Ulysses, respectively. The bottom horizontal panel shows the sunspot number plotted with respect to time. The observed velocity is plotted over solar images on a typical day during solar minimum (17 August 1996) and during solar maximum (07 December 2000). (Courtesy: McComas et al., 2003)

(Figure 1.6) (Cranmer, 2009).

1.1.6 Heliospheric Current Sheet

Beyond the surface (source surface), where solar-wind plasma parcels drag the magnetic field of the Sun, the oppositely directed magnetic field lines are not allowed to form closed loops in the heliosphere. Therefore, a boundary exists between the inward and outward magnetic fields. In this boundary region, the oppositely directed open field lines run parallel to one another, separated by a thin current sheet referred to as the "interplanetary current sheet" or "heliospheric current sheet." This current sheet is tilted due to an offset between the rotational and magnetic axes of the Sun, and it is warped depending on the overall solar magnetic field. As a result, it exhibits a wavy, "ballerina skirt"-like struc-

ture as it extends into interplanetary space, as shown in Figure 1.7 (Schwenn, 2006). Because Earth occasionally resides above and sometimes below the rotating current sheet, it experiences regular, periodic changes in the polarity of the interplanetary magnetic field (IMF). These alternating periods of positive polarity (directed away from the Sun) and negative polarity (directed toward the Sun) are known as magnetic sectors.

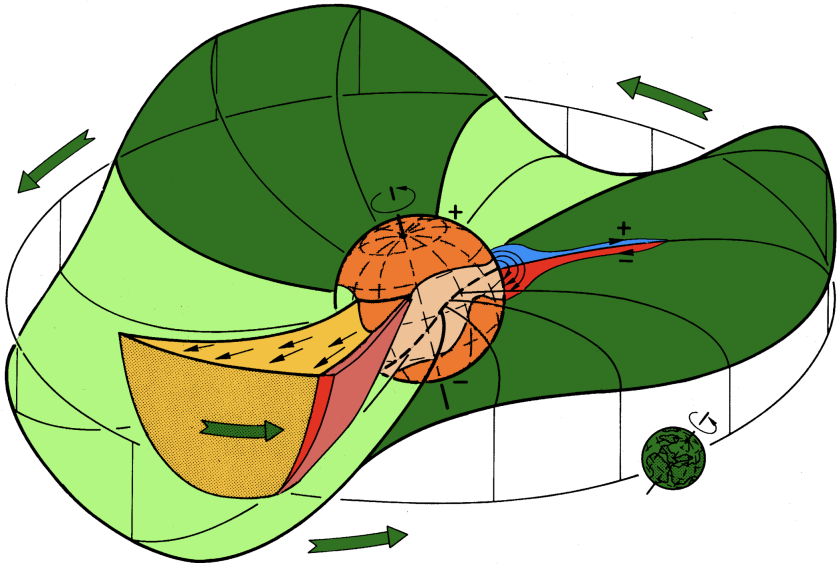

Figure 1.7: Depiction of heliospheric current sheet based on Alfven (1977) (Adapted from Schwenn (2006)).

1.1.7 Coronal and Solar Wind Modeling

Schatten and Wilcox (1968) suggested that the solar magnetic field in a low plasma β environment up to some reference height called the source surface can be extrapolated based on assumptions of current-free approximation. This assumption makes the field a potential field, i.e., solvable using the Laplace equation. Therefore, using the two boundary conditions provided by the photospheric magnetic field and the assumption that the field is radial at the reference height, the Laplace equation for the magnetic field can be solved in the domain. PFSS is the first-order and lowest-energy approximation of the magnetic field of the

Sun as compared to other computationally expensive and more advanced magnetic field models like Nonlinear Force-Free Field (NLFFF; Wiegelmann, 2004; He et al., 2011) and Linear Force-Free Field (LFFF; Alissandrakis, 1981) models.

During the Skylab era (1973-1974), it was discovered that high-speed solar wind streams originate from large coronal holes, which were later identified as regions with open and rapidly diverging magnetic field structures (Wang and Sheeley, 1990). These observations further motivated theoretical investigations into the relationship between solar wind acceleration and the nonradial expansion of the magnetic field near the Sun.

Wang and Sheeley (1990) examined the relationship between solar wind speed at 1 AU and the expansion of magnetic flux tubes (Eq:1.10), in the solar corona. They utilised 22 years (1967–1988) of solar wind velocity data from the Vela, IMP, and ISEE 3/ICE spacecraft, along with magnetograms from the Mount Wilson Observatory (MWO). Their analysis revealed an inverse correlation between solar wind speed and the magnetic flux-tube expansion factor (Eq:1.10), denoted as f_s.

$$f_s = \left(\frac{R_\odot}{R_1}\right)^2 \frac{B_r(R_\odot, \theta_0, \phi_0)}{B_r(R_1, \theta_1, \phi_1)} \tag{1.10}$$

Where $R_\odot$ and R_1 are the photospheric radius and radius of the source surface, respectively and $B_r(R_\odot, \theta_0, \phi_0)$ and $B_r(R_1, \theta_1, \phi_1)$ are the corresponding values of the magnetic field values at the respective heights along the same field line.

To predict solar wind speeds, Wang and Sheeley (1990) applied the potential field model developed by Schatten and Wilcox (1968), and investigated the role of coronal hole structures in the generation of high-speed solar wind streams.

$$V_{\mathrm{WS}}(f_s) = V_{\mathrm{slow}} + \frac{(V_{\mathrm{fast}} - V_{\mathrm{slow}})}{(f_s)^\alpha} \tag{1.11}$$

Arge and Pizzo (2000) modified the method of Wang and Sheeley (1990) by introducing an empirical model (the WS model) that relates the magnetic expansion factor of open magnetic field lines to the solar wind speed at the source surface rather than at Earth (Eq:1.11). They also implemented a simplified propagation method assuming radial solar wind streams. Their model achieved a 75% accuracy in predicting IMF polarity and a correlation coefficient of up to 0.8 for

solar wind speed at L1. Later, Riley et al. (2001) introduced a different empirical approach that modeled solar wind speed at 30 $R_\odot$ based on the distance of magnetic footpoints from coronal hole boundaries, reflecting faster wind originating deep within coronal holes and slower at their edges. Arge et al. (2003) further improved the WS model with the Wang-Sheeley-Arge (WSA) model, which combines the dependence on both the expansion factor and the angular distance from coronal hole boundaries. Their model used polar field-corrected MWO Carrington maps and provided a more refined solar wind speed prediction.

1.2 Coronal Mass Ejections (CMEs)

Coronal mass ejections (CMEs) are massive eruptions of plasma and magnetic fields from the Sun. They can carry a mass exceeding 10^{13} kg and reach speeds of several thousand kilometers per second. Typically, a CME has a mass ranging from 10^{11} to 10^{12} kg and travels at speeds between 400 and 1,000 km/s. They often span several tens of degrees in heliographic latitude and likely in longitude as well. In comparison, Earth has a mass of approximately 6×10^{24} kg and a heliographic latitude of about 0.005°. CMEs are primarily detected by coronagraphs that block out the majority of light from the photosphere, leaving the surrounding corona, which is relatively faint (Howard (2011) and references therein). Figure 1.8 shows an image of a CME captured by the LASCO coronagraph (Brueckner et al., 1995) aboard the SOHO spacecraft (Domingo et al., 1995). This example represents a "classic" three-part structure of a CME, consisting of a bright leading edge, followed by a dark cavity region (likely a flux rope), and followed by a bright filament.

CMEs generally erupt from the Sun at a rate of about one CME per two days during solar minimum and increase to 5–6 events per day during solar maximum. Only a small fraction ($\approx$ 1-2 %) of these CMEs are directed toward Earth (Robbrecht et al., 2009; Lamy et al., 2019).

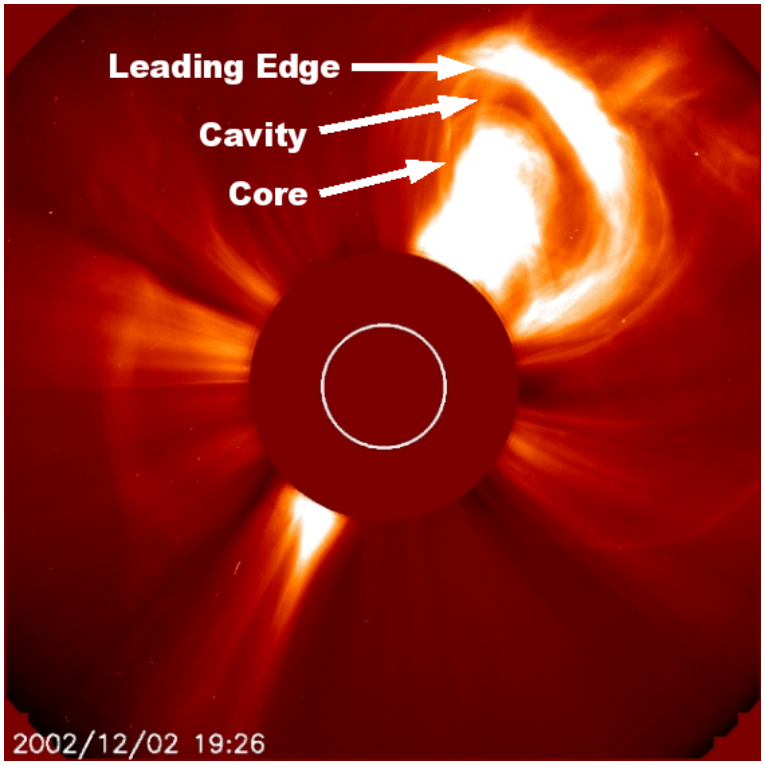

Figure 1.8: A CME on the solar limb as recorded by LASCO/C2 coronagraph on SOHO on 2 December 2002. The dark, low-density region enclosed by the bright loop of streamer material is believed to represent the magnetic flux rope structure, as predicted by contemporary CME initiation models (Adapted from Colaninno (2012)).

1.2.1 CME Initiation Mechanism

CMEs are the process through which magnetic field energy is released in the heliosphere by the Sun. The general idea of CME initiation and eruption is that a magnetic structure, held in equilibrium in the corona (and lower in the solar atmosphere) by a balance of gravity, magnetic and hydrodynamic pressure, is disturbed by the mechanism of CME onset, which disturbs the equilibrium causing parts or all of the structure to erupt in the heliosphere.

During the eruption, the coronal magnetic field must have energies comparable to the typical observed energies of the CMEs, i.e., that can accelerate a mass of 10^{13} kg to the speeds of $100 - 1000$ km/s.

CME launch is a phenomenon observed in the solar corona. This means that the energy responsible for the initial acceleration of the CME originates from

the corona itself. The energy linked to coronal electric currents is referred to as free magnetic energy. Because β in the corona is typically low, which indicates a magnetically dominated environment, suggesting the gas pressure alone cannot provide all the energy involved. Therefore, the energy of a CME is primarily supplied by the magnetic field, specifically the field present in the corona. Over time, energy accumulates in the corona due to the increasing emergence of new magnetic fields. Eventually, following a disruption or onset, it is explosively released, allowing for the emergence of new fields into a less energetic and complex region. Thus, the state of the coronal magnetic field prior to the CME launch plays a crucial role in determining both the initiation and nature of the CME.
In general, there are two classes of CME onset theories. First, those that do not require non-ideal MHD processes (magnetic reconnection), e.g., Magnetic Buoyancy, Toroidal Instability and Kink Instability. Second, there are those that involve non-ideal MHD processes, although some of these mechanisms may take place with or without magnetic reconnection, e.g., Tether cutting and Breakout model.

Magnetic Buoyancy

This mechanism explains the evolution of slowly accelerating CMEs as a result of the interplay between two natural forces (Low, 1994). First, the heated coronal plasma tends to expand outward into interplanetary space. Second, the coronal magnetic field resists being opened. When the thermal energy in the corona is sufficient to overcome both magnetic and gravitational constraints, a continuous expansion starts. According to Low (1994), the Lorentz force ($\vec{j} \times \vec{B}$) arising from the magnetic field facilitates the expansion of the plasma. However, this is countered by inward-directed magnetic curvature forces. As a result, the corona exhibits a mixture of magnetic field topologies, leading to regions with varied plasma outflows. Magnetic buoyancy thus stems from the inherent drive of the corona to expand into the heliosphere.

Toroidal Instability

This model considers the CME as a magnetic flux rope initially in equilibrium. The eruption is triggered by the injection of poloidal magnetic flux from the photosphere, which destabilises the flux rope (Chen, 1989). Although this process can lead to an eruption, it is challenging to account for the initiation and early acceleration without invoking magnetic reconnection. In this scenario, the total current $\vec{J}$ and magnetic field $\vec{B}$ generate a Lorentz force $\vec{J} \times \vec{B}$, which propels the flux rope outward from the Sun.

Kink Instability

In this mechanism, a magnetic flux rope anchored in the solar photosphere develops a twist due to the rotational motion of its footpoints (Sakurai, 1976; Fan, 2005). As the twist increases, the flux rope reaches a critical threshold, leading to instability and eruption (see Figure 1.9). Notably, kink instability can occur without magnetic reconnection. It accounts for various observed features such as sigmoid structures, soft X-ray emissions, and the twisted morphologies frequently seen in CMEs and prominences. Additionally, it provides a framework for explaining the accumulation and explosive release of plasma and energy.

Tether-Cutting Model

This model describes CME initiation as a non-ideal MHD process involving magnetic reconnection (Moore and Labonte, 1980). Reconnection rearranges magnetic field lines and converts magnetic energy into kinetic energy, heat, and particle acceleration. In the tether-cutting model, the eruption begins when magnetic reconnection beneath a sheared core field reduces the overlying strapping magnetic tension. The sheared core initially rises due to an imbalance between upward pressure and downward magnetic tension. This leads to the formation of a current sheet beneath the core, where reconnection further weakens the restraining field. As the core field erupts, it stretches surrounding magnetic field lines, which in turn fuels additional reconnection and energizes the eruption. Figure 1.10 illustrates the schematic of this process.

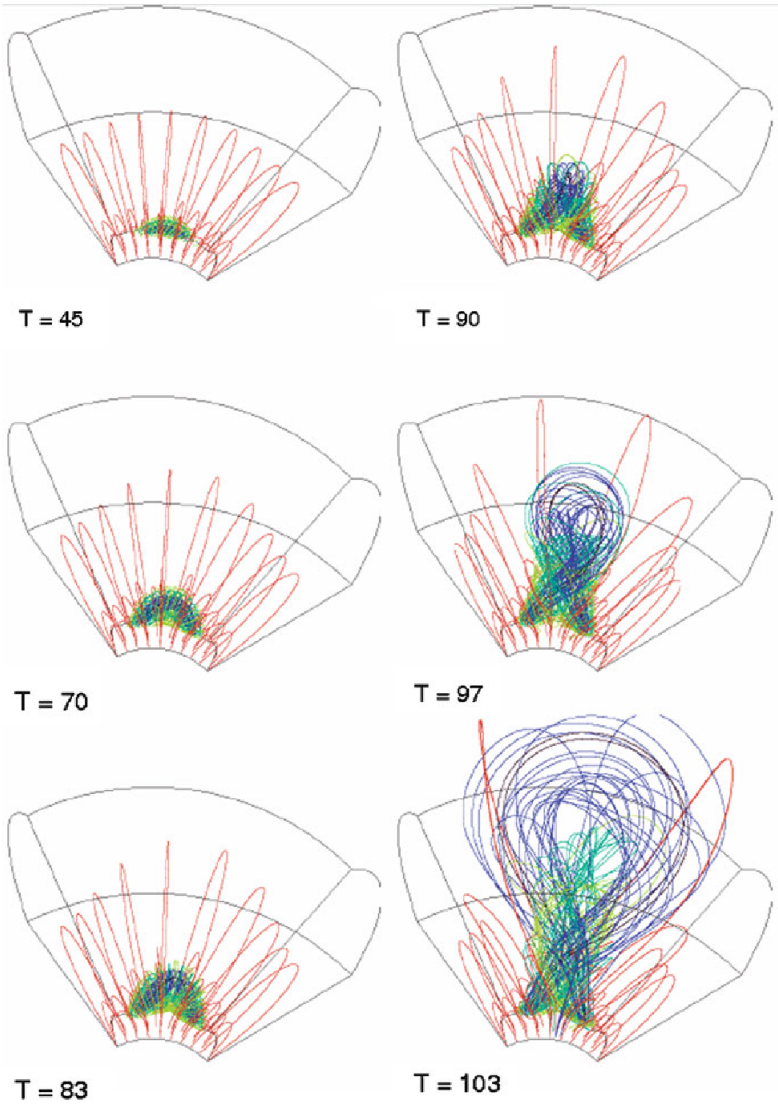

Figure 1.9: Sequence illustrating the three-dimensional evolution of the coronal magnetic field based on the kink instability model (Adapted from Fan (2005)). The thick blue/green lines depict the kinked flux rope as it erupts through the overlying magnetic field structure (shown in red), which is displaced in the process.

Magnetic Breakout Model

This model provides an alternative scenario to the tether-cutting mechanism (Antiochos et al., 1999). It also relies on magnetic reconnection, specifically between a sheared magnetic arcade and its surrounding field structures during the eruption. A key advantage of the breakout model is its ability to overcome the energy limitations of the tether-cutting model. It assumes that the CME originates as

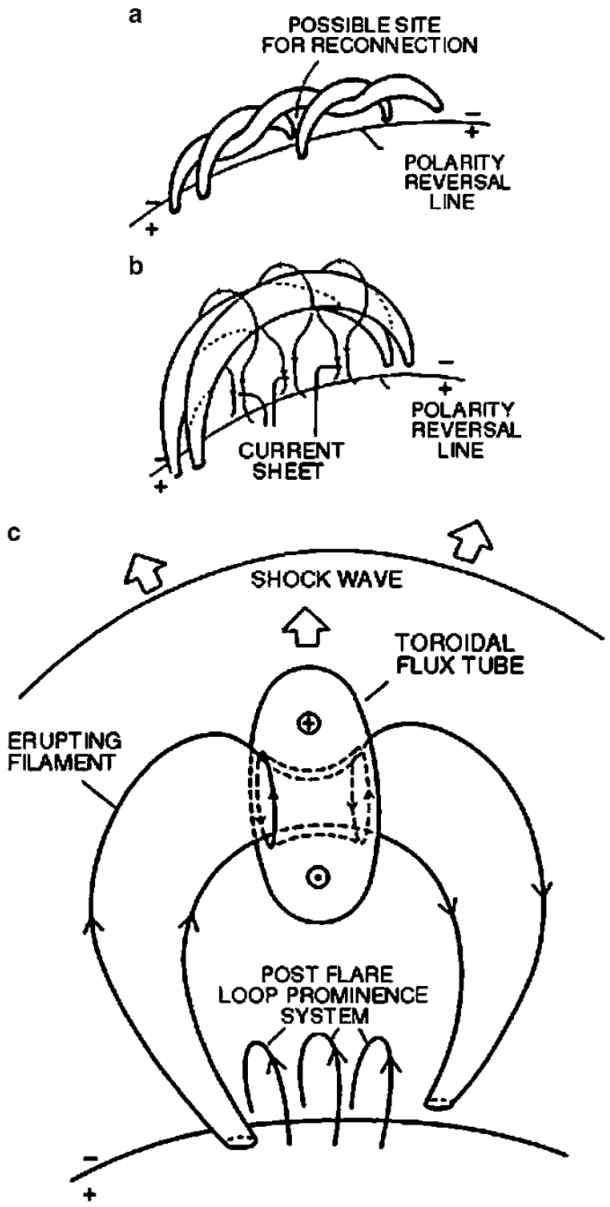

Figure 1.10: The diagram of the schematic of the Tether Cutting model according to Sturrock (1989). (a) The magnetic field configuration before the launch is associated with prominence, showing the site of the reconnection that can trigger the CME onset. (b) The launch of the structure is after magnetic reconnection, and once the structure is no longer connected to the photosphere, (c) The final magnetic field configuration, following the onset.

a closed plasmoid within an existing magnetic topology. During eruption, this plasmoid "breaks out" via reconnection with the overlying magnetic field, which remains closed. Unlike tether-cutting, the breakout model involves reconnection above the core field, allowing the erupting structure to escape by displacing the

restraining field lines.

1.3 Interplanetary Coronal Mass Ejections

An Interplanetary Coronal Mass Ejection (ICME) is the heliospheric counterpart of a CME, i.e., when the CME is at a much larger distance from the Sun (greater than 50 $R_{\odot}$). A highly structured helical magnetic field with an enhanced total magnetic field is observed within ICMEs as revealed by in-situ observations, and these are called magnetic clouds (MC), which are the counterpart of the CME flux rope (Section 1.2). Ahead of the MC, there is a turbulent region where all the in-situ parameters fluctuate rapidly, and this feature is a counterpart of the bright leading edge of CME, which shows a plasma pile-up between the CME flux rope and the shock region. However, due to the expansion of the CMEs in the heliosphere, the filament part of the CMEs is rarely observed in the in-situ observations (Figure 1.11). Moreover, the observed structure in the in-situ observations actually depends upon the relative trajectory of the ICME and spacecraft and inherent CME parameters. Given the fact that CME flux rope has geometrical parameters, modeling of the inherent helical magnetic field structures of the ICMEs in in-situ observations provides an excellent opportunity to estimate these parameters of the CME flux rope when the direct observations of ICME are not available (one of the tools used in this thesis to study ICMEs).

1.4 Evolution of CMEs in the Heliosphere

Previous studies of CMEs based on the observations made by the Large Angle and Spectroscopic Coronagraph (LASCO) (Brueckner et al., 1995) field of view (FOV) on board the SOHO mission (Domingo et al., 1995) suggested that CMEs follow a three-step evolutionary phase (Zhang et al., 2001). This includes an initiation phase, an impulsive acceleration phase, and a propagation phase (Figure 1.12). In the propagation phase, most CMEs are expected to maintain a constant direction of propagation in the heliosphere (Vourlidas et al., 2010). As a CME propagates through the heliosphere, it moves from a region of higher pressure to a region of lower pressure. Additionally, the internal magnetic pressure of the CME remains

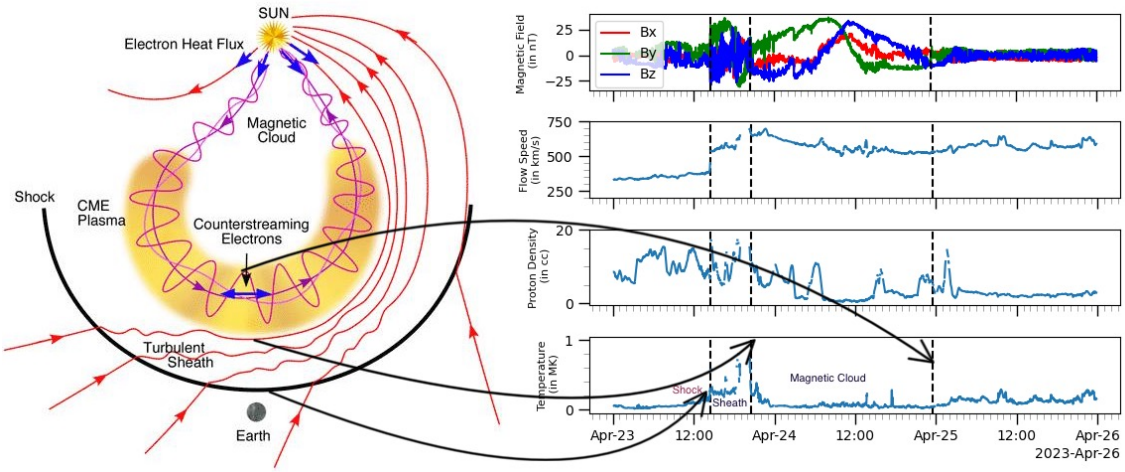

Figure 1.11: Left: Schematic illustration of an interplanetary CME (ICME), showing the leading fast-forward shock (arc), the sheath region and magnetic flux rope (Adapted from (Kilpua et al., 2017)). Right: In-situ observation of IMF, flow speed, proton density, and temperature, from top to bottom, respectively, by STEREO spacecraft observed from 23 April 2023 to 26 April 2023. The first dotted black line denotes the arrival of the shock of the CME, and the second and third dotted lines represent the start time and end time of the magnetic cloud, respectively.

more significant than the surrounding ambient pressure at all points. Assuming the ambient solar wind speed is asymptotic and a spherically symmetric ambient medium around the Sun, most CMEs are, therefore, expected to expand in a "self-similar manner." This means that, at any given time, the dimensions of the CME grow in proportion to its distance from the centre of the Sun, following the initial shape of the CME. The proportionality constant governing this expansion is commonly referred to as the "aspect ratio" (Thernisien et al., 2006; Isavnin, 2016; Sarkar et al., 2020). This type of evolution ensures that the CME maintains its original shape while expanding its size as it propagates outward. Most of the CME models, including the geometrical shape of the CME and internal magnetic field description, follow the approaches of self-similar expansion in the heliosphere (Thernisien et al., 2006; Isavnin, 2016; Sarkar et al., 2020). Previous studies have shown that while many CMEs exhibit self-similar propagation in the heliosphere, this is not always the case due to CME interaction with ambient solar wind and magnetic field (Vourlidas et al., 2010; Colaninno, 2012). Such

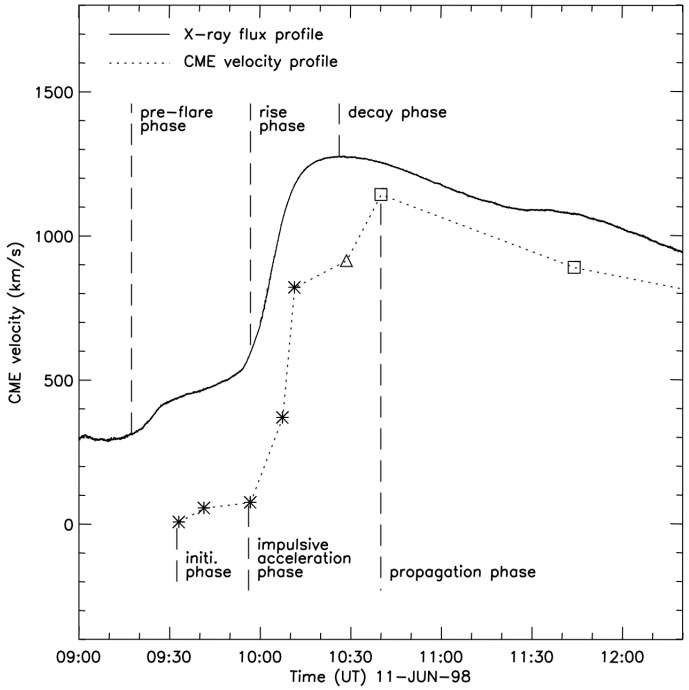

Figure 1.12: Illustration showing the three phases of the CME velocity-time profile (dotted line) alongside the temporal profile of the soft X-ray flux (solid line) for the 11 June 1998 CME. Notably, the impulsive acceleration phase of the CME aligns closely with the rise phase of the flare (Adapted from Zhang et al. (2001)).

variability can cause different parts of a CME to experience distinct interactions, leading to deflections, particularly in the lower corona, where CMEs tend to be redirected toward the HCS region. This deflection complicates the prediction of CME arrival and impact at Earth (Zhuang et al., 2017). However, there have been many studies reporting on the deflection and rotation of the CMEs in the heliosphere due to the interaction with the ambient medium(MacQueen et al., 1986; Gopalswamy and Thompson, 2000; Filippov et al., 2001; Shen et al., 2011; Gui et al., 2011; Kay et al., 2015).

1.5 Geomagnetic Storms and Space Weather

The Earth is protected from the energetic particles in CME and solar wind by the magnetosphere. Most of the time, particles in the solar wind and CMEs are deflected along the magnetosphere, thereby shielding the Earth from these eruptions. However, there are certain situations when the particles in the solar wind

or ICME make their way into the magnetosphere of the Earth, leading to global magnetospheric and ionospheric changes. This happens when the southward component of the IMF arrives at the Earth, leading to the "magnetic reconnection" at the outer edge of the magnetosphere of the Earth. Magnetic reconnection is a physical process in highly conducting plasmas where the magnetic topology is rearranged and magnetic field lines break and reconnect, leading to a rapid conversion of magnetic energy into kinetic energy, thermal energy, and particle acceleration. This leads to the opening of more field lines on the day side of the magnetosphere, causing the cusp to shift towards the equator. Although changes in ram pressure do not directly open or close field lines, they can alter the size of polar cusps. This phenomenon is called geomagnetic storms. It leads to the depression of the horizontal components of the magnetic field of the Earth (as shown in Figure 1.13). This dip is measured as an index called the disturbed storm time (Dst) index. It measures the global average decrease in the horizontal magnetic field of the Earth near the equator during geomagnetic storms. It reflects the strength of the ring current, with negative values indicating stronger storms. Furthermore, geomagnetic and solar storms can significantly impact various aspects of life on Earth. Particle injections at high latitudes can expose airline passengers to elevated levels of radiation. Particle precipitation into the upper atmosphere increases atmospheric drag, affecting the orbits of satellites and spacecraft near Earth. Disturbances in the ionosphere can disrupt telecommunications and navigation systems. High-energy particles may damage spacecraft hardware, while large-scale fluctuations in Earth's magnetic field can induce strong electric currents in power grids, potentially leading to widespread electrical failures. Recently Baruah et al. (2024) demonstrated that even moderate geomagnetic activity, enhanced by consecutive CMEs and fast solar wind, can increase atmospheric drag, leading to the loss of satellites shortly.

It is important to note that if the magnetic field of the CME is oriented northward, a major geomagnetic storm is unlikely to occur. This is because the geomagnetic field points from geographic south to north (with the geographic south pole corresponding to the magnetic north pole), which inhibits magnetic reconnection

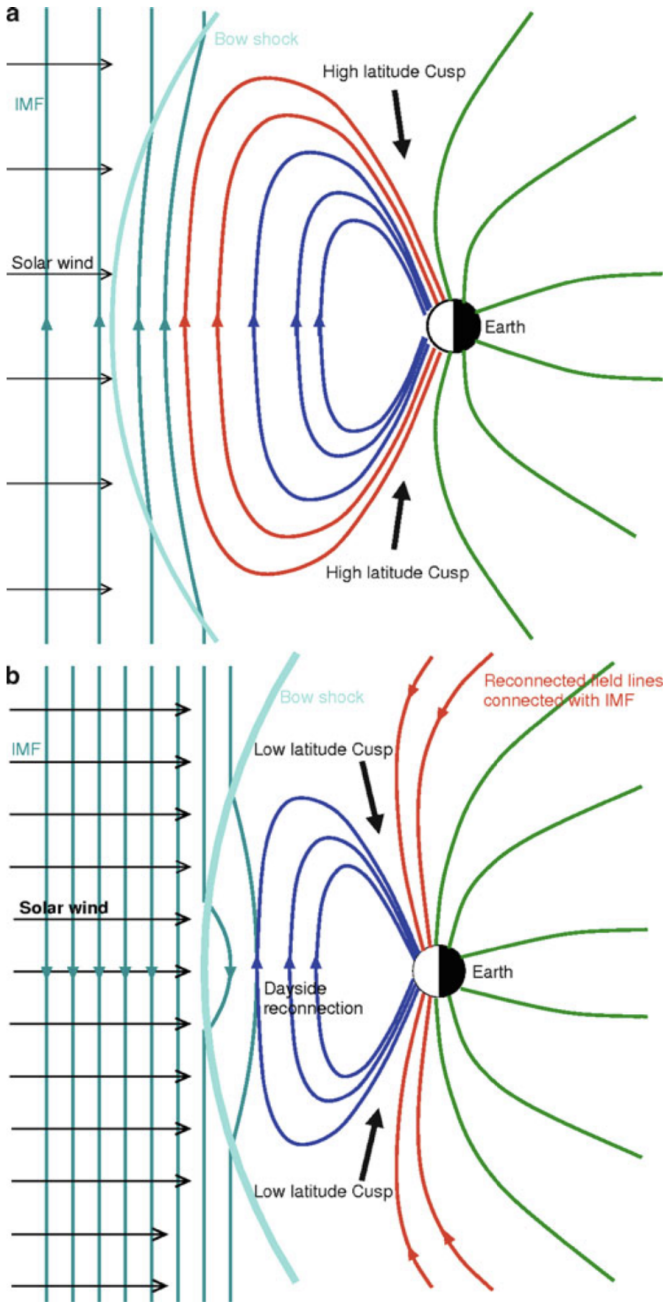

Figure 1.13: This diagram illustrates a simplified version of the magnetosphere of the Earth. (a) When the northward IMF arrives at the Earth, it is located in the cusp region at high latitudes. (b) When a southward IMF reaches the Earth, magnetic reconnection allows more day-side field lines to open (Adapted from Howard (2011)).

on the dayside. Nonetheless, some minor effects may still be observed due to increased solar wind pressure, such as expansion of the auroral oval or compression of the magnetosphere. While magnetic reconnection can still occur on the

night-side under northward or zero north–south magnetic field conditions, it does not result in geomagnetic storm activity.

1.6 Motivation for the Thesis

Understanding the propagation of CMEs through the heliosphere and their interaction with the ambient solar wind is a critical aspect of space weather research. Since CMEs travel through the solar wind, the surrounding plasma environment significantly influences their trajectory, speed, and evolution. Moreover, high-speed solar wind streams, which account for approximately 70% of geomagnetic activity outside the solar maximum phase (Richardson et al., 2000), play a particularly crucial role in shaping space weather conditions.

The solar wind affects CME propagation, leading to changes in the direction, orientation, and kinematic properties of CMEs (Shen et al., 2011; Wang et al., 2004). Therefore, studying CMEs in isolation is insufficient, and a comprehensive analysis requires a detailed understanding of the solar wind environment. To improve space weather forecasting and trajectory predictions of CMEs, multi-point remote sensing observations and the development of accurate models of the ambient solar wind are necessary. This thesis addresses two broad scientific questions on:

1. **Solar Wind Modeling and Optimization** – We analyze and optimize solar wind velocity prediction frameworks at L1 to improve forecasting accuracy across different solar cycle phases.

2. **Impact of Solar Wind on CME Propagation**– We investigate how interactions with the solar wind influence the propagation of CMEs, leading to changes in their trajectory, including deflection and rotation, as they travel through the heliosphere.

1.7 Organisation of the thesis

1.7.1 Chapter 1: Introduction

This chapter describes the structure of the Sun and the space weather phenomena and their origin, such as solar wind and CMEs. The Sun, with its complex magnetic activity, periodically emits energetic particles that affect the heliosphere and magnetosphere of the Earth. CMEs, which are large-scale expulsions of plasma and magnetic fields from the solar corona, are highlighted as the primary drivers of severe geomagnetic storms. The chapter explains the evolution of CMEs. The response of the Earth to these events is also discussed. Finally, we introduce the motivation for the research work carried out in the thesis.

1.7.2 Chapter 2: Datasets and Models

This chapter provides detailed information about the instruments, spacecraft, and datasets utilised in the thesis work. The scientific questions on CME propagation and solar wind velocity forecasting are addressed using different observations and models. We have used both remote sensing and in-situ observations. The remote sensing data primarily consists of observations of CMEs from space-based coronagraphs and heliospheric imagers. A brief description of the instruments on board different spacecraft is given in this chapter.

The in-situ parameters (at L1) include the interplanetary magnetic field (IMF), proton number density, and solar wind temperature, measured by different spacecraft like Wind, ACE and STEREO. In addition, in this chapter, we discuss the models that were used, developed, and implemented to address the research objectives of the thesis. It includes the descriptions of the computational models (analytical and empirical) specifically used, implemented and developed to carry out the work presented in this thesis.

1.7.3 Chapter 3: Solar Wind Velocity Forecasting Models – A Parametric Study

In this chapter, we develop a solar wind forecasting framework at L1. This chapter further investigates the performance and optimization of solar wind forecasting models using a large dataset spanning 60 Carrington Rotations (CR2047–CR2107), covering the declining phase of solar cycle 23 and the rising phase of cycle 24. The model framework combines three components: PFSS and SCS (for magnetic field extrapolation), WSA (for solar wind speed estimation based on expansion factor and coronal hole boundary distance), and HUX (for solar wind propagation). We found that the performance of the model significantly degrades during the deep minimum of SC23 (2008–2009), attributed to reduced coronal hole areas. A good correlation is found between the area of the coronal hole at low-mid latitudes and model performance. Distinct parameter sets are optimal during different phases of the solar cycle, highlighting the need for dynamic parameter adaptation. The chapter concludes that solar wind forecasting is sensitive to both the solar cycle phase and observed coronal hole geometry. This motivates further refinement of the model, particularly through source surface height (R_{ss}) optimization and better magnetic field input, explored in the next chapter.

The work presented in this chapter has been published in Kumar and Srivastava (2022).

1.7.4 Chapter 4: Improving Solar Wind Velocity Forecasting Models

In this chapter, we optimise R_{ss} in the PFSS model with the phase of the solar cycle to be used in the WSA model. We evaluated the performance of the solar wind velocity prediction framework (PFSS+WSA+HUX) at L1 using three different R_{ss} and three different line-of-sight GONG maps. i.e., zero-point-corrected (ZPC), hourly updated zero-point-corrected (HU ZPC) and standard maps (STD), on 16 Carrington Rotations (CRs) selected at different phases of SC24 and SC25. Our study suggests using a higher R_{ss} (3.0 $R_{\odot}$) compared to the

conventional R_{ss} (2.5 $R_{\odot}$) near the solar minimum, resulting in an up to 22 % increase in the average performance of the framework for ZPC maps. We found that by using the ZPC maps, as compared to the STD full Carrington maps, the performance of the framework was improved by a factor of two, which can be attributed to the capability of ZPC maps to capture the global magnetic field. This was also confirmed by comparing the extrapolated global magnetic field structures with the observed large-scale coronal features. We further extended our study using ZPC maps and default WSA parameters over the SC24 and SC25 (CR2092-CR2272). Our investigation from this long-term study suggested similar results as suggested by the study of 16 CRs.

The work presented in this chapter has been published in Kumar et al. (2025).

1.7.5 Chapter 5: Heliospheric Propagation of Coronal Mass Ejection: Deflection

In this chapter, we analyse a set of geo-effective CMEs using reconstruction techniques in both the corona and heliosphere. Each CME is continuously tracked to study its trajectory throughout the heliosphere. We apply a geometrical reconstruction model on coronagraph images to trace CME evolution, utilising a customised Python-based implementation. The module was further enhanced to incorporate heliospheric imager data, enabling continuous tracking of CME structures beyond the corona. We examine the changes in CME trajectories and their possible correlation with the surrounding heliospheric environment, particularly the solar wind and magnetic field conditions. The focus is on events that exhibit noticeable deflection in either latitudinal or longitudinal directions.

The work presented in this chapter has been published in Kumar et al. (2024).

1.7.6 Chapter 6: Heliospheric Propagation of Coronal Mass Ejection: Rotation

In this chapter, we investigate the evolution of CMEs that exhibit significant rotation during their heliospheric transit. CME rotation is a lesser-understood

but critical factor influencing the magnetic orientation and geoeffectiveness of CMEs. Our analysis revealed noticeable changes in the tilt of the CME structures as they propagated through the heliosphere. We found that persistent rotation in the heliosphere requires favourable conditions in both the magnetic field and solar wind structure. The study illustrates that predicting the geoeffectiveness of CMEs solely from near-Sun observations can be challenging. In this context, heliospheric imager (HI1) observations play an important role in bridging the observational gap between the Sun and Earth, thereby enhancing our understanding of CME propagation through the heliosphere. *The work presented in this chapter has been published in Kumar et al. (2023) and Kumar et al. (2024).*

1.7.7 Chapter 7: CME Deflection and its Impact on CME Arrival Time Estimation

In this chapter, we report on the propagation characteristics of the 21 April 2023 CME, which reached the Earth on 23 April 2023, leading to a strong geomagnetic storm on April 24, 2023, with a Dst index of -213 nT. Based on the 3D reconstruction of the CME close to the Sun, we estimate the arrival time of the CME by implementing the Advanced Drag Base Model (ADBM) and compare it with the actual arrival time obtained from the in-situ observations. We discuss the propagation characteristics of the CME at different spacecraft in the interplanetary medium and their impact on the arrival of the CME. Given the errors in the direction of propagation in the GCS model, we performed different analyses to estimate the direction of propagation with smaller errors. Our study also highlights the uncertainties in estimating the direction of the 21 April 2023 CME due to limited viewpoints and the consequences of these uncertainties ($\approx 20^{\circ}$ in longitude) on the prediction of the arrival time of the CME. The analysis reveals the importance of heliospheric imaging and the availability of observations from several vantage points for improving the estimation of the direction of propagation of CMEs and of arrival time.

A part of the work presented in this chapter is under review in ***Journal of Astrophysics and Astronomy****.*

1.7.8 Chapter 8: CME Modeling in the Heliosphere

In this chapter, we focused on the development and validation of a comprehensive heliospheric modeling framework aimed at improving the simulation and forecasting of CME propagation. As part of this effort, we developed an approach for inserting CMEs into the heliospheric domain by integrating an elliptical cone model into a background solar wind environment derived from the WSA model and PLUTO. To accurately represent the internal magnetic structure and evolving geometry of CMEs, we implemented the FRi3D model and extended its utility by validating the associated graphical user interface (GUI) through comparison with the well-established GCS model. This allowed for improved fitting of CME flux ropes near the Sun. We tested this framework on the 5 October 2012 CME by comparing the flux rope geometry near the Sun (from FRi3D geometric fitting) with that derived at L1 (from FRi3D magnetic field fitting). We observed significant rotation in the flux rope tilt from 54° to 95°.

1.7.9 Chapter 9: Summary and Future Scope

This chapter provides the summary and future scope of the work presented in the thesis. First, we discuss different areas of improvement in the solar wind forecasting models. Second, our study of the heliospheric propagation of the CMEs indicates that the solar wind medium plays a crucial role in the dynamics of the CMEs in the heliosphere. Further multi-in-situ multi-spacecraft studies are required, with larger data sets, to further establish and understand heliosphere rotation of the CMEs in the heliosphere. The incorporation of the advanced CME models, implemented and validated in Chapter 8, for tracking CMEs in the heliosphere, combined with full MHD modeling of the ambient solar wind, can be utilized to comprehensively understand the heliospheric propagation of CMEs.

Chapter 2

Datasets and Models

2.1 Introduction

The scientific questions on CME propagation and solar wind velocity forecasting are addressed using different observations and models. We have used both remote sensing and in-situ observations. This chapter provides detailed information about the instruments, spacecraft, and datasets utilized in the research carried out for the thesis. The remote sensing data primarily consists of observations of CMEs from space-based coronagraphs and heliospheric imagers. The in-situ parameters analyzed in this study include the interplanetary magnetic field (IMF), proton number density, solar wind temperature, and various plasma properties. These measurements are obtained from multiple spacecraft, which are detailed in the subsequent sections of this chapter. Furthermore, this chapter outlines the models that were utilized, developed, and implemented to fulfil the research objectives of the thesis. It also provides an overview of the computational frameworks—both analytical and empirical—specifically constructed and employed for the investigations presented herein.

2.2 Data

2.2.1 Large Angle Spectroscopic Coronagraph

The Large Angle Spectroscopic Coronagraph (LASCO; Brueckner et al., 1995) is a three-coronagraph system on the SOHO mission, capturing images of the solar corona from 1.1 to 30 $R_\odot$ from Earth's viewpoint. These three different coronagraphs have overlapping FOVs. It consists of LASCO-C1 (1.1–3 $R_\odot$, currently not operational), C2 (1.5–6 $R_\odot$), and C3 (3.7–30 $R_\odot$). The specifications for LASCO- C1, C2 and C3 coronagraphs are mentioned in the Table 2.1. The

Table 2.1: Instrument parameters for LASCO-C1, C2 and C3 coronagraphs. FOV, objective element (OE) and brightness range (BR) are listed here. $B_\odot$ represents the solar brightness.

	FOV ($R_\odot$)	**Occulter**	**OE**	**Pixel Size**	**BR($B_\odot$)**
C1	1.1 - 3.0	Internal	Mirror	5.6"	2×10^{-5} to 2×10^{-8}
C2	1.5 - 6.0	External	Lens	11.4"	2×10^{-7} to 5×10^{-10}
C3	3.7 - 30	External	Lens	56.0"	3×10^{-9} to 1×10^{-11}

Sun-Earth Connection Coronal and Heliospheric Investigation (SECCHI; Howard et al., 2008) is a five-telescope suite on NASA's STEREO (Kaiser et al., 2008) mission. STEREO spacecraft observe the Sun from two different viewpoints, ahead (SETEREO-A) and behind the position of the Earth (SETEREO-B), in the heliosphere. It images the heliosphere from the solar photosphere out to beyond 1 AU, using a suite of instruments: an Extreme Ultraviolet Imager (EUVI), two coronagraphs (COR1 and COR2), and two Heliospheric Imagers (HI1 and HI2) (Eyles et al., 2009). Each instrument employs 2048×2048 pixel CCD arrays, with specialised coatings for optimal performance. Nearly identical instruments are aboard the STEREO-A and STEREO-B spacecraft. The EUVI images the Sun 304 $\mathring{A}$, 171 $\mathring{A}$, 195 $\mathring{A}$ and 284 $\mathring{A}$ providing a FOV of $\pm$ 1.7 $R_\odot$.

COR1

COR1 is a Lyot-type internally occulting refractive coronagraph (Lyot, 1939), with a field of view (FOV) ranging from 1.3 $R_{\odot}$ to 4.0 $R_{\odot}$. The use of internal occultation allows for improved spatial resolution near the solar limb. COR1 produces 2 × 2 binned images of size 1024 × 1024 pixels, with an image resolution of 7.5″ per pixel and a temporal cadence of 8 minutes. The paired COR1 telescopes observe the white-light K-corona from 1.4 to 4 $R_{\odot}$ with a pass-band of 225 $\mathring{A}$ wide centered at the H_{α} line at 6563 $\mathring{A}$.

COR2 Coronagraph

COR2 is an externally occulted Lyot coronagraph. The external occulter shields the objective lens from direct sunlight, reducing stray light and enabling observations at greater distances from the Sun. COR2 complements COR1, which focuses on regions closer to the Sun. It has a bandpass from 650 to 750 nm. The main function of COR2 is to observe CMEs in polarisation brightness (pb) with a spatial resolution of 15 arcseconds per pixel. To achieve this, it captures a sequence of three linearly polarised images in quick succession to minimise motion blur.

Helisospheric Imager (HI)

Heliospheric imagers (HI1 and HI2) (Eyles et al., 2009) are mounted on the two sides of the two STEREO spacecraft, i.e., A and B. They are wide-angle visible light imagers. This instrument has two cameras, HI1 and HI2, having a FOV of 20° and 70° respectively. HI1 is off-pointed 14° from Sun and HI2 is off-pointed from Sun with 53.7° (Figure 2.1). Therefore, these two instruments, along with other instruments (COR1 &2, EUVI) of SECCHI, provide full coverage of the Sun-Earth line. The HI detectors use 2048 × 2048 pixel CCDs, with each pixel measuring 13.5 × 13.5 μm. Typically, onboard binning reduces the resolution to 1024 × 1024 bins, resulting in angular image sizes of 70 arcseconds for HI1 and 4 arcminutes for HI2. In this thesis, mainly the images from coronagraphs (COR1 & COR2) and HI1 of the SECCHI package are utilized to track the CMEs in

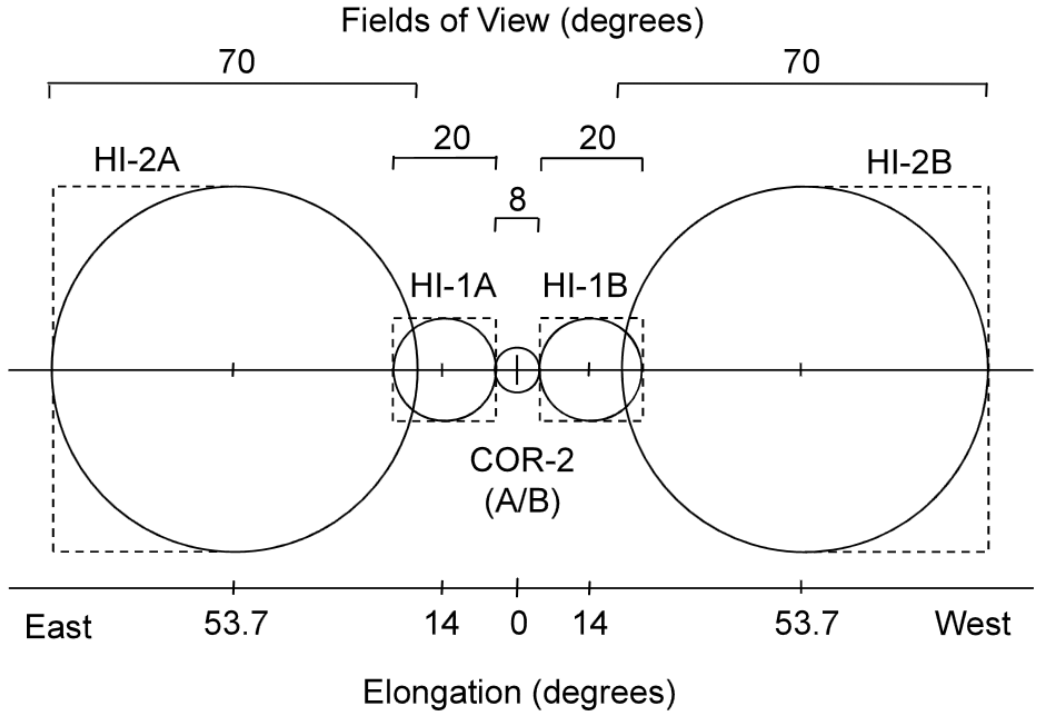

Figure 2.1: FOV coverage of different coronagraphic and heliosphere imaging instruments of SECCHI (Howard et al., 2008).

the heliosphere because CMEs generally become too faint as they reach the HI2 FOV.

Table 2.2: FOV of different Coronagraphs and Heliospheric Imager.

Coronagraph/Instrument	**Field of view**
STEREO/COR1	1.3-4.0 $R_{\odot}$
STEREO/COR2	2.0-15 $R_{\odot}$
SOHO/LASCO/C2	2.0-6 $R_{\odot}$
LASCO/C3	3.7-30 $R_{\odot}$
STEREO/HI1	20° approx 20-80 $R_{\odot}$

2.2.2 Sun Watcher using Active Pixel System Detector and Image Processing (SWAP)

We have used observations from the SWAP (Sun Watcher using Active Pixel System Detector and Image Processing) instrument, which is an EUV imager with a passband centred at 174 Å onboard the PROBA2 (Project for Onboard Autonomy 2) mission (Berghmans et al., 2006; Santandrea et al., 2013; Halain et al., 2013; Seaton et al., 2013; West et al., 2022). SWAP images the solar corona at a cadence of 110s and has a FOV of 1.7 $R_{\odot}$ on the side and 2.5 $R_{\odot}$ in the corners. This passband provides an excellent opportunity to observe features like active regions (ARs), streamers, and coronal fans that dominate the large-scale structure of the lower corona.

2.2.3 Advanced Composition Explorer (ACE)

The Advanced Composition Explorer (ACE; Stone et al., 1998) carries six high-resolution spectrometers that analyse the elemental, isotopic, and ionic charge composition of nuclei from hydrogen to nickel ($1 \leq Z \geq 28$). These measurements span energy ranges from $\approx$ 1 keV/nucleon (solar wind) to $\approx$ 500 MeV/nucleon (galactic cosmic rays). The ACE spacecraft carries nine scientific instruments designed to study the composition and behaviour of energetic particles from the solar wind, interstellar medium, and galactic cosmic rays. Each instrument is optimised for specific measurements across a broad energy range. In this thesis, the data from the following instruments are used.

1. Solar Wind Electron, Proton, and Alpha Monitor (SWEPAM): It measures three-dimensional characteristics of solar wind electrons and ions of energy range: $\approx$ 1 eV – 35 keV (McComas et al., 1998).
2. Magnetometer (MAG): It is a twin triaxial fluxgate magnetometer to measure the vector magnetic field in the interplanetary medium (Smith et al., 1998).

A 64-second average from the MAG and SWEPAM taken from (`https://izw1.`

caltech.edu/ACE/ASC/level2/lvl2DATA_MAG-SWEPAM.html) is utilised to model the ICME magnetic field at L1.

2.2.4 OMNI Database

The OMNI database includes Low-Resolution OMNI (LRO) and High-Resolution OMNI (HRO) datasets. Detailed information on LRO and HRO is available on OMNI Web (https://omniweb.gsfc.nasa.gov/form/dx1.html).

1. LRO data are available on hourly, daily and 27-day cadence (used in this thesis).
2. HRO data are available at 1-minute and 5-minute intervals.

In this thesis, hourly-averaged solar wind velocity data from the OMNI database (LRO data) are used to compare with the modeled solar wind velocity at L1. The LRO dataset spans from 1963 to the present and is compiled from various spacecraft operating in geocentric and L1 orbits. Apart from ACE, the WIND (Harten and Clark, 1995) spacecraft of NASA is a solar wind monitoring mission positioned near the Lagrange point L1, providing crucial upstream measurements of solar wind plasma, magnetic fields, and energetic particles. The OMNI data have been extensively cross-compared and, in some cases, cross-normalised between different spacecraft and parameters. In particular, the cross-normalization between ACE and Wind measurements is described in detail in King and Papitashvili (2005).

2.2.5 Global Oscillation Network Group (GONG) Magnetograms

GONG is a global, ground-based solar observing network mainly developed for helioseismology (Harvey et al., 1996; Hill, 2018). The six observatories of the GONG program are the Teide Observatory (Canary Islands), the Learmonth Solar Observatory (Western Australia), the Big Bear Solar Observatory (California), the Mauna Loa Observatory (Hawaii), the Udaipur Solar Observatory (India) and the Cerro Tololo Inter-American Observatory (Chile).

GONG magnetograms[1] are full-disk solar line-of-sight magnetic field maps taken at a cadence of 1 minute. GONG uses the Ni I 6768 Å spectral line for its magnetic field observation. 1-minute images are averaged over 10 minutes, with quality control (bad images removed), then sent to the Boulder data centre. These are then used to make hourly updated synoptic maps. GONG telescopes have a resolution of 5 arcsec, and full-disk images are 1024×1024 pixels (Harvey et al., 1996).

GONG provides several types of solar magnetograms for studying the photospheric magnetic field of the Sun and modeling space weather phenomena. The most basic and widely used are the line-of-sight (LOS) magnetograms, which measure the component of the solar magnetic field directed along the line of sight. To improve accuracy, zero-point corrected (ZPC) magnetograms are produced by removing instrumental biases. GONG also provides merged magnetograms, which combine data from its six ground-based observatories to generate high-coverage full-disk maps (Hill, 2018).

For large-scale studies, synoptic magnetograms or standard synoptic maps (hourly updated) are produced by stacking full-disk magnetograms of the GONG over a solar rotation (27.27 days) into a global magnetic field map. These maps are generated by averaging 1-minute cadence magnetograms into 10-minute intervals, remapping them into heliographic coordinates, and combining them with a cosine(longitude) weighting scheme in the Carrington frame. Prior to remapping, LOS data are converted to magnetic flux density under the assumption of approximately radial fields at the photosphere, which holds reasonably well outside strong active regions. Corrections are also applied for polar limb noise using polynomial fits, since direct observations at high latitudes are limited. These maps offer a reliable picture of the steady-state field but are less sensitive to short-lived magnetic features.

To address this limitation, GONG provides Janus synoptic magnetogram maps, which are composite maps combining the most recent hourly-averaged full-disk magnetograms with the classic synoptic map for the far side of the Sun. These

[1] https://gong.nso.edu/data/magmap/archive.html

Janus maps are especially useful for capturing transient magnetic structures in the Earth-facing hemisphere, offering an improved estimate of the full-surface field distribution at a given hour. Hourly synoptic magnetic maps (180×360 pixels) in sin latitudes are used in this thesis.

2.2.6 Python Packages Used

Most of the remote sensing and in-situ data mentioned in the above Sections, used in this thesis, are mainly accessed through the following Python packages.

1. Sunpy (The SunPy Community et al., 2020): It is a Python library for solar data analysis, offering tools for accessing, processing, and visualizing solar physics datasets.

2. pySpedas (Grimes et al., 2024): It is a Python implementation of the Space Physics Environment Data Analysis System, used for loading and analyzing space-based mission data.

3. Helioviewer (Stys et al., 2015): It is a web-based and API-accessible tool for browsing and visualizing solar and heliospheric images from multiple spacecraft missions.

2.3 Models

2.3.1 Coronal Magnetic Field Models

As mentioned in Chapter 1, in the solar corona, plasma dynamics and magnetic field are closely interlinked. In particular, within low plasma β regions, when the plasma dynamics is dominated by the magnetic field, accurate modeling of the magnetic field is essential for understanding the overall plasma dynamics. In this section, we discuss the magnetic field models that are applicable to the solar corona. We used the following models to model the coronal magnetic field.

Potential Field Source Surface (PFSS) Model

In the solar corona, the plasma beta is low, i.e.,

$$\beta = \frac{P_{\text{gas}}}{P_{\text{mag}}} \ll 1, \tag{2.1}$$

where P_{gas} is the gas pressure and $P_{\text{mag}} = \frac{B^2}{2\mu_0}$ is the magnetic pressure. Therefore, the magnetic field dominates and the Lorentz force must vanish for a steady-state solution (LHS of Eq:1.2=0):

$$\mathbf{J} \times \mathbf{B} = \mathbf{0}. \tag{2.2}$$

Using Ampère's law ($\mathbf{J} = \frac{1}{\mu_0}\nabla \times \mathbf{B}$), this gives the force-free condition:

$$(\nabla \times \mathbf{B}) \times \mathbf{B} = \mathbf{0}. \tag{2.3}$$

This implies that the current density $\mathbf{J}$ is parallel to the magnetic field $\mathbf{B}$:

$$\nabla \times \mathbf{B} = \alpha(\mathbf{r})\mathbf{B}, \tag{2.4}$$

where $\alpha(\mathbf{r})$ is a scalar function that may vary with position. The magnetic field must also satisfy the solenoidal (divergence-free) condition:

$$\nabla \cdot \mathbf{B} = 0. \tag{2.5}$$

Based on the value of α, there are three types of force-free fields:

- **Potential field:** $\alpha = 0$
- **Linear force-free field:** $\alpha =$ constant
- **Nonlinear force-free field:** $\alpha = \alpha(\mathbf{r})$

PFSS (Schatten et al., 1969) stands for Potential Field Source Surface. It is a magnetic field extrapolation method to obtain the structure of the magnetic field from the solar surface to source surface height for $\alpha = 0$. In particular, the magnetic field on the solar surface can be extrapolated based on assumptions that the current density J=0, identically, in the region between the solar surface and the source surface.

$$J = \nabla \times \vec{B} \;\; = \;\; 0 \tag{2.6}$$

The direct implication of the above equations is that the magnetic field in this region is a potential field, $\nabla\Psi$, i.e,

$$\vec{B} = -\nabla\Psi \tag{2.7}$$

$$\nabla^2\Psi = 0 \tag{2.8}$$

Using the appropriate boundary conditions given below, we can extrapolate the field to the source surface by solving the above boundary value problem.

1. $\vec{B}$ is radial at solar surface (from photospheric magnetic field maps).

2. At the source surface B_θ=0, B_ϕ =0.

Using these two boundary conditions, we can calculate $\vec{B}$ in this region. It is worth noting that, although the height of the source surface is theoretically determined by the balance between the magnetic field and the plasma energy density in the solar atmosphere (Schatten and Wilcox, 1968), a conventional value of 2.5 $R_\odot$ is commonly used in practice Nikolić (2019).

2.3.2 Schatten Current Sheet (SCS) Model

The PFSS model becomes increasingly inaccurate for magnetic field extrapolation beyond approximately 2.5 $R_\odot$. This limitation arises because the radial and transverse components of the magnetic field decay at different rates with distance from the Sun. Consequently, the assumption of a current-free (potential) field breaks down in this region. To incorporate the effects of electric currents beyond 2.5 $R_\odot$, alternative models have been considered. One such model is the Schatten Current Sheet (SCS) model (Schatten, 1972). This model assumes a unipolar magnetic field at the source surface and relaxes the field into a minimum-energy configuration. To achieve this, a current sheet is introduced between regions of opposite magnetic polarity, effectively preventing field lines of different polarities from directly connecting. The resulting electric current flows primarily in the transverse direction. To apply the SCS model for magnetic field extrapolation beyond the source surface, the first step is to enforce a radially outward orientation of all field lines at the source surface. Specifically, wherever the radial component B_r

is negative, the signs of B_r, B_θ, and B_ϕ are reversed to ensure consistent outward direction. After establishing a fully radial field at the source surface, the magnetic field is extrapolated outward using a spherical harmonics expansion. This provides analytical expressions for the magnetic field components at any point above the source surface.

$$B_r = \sum_{n=0}^{\infty}(n+1)\left[\frac{R_1}{r}\right]^{n+2}\sum_{m=0}^{n}(g_n^m \cos m\phi + h_n^m \sin m\phi)P_n^m(\cos\theta) \tag{2.9}$$

$$B_\theta = -\sum_{n=0}^{\infty}\left[\frac{R_1}{r}\right]^{n+2}\sum_{m=0}^{n}(g_n^m \cos m\phi + h_n^m \sin m\phi)P_n'^m(\cos\theta) \tag{2.10}$$

$$B_\phi = \sum_{n=0}^{\infty}\left[\frac{R_1}{r}\right]^{n+2}\sum_{m=0}^{n}\frac{m}{\sin\theta}(-h_n^m \cos m\phi + g_n^m \sin m\phi)P_n^m(\cos\theta) \tag{2.11}$$

Here, the prime symbol ($'$) denotes differentiation with respect to θ, and R_1 represents the source surface radius. By seeding the magnetic field components B_r, B_θ, and B_ϕ at R_1, the spherical harmonic coefficients g_n^m and h_n^m can be determined using a least-squares fitting method. It is important to note that these are reoriented fields, enforced to be radially outward at the source surface. Initially, this reorientation may appear to violate the Maxwell equation $\nabla \cdot \mathbf{B} = 0$. To address this, the field vectors must be reoriented back from radially outward to inward at locations where their directions were previously altered, before finalising the solution. Such a reversal of field direction does not affect the energy configuration of the system, as Maxwell's stress-energy tensor remains invariant under this transformation. Moreover, to separate the radially inward and outward field lines at the boundary, a current sheet must exist between them—hence the term "Schatten Current Sheet." It should also be noted that the boundary conditions used in the PFSS and SCS models are inherently incompatible. This mismatch may introduce discontinuities or kinks at their interface. To mitigate such issues, the PFSS solution at a slightly lower height $2.3\,R_\odot$, was used as the input boundary for the SCS model. This adjustment helps ensure a smoother transition between the two models (McGregor et al., 2008).

2.3.3 Solar Wind Modeling in the Heliosphere

We divide the region from the solar photosphere to the L1 point into two domains. The first region spans the inner corona up to 2.5–5 $R_\odot$, and the second region extends from there to L1. Solar wind velocity prediction at L1 involves:

- Computing the coronal magnetic field (first domain) via extrapolation methods (e.g., PFSS, SCS) using observed photospheric magnetic fields.
- Applying an empirical velocity relation based on magnetic field line properties at the coronal outer boundary.
- Propagating the velocity estimates from this boundary to L1.

Empirical velocity relation in the coronal domain

Extrapolated magnetic field lines up to the source surface outline the magnetic structure of the inner corona. Empirical models such as Wang-Sheeley (WS; Wang and Sheeley, 1990), Wang-Sheeley-Arge (WSA; Arge et al., 2003), and Distance from Coronal Hole Boundary (DCHB; Riley et al., 2001) estimate solar wind speeds at the outer coronal boundary (2.5–5 $R_\odot$) using open field line properties. This thesis uses the well-established WSA model from Riley et al. (2015) for solar wind velocity estimation. It accounts for the expansion factor (f_s) and the angular distance (θ_b) between a footpoint of the open field line and the nearest coronal hole boundary (Arge et al., 2003). Since coronal holes are sources of fast wind, this position is crucial in velocity estimation at the outer boundary (e.g., from PFSS or SCS models).

Extrapolation of Solar Wind Velocity into the Heliospheric domain

The WSA model provides the solar wind velocity maps at the outer boundary of the coronal domain, i.e., at 2.5 $R_\odot$ or 5 $R_\odot$ based on the choice of magnetic field extrapolation method. For comparison with the observed solar wind velocities at the L1 point by the in-situ spacecraft, it is required to extrapolate these velocities into the inner heliosphere. This requires the coupling of the coronal model with heliospheric velocity extrapolation models. We have employed one such model

called Heliospheric Upwind eXtrapolation (HUX; Riley and Lionello, 2011) to extrapolate from the outer boundary of the coronal domain to L1. The HUX model assumes the solar wind flow at the outer boundary of the coronal domain to be time-stationary. The HUX is essentially a 1D extrapolation model that neglects the effects of magnetic fields, pressure gradients and gravity. Apart from 1D extrapolation of from HUX we also employ the MHD code PLUTO (Mignone et al., 2007) to estimate the solar wind velocity profile in the heliosphere in full 3D for CME simulation in the heliosphere (Chapter 8).

2.3.4 CME Tracking and Dynamics

In order to study the evolution of the structure/configuration of a CME, throughout its propagation from the Sun to the Earth 3D stereoscopic reconstruction of the CME is required using images from different viewpoints of the Sun.

Graduated Cylindrical Shell (GCS) Model

Graduated Cylindrical Shell reconstruction is a technique to describe the self-similar expansion of a CME (Thernisien et al., 2006). This model describes the shape of the CME, containing two conical legs on which a cylindrical shell is graduated. Figure 2.2 represents an illustrative example of the GCS model. GCS model reconstruction has parameters as follows:

1. Latitude of the axis (θ).
2. Longitude of the axis (ϕ).
3. Half angle between the legs of the axis (α).
4. Height of the modeled flux rope (h).
5. Tilt of the modeled axis with respect to the ecliptic plane (γ).
6. Aspect ratio (κ=sin(δ)).

The first two parameters give us an estimate of the direction of propagation of the CME. The last four parameters define the overall configuration of the CME. We used the running difference images from SOHO/LASCO C2 and C3

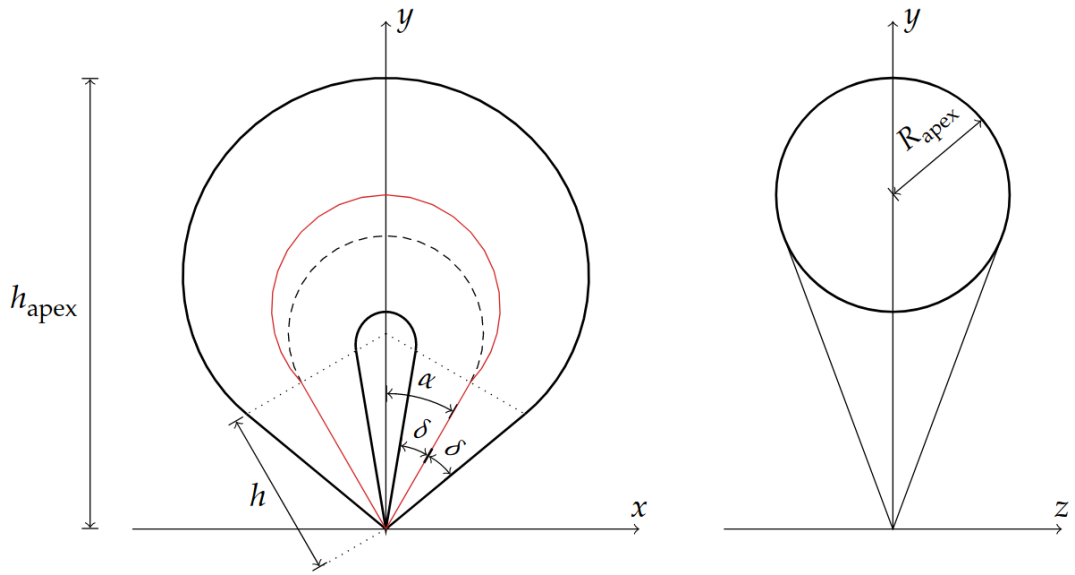

Figure 2.2: Illustration of the Graduated Cylindrical Shell (GCS) model and the definitions of the parameters h, α, δ, and R_{apex}. The left panel presents a side view of the CME in the x–y plane. The thick black line outlines the outer boundary of the flux rope, while the red line represents its central axis. The dotted lines indicate the transition between the front section and the legs of the CME. The dashed circular arc illustrates that the curvature of the front section varies and does not maintain a constant radius. The right panel shows a cross-section in the perpendicular y–z plane, where the thick circle marks the cross-sectional outline of the CME front, and the thin lines represent the conical legs (Adapted from Thernisien et al. (2006)).

coronagraphs for the GCS reconstruction. We also used COR2 images from the STEREO (A & B) spacecraft. The images from these coronagraphs are conventionally used by the community for GCS reconstruction of CMEs; since our goal is to trace the GCS parameters as far as possible, we also incorporated the HI1 images for GCS reconstruction. We have developed an existing Python module for GCS reconstruction to incorporate HI1 level 2 images (`https://github.com/johan12345/gcs_python`). Using this module, we continuously tracked the CMEs up to $\approx 50\ R_{\odot}$.

In-Situ Interplanetary Magnetic Field (IMF) Modeling

As the CMEs travel in the heliosphere, they become too faint, and therefore it becomes difficult to apply stereoscopic reconstruction (e.g., the GCS model) in

the HI1 images. However, modeling the in-situ parameters offers an alternative approach to estimate the geometrical properties of CMEs in the heliosphere at different heliocentric distances. To determine the geometrical parameters of the flux rope at L1, we used the cylindrical and toroidal flux rope models developed by Marubashi to fit the observed IMF data from the ACE. Cylindrical and toroidal flux rope models assume a force-free configuration with a constant α. The cylindrical fitting provides the latitude (θ_a) and longitude (ϕ_a) of the flux rope axis in GSE coordinates (Marubashi and Lepping, 2007; Marubashi et al., 2017), from which the axial tilt angle (Φ_c) can be derived:

$$\sin\Phi_c = \sin\theta_a / \sqrt{\sin^2\theta_a + \cos^2\theta_a \sin^2\phi_a} \tag{2.12}$$

$$\cos\Phi_c = \cos\theta_a \sin\phi_a / \sqrt{\sin^2\theta_a + \cos^2\theta_a \sin^2\phi_a} \tag{2.13}$$

We also used the torus fitting of the IMF to derive the tilt of the toroidal flux rope at 1AU. We used the two parameters of the Marubashi toroidal model fitting, that is, θ_n and ϕ_n (latitude and longitude of the normal of the plane containing the axial field of the torus). These parameters provide the tilt of the toroidal flux rope (Φ_t) at L1 given by:

$$\cos\Phi_t = -\sin\theta_n / \sqrt{\sin^2\theta_n + \cos^2\theta_n \sin^2\phi_n} \tag{2.14}$$

$$\sin\Phi_t = \cos\theta_n \sin\phi_n / \sqrt{\sin^2\theta_n + \cos^2\theta_n \sin^2\phi_n} \tag{2.15}$$

Advanced Drag Based Model (ADBM)

The CME model discussed in the previous section is mainly used to track the CMEs and study kinematics or to estimate its geometrical parameters in the heliosphere. This information is insufficient to predict the CME impact and its arrival time at Earth because, as the CME propagates in the heliosphere, it interacts with the ambient solar wind. To predict the time of arrival of CME, we need to incorporate models for heliospheric propagation and its interaction with the ambient solar wind. This involves full 3D MHD modeling of the ambient solar wind and CME structures (e.g., Kumar et al., 2020; Xie et al., 2004; Odstrčil and Pizzo, 1999; Isavnin, 2016; Singh et al., 2020). While these models can predict in-situ properties of CMEs at L1, they are computationally intensive. Given

the drag-dominated nature of heliospheric propagation, simpler models are often preferred for their speed and arrival time estimation with reasonable accuracy. The drag-based model (DBM) estimates the arrival time of the CME apex at Earth, accounting for acceleration or deceleration due to drag, but neglects CME geometry (Vršnak and Žic, 2007; Vršnak et al., 2013). The advanced drag-based model (ADBM) improves on this by including both the drag force and CME geometry (Žic et al., 2015). This model is based on the assumption that beyond a certain heliocentric distance, the ICME propagation is governed solely by its interaction with the ambient solar wind. In a simplistic case, the interaction of CME and ambient medium can be considered to be dominated by drag only, and the equation of the CME apex in this case can be written as:

$$a = -\gamma(v - w)|v - w| \tag{2.16}$$

where:

- a is the ICME front acceleration,
- v is the ICME speed,
- w is the ambient solar wind speed,
- γ is the drag parameter (drag efficiency).

The drag parameter γ is defined as:

$$\gamma = \frac{C_d A \rho_{\mathrm{SW}}}{M} \tag{2.17}$$

where:

- C_d is a dimensionless drag coefficient,
- A is the ICME cross-sectional area,
- ρ_{SW} is the solar wind density,
- M is the ICME mass. It is important to note here that in ADBM & DBM the mass of the CME is considered to be constant.

Under the assumption that the cross-sectional area of the CME is proportional to the square of heliocentric radial distance and an inverse relation for the density of the solar wind and constant CME mass, γ can be expressed as:

$$\gamma \approx C_d \frac{1}{L} \frac{\rho_{\mathrm{SW}}}{\rho_{\mathrm{ICME}}} \tag{2.18}$$

where L is the ICME thickness and ρ_{ICME} its density.

Cone Geometry Extension

To account for the ICME shape, the DBM is extended using cone geometry. For a cone with angular half-width ω, the radial distance R_α of an element at angle α from the apex is:

$$R_\alpha = \frac{R_0}{\cos\alpha + \frac{\sqrt{\tan^2\omega - \sin^2\alpha}}{1+\tan\omega}} \tag{2.19}$$

Similarly, the speed of this element is:

$$v_\alpha = \frac{v_0}{\cos\alpha + \frac{\sqrt{\tan^2\omega - \sin^2\alpha}}{1+\tan\omega}} \tag{2.20}$$

where R_0 and v_0 are the apex distance and speed.

In this thesis, we used the online tool[2]for the ADBM model discussed above to estimate CME arrival time at the Earth.

2.4 Codes and Models Implemented/Developed for CME and solar wind study

In addition to the models discussed in this chapter (Section), we have developed and implemented several other CME and solar wind models. Recognizing the limited applicability and lack of physical detail in the ADBM and simple geometrical models, we have modeled CME propagation in a more realistic solar wind background. Specifically, we developed a code for the WSA model using the pfsspy library (Stansby et al., 2020a) to generate solar wind boundary conditions. These boundary conditions are then coupled with a heliospheric model based on the PLUTO code (Mignone et al., 2012), which simulates the ambient solar wind

[2] https://ccmc.gsfc.nasa.gov/requests/SH/cdbm_20150204/dbm.php

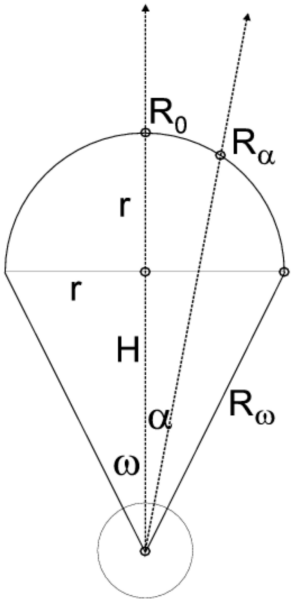

Figure 2.3: Geometry of a CME as assumed in the advanced drag-based model. Here, the leading edge is considered to be a semi-circle, spanning over the full angular width of the ICME, 2ω.

environment for CME propagation.

For the CME modeling, we implemented an elliptical CME model to be launched in the ambient solar wind. To capture the internal magnetic field configuration of CMEs, we implemented the Flux Rope in 3D model (FRi3D; Isavnin, 2016). These models are discussed in Chapter 8, and there we also discuss validation for these model implementations.

This chapter presented the data sources, instruments, and models used to study the solar wind and CMEs. The work presented in this thesis combines in-situ and remote sensing observations with numerical models to explore solar wind structures and the heliospheric evolution of CMEs. In the upcoming chapters, we describe the work that was carried out to address the scientific objectives of the thesis.

Chapter 3

Solar Wind Velocity Forecasting Models: A Parametric study

3.1 Introduction

Many of the semi-empirical physics-based operational space weather forecasting frameworks, such as WSA-ENLIL (Arge and Pizzo, 2000; Odstrcil et al., 2004), European Heliospheric Forecasting Information Asset (EUHFORIA; Pomoell, Jens and Poedts, S., 2018), and Space Weather Adaptive SimulaTion Framework for solar wind (SWASTi-SW; Mayank et al., 2022), are based on magnetic field extrapolation models. These frameworks combine the coronal magnetic field and heliospheric models to forecast the solar wind properties at L1. Generally, Potential Field Source Surface (PFSS; Schatten et al., 1969) extrapolation model, which provides an overall magnetic field environment, is used as an input in empirical solar wind models. PFSS is the first-order and lowest-energy approximation of the magnetic field of the Sun as compared to other computationally expensive and more advanced magnetic field models like Nonlinear Force-Free Field (NLFFF; Wiegelmann, 2004; He et al., 2011) and Linear Force-Free Field (LFFF; Alissandrakis, 1981) models. Further, there is a class of models providing full 3D MHD treatment of the coronal domain, such as Alfvén Wave Solar Model (AWSoM; van der Holst et al., 2014) and data driven COolfluid COroNa UnsTructured (COCONUT; Perri et al., 2022) model. The quick computation time

makes PFSS a suitable choice for use in operational space weather forecasting frameworks.

One-dimensional (1D) kinematic methods, such as Heliospheric Upwind eXtrapolation (HUX; Riley and Lionello, 2011) and its time-dependent version HUXt (Owens et al., 2020), offer efficient velocity forecasts but lack detail on other plasma properties. Accurate solar wind modeling relies on understanding ambient conditions, with early efforts led by the Wang–Sheeley (WS) model, which linked the solar wind speed at L1 to the expansion factor f_s of the open field lines, via an inverse relationship (Wang and Sheeley, 1990).

In addition to the coronal magnetic field-based models, WS, Wang-Sheeley-Arge (WSA), Distance from Coronal Hole Boundary (DCHB) discussed in the Chapter 2, solar wind forecasting models also include statistical models. These models use historical solar wind data to generate ensembles and predict parameters such as velocity by matching current conditions to past patterns (Owens and Riley, 2017). Statistical models lack physical interpretability and cannot capture sudden environmental changes (MacNeice et al., 2018).

Riley et al. (2015) evaluated empirical solar wind models (WS, WSA, and DCHB) using HUX, for 14 CRs between CR1900 and CR2100 without applying the Schatten Current Sheet (SCS) model. They found the WS model performed poorly from mid-2007 to 2009, likely due to the presence of the pseudo-streamers on the Sun. They reported that on average, the WS model had a correlation coefficient (cc) between modeled and observed solar wind velocity profile at L1 of 0.27, while WSA scored 0.39.

The performances of the empirical models (WSA or WS) are often related to the curvature of the Polarity Inversion Line (PIL) on the source surface the outer boundary of the PFSS model across which the radial component of the magnetic field changes its sign (McGregor et al., 2008). A significant curvature of the PIL near the sub-Earth point is often related to the minimum error in the predictions made by empirical models like WSA.
Although the solar community uses a fixed value of PFSS surface (2.5 $R_\odot$), however the source surface height might change with the phase of the solar cycle (SC).

Previous studies have shown that during the solar minimum, a lower source surface radius gives better magnetic field extrapolation in the heliosphere and in the corona (Lee et al., 2011). Therefore, the optimum parameters of WSA might change with the reference radius of the PFSS model, i.e., source surface.

In this chapter, we focus on studying the overall performance of the solar wind velocity framework (PFSS+WSA+HUX) with the SC phase. We implement two approaches with a fixed source surface radius (2.5 $R_{\odot}$) in the PFSS model, and the second one by incorporating the SCS model (PFSS+SCS+WSA+HUX). Our approach is to select the values of input parameters based on the best performance of the models over a reasonable range of parameters.

The chapter is structured as follows: Section 3.2 presents the methodology employed along with the parameter values used in the solar wind velocity forecasting frameworks (PFSS+WSA+HUX or PFSS+SCS+WSA+HUX). We also describe the chosen parameter sets for predicting solar wind velocity across 60 selected CRs and a statistical evaluation of their accuracy. The results obtained from the adopted models are discussed in Section 3.3. Section 3.4 offers interpretations for the observed trends in model performance during the selected time frame.

3.2 Methodology

We separate the region between the solar photosphere and the Lagrangian point L1 into two domains. The first domain includes the inner coronal region extending from the photosphere up to 2.5 $R_{\odot}$ or 5 $R_{\odot}$. The second domain extends from 5 $R_{\odot}$ up to the L1 point. Data-driven prediction of solar wind velocity at the L1 point involves the following steps -

- To calculate the magnetic field in the coronal region, in the first domain, through various extrapolation methods like PFSS and SCS, by using the observed photospheric magnetic field as input.
- To apply the empirical velocity relation based on the magnetic field line properties, obtained from extrapolation at the outer boundary of the coronal region.

- To extend the velocity estimates from the outer boundary of the coronal region (first domain) up to L1.

Empirical Velocity Relation in the Coronal Domain

As discussed in Chapter 2, empirical solar wind velocity relations like WSA, WS, and DCHB give the velocity at the outer boundary (2.5 or 5 $R_{\odot}$) of the inner corona, based on the properties of the open magnetic field lines. In this parametric study, we chose the best-performing and well-developed WSA empirical model as compared to other empirical models to estimate the solar wind velocity in the coronal domain (Riley et al., 2015). The WSA model incorporates the effect of the minimum angular distance of the footpoint of the field line from the coronal hole boundary (θ_b), along with the expansion factor (f_s) of the open field lines (Arge et al., 2003). Further, it is well known that coronal holes produce fast streams of the solar wind. Therefore, the position of the footpoint of the field line in the coronal hole plays a significant role in estimating solar wind velocity at the outer boundary of the coronal model (PFSS or SCS). The empirical relation from the WSA model is used in this thesis-

$$v_{sw}^{wsa}(f_s, \theta_b) = v_{slow} + \frac{v_{fast} - v_{slow}}{(1+f_s)^{\alpha}} \left(\beta - \gamma e^{-(\theta_b/w)^{\delta}}\right)^{3.5} \tag{3.1}$$

Here, the parameters v_{slow} and v_{fast} correspond to the velocity of the fastest and slowest solar wind stream. θ_b is the minimum angular distance for the footpoint of the field line from a coronal hole boundary at the solar surface. f_s is the expansion factor of the field line. We calculate the expansion factor (f_s) based on flux tube expansion only to the source surface for both magnetic field extrapolation methods. α, β, γ, δ and w are the tunable parameters of the model.

Extrapolation of Solar Wind Velocity into the Heliospheric Domain

As discussed above, the WSA model provides the solar wind velocity maps at the outer boundary of the coronal domain, i.e., at 2.5 $R_{\odot}$ or 5 $R_{\odot}$ based on the choice of magnetic field extrapolation method. In order to compare with the observed solar wind velocities at the L1 point by the in-situ spacecraft, it is

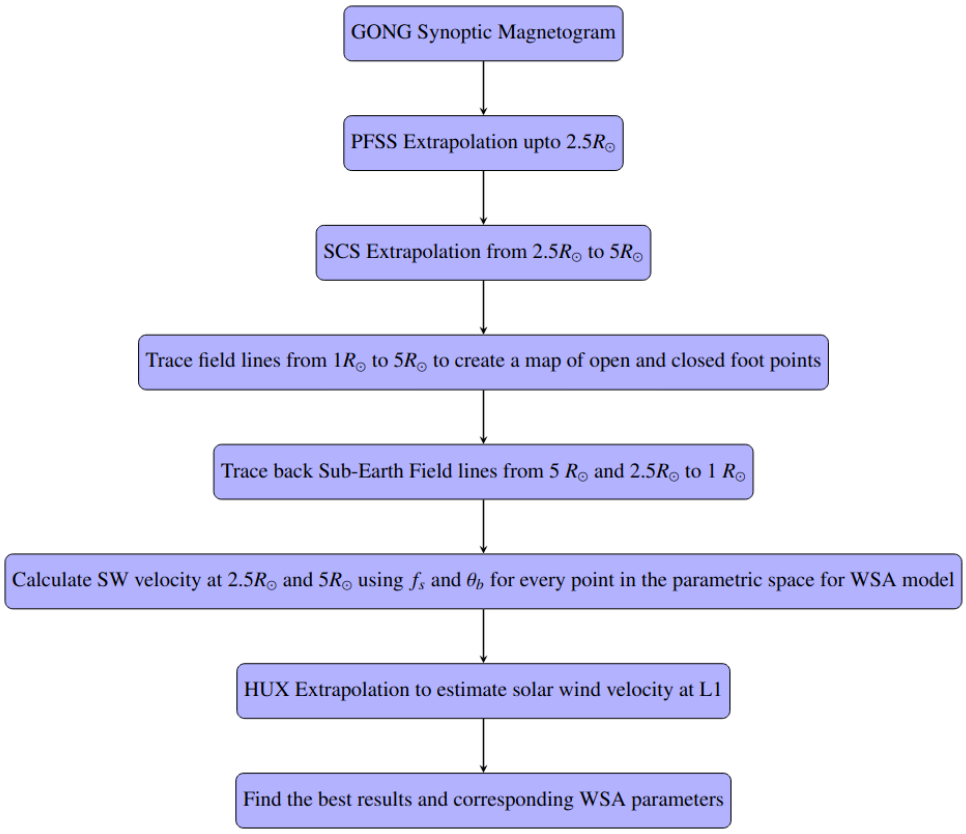

Figure 3.1: Flow chart explaining the steps of the framework adopted in this work.

required to extrapolate these velocities into the inner heliosphere. This requires the coupling of the coronal velocity models (like WSA) with heliospheric velocity extrapolation models. We have employed the HUX model to extrapolate from the outer boundary of the coronal domain to L1. The HUX model assumes the solar wind flow at the outer boundary of the coronal domain to be time-stationary. The extrapolation of the solar wind velocities in an r-ϕ grid can then be kinetically approximated using

$$v_{r+1,\phi} = v_{r,\phi} + \frac{\Delta r \Omega_\odot}{v_{r,\phi}} \left(\frac{v_{r,\phi+1} - v_{r,\phi}}{\Delta \phi} \right) \tag{3.2}$$

where, Δr and $\Delta \phi$ represent the grid spacing in r and ϕ directions respectively. $\Omega_\odot$ is the angular velocity of the Sun calculated assuming a rotation time period of 27.27 days. The HUX is essentially a 1D extrapolation model that neglects the effects of magnetic field, pressure gradient and gravity.

3.2.1 Model Definitions and Parametric Space

In our framework, we use two different approaches: PFSS + WSA + HUX, referred to as **Model1** and PFSS + SCS + WSA + HUX, referred to as **Model2**, with the difference being whether or not the coronal domain includes the SCS model. Solar wind velocity extrapolation in the heliosphere in both Model1 & Model2 is done using the HUX model. It is important to mention that our Model1 is similar to one of the models used in Riley et al. (2015). The details of these models are described in the Chapter 2. The steps adopted in the framework are explained in the flow chart shown in Figure 3.1.

We applied these two models (Model1 and Model2) to 60 CRs spanning the declining and minimum phase of SC 23 and the ascending phase of SC24. We define our parametric space to find the best parameter of the WSA model for each CR as described in the Table 3.1. Here, our goal is to access the overall best performance of the framework in our parametric space (defined in the next section). Our choice of parameter values for different WSA parameters is around those obtained in previous studies for individual CRs (Riley et al., 2015; Pomoell and Poedts, 2018; Kumar et al., 2020). The values are chosen to account for any SC dependency of parameters in the model and to look for the best possible set of parameters for every CR under consideration. We have also provided a practical solution for the choice of possible parameters, for e.g. β should be greater than γ in order to avoid mathematical errors in Eq : 3.1. We compute the velocity profile for each possible set of combinations of seven parameters in the WSA model in Eq:3.1.

For each CR we tried 23040 ($V_{slow} \times V_{fast} \times \alpha \times \beta \times w \times \gamma \times \delta$=3 $\times$ 3 $\times$ 8 $\times$ 4 $\times$ 5 $\times$ 4 $\times$ 4) combinations of set of solutions constituting all the points in our parametric space of Eq: 3.1, to find the optimum set of parameter values for both the models, are listed in Table 3.1. Figure 3.2 shows the PFSS-extrapolated source surface magnetic fields and input magnetograms for CR2051, CR2088, and CR2105. These CRs represent the descending and deep minimum phase of SC23 and the ascending phase of SC24, respectively. The different phases of selected CRs are also reflected in both the input and extrapolated magnetic fields.

Table 3.1: Parametric space to obtain the best parameters of WSA model.

V_{slow}	200-300 km s^{-1}, 3 points
V_{fast}	850-950 km s^{-1}, 3 points
α	0.1 to 0.25 step of 0.05 and 0.3 to 0.6 step of 0.1,
β	1, 1.25, 1.5 and 1.75, 4 points
w	0.01, 0.02, 0.03, 0.04 and 0.05, 5 points
γ	0.6, 0.7, 0.8 and 0.9, 4 points
δ	1, 1.25, 1.5 and 1.75, 4 points

CR2051, from the descending phase of SC23, shows stronger magnetic fields in ARs and a more complex PIL (blue line) at the source surface. In contrast, CR2088 and CR2105, corresponding to the deep minimum and ascending phases, exhibit weaker AR fields and a simpler, near-equator PIL.

3.2.2 Statistical Measures of Forecast Performance

The performance of a forecast can be assessed by comparing the forecast outcome of continuous variables (e.g., solar wind velocity) with the observed values. We used the OMNI database (https://omniweb.gsfc.nasa.gov/form/dx1.html) for the observed solar wind velocity profiles at L1. We calculated several scalar measures of forecast accuracy, which have previously been used by Reiss et al. (2016) and Wu et al. (2020). We used Mean Absolute Percentage error (MAPE), Root Mean Square Error (RMSE), standard deviation (SD) and Pearson Correlation Coefficient (cc) metrics between the observed and the model values of solar wind velocity at L1. Given a set of modeled values m_n and a set of corresponding observed values o_n, Mean Absolute Percentage Error (MAPE) is one such measure, which is given by

$$MAPE = \frac{100}{N} \sum_{n=1}^{N} \left| \left(\frac{m_n - o_n}{o_n} \right) \right| \tag{3.3}$$

The Root Mean Square Error or RMSE is also used sometimes as a performance statistic for a model and is given by

$$RMSE = \sqrt{\frac{1}{N}\sum_{n=1}^{N}(m_n - o_n)^2} \tag{3.4}$$

After tracing sub-Earth field lines (from the outer boundary of PFSS or SCS to the photosphere to estimate f_s and θ_b) for each CR, we optimized the performance of the two models based on the MAPE, RMSE, SD and *cc* by iterating the WSA parameter values from the parametric space defined in the Table 3.1.

We have assessed the results of the framework using two different approaches. In the first case, we analyzed the framework performance solely based on the *cc* values, i.e., we estimated the highest *cc* in the parametric space for every CR. In the second approach, we examined the corresponding values of the other metrics (RMSE, MAPE and SD).

It is important to mention that it is very unlikely to find a single set of WSA parameters that can optimize all the metrics simultaneously. Moreover, some of the parameters of the WSA model (like δ and β) do not have significant effect on *cc*; however they can alter the other metrics significantly. In addition to this, it was observed that overall lower values of RMSE, MAPE, and SD were related to higher *cc* values.

We put a maximum threshold tolerance equal to the minimum value of each metrics (MAPE, RMSE and SD) in the parametric space, around the minimum of MAPE and RMSE and SD for every CR. We found a common set from the above individual reduced sets of metrics that are centered around the minimum of each metric. Then we chose the highest *cc* from the above common set of parametric combinations. Therefore, the tolerance around the best values of the metrics and the fact that overall lower values of RMSE, MAPE, and SD were related to higher *cc* values, provided us a reasonable optimization of the other metrics. This helped us to arrive at the 'optimized/best' parameters in very close proximity of the highest *cc* (first method) for every CR, as discussed in the next section.

The discussion on the optimized parameters of WSA in Section 3.3.2 is based on our second optimization method. Although there is no significant difference be-

tween the 'optimized *cc*' along with other metrics (RMSE, MAPE and SD), and the first method, but the values for the other metrics are significantly improved for the second method. We also need to mention here that the tolerance values for RMSE, MAPE and SD are arbitrary. Increasing their values tends to shift our optimized *cc* toward the highest *cc*, which will lead to a significantly poorer optimization for other metrics as compared to our second method. However, following a more practical approach, our notion of 'Model/framework performance' is exclusively based on the values of the Pearson Correlation Coefficient.

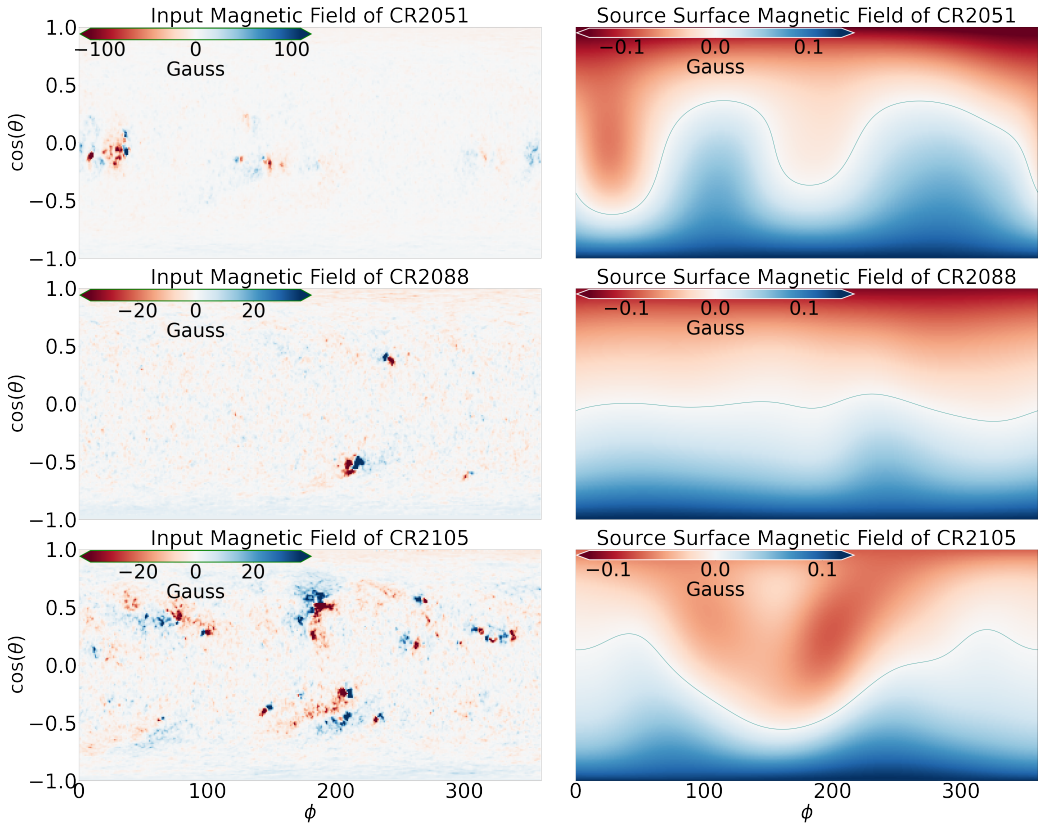

Figure 3.2: Input (left column) and extrapolated (right column) magnetic field in Gauss at 2.5 $R_{\odot}$ displayed for three CRs. Top: CR2051, middle: CR2088 and bottom: CR2105. Here θ = 90 - θ_{cr}, where θ_{cr} is the Carrington Latitude.

3.3 Results on the Performance of the Framework

3.3.1 Case Studies of Selected CR

In this section, we present our results of solar wind velocity estimation at L1 using the method described in Section 3.2 for CRs spanning the declining phase of cycle 23, near the solar minimum and the rising phase of SC 24. Specifically, we discuss three CRs, i.e., CR2051 (from 12 Dec 2006 to 8 Jan 2007), CR2061(from 10 September 2007 to 8 October 2007) and CR 2105 (from 24 December 2010 to 20 January 2011) as representatives of the different phases of SC, in order to show the applicability of the framework for the three phases of SC. We also discuss the limitations of the framework in view of the obtained results. This is important and holds relevance for the main conclusion of the study as discussed in Section 3.4.

CR2051 (SC23 Declining Phase)

CR2051 depicts a relatively quiet phase of the Sun occurring during the decline of SC23. The source surface extrapolation is illustrated in the top right panel of Figure 3.2. While it exhibits an overall bipolar nature of the magnetic field, the PIL (blue line), is noticeably corrugated. During this period, two small active regions are evident at low latitudes, as shown in the top-left panel of Figure 3.2. However, the magnetic field strength in the active regions of CR2051 is significantly higher than that observed in the active regions illustrated in CR2088 and CR2105. The source surface magnetic fields for these three CRs records reflect the typical evolution of cycle 23 (in the years 2007 and 2009) and the ascending phase of cycle 24 (beginning in 2011), respectively.

We present the modeled solar wind profile for the same period. In Figure 3.3 one can notice that the simulated/modeled solar wind velocity profile matches well with the observed velocity with cc=0.68 for Model1 and 0.67 for Model2. Bottom panel of Figure 3.3 shows that the simulated velocity pattern deviates from the

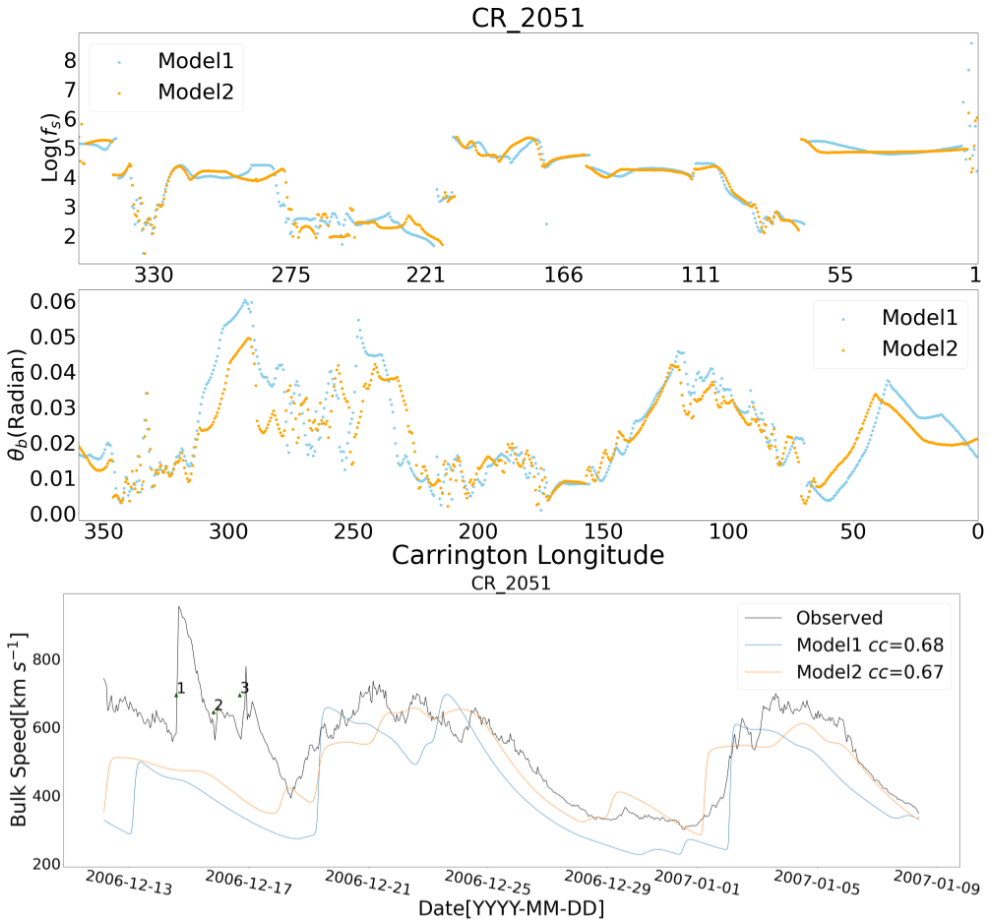

Figure 3.3: Plots of expansion factor, f_s and θ_b with the Carrington longitude for CR2051 are shown in the top and middle panels respectively. The bottom panel shows the observed velocity profile at L1 and the simulated velocity profiles obtained using Model1 & 2. Solar wind velocity plot in the bottom panel shows three peaks (1, 2 and 3) in the beginning, which mark the arrival of three CMEs on the Earth.

observed profile, only in the initial time period of the CR. It is also worth pointing out that during this initial period, three CMEs reached the Earth on 14, 15, and 16 December, where the modeled values do not match with the observed values. Furthermore, the middle and bottom panels of Figure 3.3 reveal that the overall observed velocity pattern matches with the θ_b profile in the inner boundary of the heliosphere. This suggests that θ_b plays a relatively dominant role in the solar wind velocity prediction at L1 compared to the expansion factor, f_s. Moreover, θ_b and f_s are inversely correlated to each other as shown in the top and middle panels of Figure 3.3. This is consistent with the findings of Riley et al. (2015), and which implies that the field lines originating from deep within the coronal

hole having higher θ_b are expected to have a lower expansion factor f_s.
Although the field line parameters, f_s and θ_b, for the two different models, corresponding to two different inner heliospheric boundaries, follow a similar trend, however, small shifts in the pattern are noticeable at a few instances. One of the possible reasons for the shift observed could be due to the acceleration of the solar wind in between the space of PFSS and SCS boundaries as suggested by Riley et al. (2015).

CR2061 and CR2105 (SC24 Ascending Phase)

To further explore the applicability of our framework across different phases of the solar cycle, we examine CR2061 and CR2105. The expansion factor for CR2061 exhibits less variability compared to CR2051 (as depicted in the top panel of Figure 3.4). As with CR2051, θ_b maintains an inverse relationship with f_s, although this inverse correlation is relatively weaker for CR2061. The velocity profile in the inner heliosphere continues to be largely influenced by the behaviour of θ_b, which is consistent with its exponential role in Eq.3.1. The third panel (from the top) of Figure 3.4 presents both the simulated and observed velocity profiles for CR2061. Model1 and Model2 yield correlation coefficients of 0.75 and 0.73, respectively, when compared with the observed solar wind velocity at L1. Again, both models exhibit similar overall velocity trends. However, the discrepancies between the two simulated profiles are more pronounced for CR2061 than for CR2051, as indicated by the sky blue and orange curves. For CR2061, Model2 estimates MAPE, RMSE, and SD values of 14, 83 km/s, and 96 km/s, respectively, improvements over the corresponding values for CR2051 (14, 102 km/s, and 114 km/s). Although the latter part of the velocity profile in CR2051 shows reasonable agreement between observed and simulated values, the overall statistical measures are inferior to those of CR2061 due to the influence of the CME that arrived early in the interval. The simulated profiles at L1 appear smoother than the observed data, which can be attributed to the fact that the HUX model ignores the pressure gradient and gravitational terms. An accurate match can be achieved by incorporating a 2D pressure gradient term, as discussed in Kumar

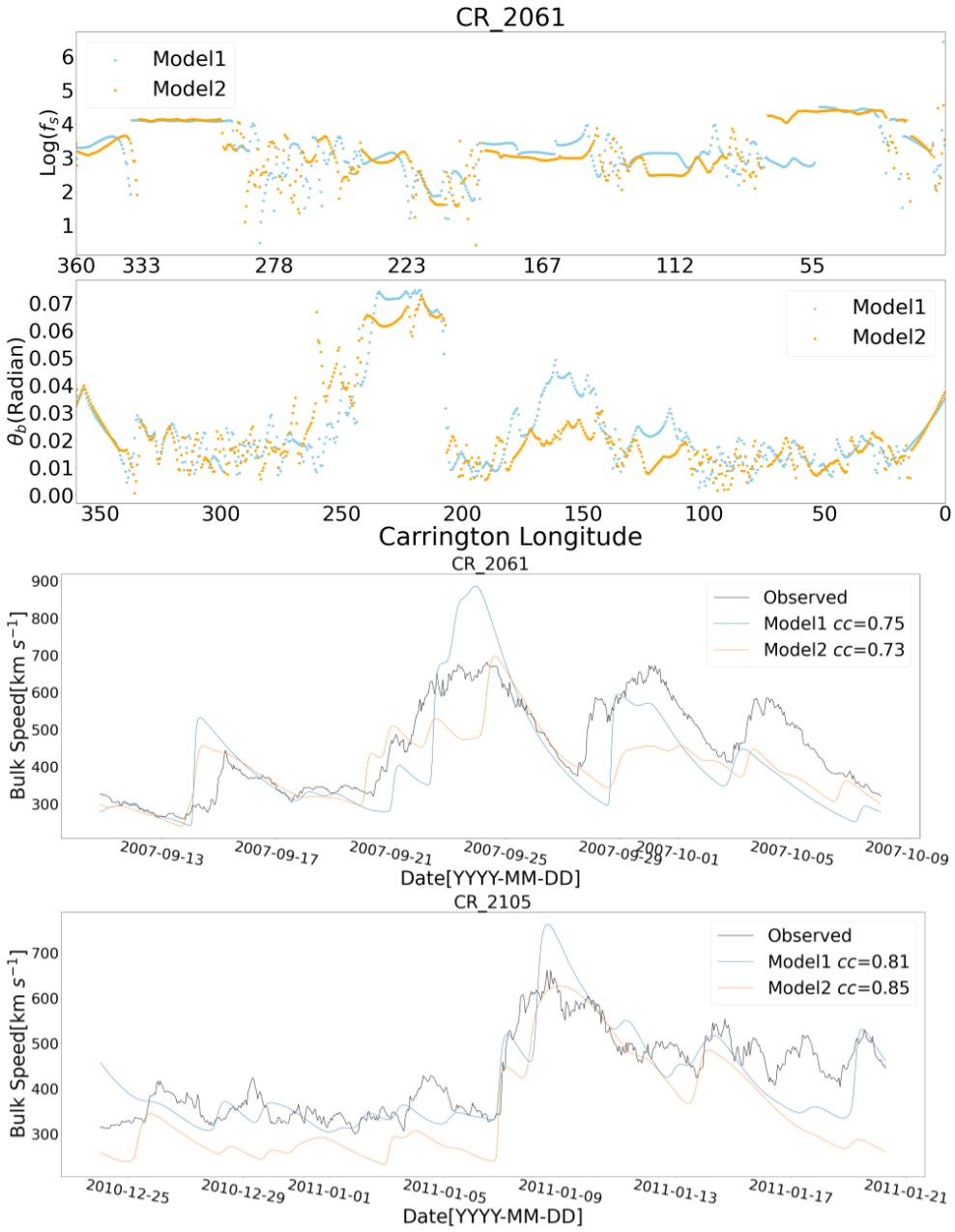

Figure 3.4: Plots of f_s and θ_b with the Carrington longitude for CR2061 are shown in the top first and second panels respectively. The bottom two panels show the observed velocity profile at L1 and the simulated velocity profiles obtained using two different models for CR2061 and CR2105, respectively.

et al. (2020). For completeness, the bottom panel of Figure 3.4 presents the velocity profile for CR2105, representing the ascending phase of SC24. This case shows stronger agreement between model and observations, with correlation coefficients of 0.81 and 0.85 for Model1 and Model2, respectively, indicating robust

model performance in replicating the observed solar wind velocity at L1.

3.3.2 Parameter Optimization for Different CRs

We explored all possible combinations of various parameters within the parameter space (Table 3.1) outlined in Section 3.2. The distributions of the optimal parameter values, identified from the best-performing combinations, are illustrated in Figure 3.5 (Model1) and Figure 3.6 (Model2) for 60 CRs, spanning CR2047 to CR2107 (excluding CR2096 for which a significantly large interval of the velocity data at L1 was missing). It is important to note that the final parameter selection for each CR follows the second approach based on other metrics described in Section 3.2.2. Notably, the *cc* values obtained from both methods are largely consistent, and the overall performance trends remain similar. However, the second approach yields marked improvements in several metrics apart from *cc*, as highlighted in Figure 3.9. The final distribution of velocity parameters (V_{slow} and V_{fast}) among the selected optimal sets shows a more uniform spread relative to other parameters for both models, as seen in Figure 3.5 and Figure 3.6. In both Model1 (PFSS+WSA+HUX) and Model2 (PFSS+SCS+WSA+HUX), the parameter β remains nearly unchanged across the best-performing combinations, supporting the commonly adopted constant value of $\beta = 1$ within the community (Arge et al., 2003). A similar behavior is observed for the parameter δ, with $\delta = 1.75$ consistently outperforming the other tested values (1.0, 1.25, and 1.5). In contrast, parameters such as α, γ, and w exhibit more variability across CRs for both models. For Model2, in particular, γ tends to cluster near the extremes (0.6 and 0.9) of the range selected, more than in Model1. The parameter w spans a range from 0.01 to 0.05 for both models, indicating that model performance (and corresponding velocity predictions) is more sensitive to w compared to other parameters. This sensitivity is expected, given that w appears in the exponential term of Eq. 3.1. Figure 3.7 presents the distribution of model performance quantified via the correlation coefficient (*cc*) between the modeled and observed solar wind velocity profiles across all CRs, using the optimised WSA parameters obtained through the second optimization method. It is worth noting that Model1

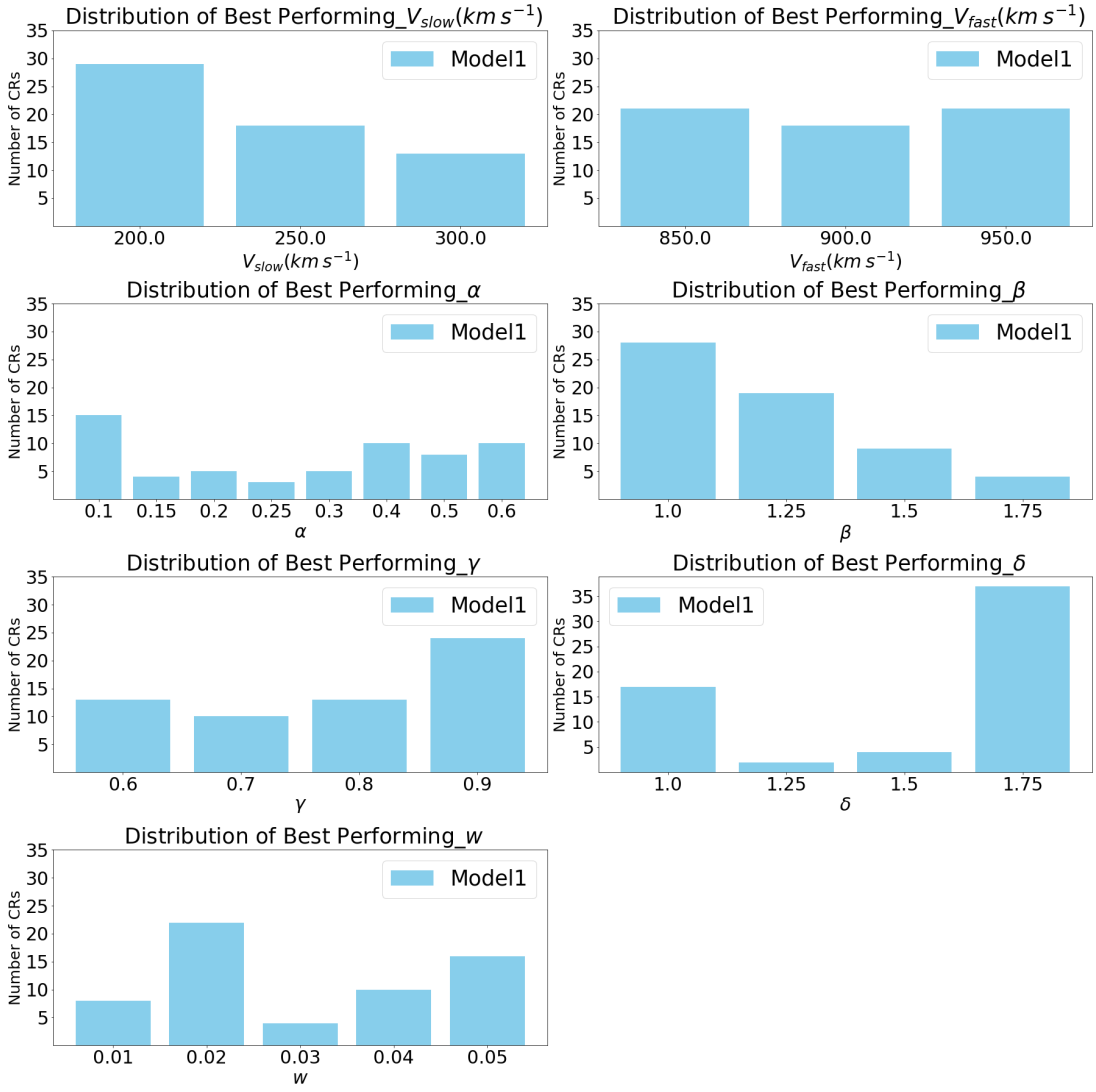

Figure 3.5: Distribution of the best-performing WSA model parameters in the parametric space across 60 Carrington Rotations (CRs) for Model 1. These parameters correspond to the optimized *cc* values obtained using the second optimization approach, as shown in Figure 3.8.

outperforms Model2 in terms of achieving higher *cc* values (0.8 to 1.0) for a larger number of CRs. In contrast, Model2 exhibits a relatively better performance in the moderate *cc* range (0.4 to 0.8), with more CRs falling into this range of *cc* compared to Model1. The average *cc* values for Model1 and Model2 are 0.65 and 0.63, respectively. These results support the conclusion that the parameter sets represent the best-performing configurations for each model. The general trend in model performance reflected in the distribution of *cc* values is consistent with that reported by Riley et al. (2015) for the overlapping interval in the two studies,

i.e., from CR2047 to CR2107. Furthermore, in addition to optimizing *cc*, we have also tuned other statistical metrics such as standard deviation (SD), mean absolute percentage error (MAPE), and root mean square error (RMSE). Our results show that approximately 60% of CRs achieve a *cc* in the range $0.6 \leq cc \geq 1.0$, a notable improvement over the 37% of the total selected CRs with $cc \geq 0.5$ reported by Riley et al. (2015) for one of their best-performing WSA-based models. The improved performance observed in our study can likely be attributed to the fact that we optimised the parameters individually for each CR. Additionally, the use of SCS magnetic field extrapolation in Model2 could have further contributed to the enhanced results. Possible reasons for the higher correlation obtained from our analysis could also be due a relatively shorter period selected for our study or a wider range of WSA parameters chosen.

For a comparison of two approaches of optimization for *cc*, MAPE, RMSE, and SD adopted in this work, we have mentioned the average values for each metric for all the CRs in Table. 3.2. The second approach gives us an overall better optimization in particular for MAPE, RMSE, and SD compared to the first method.

Table 3.2: Comparison of the overall results of two methods of optimization (average values of metrics). Here, 1 and 2 correspond to two different methods of optimization in metrics parameters.

Metrics	Model1	Model2
*cc*1	0.68	0.64
*cc*2	0.65	0.63
MAPE1	36.0	24.0
MAPE2	19	19
RMSE1	164	123
RMSE2	101	103
SD1	81	79
SD2	74	75

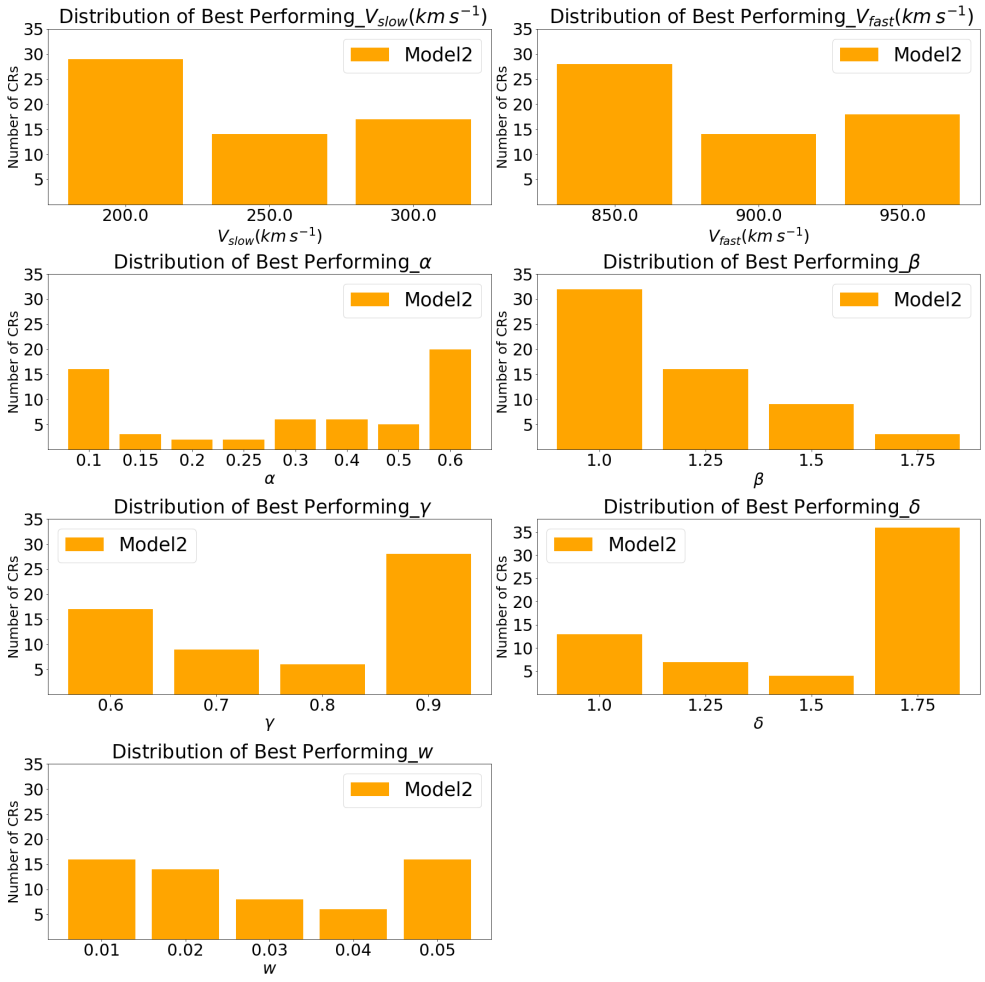

Figure 3.6: Same as Figure 3.5 for Model2

3.4 Discussion

In this parametric investigation of empirical models for predicting solar wind velocity at L1, we aimed to identify the key factors influencing the performance of two modeling frameworks: PFSS+WSA+HUX (Model1) and PFSS+SCS+WSA+HUX (Model2). We performed optimization for each CR of the WSA parameters. The study period was divided into three distinct intervals: T1) CR2047 to CR2077 (August 2006 to November 2008), T2) CR2078 to CR2093 (December 2008 to January 2010), and T3) CR2094 to CR2107 (February 2010 to December 2010). These intervals represent the descending phase, deep solar minimum of SC23, and the ascending phase of SC24, respectively. We observe that the correlation

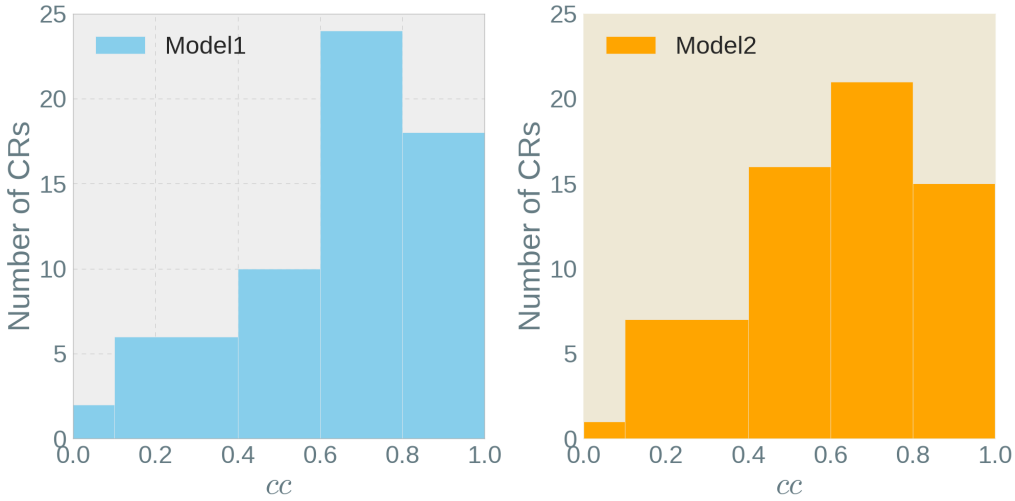

Figure 3.7: Histogram showing the distribution of framework performance (best *cc* with optimum parameters) for all the CRs. The left plot shows the distribution of *cc* (between modeled and observed solar wind velocity) among all the CRs for Model1(PFSS+WSA+HUX). A similar plot for Model 2 (PFSS+SCS+WSA+HUX) is shown on the right.

coefficients (*cc*) for both Model1 and Model2 exhibit similar trends across all three periods, with no significant deviation between the two, as illustrated in Figure 3.8. Based on the analysis, two key observations regarding the framework can be highlighted:

1. In the first (T1) and third (T3) periods, our framework performed significantly better as compared to the time period T2. The average *cc* of Model1 for time periods T1, T2 and T3 were 0.75, 0.48 and 0.63, respectively. Performance of Model1 in T2 is less than the overall average of 0.65 (represented by the green dotted line in Figure 3.8), as the time period T2 corresponds to the deep minimum phase of the cycle 23. In case of Model2, the average *cc* for T1, T2, and T3 are 0.70, 0.43 and 0.66, respectively, which shows a similar trend as Model1.

2. There are a few CRs in the three time periods for which the performance of both models is found to be poor. For example, CR2058, CR2059, CR2068 and CR2069 in the T1, CR2083 in the T2 and CR2099 in the T3 period, for which the performance of both Model1 and Model2 is relatively poor as compared to the neighbouring CRs.

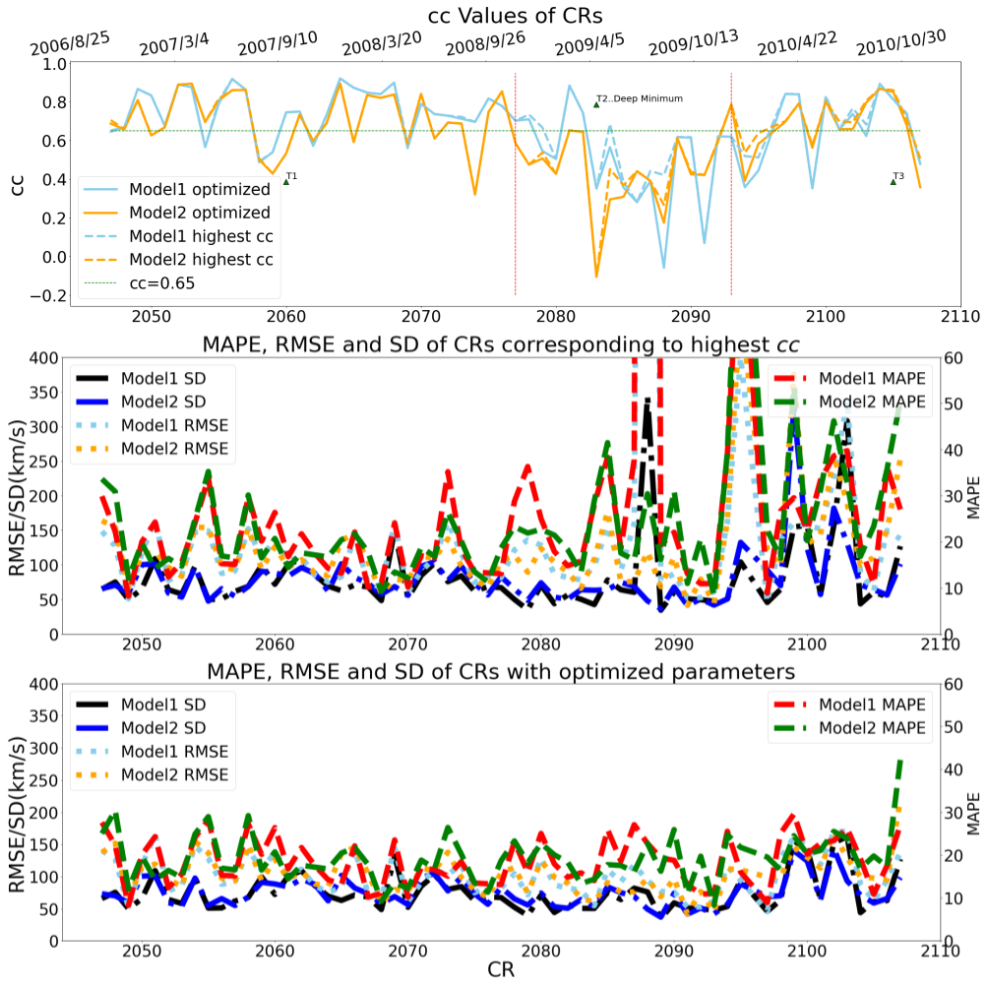

Figure 3.8: Top panel shows the highest *cc* (dotted lines) and optimized *cc* (solid lines) along with other metrics, for Model1 and Model2. The horizontal green dotted line corresponds to cc=0.65. The middle panel shows the MAPE, RMSE and SD corresponding to those highest *cc* (the dotted lines of the top panel). Bottom panel shows the optimised MAPE, RMSE and SD corresponding to the solid line in the top panels.

It is worth noting that time period T2 corresponds to the deep minimum phase of SC23, during which coronal holes are primarily located near the poles, far from sub-Earth points (Lowder et al., 2016). For our better understanding of the performance of the framework, the following points are important to note:

1. The HUX model extrapolates solar wind velocities assuming a steady-state background (Riley et al., 2015).

2. Magnetogram near the poles are generally unreliable (Hoeksema et al., 2006; Prabhu, A. et al., 2020).

3. Steady-state models, such as those used in this work, cannot reproduce transient events like CMEs. This limitation is evident in Figure 3.3, where the simulated velocity diverges from observations due to CME-related enhancements (Kataoka et al., 2009).

The reduced model performance during T2 can be largely attributed to the unreliability of magnetic field data near the poles (point 2). To explore this further, we calculated the area of low- and mid-latitude coronal holes (LMCHs) during the study period using SOHO/EIT synoptic maps. Specifically, we used 19.5 nm images, which are optimal for detecting coronal holes (`http://satdat.oulu.fi/solar_data/`). Details of the synoptic map generation process are provided in Hamada et al. (2019). We extracted LMCH areas between 60°S and 60°N latitudes where magnetogram data are the most reliable. Six CRs were excluded from the analysis due to insufficient coronal hole coverage ($\leq$90%).

During the time period T2, we observed a significant reduction, approximately 50%, in the coronal hole area at low and mid-latitudes (LMCH), as indicated by the red curve in Figure 3.9. This overall decline in the LMCH area is consistent with the findings of Lowder et al. (2016) for the overlapping period of our study. Furthermore, the LMCH area and the running average of model performance, represented by the orange curve for Model2 and the blue curve for Model1 exhibit a clear correlation, with all three curves displaying a similar overall trend in Figure 3.9. For the second method of optimization, we find that the performance trend of Model2 and Model1 shows a correlation coefficient of 0.61 and 0.33, respectively, with the trend of the LMCH area. When applying the first optimization method (selecting only the maximum *cc* per CR), the corresponding *cc* values are 0.67 for Model2 and 0.39 for Model1. These results demonstrate that both optimization approaches are consistent with the overall relationship between model performance and the variation in coronal hole area.

The performance of empirical solar wind models has been evaluated in earlier studies. For instance, McGregor et al. (2008) suggested that PFSS model accuracy is influenced by the curvature of the heliospheric current sheet near sub-Earth points at the source surface, which introduces uncertainties in identi-

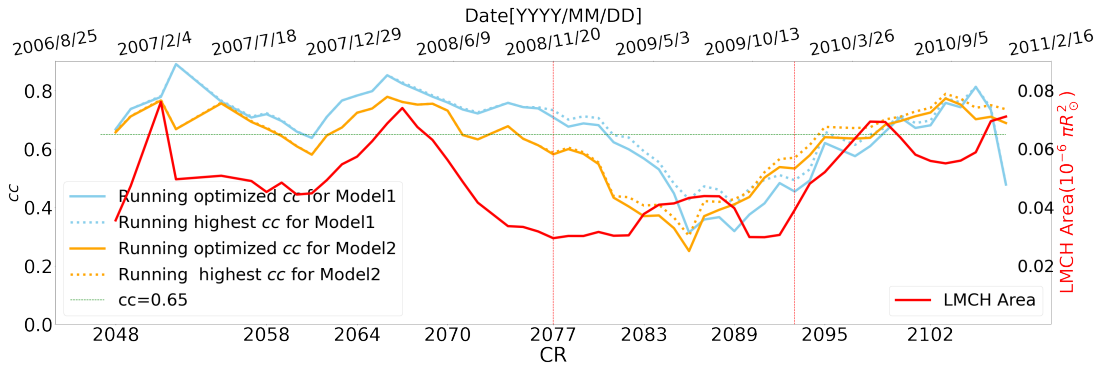

Figure 3.9: Running average of LMCH area of 6 CRs, derived from SOHO/EIT 19.5 *nm* channel synoptic maps (shown in red) and running average of *cc*, of simulated solar wind velocity with the observed solar wind velocity, for Model1 (blue) and Model2 (orange).

fying the footpoints of sub-Earth field lines. Building on our findings, we propose that the notably reduced LMCH area during the deep minimum phase of SC23 also plays a key role in reduced model performance. Since coronal holes at low and mid-latitudes are the primary source regions of solar wind reaching Earth, they critically shape the velocity profile observed at L1. As the T2 interval is characterised by a particularly small LMCH area, the solar wind velocity profile is mainly governed by contributions from polar coronal holes (spanning 60° to 90° in both hemispheres). However, magnetic field measurements in the polar regions are known to be less reliable, which can propagate errors through PFSS extrapolations based on line-of-sight magnetograms, resulting in reduced model performance. As the LMCH area increases during the ascending phase of cycle 24, the overall performance of the models improves, which is indicated by the higher average *cc* values during the time period T3 (Figure 3.9).

3.5 Summary

This study provides a comprehensive evaluation of two forecasting frameworks for solar wind velocity at L1 : Model1 (PFSS + WSA + HUX) and Model2 (PFSS + SCS + WSA + HUX). The analysis spans 60 Carrington Rotations (CR2047–CR2107), covering the declining and deep minimum phase of SC23 and the ascending phase of SC24. By systematically exploring over 23,040 combinations of model parameters for each Carrington rotation, we optimized the WSA

empirical model to improve forecast accuracy of solar wind velocity at L1. The results show that Model1 achieved an average Pearson correlation coefficient (cc) of 0.65, while Model2 had a slightly lower average cc of 0.63. Despite this, Model2 demonstrated a consistent performance across CRs, especially during periods of moderate solar activity. We also found a significant correlation between model performance and the observed LMCH area. A notable drop in performance during the deep solar minimum was attributed to a reduction in LMCH area and the dominance of polar coronal hole regions where magnetogram data are often unreliable. The future scope of the work includes several directions. First, incorporating more accurate polar magnetic field measurements or re-meshing magnetograms on a regular latitude (θ) grid can enhance extrapolation accuracy. Second, expanding the framework to include dynamic or time dependent models such as 2D/3D, MHD simulations can allow to capture the transient events like CMEs, which is missed by the current steady state models. Further, in this study, we utilized a constant source surface height (2.5 $R_{\odot}$) in the PFSS model. However, previous studies has indicated that the source surface height changes in relation to the phases of the SC (Lee et al., 2011; Arden et al., 2014; Nikolić, 2019). Additionally, we relied solely on the standard GONG magnetic maps for the analysis, whereas another study by Li et al. (2021) has shown that different synoptic magnetic maps can yield varying results. Thus, it would be valuable to examine how these factors influence the performance of our framework. This aspect will be explored in detail in the next chapter.

The work presented in this chapter has been published in Kumar and Srivastava (2022).

Chapter 4

Improving Solar Wind Velocity Forecasting Models

4.1 Introduction

The operational space weather forecasting frameworks, such as WSA-ENLIL (Arge and Pizzo, 2000; Odstrcil et al., 2004), European Heliospheric Forecasting Information Asset (EUHFORIA; Pomoell, Jens and Poedts, S., 2018), and Space Weather Adaptive Simulation Framework for Solar Wind (SWASTi; Mayank et al., 2022), use empirical solar wind models to define their inner boundary conditions. These empirical solar wind models like Wang-Sheeley (WS; Wang and Sheeley, 1990), Distance from Coronal Hole Boundary (DCHB; Riley et al., 2001) and the Wang-Sheeley-Arge (WSA; Arge et al., 2003), are based on magnetic field from Potential Field Source Surface (PFSS) model extrapolation.

The main PFSS parameter is the height of the source surface, and it is crucial for the extrapolation of the field above the photosphere. The source surface height (R_{ss}) in the PFSS model defines the upper boundary where the magnetic field lines are open and radial in the heliosphere. This parameter has two physical effects. First, R_{ss} controls the open flux in the heliosphere (Lee et al., 2011). Second, this height also changes the overall magnetic field structure and connectivity of the Sun to the Earth. The effects of changing the shape of the source surface from a sphere to an ellipsoid have been investigated recently Kruse et al.

(2020).

Due to the change in the state of the solar magnetic field structure with the phase of the solar cycle (SC), the source surface height is expected to change accordingly (Schatten et al., 1969). This change in source surface height can be studied through various observable outputs provided by the PFSS model. These outputs include the open flux at L1, which can be compared with IMF data obtained from in-situ observations. The PFSS model can also be used to estimate the photospheric footpoints of the open field lines. These footpoints can then be compared to coronal hole locations identified in synoptic images taken in different wavelengths (Lowder et al., 2017).

Recently, Meyer et al. (2020) used a global non-potential coronal magnetic field model to estimate the global magnetic field structure, which was compared with the features observed in Sun Watcher using SWAP images onboard PROBA2 to study the short-term evolution of the solar magnetic field over the maximum phase of the SC24. However, their global coronal magnetic field model is computationally expensive to apply over the entire SC compared to PFSS and also for operational space weather forecasting models. Several attempts have been made to assess the change of source surface height in the PFSS model with the phase of the SC. For example, using photospheric magnetic synoptic maps from Mount Wilson Observatory (MWO), Lee et al. (2011) reported that R_{ss} values of 1.9 $R_{\odot}$ and 1.8 $R_{\odot}$ produced the best results for the modeled IMF at L1 for the minimum activity periods of SC22 and SC23, respectively. Moreover, they found that 1.5 $R_{\odot}$ and 1.8 $R_{\odot}$ provided the best IMF during the SC23 maximum and minimum, respectively. A study by Arden et al. (2014) using synoptic maps from Solar and Heliospheric Observatory's Michelson Doppler Imager (SOHO/MDI; Scherrer et al., 1995) and Solar Dynamics Observatory's Helioseismic and Magnetic Imager (SDO/HMI; Scherrer et al., 2012) showed that raising R_{ss} by 15–30% (2.88 $R_{\odot}$-3.28 $R_{\odot}$) during the SC 23 minimum as compared to the conventional R_{ss} (2.5 $R_{\odot}$) better reproduces the observed open flux at L1. Therefore, both studies (Lee et al. (2011) and Arden et al. (2014)) using different input magnetic maps reported an increase in the source surface height during the SC minimum

as compared to the maximum. A study by Nikolić (2019) suggested a lower source surface height (1.5 $R_\odot$ –2.0 $R_\odot$) as compared to the conventional source surface height during the maximum phase of the SC24. The above-mentioned three studies disagree with each other in terms of the best absolute values of the source surface heights. However, they agree in terms of the relative changes in the best source surface heights with the phase of the SC, i.e., to use a higher source surface height during solar minimum as compared to solar maximum. A recent study by Huang et al. (2024) showed that slightly lower and higher values compared to the conventional value of R_{ss}= 2.5 $R_\odot$, at SC minimum and maximum, respectively, provide better values of unsigned open flux at L1. Similarly, Badman et al. (2020), based on the Parker Solar Probe (PSP; Fox et al., 2016) IMF observations during the Oct-Nov 2018 period, showed that reduced source surface height improves accuracy of the predicted IMF on specific days (2018-10-20 and 2018-10-29) at PSP which was then located at 0.5 AU. It is important to mention that the two studies focused on distinct selective time periods, whereas the findings of Lee et al. (2011) and Nikolić (2019) are based on long-term analysis for R_{ss} in a different context.

One of the important aspects of R_{ss} optimization is in the context of the use of PFSS in solar wind velocity prediction models at L1. Forecasting solar wind throughout the heliosphere requires accurate magnetic-field extrapolation from the photosphere to the outer boundaries of the coronal domain and, after that, tracing of the magnetic field lines in the coronal domain. Using the properties of the traced field lines in the coronal domain, empirical solar wind models, like WSA, provide the solar wind velocity profile at the outer boundary of the coronal domain.

Currently, the community uses a constant source surface radius (2.5 $R_\odot$) for PFSS in the WSA model with the standard synoptic magnetic maps from the Global Oscillation Network Group (GONG) network (Riley et al., 2015; Reiss et al., 2019; Kumar et al., 2020; Narechania et al., 2020; Kumar and Srivastava, 2022; Mayank et al., 2022). As reported by Lee et al. (2011), a small change in the R_{ss} can change the degree of agreement between the modeled and observed values of

IMF at L1. In Chapter 3, we showed on the basis of our study that the performance of solar wind velocity forecasting models decreased significantly during the deep solar minimum of SC23. This study considered a fixed source surface radius in the PFSS model. Since previous studies suggested that R_{ss} changes with the phase of the SC, therefore, one of the reasons for the decreased performance of the framework in our study can also be attributed to the usage of a fixed R_{ss}, i.e., 2.5 $R_{\odot}$.

The output of the WSA model changes with the source surface radius because changing R_{ss} affects the overall simulated magnetic field structure of the Sun, leading to changes in the connectivity of sub-Earth field lines. Thus, there is a clear need to optimize R_{ss} and the WSA parameters for solar wind forecasting at L1. In this chapter, we optimize R_{ss} in the PFSS model with the phase of the SC to be used in the WSA model to improve the solar wind velocity forecasting models. First, we evaluated the performance of the solar wind velocity prediction framework (PFSS+WSA+HUX, described in Chapter 3) at L1 using different R_{ss}, for 16 CRs selected at different phases of SC24 and SC25 as shown in Figure 4.1. We further extended this study over the SC24 and SC25 using an approach of default WSA parameters and only one type of magnetic map with more refined choices of R_{ss}. Section 4.2 describes the data selected and the methodology, consisting of the extrapolation method for the magnetic field and the estimation of solar wind velocity in the heliosphere. Section 4.2.1 provides details about the models used in the framework and the parametric space for the source surface radius in the WSA model. In Section 4.3, we discuss the main results and their interpretations. Finally, in Section 4.4, we present our main conclusions.

4.2 Data and Methodology

As described in Chapter 3, we consider the space between the Sun and the Lagrangian point L1 as two distinct regions. The first region extends from the photosphere to the source surface. The second region extends from the source surface to the L1 point. In Chapter 3, we used two models (Model1 and Model2)

for solar wind velocity forecasting at L1. Since the performances of both models were found to be similar, therefore, for the sake of convenience we use only Model1, i.e., PFSS+WSA+HUX, for solar wind velocity forecasting at L1, the analysis described in this chapter.

In Chapter 3, we restricted the analysis to standard GONG maps as input. In this chapter, we explore the use of the three different types of magnetic field maps, taken from the GONG[1]. Out of the three types of magnetic maps, two are full (CR) synoptic maps commonly used by the community: standard magnetic ("mrmqs" in the GONG file name) and integral zero point corrected (ZPC) maps ("mrnqs" in the GONG file name). Due to differences in location and observing conditions between the various sites of the GONG network, strong background variations were observed in the standard magnetic GONG maps (Hill, 2018). These so-called zero-point errors reached amplitudes of the order of 10 G but were reduced to 1G with an automated comparison between sites and day-to-day variations, resulting in the ZPC maps. We also used the hourly updated ZPC (HU ZPC) synoptic maps ("mrzqs" in the GONG file name) at an interval of five hours. The HU ZPC maps were chosen to provide an updated representation of the magnetic field of the Sun. Monthly sunspot data were obtained from the SILSO website[2] to identify different phases of the SC and select different time periods of study. Further, we used the in-situ observations of hourly averaged solar wind velocity recorded at L1 in the OMNI database[3] to compare with the modeled solar wind velocity profiles at L1.

Since we aim to optimise the source surface height at different phases of the SC, we selected CRs as representatives of different phases of the SC for our study. We selected in total 16 CRs: four consecutive CRs at the maximum phase of the SC24 (CR2143 - CR2146, October 2013-January 2014), 8 CRs in the declining and minimum phase of the SC24 (CR2182 - CR2185, September-December 2016 and CR2193 - CR2196, July-October 2017), and 4 CRs at the maximum phase of the SC25 (CR2272 - CR2275, January-September 2023), as shown by red, yellow,

[1](https://gong.nso.edu/data/)
[2](https://www.sidc.be/SILSO/)
[3](https://omniweb.gsfc.nasa.gov/form/dx1.html)

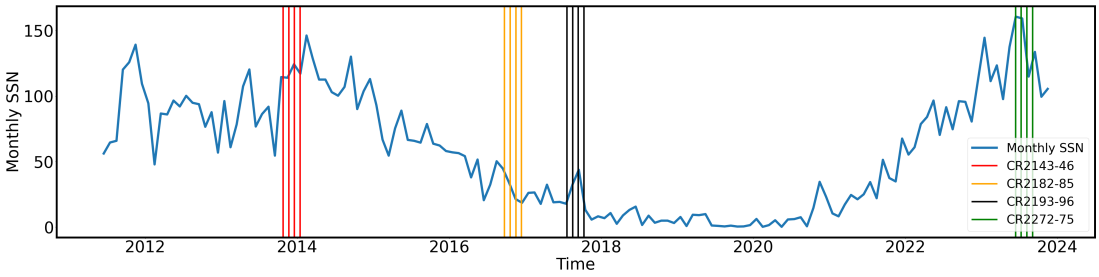

Figure 4.1: Monthly sunspot numbers (blue line) plotted with time, indicating different phases of solar activity cycle 24 & 25. Vertical lines mark the CRs selected for analysis at different phases of the SC.

black and green vertical lines respectively, in Figure 4.1. We further extended our analysis only using ZPC maps and default WSA parameters over the entire phase of the SC24 and SC25 (CR2093-CR2272), to validate the results from the selective detailed study of the above 16 CRs.

We estimate solar wind velocity at the L1 point for these 16 CRs by selecting the best R_{ss} among three choices, i.e., 2.0 $R_\odot$, 2.5 $R_\odot$, and 3.0 $R_\odot$, for each type of input magnetic map (discussed above) in the framework. This involves the following steps:

1. Calculate the coronal magnetic field in the coronal domain up to R_{ss}, using the PFSS extrapolation with a python module pfsspy (Stansby et al., 2020b). We use three different values of R_{ss} (2.0 $R_\odot$, 2.5 $R_\odot$, and 3.0 $R_\odot$), for each of the three different types of input synoptic magnetic maps.

2. Trace the magnetic field lines starting from the photosphere to create a map of open and closed field lines with 1° resolution (Section 4.2.2).

3. Trace the sub-Earth field lines from R_{ss} to the photosphere (Section 4.2.2).

4. Utilize the WSA empirical velocity relation to estimate solar wind velocity profile at R_{ss}, based on the magnetic field line properties, using:

   (a) default WSA parameters;

   (b) a parametric space of WSA parameters. Using parametric space involves a range of values of WSA parameters to arrive at a conclusion independent of the choice of parameters (Section 4.2.3).

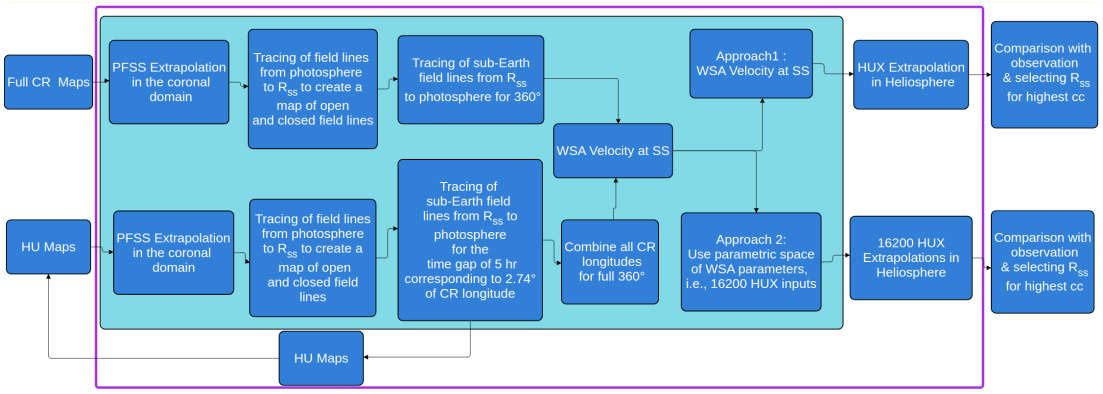

Figure 4.2: Flow chart of the methodology adopted in this chapter to find optimal R_{ss}. Steps mentioned in the magenta colour box are repeated for all the three choices of R_{ss}, i.e., 2.0 $R_{\odot}$, 2.5 $R_{\odot}$, and 3.0 $R_{\odot}$.

5. Extrapolate velocity estimates from the outer boundary of the coronal domain (R_{ss}) up to the L1 point using the HUX extrapolation (heliospheric domain) (Section 4.2.1).

6. Apply the first three steps for each value of R_{ss}, with default WSA parameters and for parametric space (Table 4.1) for each type of magnetic map, and calculate the performance matrix defined by the Pearson correlation coefficient between the modeled and observed solar wind velocity values at L1 to find the best R_{ss} (Section 4.2.3).

To compare the PFSS extrapolation using different synoptic magnetic maps with the actual observation near the Sun, we used PROBA2/SWAP observations. SWAP captures the images of the lower corona every 110 seconds at 174 Å, revealing key structures like active regions, streamers, and coronal fans. Even though 174 Å is not an ideal wavelength for observing coronal holes and filaments, these features are still visible in SWAP images. All these features have a direct connection with the overall magnetic field configuration of the corona. SWAP has a wide field of view (FOV) spanning 54', and using the off-pointing capability of PROBA2, the SWAP FOV can be shifted in any direction in order to track coronal features of interest up to more than 2 $R_{\odot}$. This extended FOV is large enough to observe the lower corona and is well within the domain of PFSS extrapolation.

We used observations from special observational campaigns to extend the FOV

of SWAP by putting the Sun at the corner of the FOV and recording 30-second exposure images in 174 Å every minute. Finally, we created a single mosaic image by stacking these off-limb images for one hour by keeping the Sun at the center of the mosaic to combine the signal (median of the photon count). This resulted in better visibility of limb features compared to the normal image of the SWAP at larger heights due to increased signal in the overlapped FOV of individual images in the stack. Specifically, we used mosaics reconstructed from the special campaigns on 20 August 2017 and 7 August 2023. These mosaics result in a larger FOV (up to 2.5 $R_{\odot}$ on the side and 3.0 $R_{\odot}$ on the corners) as compared to a standard SWAP image centered at the Sun (up to 1.7 $R_{\odot}$ on the side and 2.5 $R_{\odot}$ on the corners). It is important to mention here that the mosaics obtained using this approach are suitable only for the study of stable and long-lived features in the corona because short-lived features are smeared out over the time span of an hour. The SWAP images obtained from the mosaic are suitable for comparison with the PFSS extrapolated global magnetic field structure.

To be noted that CRs 2194 and 2274 and their neighbouring CRs during the maximum phase of SC25 and declining phase of SC24 were mainly chosen for this study to include the period for which the extended FOV PROBA2/SWAP mosaic images were available. This was required to compare the SWAP images with the PFSS extrapolation around the time of the optimization of the WSA model. Moreover, we selected a relatively stable period during the SC24 maximum, when the HUX model is expected to give better results since it is essentially a steady-state extrapolation model. The following sections explain the empirical formulation for solar wind velocity, the extrapolation technique in the heliosphere, and the parametric space of the WSA model, as well as methods of assessment of the framework.

4.2.1 Coronal and Heliospheric model

As explained in Chapter 3, we first extrapolate the magnetic field in the coronal domain using the PFSS model, then we trace the magnetic field lines from the photosphere to the R_{ss}. We further use the particular form of WSA model given in Riley et al. (2015) to estimate the solar wind velocity profile at the inner

heliospheric boundary (R_{ss}):

$$v_{sw}^{wsa}(f_s, \theta_b) = v_{slow} + \frac{v_{fast} - v_{slow}}{(1+f_s)^{\alpha}} \left(\beta - \gamma e^{-(\theta_b/w)^{\delta}}\right)^{3.5}. \tag{4.1}$$

As mentioned in the earlier in this section, apart from the parametric space in the Table 4.1 we also used default values WSA parameters set as $v_{\rm slow} = 250$ km/s and $v_{\rm fast} = 750$ km/s, $\beta = 1.0$, $\alpha = 1.5/9$, $w = 0.01$, $\gamma = 1.0$, and $\delta = 1.5$. These values provide overall optimal results for the time periods analysed, but they are not necessarily the best values for each CR. The use of the parametric space, makes the final results independent of the choice of the WSA parameters (Section 4.2.3).

Comparing the estimated solar wind velocity values with those observed from OMNI database by spacecraft (Wind and ACE) at the L1 point requires connecting the solar wind velocity obtained from the WSA model with heliospheric velocity extrapolation models. As mentioned earlier, we use the Heliospheric Upwind eXtrapolation (HUX; Riley et al., 2001), with 0.55° (≈ 1hr in CR time period) resolution to compare with hourly average data at L1. The same resolution is also used for tracing the sub-Earth field lines from R_{ss} to the solar surface. After the extrapolation of the solar wind velocity profile from R_{ss} at L1 using HUX, we compared the values of estimated solar wind velocity with the observed values at L1. We use the Pearson correlation coefficient (cc) to assess the performance of the framework, which can have values between $[-1, 1]$, with 1 indicating a direct linear correlation and -1 an inverse correlation. Since we aim to find a modeled solar wind profile that closely matches with the observed profile, for our study a cc value close to 1 is desirable and lower values of cc, including negative ones, are considered as poor correlation.

We also calculate other metrics, such as MAPE and SD, as discussed in Chapter 3. For the sake of simplicity, the assessment of the performance of the framework in this chapter is solely based on the maximum values of cc. However, we will discuss the results based on the values of MAPE and SD in the specific case of SC25 maximum phase (see Section 4.3).

4.2.2 Field Line Tracing Approaches Corresponding to Different Types of GONG maps

We have used three types of synoptic magnetic maps obtained from GONG as mentioned in Section 4.2.1. Two out of the three maps are full CR maps, i.e., zero point corrected (ZPC) and standard maps (STD), that give us an idea about the overall magnetic field over 27.27 days (Carrington Rotation time period). We also used hourly updated zero point corrected (HU ZPC) maps which provide an updated version of the magnetic field. Therefore, we have two types of magnetic maps, i.e., full CR maps and hourly updated synoptic maps. Further, we use two different extrapolation schemes for these three types of maps while tracing the sub-Earth field lines.

For both full (ZPC and STD) and HU ZPC synoptic maps obtained from the GONG network, we traced field lines all over the photosphere to create a map of footpoints of open (field lines reaching at R_{ss}) and closed field lines (field lines closing back to the photosphere) used for the calculation of θ_b. In the case of full CR maps, we created a 360° (corresponding to full CR) input for the HUX model and then calculated f_s and θ_b (parameters for the WSA model) for all sub-Earth field lines from Carrington longitude 0° to 360° by tracing all sub-Earth field lines from R_{ss} to the photosphere for a single CR map.

Each HU ZPC map corresponds to a specific central Carrington longitude for a given Carrington rotation based on the observation time. It also represents a full rotation with updated observations for the next 60° of the upcoming Carrington longitude, as described on the GONG website[4]. Further, tracing the sub-Earth field lines for 129 HU ZPC maps selected at an interval of 5 hr, for a CR involves the following steps:

1. For a given HU map of a given time, trace the field lines all over the photosphere with 1° resolution, from the photosphere to R_{ss} to create a map of the footpoints of open and closed field lines at the photosphere. This step is vital for the calculation of θ_b using an updated magnetic map.

[4](https://gong.nso.edu/data/)

2. Trace the sub-Earth field lines, from R_{ss} to the photosphere (to calculate f_s and θ_b), corresponding to the 5-hr time gap between the two maps. It corresponds to tracing the field line for the Carrington longitudinal gap of $\approx 2.74°$. Therefore, each HU map is used to create an HUX input for $\approx 2.74°$ only.

3. Repeating the above two steps for all the HU maps for a given CR to create a full 360° input for the HUX model.

This approach provides an updated view of the coronal magnetic field than a single full CR map. A detailed explanation about the tracing of field lines can be found in Reiss et al. (2019). Figure 4.2 shows the flowchart of the overall methodology adopted for the analysis reported in this chapter.

4.2.3 Optimization of the Source Surface Height Using Two Approaches

We applied two different approaches for each type of magnetic map used as input (STD, ZPC, and HU ZPC) to find the best R_{ss} for each CR. In our first approach, we used default parameters (v_{slow} = 250 km/s, v_{fast} = 750 km/s, α = 1.5/9, β = 1.0 , w = 0.01, γ = 1.0 and δ = 1.5) in the WSA model for every CR. For each of the three values of R_{ss} (2.0 $R_\odot$, 2.5 $R_\odot$ and 3.0 $R_\odot$), the velocity profile at the outer boundary of the coronal domain was obtained. This was provided as input to the HUX model to give us velocity output at L1. We then compared these values with the observed solar wind profile at L1 from the OMNI database and estimated the Pearson correlation coefficient (cc). The R_{ss} corresponding to the maximum cc was selected as the best performing for each CR.

In the second approach, we use various combinations of WSA parameters (similar to Chapter 3) with values around the default values mentioned in Table 4.1 to estimate the maximum value of cc for each R_{ss}. This involves creating 16200 velocity profiles using an automated Python code for each value of the R_{ss}, which corresponds to a combination in the parametric space covering V_{slow}, V_{fast}, α, β, γ, δ, and w (16200=$3 \times 5 \times 6 \times 4 \times 5 \times 3 \times 3$) defined in Table 4.1. For a

Table 4.1: Parametric space used for WSA model.

Parameter	Range	No. of Points
V_{slow}	200-300 km/s	3 points
V_{fast}	600-800 km/s	5 points
α	0.1 to 0.3	6 points
β	1 to 1.75	4 points
w	0.01 to 0.05 radian	5 points
γ	0.6 to 1.0	3 points
δ	0.8 to 1.5	3 points

given R_{ss}, it further involves extrapolation of each velocity profile (corresponding to each parametric combination) up to L1 using HUX, and calculating *cc* for each extrapolated velocity profile with the observed in-situ solar wind profile at L1. Thereafter, R_{ss} corresponding to the highest *cc* (among the three values of R_{ss}) is selected as the best R_{ss} for every CR. Therefore, using parametric space enables us to estimate the best performing R_{ss} independent of the choice of WSA parameters.

4.3 Results and Discussion

We used two approaches to estimate the optimized value of R_{ss} for 16 CRs selected at three different phases, i.e., 8 CRs at the minimum of SC24 and 4 CRs each at the maximum of SC24 and SC25, as shown in Figure 4.1. In our first approach, we used default WSA parameters, and in the second, we used the parametric space for each R_{ss} (as explained in Section 4.2.3). For both approaches, we also used three different magnetic maps as input (as mentioned in Section 4.2). Therefore, we have a total of 24 ($4 \times 2 \times 3$), 48 ($8 \times 2 \times 3$), and 24 ($4 \times 2 \times 3$) different instances (no. of CRs $\times$ no. of methods $\times$ no. of maps) to evaluate the best performing R_{ss} at each phase of the SC24 maximum, SC24 declining/minimum phase, and SC25 maximum, respectively. In Section 4.3.1, we discuss our results obtained from the two approaches and the statistical results based on the analysis

of selected CRs at different instances. In Section 4.3.2, we discuss how different values of R_{ss} affect the modeled solar wind profile at L1, specifically for CR2143 and CR2183. In Section 4.3.3, we compare the extrapolated magnetic field structures using different magnetic maps with the observed large-scale structures in PROBA2/SWAP images with extended FOV. Finally, in Section 4.3.4 we discuss the results from the long-term analysis of default WSA approach using ZPC maps only with more refined choices of R_{ss} (from 1.5 $R_{\odot}$ to 3.25 $R_{\odot}$) for all the CRs covering the entire SC24 and SC25 (from January 2010 to September 2023).

4.3.1 Source Surface Height Optimization at Different Phases of SC24 and SC25

Figure 4.3 depicts the performance of the framework in terms of Pearson correlation coefficient obtained between the observed and modeled values of solar wind velocity at L1 for different CRs with different R_{ss} based on default WSA parameters, for the three kinds of synoptic maps used. In this figure, blue, orange, and green dots represent the performance of the framework (cc), for R_{ss} of 2.0 $R_{\odot}$, 2.5 $R_{\odot}$, and 3.0 $R_{\odot}$, respectively for each CR. Horizontal dashed lines show the average performance in the respective phase for each R_{ss} and all CRs. The annotated value shows the average value of cc for each input map and SC phase for all three R_{ss} (dashed lines). From Figure 4.3, we can draw the following conclusions:

1. The overall performance during the declining phase of SC24 (cc_{avg}=0.45 averaged over all R_{ss}, CRs, and maps) is better compared to the performance during the maximum of SC24 (cc_{avg}=0.38).
2. The framework performed best for R_{ss} = 3.0 $R_{\odot}$ (green dots) in the declining/minimum phase of SC24 for most of the cases (17/24 combined for all the maps). The orange dashed lines show the average cc for R_{ss} = 2.5 $R_{\odot}$, which is estimated to be 0.61 for ZPC maps and 0.52 for HU ZPC maps. The green dashed lines show the average cc for R_{ss} = 3.0 $R_{\odot}$, which is estimated to be 0.75 for ZPC maps and 0.61 for HU ZPC maps. These values show clear improvement using R_{ss} = 3.0 $R_{\odot}$ in comparison to R_{ss} = 2.5

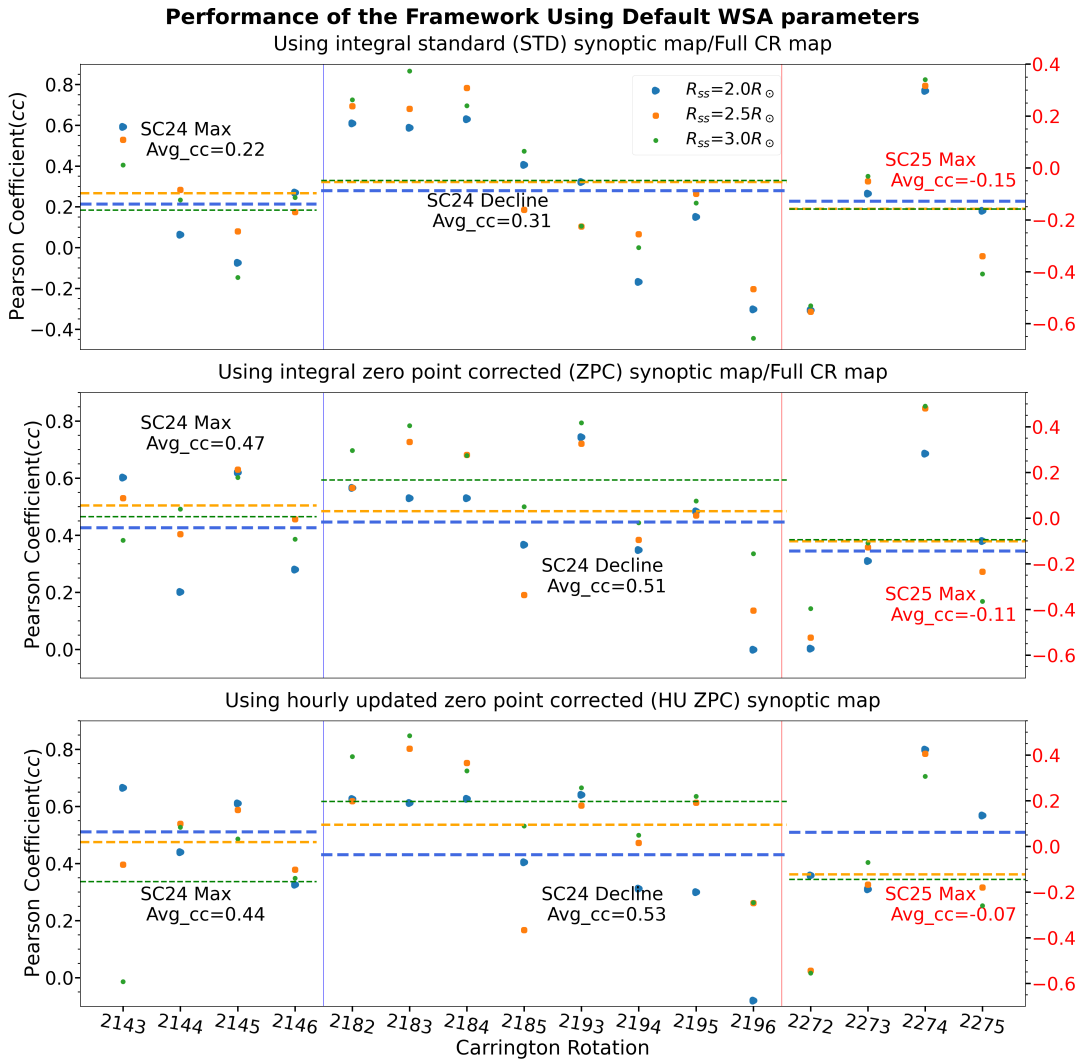

Figure 4.3: The performance of the framework (cc) for different CRs with different R_{ss} based on default WSA parameters. For SC24, refer to the left Y-axis, whereas for SC25 maximum, refer to the right Y-axis in red. The top panel shows the result using STD, the middle panel is for the ZPC, and the bottom panel is for HU ZPC. Blue, orange, and green dots represent the performance of the framework, i.e., cc, for R_{ss} of 2.0 $R_\odot$, 2.5 $R_\odot$, and 3.0 $R_\odot$, respectively. Horizontal dashed lines show the average performance in the respective phase for each R_{ss} and all CRs. The annotated value shows the average value of cc for each input map and SC phase for all the three R_{ss} (dashed lines).

$R_\odot$, for both the maps. In contrast, the STD maps do not show a significant improvement in performance when using $R_{ss} = 3.0\ R_\odot$ as compared to $R_{ss} = 2.5\ R_\odot$.

3. During the SC24 maximum phase, the average performance of the framework for all 4 CRs is the best for either $R_{ss} = 2.5\ R_\odot$ or $R_{ss} = 2.0\ R_\odot$ for all the three types of magnetic maps (blue and orange dashed line). It is also important to note that, in none of the maps, the average performance reaches its highest value at $R_{ss} = 3.0\ R_\odot$, indicating that $R_{ss} = 3.0\ R_\odot$ is not a good choice for SC maximum.
4. The overall performance using full ZPC maps is found to be better than standard CR maps at the SC24 maximum and declining phases and for all the three values of R_{ss}. This is highlighted by the increase in the average *cc* during the minimum phase of the SC24 from 0.31 (for STD maps) to 0.51 (for ZPC maps), and from 0.22 to 0.47 during the maximum phase of the SC24. We also note that the performance using hourly updated ZPC and full CR ZPC maps is similar.
5. Average *cc* was consistently negative ($cc_{avg} = -0.11$) during the SC25 maximum when default WSA parameters were used with all magnetic maps, indicating the poor performance of the framework for this time period.

Figure 4.4 displays the performance of the framework for different CRs with different R_{ss} based on optimized *cc*, by using the parametric space of WSA parameters. Each dot represents the highest *cc* in the parametric space for each selected value of R_{ss}. It is important to note that during SC25 maximum, *cc* optimization showed unrealistic improvement in *cc* (Figure 4.4) as compared to other phases, i.e., average *cc* increased from negative values to significant positive values for all the maps. In such a case, it becomes important to check the values of the other metrics as well to examine whether this improvement represents a better match or not. Interestingly, we found that other metrics, such as the average MAPE, increased significantly for the SC25 maximum. In this time period, average MAPE increased from approximately 20-22% (for all maps), to 58%, 114% and 39% for STD, ZPC and HU ZPC maps, respectively. Physically,

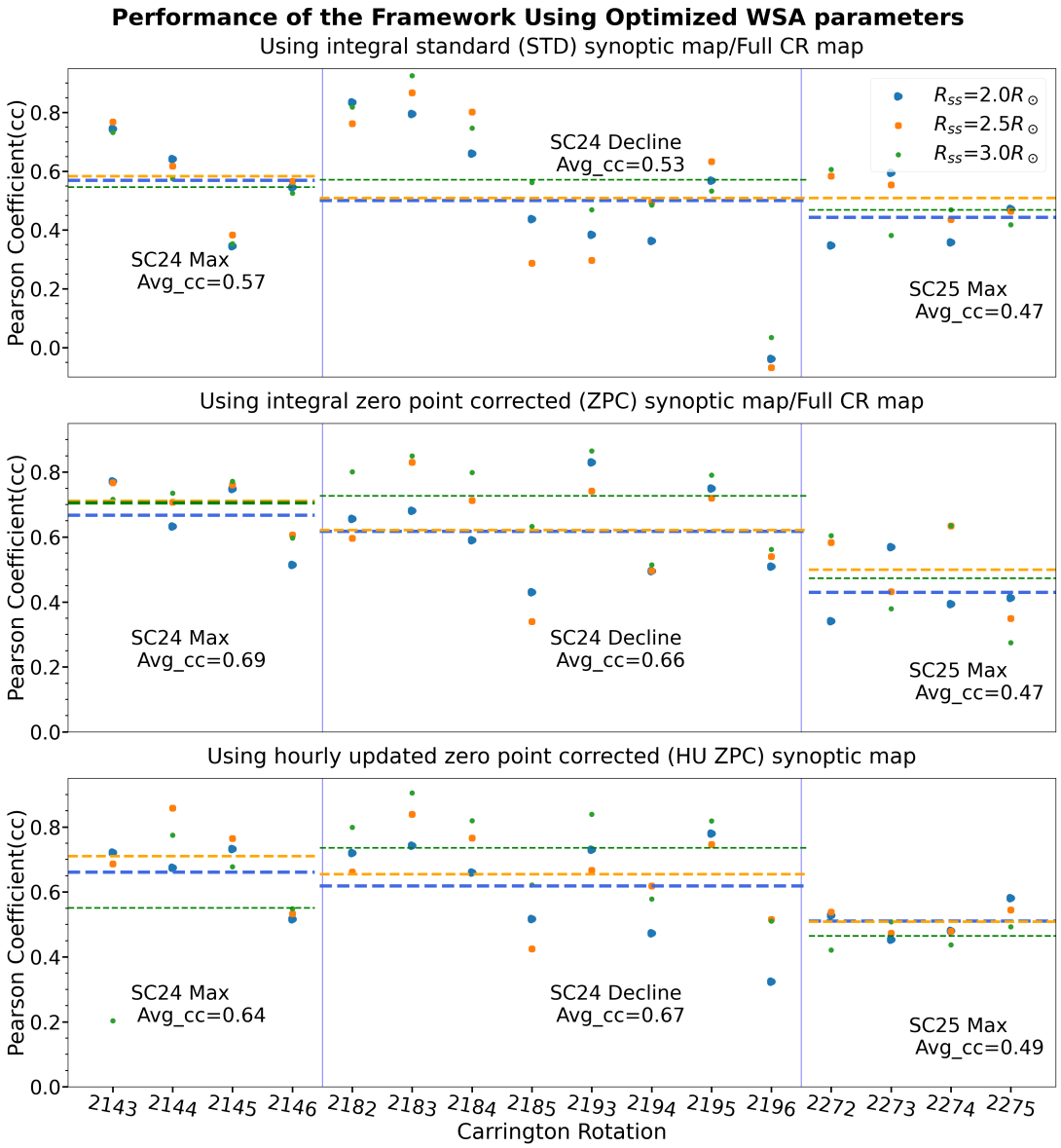

Figure 4.4: Similar to Figure 4.3 for optimised WSA parameters.

MAPE represents the mean of the absolute percentage difference between each point in the time series of the modeled and observed solar wind velocity profile for a given CR, and it should be lower for a better match. Similarly, a considerable increase in SD also occurred during the maximum phase of SC25 in ZPC maps, rising from 93 km/s to 160 km/s as a result of *cc* optimization. Therefore, despite the increase in average *cc* during the SC25 maximum phase through optimization of WSA parameters, it does not represent an improved match in the solar wind velocity at L1 because of the increase in errors. On the other hand, during the

maximum and declining phases of SC24, the default WSA parameters yielded better performance compared to the SC25 maximum, even without optimization. Furthermore, optimization of the *cc* parameter during the SC24 declining and maximum phase did not result in a significant increase ($\leq$ 40%) in MAPE and SD, as compared to the increase in the MAPE (up to 200%) and SD (up to 70%) in the case of the SC25 maximum.

Although we used the parametric space (second approach) to obtain the best R_{ss}, independent of WSA parameters, however, during the declining phase of the SC24, both approaches led to $R_{ss} = 3.0\ R_{\odot}$ as the best performing R_{ss}. Moreover, during the SC24 maximum, either of the two R_{ss}, i.e., $R_{ss} = 2.0\ R_{\odot}$ or $2.5\ R_{\odot}$ outperformed $R_{ss} = 3.0\ R_{\odot}$ for our second approach by using HU ZPC and STD maps.

The trend of the best-performing source surface height at each phase, as mentioned earlier, remains the same even after using parametric space for three types of input magnetic maps. Therefore, the improvement in performance on using the higher values of R_{ss} in every CR is independent of the choice of the different maps and the WSA parameters. We can make the following inferences from the Figure 4.4:

1. Optimization of WSA parameters resulted in a significant increase in *cc* for every CR and at every R_{ss}.

2. The overall trend of the performance in the declining/minimum phase of the SC24 remains the same, as it was for the default WSA parameters approach, for different R_{ss}, i.e., the best performing R_{ss} in most cases (18/24 combined for all the maps) is $3.0\ R_{\odot}$ (green dots). The average *cc* values for $R_{ss} = 2.5\ R_{\odot}$ (orange dashed lines) corresponding to the STD, ZPC, and HU ZPC maps have been estimated to be 0.49, 0.61, and 0.64 respectively. The average *cc* values for $R_{ss} = 3.0\ R_{\odot}$ (green dashed lines) corresponding to STD, ZPC and HU ZPC maps have been estimated as 0.55, 0.72 and 0.72, respectively. These values demonstrate clear improvement in framework performance for all the three maps when using $R_{ss} = 3.0\ R_{\odot}$ as compared to $R_{ss} = 2.5\ R_{\odot}$.

3. During the SC24 maximum phase, the average performance of the framework is the best for either R_{ss} = 2.5 $R_{\odot}$ or 2.0 $R_{\odot}$ for all maps (orange and blue dashed lines). The relative increase in average performance is not as significant as it is during the minimum phase.

As mentioned at the beginning of this section, we have a total of 24, 48, and 24 different instances to evaluate the best performing R_{ss} at the SC24 maximum, SC24 declining/minimum phase, and SC25 maximum, respectively. Figure 4.5 shows a histogram indicating when different values of R_{ss} were found to be the best choice at different phases of SC24 and SC25 (please note that CR2182-85 and CR2193-96 are in SC24 declining phase). This bar graph shows that R_{ss} = 3.0 $R_{\odot}$ is the most suitable choice for the maximum number of CRs (35/48) during the declining/minimum phase (middle panel Figure 4.5).

Moreover, it may be safe to mention that the number of cases of best performance at lower R_{ss} is larger during the maximum of SC24 ((8 + 12)/24, Figure 4.5), as compared to SC24 minimum ((11 + 2)/48, Figure 4.5) leading to an average best performance at R_{ss} = 2.5 $R_{\odot}$ or 2.0 $R_{\odot}$ (orange and blue dashed lines in Figure 4.3 and Figure 4.4). Based on this, we can say that lower R_{ss} (2.0 $R_{\odot}$ or 2.5 $R_{\odot}$) might be a preferable choice for the SC24 maximum (left panel of Figure 4.5), however with only a very small improvement in the average performance as compared to the SC minimum.

Furthermore, as the average performance of the overall framework increases from SC25 maximum, SC24 maximum to SC24 declining phase in our first approach (Figure 4.3), the distinction of the best performing R_{ss} becomes more obvious in Figure 4.5. Based on Figure 4.5, it is difficult to comment conclusively on the best-performing R_{ss} during SC25 maximum, given the fact that for half of the cases framework performed poorly (corresponding to default WSA parameters with negative *cc*) and after optimization. It led to a drastic increase in MAPE.

In summary, during the declining phase, R_{ss} = 3.0 $R_{\odot}$ was found to be the optimal source surface height. Similar results during the SC minimum have been reported in the context of observed open flux at L1 (Arden et al., 2014). They

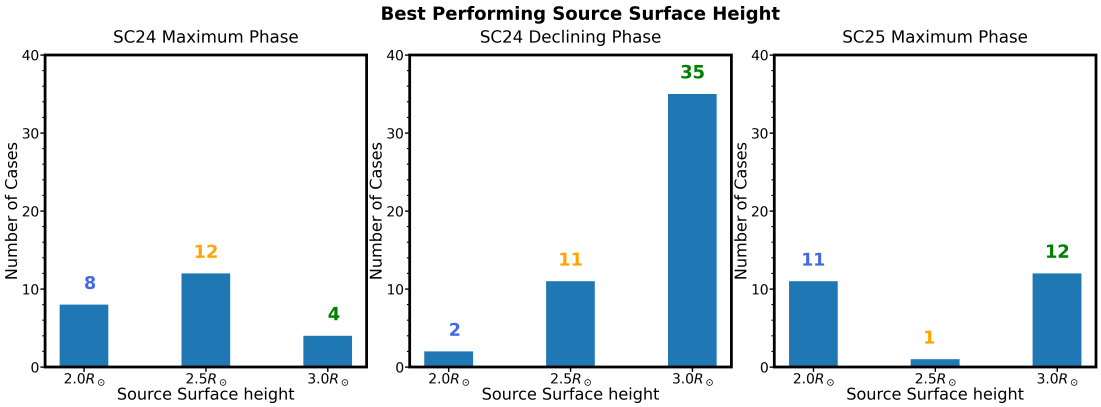

Figure 4.5: Number of cases for different R_{ss} in the best-performing scenario during the selected phase of the SC. Note, as explained in Section 4.3, the framework performed poorly for the SC25 maximum phase. Therefore, the results from the right panel are inconclusive.

found that by increasing the R_{ss} by 15-30% as compared to the conventional R_{ss} (2.5 $R_\odot$) during the minimum phase gives a better estimate of open flux measured at L1. Our study shows that during the SC24 maximum, either R_{ss} = 2.0 $R_\odot$ or R_{ss} = 2.5 $R_\odot$ are preferable, as seen in the left panel of Figure 4.5. Here, observed skewness toward R_{ss} = 2.0 $R_\odot$ at SC24 maximum agrees with the findings of Nikolić (2019), who reported a lower source surface height at the solar maximum as compared to the conventional R_{ss}. However, it differs in the absolute values, which could be due to a shorter time period, a smaller number of choices of R_{ss} or different maps and methodologies adopted in our study. Moreover, the results obtained for SC25 maximum period remained inconclusive due to increased activity, suggesting a poorer performance of the framework. The improvement in the performance of the framework using optimized R_{ss} proved to be consistent irrespective of the choice of the magnetic synoptic maps and for all CRs and choices of WSA parameter settings. Further, it is important to mention that PFSS extrapolation itself is not a good approximation during periods of high solar activity as shown by Lee et al. (2011). To investigate the possible reasons for the poor performance of the framework during CR2272-2275, we examined the Carrington rotation movies[5] of SWAP images during this period. We compared it with the period of CR2143-2146, where the framework performed relatively

[5] http://proba2.sidc.be/swap/data/mpg/movies/carrington_rotations/

better. We noted that the CRs during SC25 maximum (CR2272-2275), for which the framework performed very poorly, exhibited a more active corona, with larger number of active regions evolving more rapidly, and a complex magnetic corona compared to that observed during the SC 24 maximum period. This also suggests a complex and dynamic solar corona with stronger currents, which challenges the assumptions of the PFSS model during CR2272-2275 (SC25 maximum) compared to the period of CR2143-2146 (SC24 maximum).

4.3.2 Case Studies of Selected CRs at SC Maximum and Minimum/Seclining Phases

In this section, we discuss the effect of varying R_{ss} on the profile of the modeled solar wind velocity at L1 at different phases of the SC. We present the results of solar wind velocity estimation using the method described in Section 4.2 for CRs selected during the maximum phase of the SC24 and the declining phase of SC24. Specifically, we select two CRs; CR2143, spanning Oct-Nov 2013, and CR2183, spanning Oct-Nov 2016, as representatives of the maximum and declining phases of SC24, respectively, to show the applicability of the framework for different phases of the SC.

(i) CR2143 (SC24 Maximum Phase)

Figure 4.6 shows the observed velocity profile taken from the OMNI database (black solid curve) and the modeled solar wind velocity profile using different synoptic magnetic maps (shown by colored dashed curves). The top, middle, and bottom panels show the velocity profile for $R_{ss} = 2.0\ R_{\odot}$, $R_{ss} = 2.5\ R_{\odot}$, and $R_{ss} = 3.0\ R_{\odot}$, respectively. The blue dashed line shows the velocity profile obtained using the STD maps obtained from GONG. The red and green dashed lines show the velocity profile obtained using HU ZPC and full ZPC maps, respectively. This figure shows the velocity profiles estimated using default WSA parameters as inputs in the model framework. The green and red shaded areas show the regions where using lower values of R_{ss} improved the solar wind velocity prediction. Green arrows in Figure 4.6 show the approximate position of the features which

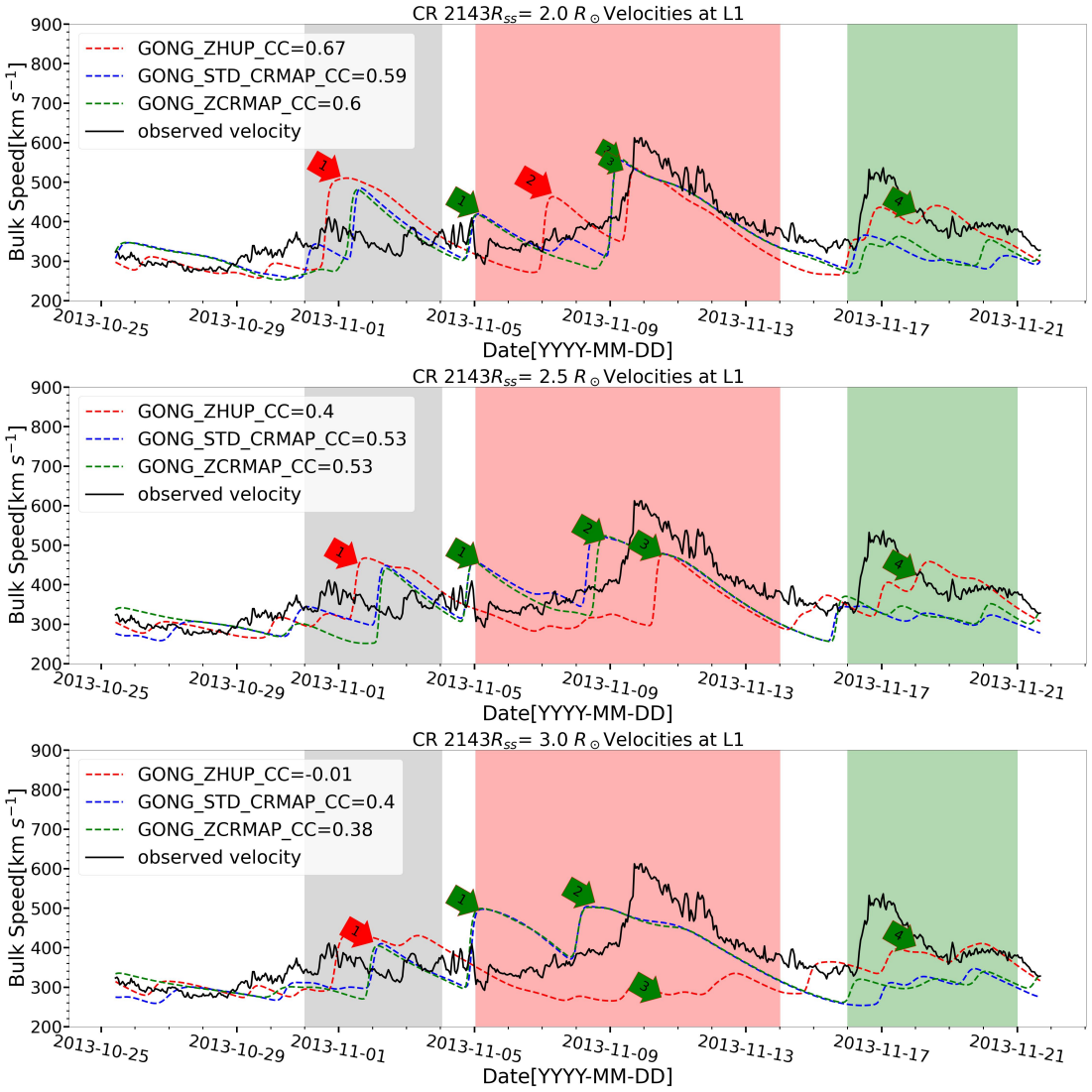

Figure 4.6: Plots of modeled (PFSS+WSA+HUX) and hourly averaged observed solar wind velocity from OMNI database at L1 (solid black line) with time for CR2143 for different R_{ss}, i.e., for R_{ss}= 2.0 $R_\odot$ (top panel), for R_{ss}= 2.5 $R_\odot$ (middle panel) and R_{ss}= 3.0 $R_\odot$ (bottom panel). The red, blue, and green dashed lines show the velocity profiles using HU ZPC, STD, and full ZPC maps, respectively. Green arrows show the time period around which R_{ss} optimization improve the match between the modeled and observed profile as R_{ss} decreases. The red arrows show the time period around which the prediction does not improve as R_{ss} decreases. The shaded regions show the time period where varying R_{ss} significantly changes the modeled velocity profile.

matched better with the measurements using lower value of R_{ss} as compared to higher values R_{ss}. As the value of the R_{ss} decrease from 3.0 $R_{\odot}$ to 2.0 $R_{\odot}$ (from bottom to top panel), the modeled velocity profiles (colored dashed curves) match better around the green arrows with the observed velocity profiles in the red and green shaded areas for all the different maps. The red arrows show the features that matched better with the observations while using higher R_{ss} as compared to lower R_{ss}. However, the overall performance, as indicated in terms of *cc*, increases as R_{ss} is decreased. For example, for ZPC maps, *cc* increases from 0.38 to 0.53 and then to 0.6, as R_{ss} decreases from 3.0 $R_{\odot}$ to 2.5 $R_{\odot}$ and then to 2.0 $R_{\odot}$, respectively, as shown in Figure 4.6. Similar trends can be observed for other maps as well. It is important to note that although CR2143 shows that the performance improves with decreasing the values of R_{ss}, this does not hold good for all the CRs during the SC24 maximum. However, by examining the average performance based on all the CRs, we can infer that lower R_{ss} values (2.0 $R_{\odot}$ and 2.5 $R_{\odot}$) perform better than 3.0 $R_{\odot}$ during SC24 maximum (Figure 4.5).

(ii) CR2183 (SC24 Declining Phase)

R_{ss} optimization during the CR2183 gave us clearer results about the effects of R_{ss} on the modeled solar wind profile at L1 than CR2143. This is due to the fact that the PFSS extrapolation during this phase is expected to be more reliable than the maximum phase of the SC. Figure 4.7 shows the modeled (dashed red, green, and blue curves) and observed solar wind velocity profiles (solid black curve) during CR2183.

One can see that increasing the values of the R_{ss} (from top to bottom panels) suppresses most of the additional peaks, as shown by the green arrows, in the modeled solar wind velocity profile, resulting in a better match of the modeled and observed solar wind velocity profile (Figure 4.7). For example, for ZPC maps, *cc* increases from 0.53 to 0.73 and then to 0.78, as R_{ss} increases from 2.0 $R_{\odot}$ to 2.5 $R_{\odot}$ and then to 3.0 $R_{\odot}$, respectively, as shown in Figure 4.7. Similar trends can be observed for other maps as well. The white region between grey and red shaded areas shows a very minute improvement at lower R_{ss}. This is very small in comparison to the improvement at higher R_{ss} in the red and grey-shaded regions.

Therefore, it is inferred that the framework performed better at higher R_{ss}, i.e., $R_{ss} = 3.0\ R_{\odot}$.

4.3.3 Comparison of PFSS Extrapolation with PROBA2/SWAP Observations in the Lower Corona

In Section 4.3.1, we found that using ZPC maps improved the overall performance (averaged over all the three R_{ss} and all CRs) of the framework. This improvement with ZPC maps, compared to STD maps, is evident from the increase in the average *cc*, computed for all three values of R_{ss}. During the minimum phase of SC24, the average *cc* increases from 0.31 (for STD maps) to 0.51 (for ZPC maps), and during the maximum phase of SC24, it rises from 0.22 to 0.47, using the default WSA parameters. Similar results for optimized WSA parameters were found, as discussed above, i.e., an increase in average *cc* from 0.57 to 0.69 during SC24 maximum and an increase in average *cc* from 0.53 to 0.66 during SC24 minimum (for full CR maps). This suggests that PFSS extrapolations from ZPC maps are likely to provide a more accurate representation of the magnetic field structure of the Sun compared to the extrapolation from standard (STD) GONG maps.

In order to verify this result, we compare the overall large-scale coronal structure during the minimum and maximum phases of the SC with the PFSS extrapolated structure from hourly updated (HU) STD and ZPC maps. For this purpose, we used the SWAP mosaics reconstructed from the special observational campaign (discussed in Section 4.2) on 20 August 2017 (CR2194, SC24 minimum) and 7 August 2023 (CR2274, SC25 maximum) with larger FOV.

Figure 4.8 illustrates the observed global coronal structure of the Sun from the PROBA2/SWAP during the minimum of the SC24 on August 20, 2017, 10:45 UT (average time of mosaic). We overlaid magnetic field lines obtained from the PFSS extrapolation using the HU STD map (20 August, 2017, 12:14 UT, top panel) and HU ZPC map (20 August, 2017, 12:14 UT, bottom panel). While the overall structure of the extrapolated field lines obtained from both extrapolations

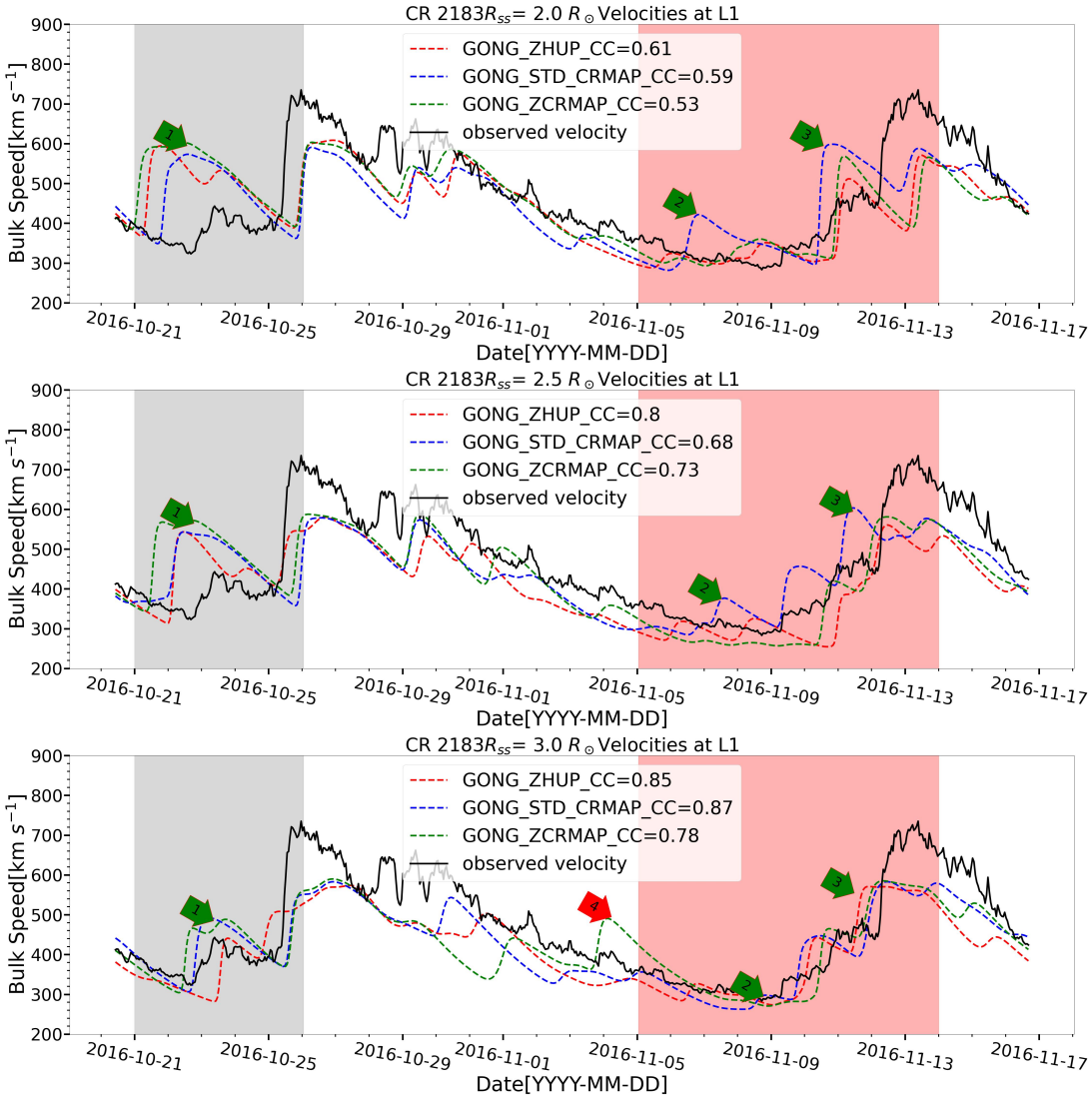

Figure 4.7: Plots of modeled (PFSS+WSA+HUX) and hourly averaged observed solar wind velocity from OMNI database at L1 with time for CR2183 for different R_{ss}, i.e., for R_{ss}= 2.0 $R_\odot$ (top panel), for R_{ss}= 2.5 $R_\odot$ (middle panel) and R_{ss}= 3.0 $R_\odot$(bottom panel). The red, blue, and green dashed lines show the velocity profile using HU ZPC, STD, and full ZPC maps, respectively. Green arrows show the time period around which R_{ss} optimization improves the match between the modeled and observed profile as R_{ss} increases. The red arrows show the time period around which the prediction does not improve as R_{ss} increases. The shaded regions show the time period where R_{ss} significantly changes the modeled velocity profile.

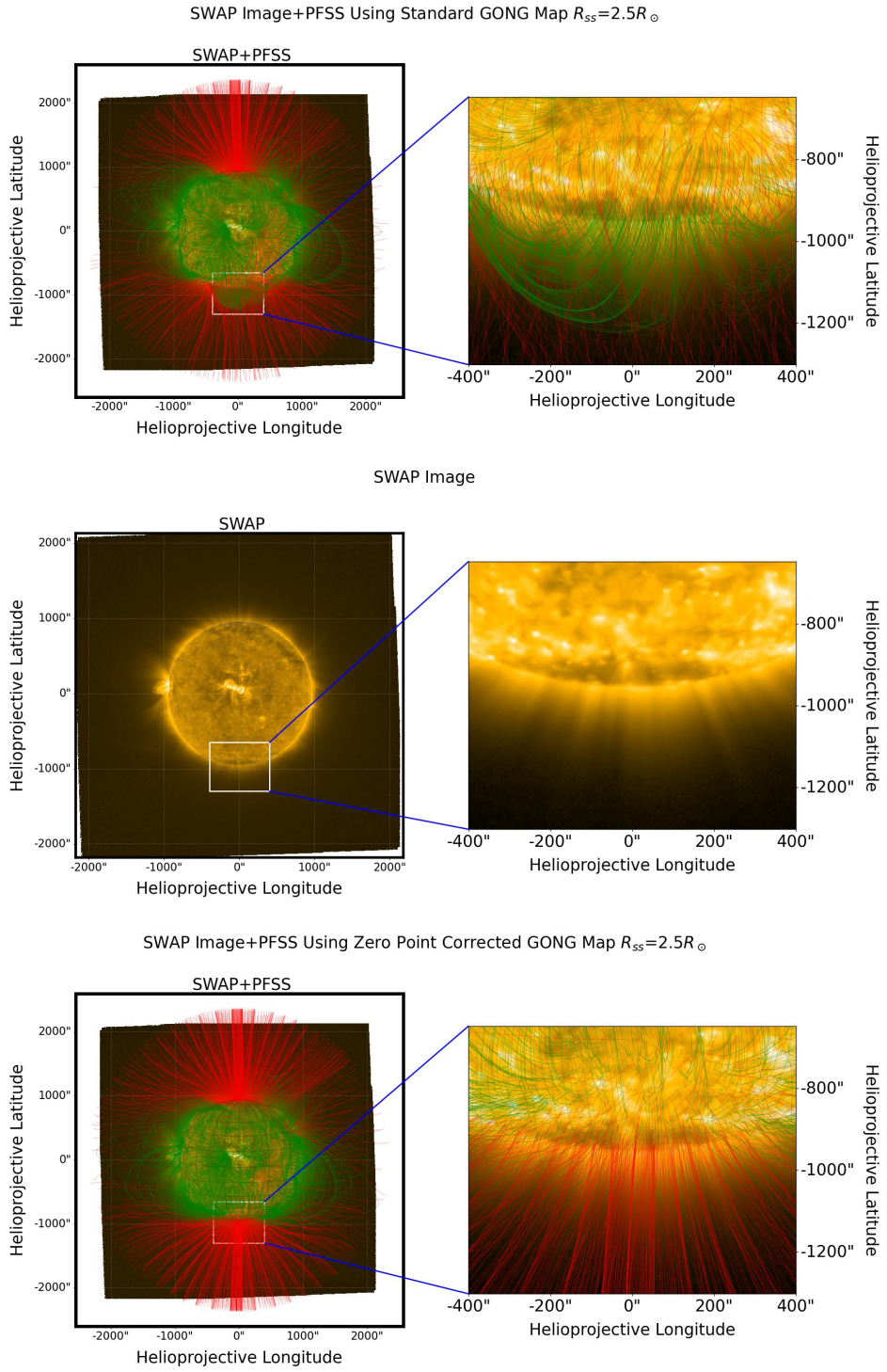

Figure 4.8: PFSS extrapolated magnetic field lines overlaid on the SWAP (top and bottom panel) image of 20 August 2017, 10:45 UT. The middle panel shows the SWAP mosaic without PFSS extrapolation. The top left panel shows PFSS extrapolation with HU STD map, and the bottom left panel with HU ZPC map (on 20 August 2017, 12:14 UT). The right panel presents a zoomed-in view of the white rectangular region highlighted in the left panel.

is similar, notable differences can be seen near the south pole (in the zoomed-in panel). In this region, the PFSS extrapolation using the HU ZPC map indicates open field lines (red color), whereas the HU STD map show closed field lines (green color). Upon closer inspection in this region, we can clearly identify a coronal hole in the SWAP images, which agrees with the PFSS extrapolation in the HU ZPC map, indicating open field lines (red color).

Similarly, we compared the extended FOV of SWAP with PFSS extrapolation near the maximum of the SC25 on 7 August 2023 (20:37 UT) (Figure 4.9, zoomed-in panels). We can see multiple coronal loop structures all over the western limb in the middle panel of Figure 4.9. The features in the northwest and southwest limb match better with the PFSS extrapolation with the HU ZPC map in the bottom panel of Figure 4.9 compared to the HU STD GONG map (top panel of Figure 4.9). PFSS extrapolation with HU ZPC map (bottom panel) shows multiple local coronal loops, which are closer to the observations in the middle panel compared to global coronal loops with HU STD map (top panel). Moreover, near the south pole (zoomed-in panel), the PFSS extrapolation from HU ZPC map exhibits more closed field lines (bottom panel) compared to the HU STD map (top panel). Upon closer examination of the SWAP mosaic (middle panel), a coronal cavity is observed at the south-west limb of the Sun. This rules out the presence of open field lines in this region. The closed field lines are not very prominent in the extrapolation from HU STD map, where the field lines connect to a larger coronal loop structure/streamer (top panel). The overlying closed loops are distinctly visible in the extrapolation from HU ZPC map (bottom panel).

Consequently, by comparing SWAP images, we found that HU ZPC maps are a better choice for both the SC minimum, i.e., 20 August 2017, and as well as for the SC maximum, i.e., 7 August, 2023, implying that HU ZPC maps yield accurate results in PFSS extrapolation, matching the coronal structure observed in 174 Å. This further resulted in accurate solar wind velocity prediction at L1. Studies by Nikolić (2019) and Li et al. (2021) demonstrated that standard GONG maps used in space weather prediction have shown a decline in accuracy over time because of

the PFSS solutions derived from GONG maps, particularly in the polar regions. As mentioned in the methodology section, HU ZPC GONG maps mitigate the zero-point inaccuracies. Our analysis of the 16 CRs at different phases of the SC shows that these inaccuracies are crucial in estimating the solar wind velocity of the WSA model at L1. Therefore, we suggest ZPC maps should be used as input in space weather prediction models.

4.3.4 Long Term Study of Source Surface Height Optimization Over SC24 and SC25 (CR2092 to CR2272)

We extended the R_{ss} optimization over the entire SC24 and SC25 (from January 2010 to September 2023). As shown in Section 4.3.1 and Section 4.3.3, the solar wind forecasting framework performed best using ZPC maps. Moreover, the performance of the framework using full ZPC maps and using HU ZPC maps, is found to be similar. Further, we noticed that using WSA parametric space does not change results significantly, i.e., the best performing R_{ss} in WSA model.

Therefore, we used only full ZPC maps for the long-term study covering every CR during SC24 and SC25, using ZPC maps and fixed WSA parameters approach. Here we further refined choices of R_{ss}, ranging from 1.5 $R_{\odot}$ to 3.25 $R_{\odot}$ with a step of 0.25 $R_{\odot}$. The results showed that the best performing R_{ss} varied from one CR to another. To observe the long-term overall pattern of the best R_{ss}, we plotted the running average of 12 CRs, of the best R_{ss} (sky blue curve) in the top panel of Figure 4.10. The solid red and dashed yellow lines show the performance of the framework with the best R_{ss} and conventional R_{ss} (2.5 $R_{\odot}$). The bottom panel of Figure 4.10 shows the solar activity cycle represented by monthly sunspot numbers from January 2010 to September 2023. Based on Figure 4.10, we conclude the following:

- The performance of the framework at the maximum of SC24 and SC25 (red curve in red shaded area lying below the $cc = 0.5$ line) is poor compared to its performance in the declining and minimum phases (red curve in grey

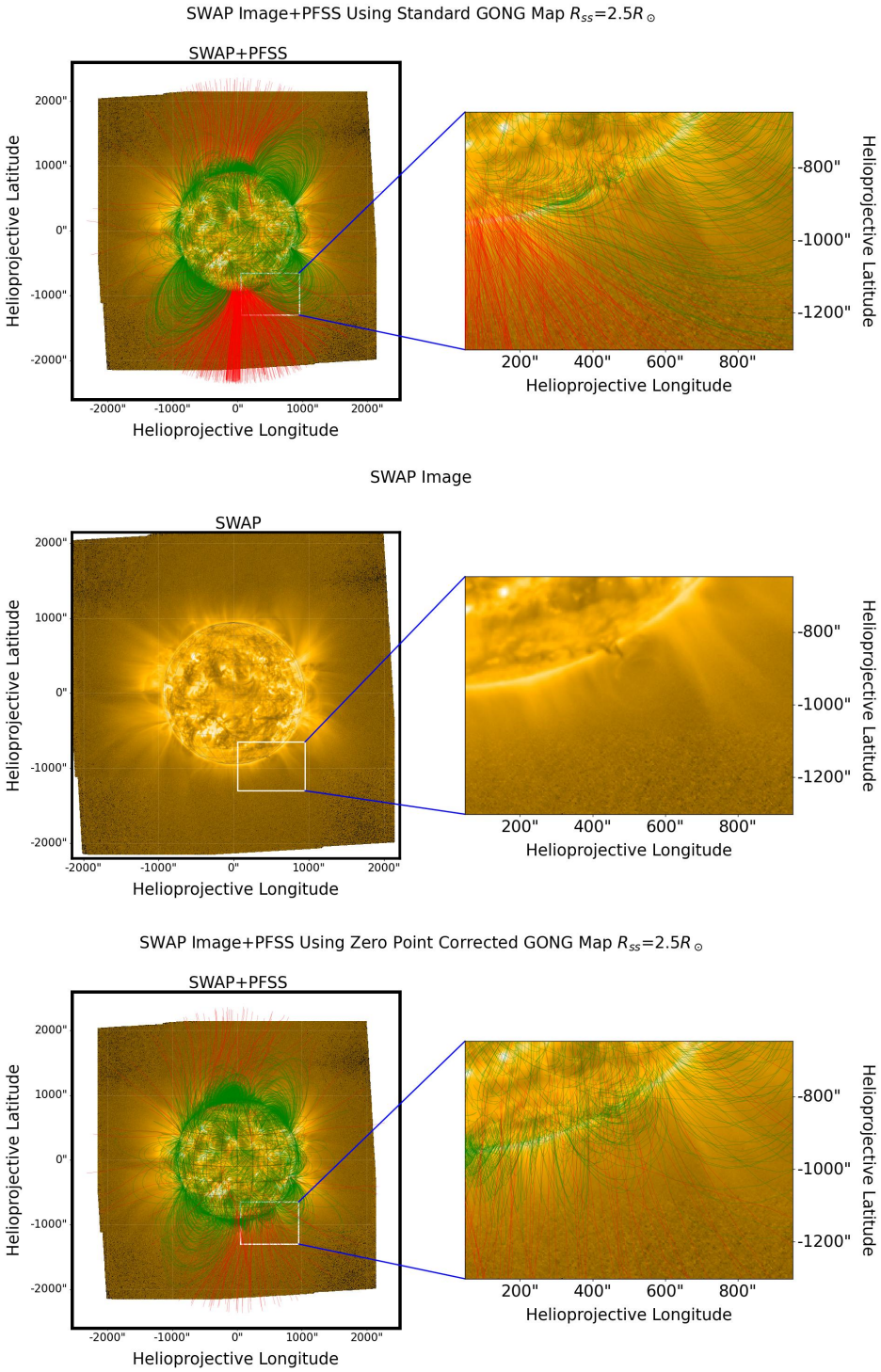

Figure 4.9: PFSS extrapolated magnetic field lines overlaid on PROBA2/SWAP images recorded on 7 August 2023, 20:37 UT. The top panel shows PFSS extrapolation with HU STD maps and the bottom panels with HU ZPC maps. The middle panel shows the SWAP mosaic without PFSS extrapolation. The right panel presents a zoomed-in view of the white rectangular region highlighted in the left panel.

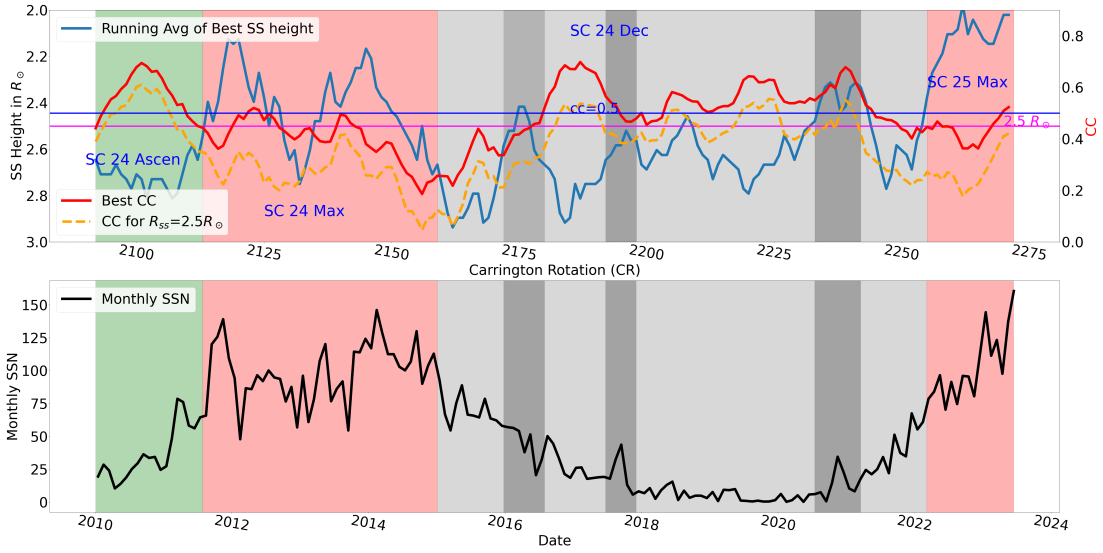

Figure 4.10: Top panel shows the 12 CR running average of the best performing R_{ss} (sky blue), cc for the best R_{ss} (red), and cc for R_{ss} = 2.5 $R_\odot$ (yellow). The horizontal blue and the magenta line show R_{ss} = 2.5 $R_\odot$ and cc=0.5, respectively. The bottom panel shows the monthly sunspot number with time.

and green shaded areas lying above the $cc = 0.5$ line).

- The average of the best R_{ss} during the declining, minimum phases of SC24 and ascending phase of SC25 is greater than the conventional R_{ss} (2.5 $R_\odot$) (sky blue curve in the grey shaded area).
- The R_{ss} during the ascending phase of SC24 is greater than 2.5 $R_\odot$ (sky blue line in green shaded area).
- The R_{ss} during the maximum phases of SC24 and SC25 is less than 2.5 $R_\odot$ (sky blue curve in the red shaded area).
- The difference between the red (performance corresponding to the best R_{ss}) and yellow curve (performance corresponding to $R_{ss} = 2.5R_\odot$) is significant in each phase of the SC. It suggests that using optimized value of R_{ss} at each phase is required.
- An overall anti-correlation is observed between solar activity (monthly sunspot number, bottom panel) and the best R_{ss} (top panel sky blue curve).

This long-term study using full ZPC maps spanning the different phases of

SC24 and SC25 supports the results obtained from the detailed study of 16 CRs, suggesting a higher values of R_{ss} than 2.5 $R_{\odot}$ in the declining and minimum phases of SC. However, it is challenging to determine the exact value of the R_{ss} during these phases, although it ranges between 3.0 $R_{\odot}$ and 2.5 $R_{\odot}$. The best performing R_{ss} during the ascending phase of SC24, greater than 2.5 $R_{\odot}$ (sky blue curve in green shaded area), also supports our results for 16 selected CRs during the declining phase of SC24, as confirmed in the Section 4.3.1. We have plotted the overall statistical results of the best performing R_{ss} from grey and green areas of Figure 4.10 in the top panel of Figure 4.11. The results of the red-shaded area are shown in the bottom panel of Figure 4.11. We note that 67 out of 115 CRs (58 %) have $R_{ss} \geq 2.75$ $R_{\odot}$ in the grey and green shaded region of Figure 4.10, i.e., ascending, declining, and minimum phase of SC24 and ascending phase of SC25. Whereas during the maximum phase of SC24 and SC25, the number of cases for best-performing source height at lower R_{ss} (≤ 2.5 $R_{\odot}$,) has significantly increased (40% to 72%), i.e., the distribution is biased toward the lower values of R_{ss}.

4.4 Conclusions

In this chapter, first we estimated the optimal value of source surface height, i.e., R_{ss} for modeling solar wind velocity at L1 by using three different types of magnetic maps as inputs for 16 CRs selected at different phases of the SC. For this study, we employed two approaches, one using default WSA parameters and the other using a range of WSA parameters to find the best values of R_{ss} among 2.0 $R_{\odot}$, 2.5 $R_{\odot}$, and 3.0 $R_{\odot}$. During the declining phase of the SC24, the model framework performed overall (average *cc*) better compared to the maximum phases of the SC24 and SC25. We also found that zero-point-corrected maps performed better as compared to standard GONG maps. Motivated by the above findings we further, extended the study spanning from January 2010 to September 2023, using ZPC maps and default WSA parameters with a more refined choice of R_{ss}, i.e., ranging from 1.5 $R_{\odot}$ to 3.25 $R_{\odot}$ with a step of 0.25 $R_{\odot}$. This study showed a similar trend of R_{ss} as our study of 16 selected CRs.

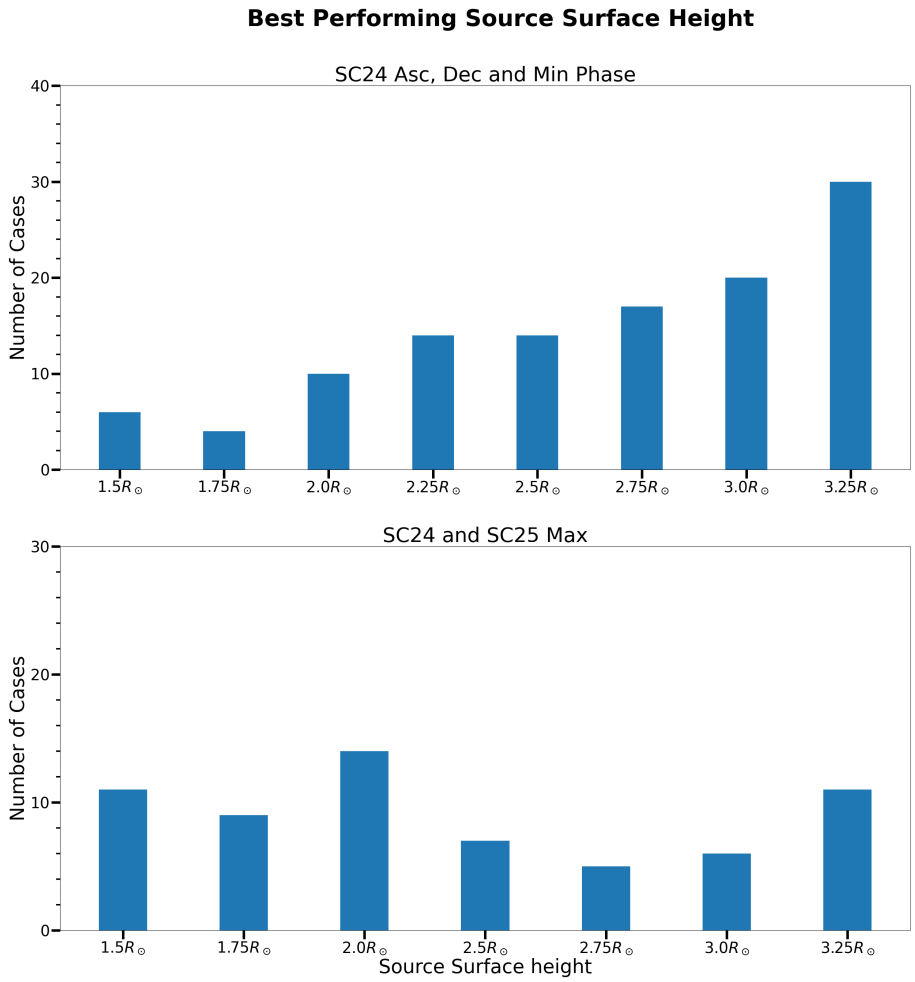

Figure 4.11: Number of cases for different R_{ss} in the best-performing scenario for the long-term study from CR2092 to CR2272, covering SC24 and SC25, using ZPC maps.

Given the complexity of the solar wind velocity prediction problem at L1, we have attempted to assess the change in the source surface height (R_{ss}) and the impact of the usage of different types of GONG maps and WSA model parameters for different phases of the SC. Our results based on the detailed study of 16 CRs, suggest using a higher surface height (3.0 $R_\odot$) in the WSA model during SC minimum as compared to the conventional R_{ss} (2.5 $R_\odot$). In contrast, during maximum phase of SC24, either R_{ss} = 2.0 $R_\odot$ or R_{ss} = 2.5 $R_\odot$ are found to be preferable. During the SC25 maximum, for the detailed study of 16 CRs, our results are inconclusive because of the poor performance of the framework.

Further, our long-term analysis of SC24 and SC25 using full ZPC maps confirms that the optimal source surface height (R_{ss}) for solar wind forecasting varies with the SC phase. While higher R_{ss} values ($\geq 2.75R_{\odot}$) are generally preferred during the declining, minimum, and ascending phases, lower values ($\leq 2.5R_{\odot}$) perform better during solar maxima.

The results agree with those obtained in previous studies (Lee et al., 2011; Arden et al., 2014), in terms of the relative changes in the best source surface heights with the phase of the SC. Previous studies were based on open magnetic flux estimation at L1. We also want to emphasize that our finding for the SC maximum should be carefully interpreted, keeping in mind the applicability of PFSS during the SC maximum as discussed by Lee et al. (2011).

We want to mention here that standard magnetic maps from GONG have been used extensively by the community in solar wind velocity forecasting frameworks, e.g., Shiota et al. (2014); Pomoell, Jens and Poedts, S. (2018); Nikolić (2019); Narechania et al. (2020); Kumar and Srivastava (2022); Mayank et al. (2022). They are also used in operational WSA-ENLIL simulations. However, our study found substantial improvement in the performance of the solar wind forecasting framework while using ZPC magnetic maps compared to standard maps. This is further confirmed by the comparison of PFSS extrapolation with the near-Sun observations obtained from the PROBA2/SWAP instrument. It thus establishes a link between the quality of near Sun PFSS extrapolation and the quality of solar wind velocity prediction at L1. Therefore, we strongly advocate the use of ZPC magnetic maps from GONG in space weather prediction models instead of standard maps. Narechania et al. (2020) suggested the use of ZPC maps compared to the standard GONG maps based on a single case study of a CR using MHD simulations. Our study further supports their results based on a more robust and long-term analysis at different phases of the SC24 and SC25. Moreover, we validated the superiority of ZPC maps over standard GONG maps in both PFSS extrapolations compared with near-Sun observations, and as input in solar wind velocity prediction models at L1. A recent study by Li et al. (2021) based upon open flux and polarity of the IMF at L1 reported that ZPC maps

outperformed standard GONG maps significantly. However, they also found that HMI maps (cc=0.71) performed slightly better than ZPC maps (cc=0.70) when compared with observed open flux. A more recent study by Mayank et al. (2022) reported that in the context of solar wind prediction at L1, GONG standard maps outperformed the HMI maps for CR2104, selected at the ascending phase of the SC24.

Badman et al. (2020) suggested the use of lower surface height (1.3- 1.5 $R_{\odot}$) to reproduce the radial component of the magnetic field observed at PSP located at 0.5 AU on specific days (2018-10-20 and 2018-10-29), which depends upon the connectivity of the magnetic field lines and the local magnetic field distribution. Our approach in this chapter is to optimise the source surface height, i.e., R_{ss} for the entire CR and compare observed and modeled solar wind velocity at L1 for each CR. It may be noted that in our study during solar minimum, for few specific short time periods (during individual CRs), we found that the modeled solar wind velocity profile for lower R_{ss} values matches better with the observed profile. Nevertheless, a higher R_{ss} (3.0 $R_{\odot}$) was found to perform better for the entire CR as inferred from the cc value. And the opposite was observed during SC maximum.

The study by Huang et al. (2024), suggested a slightly lower R_{ss} than 2.5 $R_{\odot}$ during a solar minimum, by comparing the unsigned, open flux at L1. It assumes an isotropic magnetic field in the heliosphere. This approach is sensitive to the area of coronal holes only, whereas our study is complex in the sense that our final modeled output, the velocity at L1, is related to the overall area of the coronal holes, the overall magnetic structure and connectivity of sub-Earth field lines on the solar surface. Moreover, we use a more sophisticated extrapolation (HUX) method in the heliosphere than previous studies. Therefore, our study highlights the challenges and intricacy of the problem in optimising the source surface height in the PFSS model while using different approaches.

It is also important to mention that we used the HUX model for solar wind velocity extrapolation for simplicity. However, a slightly advanced version of this model, i.e., HUXt (Barnard and Owens, 2022), could be used in future work

to provide a more realistic framework. This model introduces an explicit time dependence in the solar wind extrapolation by introducing a residual acceleration in the solar wind. Further, the optimization approach relying solely on Pearson coefficient has its own drawbacks as it disregards other metrics and does not account for overall features. Therefore, advanced metrics, e.g., Dynamic Time warping (Samara et al., 2022) or a combination of metrics, can be used to obtain more robust and conclusive results.

In summary, our study of SC24 and SC25 improves our understanding of how the height of the source surface (R_{ss}) and different kinds of maps in the PFSS model influence solar wind velocity modeling across different phases of the SC. This knowledge can contribute to refining predictions of solar wind velocity, as well as for operational space weather frameworks.

A part of the work presented in this chapter has been published in Kumar et al. (2025).

Chapter 5

Heliospheric Propagation of Coronal Mass Ejections: Deflection

5.1 Introduction

The solar wind plays a vital role in the heliospheric propagation of CMEs. In Chapters 3 and 4, we reviewed various solar wind forecasting models, evaluating their applicability and performance across different phases of the solar cycle. We also discussed potential improvements to enhance forecast accuracy. In the remaining chapters, we investigate how solar wind and ambient magnetic field conditions influence CME trajectories in the heliosphere.

Understanding the propagation and interaction of CMEs with the solar wind is essential to assess their potential impact on Earth. Most of the CMEs expand in a "self-similar manner" with a constant direction of propagation. This means that, at any given time, the dimensions of the CME grow in proportion to its distance from the center of the Sun. Previous studies have shown that many CMEs follow a self-similar expansion without significant deflection (Vourlidas et al., 2010; Colaninno, 2012). The solar wind contains structured flows, with alternating slow and fast streams. As different parts of a CME encounter varying solar wind conditions, they may experience differential propagation. CMEs are

also known to deflect in the low corona toward the heliospheric current sheet (HCS), driven by interactions with the magnetic field of the Sun. These effects introduce significant uncertainty in predicting CME arrival times and properties at L1, complicating space weather forecasting.

MacQueen et al. (1986) analysed 29 CMEs observed during the Skylab period (1973–1974) and 19 CMEs during the Solar Maximum Mission (SMM) (1980). They found that CMEs observed during the Skylab period, which coincided with solar minimum, exhibited equatorward deflection. In contrast, CMEs observed during the SMM period, which occurred during solar maximum, did not show such behaviour. The equatorward deflection during the Skylab period was attributed to the influence of the large-scale bipolar magnetic field and associated solar wind flow patterns typical of solar minimum.

Gopalswamy and Thompson (2000) investigated the CME associated with a prominence eruption on 14 December 1997, using LASCO-C2 observations. This event showed an equatorward deflection of approximately 30°, shifting from about S30 latitude to near the equator, where a coronal streamer was located. Subsequently, Filippov et al. (2001) proposed a simple model to explain the non-radial motion of eruptive prominences. By treating the prominence as a toroidal current and employing extrapolations of the global coronal magnetic field, their model reproduced the deflection behaviour observed during solar minimum. Later, Gopalswamy et al. (2008), based on a long-term study of 99 CMEs primarily from SC23, suggested that a strong global dipolar magnetic field can guide CMEs toward the ecliptic plane.

Kay et al. (2015) using Forecasting a CME's Altered Trajectory (ForeCAT) model studied the CMEs observed during CR 2029 and CR 2077. They reported that CMEs with lower mass and speed and a strong ambient medium with a strong gradient of magnetic field during SC minimum were deflected to maximum magnitude. Shen et al. (2011) studied the kinematic evolution of the 8 October 2007 CME using 3D stereoscopic reconstruction of the CMEs using the Graduated Cylindrical Shell (GCS) model. They used multi-viewpoint images from STEREO-A & B and SOHO/LASCO.

They found that the gradient of radial field energy in the $\theta - \phi$ (heliographic latitude and longitude) sphere (constant R), i.e., pressure gradient force, pushed this CME in the regions of lower energy density, i.e., the region of the HCS. After its alignment with the HCS, the CME propagated almost radially. Later Gui et al. (2011) extended the study by Shen et al. (2011) to 10 CMEs observed during 2007-2008 and found that the observed deflection in 8 of the CMEs is consistent in strength and direction with the gradient of the magnetic energy density.

Using a coronal hole influence parameter (CHIP) (Gopalswamy et al., 2009), Makela et al. (2013) suggested that CMEs can be deflected by nearby coronal holes towards the polarity inversion line (PIL). They also studied the influence of coronal hole magnetic fields on magnetic cloud (MC) and non-magnetic cloud associated events. Based on the events with CHIP values larger than 2.6 G, Makela et al. (2013) reported that non-MC events were deflected away from the Sun-Earth line, whereas MC events were deflected towards the Sun-Earth line. Their finding supported the idea that all ICMEs are MC/flux rope, and those events that are observed as non-MC at 1 AU were deflected away from the Sun-Earth line by nearby coronal holes.

Based on a study of 36 CMEs observed during 2007 and 2010, Jones et al. (2017) found that 28 of the CMEs were deflected toward the HCS region. Their findings also suggest that the magnitude of deflection is directly proportional to the latitudinal distance of the CME from the HCS. An east-west asymmetry in the distribution of the source region of the CMEs related to geomagnetic storms has been known for a long time (Newton, 1943) and has been confirmed using modern data by Wang et al. (2002).

The east-west asymmetry of the Earth encountering halo CMEs has been found to be dependent upon the transit speed with respect to ambient solar wind speed. The source distribution of fast CMEs was found to be shifted toward the west limb, and that of slow CMEs was shifted toward the east limb of the Sun. This asymmetry was related to the longitudinal deflection of the CMEs by the solar wind in the interplanetary space (Gosling et al., 1987; Wang et al., 2002). Wang et al. (2004) reported that faster CMEs, while propagating in a slower solar wind

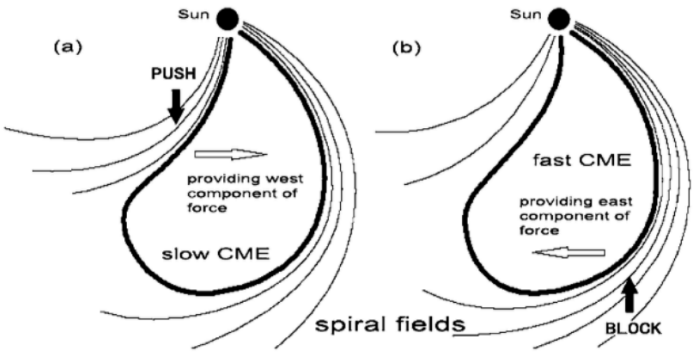

Figure 5.1: (a) Eastward deflection of slow CMEs by the fast solar wind behind them and (b) Westward deflection of the fast CMEs because of slow solar wind in front of it (Adapted from Wang et al. (2004)).

environment, will experience drag from solar wind ahead of them, deflecting them in the eastward direction, while, the slow CMEs propagating in a faster solar wind environment will experience a push/drag from the faster solar wind behind them, resulting in a westward deflection of such CMEs (Figure 5.1). Wang et al. (2020) analysed the deflection behaviour of 30 CMEs observed in the LASCO coronagraph FOV, in relation to the direction of the ambient magnetic field. They found that 87% of these deflections were consistent with the observation made in previous studies (Shen et al., 2011; Gui et al., 2011; Kay et al., 2015). Of these, 69% of the CMEs were deflected toward the HCS, while 31% were deflected toward pseudo-streamer regions.

A similar study by Wang et al. (2023) examined 124 halo CMEs originating from 40 active regions to determine whether multiple CMEs from the same source region tend to be deflected in the same direction. Their analysis, based on PFSS extrapolations and coronal magnetic field data, aimed to identify the underlying causes of CME deflection in the corona. They reported that 23 groups of CMEs (each group originating from a single active region) exhibited significant deflection, with 91% of the events aligning with the ambient magnetic field structure. Among these, 86% were deflected toward the HCS, and the remaining 14% toward pseudo-streamer regions.

In this chapter, we analyse 15 geo-effective (Dst $\leq$ -75 nT) CMEs observed during April 2010 to August 2018 using GCS reconstruction in the corona and heliosphere. Most of the previous studies tracked CMEs only up to the LASCO-C3 field of view (FOV), i.e., up to 30 $R_{\odot}$ (Shen et al., 2011; Gui et al., 2011; Kay et al., 2015; Martinić et al., 2023), whereas we continuously track each CME upto the HI FOV ($\approx$ 80 $R_{\odot}$) to study its trajectory in the heliosphere. This approach allows us to study the dynamics of the CME for a longer duration. We investigate and correlate the observed changes in the trajectories of the CME with the ambient medium of the CME, i.e., solar wind and magnetic field conditions of the ambient medium.

5.2 Observations and Analysis

5.2.1 Data Selection

We selected Earth-impacting CMEs that occurred between April 2010 and August 2018 and were associated with geomagnetic storms with a Dst index $\leq$ -75 nT. These events were further filtered based on the availability of data from various coronagraphs, i.e., LASCO-C2 & C3 onboard SOHO (Domingo et al., 1995) and SECCHI-COR2 (Howard et al., 2008) and HI1 (Eyles et al., 2009) onboard the STEREO spacecraft (Kaiser et al., 2008), allowing maximum possible viewpoints for stereoscopic reconstruction. Finally, we had 15 events, fulfilling the selection criteria. Table 5.1 provides a summary of the selected events, including the date and time of the first detection of CMEs in LASCO-C2 images. The source location mentioned in the table is taken from the CDAW Data Center, SOHO/LASCO CME CATALOG (`https://cdaw.gsfc.nasa.gov/CME_list/`) (Yashiro et al., 2004; Gopalswamy et al., 2009). We used the coronagraphic images from LASCO-C2 & C3, SECCHI-COR2, and HI1 instruments to track the CME, i.e., up to 80 $R_{\odot}$ (HI1 FOV). We also used the interplanetary magnetic field (IMF) data taken by the ACE to model the CME flux rope at L1. We used the standard synoptic magnetic maps of the Sun from the GONG website (`https://gong.nso.edu/data/magmap/crmap.html`) to investigate the ambient magnetic field of the Sun (Hill, 2018). We also employed the WSA model from NASA CCMC (Arge et al.,

2003) to estimate the background solar wind velocity at 21 $R_{\odot}$.

5.2.2 CME Flux Rope Model in the Corona and Heliosphere

As discussed in Chapter 2, Section 2.3.4, Graduated Cylindrical Shell (GCS) reconstruction (Thernisien et al., 2006) is a framework to model the CME flux rope assuming that a CME expands self-similarly. This model is defined by six parameters, i.e., latitude θ and longitude ϕ, of the axis, the half angle between conical legs (α), the tilt of the model axis with the ecliptic plane (γ), the apex height (h), and the aspect ratio (κ).

We implemented the GCS reconstruction model on the images from the SOHO/LASCO-C2 & C3, and STEREO/COR2 running difference images to track a selected CME in the heliosphere using a module in Python[1] (von Forstner, 2021). We enhanced the existing Python module to incorporate HI1 level2[2] images and were able to continuously track the CME structure in the HI1 FOV. For example, we were able to continuously track the CME structure for the 5 October 2012 CME (Event 7) up to ≈ 58 $R_{\odot}$ (Figure 5.2).

Figure 5.2 shows images of the 5 October 2012 CME at 9:54 UT with the GCS flux rope superposed. We performed the GCS fittings starting from 07:24 UT (last frame of COR2) to 20:09 UT (last HI1 frame with clear CME signature), i.e., for approximately 13 hours, for this event.

The approach followed is similar to that Gopalswamy et al. (2022) who implemented GCS reconstruction on the HI1 images of the 21 August 2018 CME. The continuous tracking of GCS parameters allowed us to effectively fit the model to observational data up to approximately 70 $R_{\odot}$ for Event 12 (Table 5.1).

It is important to note that for events until October 2014, we had observations available from three viewpoints up to the LASCO-C3 FOV, i.e., from STEREO-A, STEREO-B and SOHO. For these events, we utilized data from both COR2 & HI1 (STEREO-A and B) and LASCO-C2 & C3 (SOHO). For all events beyond LASCO-C3 FOV, we were restricted to observations from the

[1] https://github.com/johan12345/gcs_python

[2] https://stereo-ssc.nascom.nasa.gov/data/ins_data/secchi/secchi_hi/L2_11_25/

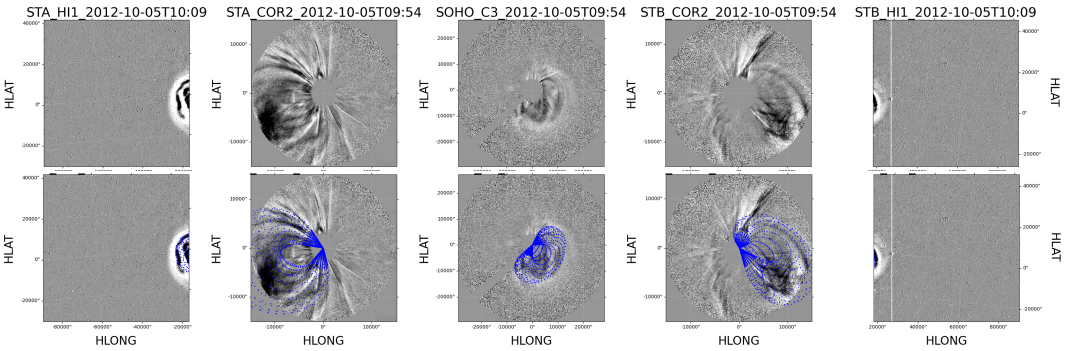

Figure 5.2: Snapshots of the 5 October 2012 CME are shown in the field of view (FOV) of coronagraphs and the heliospheric imager in the upper panel, along with the corresponding Graduated Cylindrical Shell (GCS) model fits in the lower panel. Observations from STEREO-A (STA) HI1 and COR2 are displayed on the left, while those from STEREO-B (STB) COR2 and HI1 are on the right. The SOHO/LASCO-C3 image is shown in the center. The HI1 images were captured at 10:09 UT, while the COR2 and LASCO-C3 images were taken at 9:54 UT. HLAT and HLONG denote the heliographic latitude and longitude, respectively.

HI1 (STEREO-A and STEREO-B) instruments alone. However, for events that occurred after October 2014, we were limited to only two viewpoints up to the LASCO-C3 FOV: SECCHI-COR2 & HI1 on STEREO-A and SOHO/LASCO-C2 & C3. Moreover, since most of the events are Earth-directed within $\pm 30^{\circ}$ of the Sun-Earth line, the actual trackable distances using 3D GCS reconstruction of these CMEs in LASCO-C2 & C3 FOV are larger than the normal FOV of LASCO-C2 & C3 due to projection effects.

5.2.3 Ambient Solar Wind and Magnetic Field Environment

To understand the ambient solar wind and magnetic field of an observed CME, we used pfsspy (Stansby, 2019) for potential field source surface (PFSS) extrapolation of the photospheric magnetic field of the Sun up to 2.5 $R_{\odot}$; PFSS extrapolation also gives us an idea of the overall structure of the magnetic field even above 2.5 $R_{\odot}$. We also used Wang–Sheeley–Arge (WSA; Arge and Pizzo, 2000; Arge et al., 2003) model code to estimate the solar wind velocity background at

21 $R_\odot$ from NASA/CCMC [3].

Table 5.1: List of 15 Earth-impacting events selected for our study. Event 7 and 12 are discussed in detail in Chapter 6. Events with superscripts YL, KG, SP, and NG were reported in Liu et al. (2011), Kay and Gopalswamy (2018), Patsourakos et al. (2016), and Gopalswamy et al. (2022), respectively.

Event	Date	Time (UT)	Source Location	Dst(nT)
1^{YL}	2010-04-03	10:33	S25E00	-81
2	2010-05-23	18:06	N16W10	-80
3^{KG}	2011-09-06	23:05	N14W18	-75
4^{SP}	2012-03-07	01:30	N15E26	-145
5	2012-07-03	21:25	N14W23	-78
6^{KG}	2012-09-28	00:12	N09W31	-122
7^{*}	2012-10-05	02:48	S23W31	-105
8	2013-06-02	16:25	N14W25	-78
9	2015-12-28	12:12	S23W11	-116
10	2016-01-14	23:24	S22W11	-93
11	2016-10-09	02:24	S02E39	-110
12^{*}	2017-05-23	05:00	S03W01	-125
13	2017-09-04	20:36	S10W16	-122
14	2017-09-06	12:24	S08W33	-109
15^{NG}	2018-08-20	21:24	N21W08	-175

5.3 Results and Discussion

5.3.1 GCS Reconstruction

Each CME selected for our analysis was tracked from LASCO-C2, COR2 and LASCO-C3 FOV up to the last frame/time in the HI1 images. Considering uncertainties in the GCS fitting (Verbeke et al., 2023), we focused on events that exhibited a change greater than 10° in latitudes and longitudes, i.e., difference in the initial and final GCS reconstruction. Our threshold for tilt change is almost

[3] https://ccmc.gsfc.nasa.gov/results/index.php

Table 5.2: Summary of the events that showed significant changes in GCS parameters. Here, EW refers to Eastward deflection, and EqW is Equatorward deflection based on the first independent fitting. The events in red denote the cases of CME rotation, and the asterisk denotes the event discussed in Chapter 6.

Event	First/Last fitted height	Change Observed	Velocity (km/s)
1	6 $R_\odot$ / 49 $R_\odot$	Long. 10° EW	800
2	8 $R_\odot$/ 34$R_\odot$	Lat. 10° EqW	450
3	9 $R_\odot$/54 $R_\odot$	Long. 11° EW	850
6	6 $R_\odot$/ 54 $R_\odot$	Lat. 10° EqW	850
7*	7 $R_\odot$/ 58 $R_\odot$	tilt 21° Anti clockwise	600
12*	10 $R_\odot$/ 70 $R_\odot$	tilt. 19°Anti clockwise	400
13	13 $R_\odot$/ 42 $R_\odot$	Long. 25° EW	1800
14	14 $R_\odot$/ 35 $R_\odot$	Long. 13° EW	1450

twice as compared to the latitude and longitude because errors in tilt can be much larger than those in latitude or longitude. The selected events that showed significant changes are listed in Table 5.2. All the changes observed and listed for each case in the table were in the same direction, i.e., continuously increasing or decreasing. Note that for each event, we selected the first image GCS reconstruction when the CME was fully visible and the flux rope structure was well developed in the COR2 and C2 FOV. This choice was made to capture the flux rope at its mature stage. The initial height for the GCS reconstruction ranged between 6 and 14 $R_\odot$ for all the selected events. Additionally, the final height of the GCS reconstruction was determined by the time at which the CME structure remained clearly visible and intact in the HI1 FOV. Although some faster CMEs were observable at higher distances, their features became too distorted at those heights to accurately implement the GCS model. Based on the height-time analysis of the 15 Events, we conclude the following:

- 7 out of 15 CMEs did not exhibit any significant deviations from self-similar expansion, i.e., no changes in the values of latitude, longitude, or tilt, indicating that CMEs reached a steady self-similar expansion state above $\approx$ 10

$R_{\odot}$ as has been shown by Vourlidas et al. (2010). They found that most of the CMEs expand in the heliosphere self similarly.

- Six events displayed significant deflection ($\geq 10°$) in either longitude or latitude.

- Two CMEs (Event 2 and 6) were latitudinally deflected toward the equator (EqW). Longitudinal deflections were observed in four events (Events 1, 3, 13 and 14) in the EastWard (EW) direction.

- Only two events (5 October, 2012, and 23 May, 2017 CME) showed an increase in tilt (marked in red color) in Table 5.2.

GCS parameters have uncertainties associated with them (Verbeke et al., 2023). Therefore, to confirm the changes in latitudes and longitudes for 6 Events (2, 6, 1, 3, 13, and 14), two independent fittings were performed, for the events showing latitudinal and longitudinal deflection: first fitting was done with a cadence of one hour, (the estimated heights from this fit are shown in Table 5.2, column 2) and the second independent fitting was done for the first, and last images selected of the first independent fitting, to confirm the change in the first set of fitting. As a part of the second independent fitting for the 4 cases of longitudinal deflection (Events 1, 3, 13 and 14) and 2 cases of latitudinal deflection (Events 2 and 6), we implemented GCS reconstruction on the CME structure at a time prior to the first fitting based on the well-developed CME feature. From the two independent fittings on well developed CME features, we found similar results for latitudinal and longitudinal deflecting CMEs from two independent fittings. However, for the case of Events 12 and 7, which showed a change in tilt, three independent fittings were performed on images taken at a cadence of 1 hour, and all three fittings showed similar results. In this chapter, we focus on the events that showed deflection in the latitudinal or longitudinal direction. The events showing significant tilt changes are discussed in detail in the next chapter.

5.3.2 Ambient Environment Investigation

5.3.3 Longitudinally Deflected Events

We examined the ambient magnetic field and solar wind speed to understand the possible reasons for the longitudinal deflection of the CMEs listed in Table 5.2. Figure 5.3 shows the solar wind background at $\approx 21 R_{\odot}$ for the longitudinally deflected events (Event 1, 3, 13 and 14). All these four CMEs propagated in a slow solar wind relative to their own speeds, as illustrated in Figure 5.3. Here, Events 13 and 14 are plotted with a smaller half angle and aspect ratio than obtained from the actual GCS fitting to show their direction of propagation properly. In Figure 5.4, Events 13 and 14 are re-plotted with the actual GCS parameters to present the real extension of CMEs in the solar wind environment. The two fast events, 13 and 14, with average speeds of 1800 km/s and 1450 km/s, respectively, occurred within two days and were longitudinally deflected in the eastward direction towards the Sun-Earth line.

The deflection of CMEs due to solar wind drag is known to be influenced by several factors, including the cross-sectional area of the CME, the velocity difference between the CME and the ambient solar wind, density and mass of the CME (Cargill, 2004). When CMEs travel through similar solar wind conditions and maintain comparable spatial extents in the heliosphere, their relative deflections are primarily governed by their average propagation speeds. Our analysis of Events 1, 3, 13 and 14 supports this relationship of CME speed and deflection. We found, the fast-moving Events 13 and 14, with speeds of 1800 km/s and 1450 km/s respectively, experienced deflections of 25° and 13°. These events were characterized by large aspect ratio values (0.67 and 0.79) and wide half-angles (72° and 78°) as obtained from the GCS fittings (see Figure 5.4). Both propagated through nearly identical ambient solar wind conditions, as illustrated in Figure 5.3 (top panel) and Figure 5.4.

Similarly, Events 1 and 3, which propagated at speeds of 800 km/s and 850 km/s, showed nearly equal deflection magnitudes of approximately 10°. The correlation between CME speed and deflection becomes more evident when comparing the

average values: Events 1 and 3 had an average speed of 825 km/s with an average deflection of 10.5°, whereas Events 13 and 14 had an average speed of 1625 km/s with an average deflection of 19°. For the faster events, specifically Events 13 and 14, solar wind drag is expected to dominate over magnetic field interactions at lower coronal heights, approximately between 3.4 and 4 $R_\odot$ (Sachdeva et al., 2017). These heights are lower than the heights of the CMEs estimated from of our initial GCS fitting, which is around 6 $R_\odot$. Consequently, in the region beyond 6 $R_\odot$, where GCS reconstruction is performed, solar wind drag is likely to play a more significant role than magnetic forces in influencing the propagation of Events 13 and 14.

To explore the potential influence of magnetic fields on slower CMEs, we examined the magnetic environment surrounding Events 1 and 3. Given their lower speeds compared to Events 13 and 14, one expects the ambient magnetic field to affect their trajectories. However, our analysis indicates that the ambient magnetic field had little to no impact on the propagation of Events 1 and 3.

5.3.4 Latitudinally Deflected Events

Figure 5.5 shows the magnetic field environment (extrapolated using PFSS) of the latitudinally deflected Event 2 as it propagated from 8 $R_\odot$ to 34 $R_\odot$ and Event 6 as it propagated from 6 $R_\odot$ to 54 $R_\odot$. The initial and final positions of both CMEs indicate a clear deflection toward the HCS region. This deflection corresponds to their movement from regions of higher magnetic pressure toward areas of lower magnetic pressure near the current sheet. The net deflections, as determined from the GCS fittings, are also depicted in Figure 5.5.

Previous studies have reported that CMEs are frequently deflected toward the equator during solar minima (Gopalswamy and Thompson, 2000; Cremades and Bothmer, 2004). Gopalswamy et al. (2009) and Shen et al. (2011) demonstrated that magnetic forces play a key role in driving this deflection. During solar minimum, the large-scale ambient magnetic field tends to exhibit a bipolar configuration, leading many CMEs to undergo latitudinal deflection toward the equator or the HCS, as observed in Event 2. This deflection occurs from regions of higher

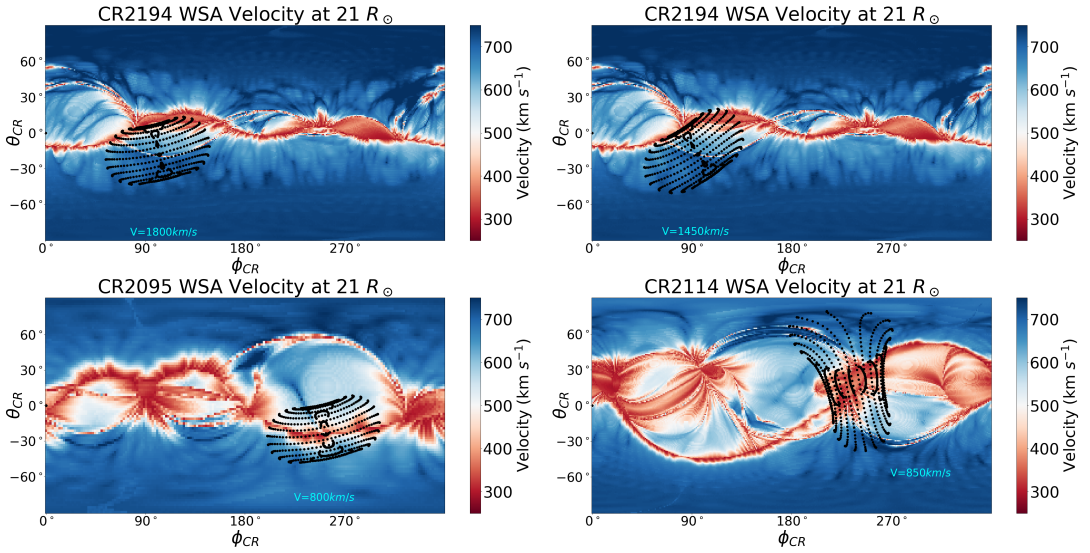

Figure 5.3: The background solar wind velocity at 21 $R_\odot$ for events exhibiting longitudinal deflection is shown. The top left and right panels correspond to Events 13 and 14, respectively, while the bottom left and right panels correspond to Events 1 and 3, respectively. The black dotted mesh indicates the CME position along with the GCS model mesh, and the nearby labels indicate the associated speed. For Events 13 and 14, a reduced half-angle and aspect ratio (compared to those used in the GCS fitting) are used to better illustrate their propagation direction. θ_{CR} and ϕ_{CR} denote the Carrington latitude and longitude, respectively.

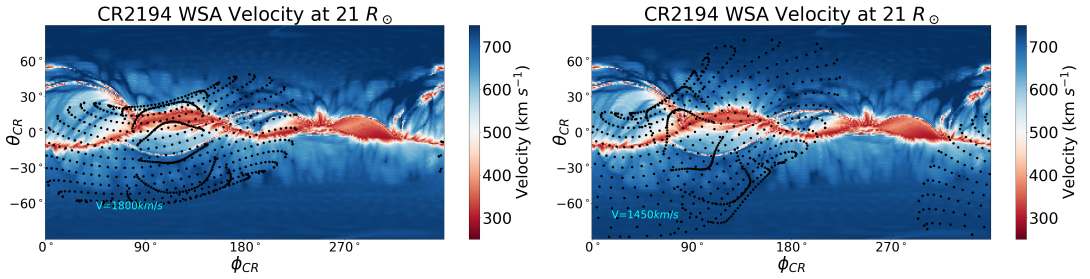

Figure 5.4: Solar wind velocity background of Events 13 and 14 at 21 $R_\odot$, respectively from left to right, plotted with the actual fitted parameters of GCS reconstruction.

magnetic pressure (far from the HCS or PIL) to regions of lower magnetic pressure (closer to the HCS or PIL) (Shen et al., 2011). Event 6 also exhibited a similar latitudinal deflection toward the PIL from a region located farther away, further supporting this interpretation.

Sachdeva et al. (2015, 2017) estimated the heliocentric distance at which either drag forces or the Lorentz force become dominant during CME propagation both

being key drivers of CME deflection in the heliosphere. They found that for faster CMEs (speed $\geq$ 900 km/s), the transition to drag-dominated dynamics occurs at lower heights, whereas for slower CMEs (speed $\leq$ 900 km/s), this transition takes place at larger heliospheric distances. Their analysis was based on CME kinematics derived from the GCS reconstruction model. Consequently, faster CMEs are primarily influenced by drag forces, while slower CMEs are strongly affected by Lorentz forces over extended distances, depending also on the background solar wind speed.

Event 2, with a speed of approximately 450 km/s, showed a clear latitudinal deflection attributed to magnetic field interaction. According to Sachdeva et al. (2017), for CMEs with comparable speeds, magnetic forces are expected to dominate over drag up to around 30 $R_{\odot}$. Notably, this is close to the final heights to which Event 2 was tracked, i.e., 34 $R_{\odot}$. Therefore, throughout the observed propagation domain of this CME, magnetic interaction is likely the dominant force driving its latitudinal deflection. As a result, solar wind drag is not expected to have played a major role in its trajectory within this range.

We analysed the solar wind environment of Event 6 and found that it had no significant influence on the propagation of the CME. Given that Event 6 is a fast CME, solar wind drag is expected to dominate from lower heights (Sachdeva et al., 2017). Therefore, the latitudinal deflection observed beyond 6 $R_{\odot}$ based on the fully developed CME structure could also result from magnetic field interactions occurring below the initial height of the GCS reconstruction. Further, from the second independent fitting of the CMEs performed at lower heights, the GCS reconstruction result showed that the latitudes of Events 2 and 6 are higher at earlier times. This indicates that these CMEs experienced substantial latitudinal deflection before becoming fully developed within the COR2 FOV. In contrast, such behaviour was not observed for events with longitudinal deflection; for those, both latitude and longitude remained unchanged with the original GCS fitting at around 6 $R_{\odot}$. Implying a constant direction of propagation below these heights. Thus, although Event 6 is a fast moving CME, it appears to have retained its latitudinal deflection momentum from a height below 6 $R_{\odot}$. This behaviour was

not observed in the other fast events with similar speeds, namely, Events 1, 3, 13, and 14, i.e., their latitudes were similar to those estimated beyond 6 $R_{\odot}$.

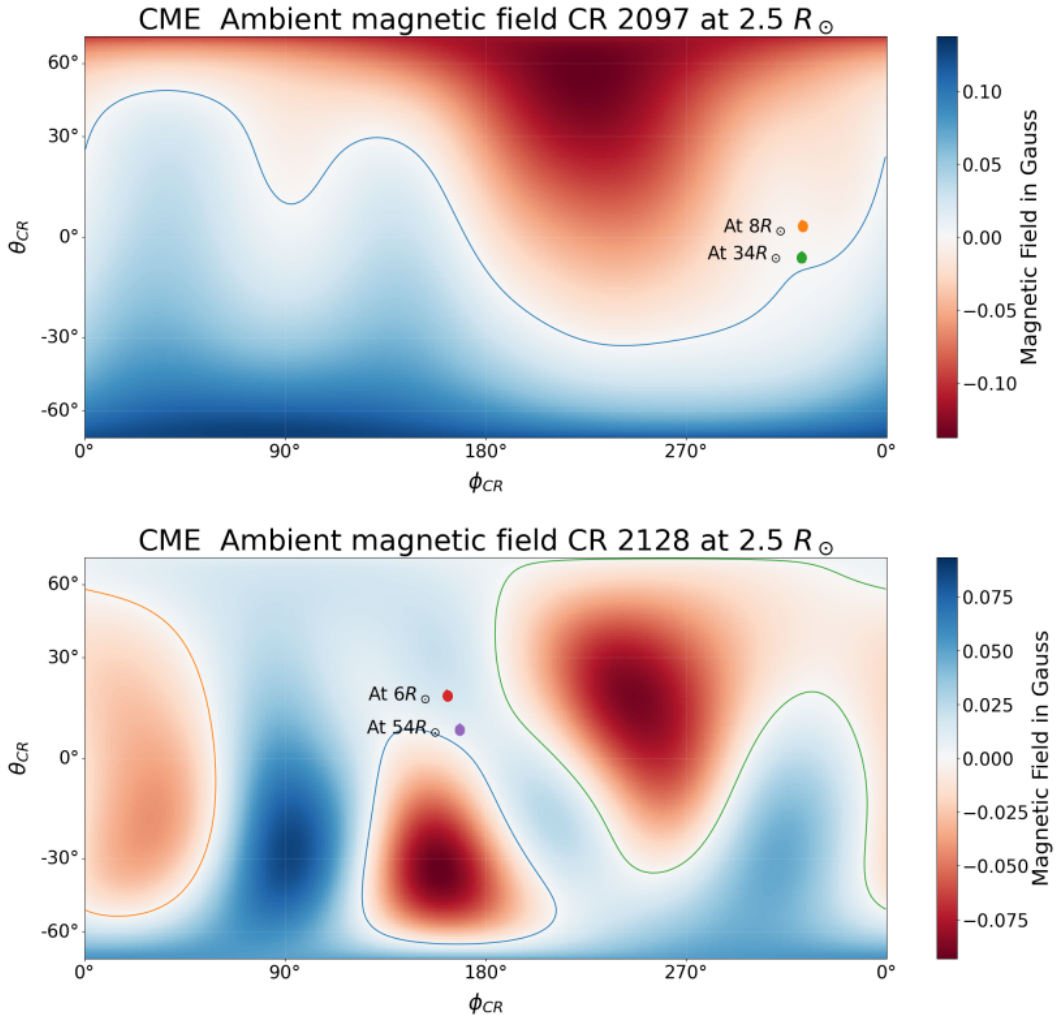

Figure 5.5: The magnetic field environment associated with the events exhibiting latitudinal deflection is shown, as inferred from the PFSS extrapolation of the corresponding Carrington magnetic field maps. The top panel displays the CME from 23 May 2010 (Event 2), while the bottom panel presents the CME from 28 September 2012 (Event 6). The color bar indicates the magnetic field strength in Gauss. θ_{CR} and ϕ_{CR} denote the Carrington latitude and longitude, respectively.

5.4 Conclusions

Our analysis of 15 geo-effective CMEs observed by SOHO/LASCO-C2 & C3, STEREO/SECCHI-COR2, and HI1 indicates that CME propagation can be influenced by the ambient magnetic field and solar wind velocity, leading to devia-

tions from self-similar expansion.

Our results show that latitudinal deflection predominantly occurred in the equatorward direction toward the HCS in two events (Events 2 and 6). The net latitudinal deflection observed for these events (from the first COR2 frame to the final frame in HI1) was directed toward the PIL, consistent with the findings of Shen et al. (2011). It is worth noting, however, that they were able to track CMEs only up to the LASCO-C3 field of view. We suggest that the continued equatorward deflection of CMEs beyond 21 $R_{\odot}$ may be attributed either to momentum acquired in the magnetically dominated region below 21 $R_{\odot}$, to solar wind interactions, or to a combination of both.

Interestingly, the faster CMEs (speeds $\geq$ 800 km/s) in our study (Events 1, 3, 13, and 14) initially propagating westward, i.e., away from the Sun-Earth line, were found to deflect eastward, i.e., toward the Sun-Earth line, likely due to interaction with slower solar wind ahead of them. This behavior agrees well with the earlier findings of Wang et al. (2004); Wang et al. (2014). Additionally, we observed that the magnitude of longitudinal deflection appears to depend on CME velocity, assuming the background solar wind remains the same.

Lastly, we believe that exploring our capabilities to track these 15 CMEs to larger heliospheric distances extending beyond the LASCO-C3 field of view allowed us to capture the extended view of the evolution of their trajectories. Compared to earlier studies limited to lower coronal heights, the inclusion of HI1 observations in our study provides a continuous view of the CME propagation from the Sun to near-Earth space, enhancing our understanding of CME propagation kinematics through the heliosphere.

The work presented in this chapter has been published in Kumar et al. (2024).

Chapter 6

Heliospheric Propagation of Coronal Mass Ejections: Rotation

6.1 Introduction

Coronal Mass Ejections (CMEs) are the primary cause of severe geomagnetic storms and solar energetic particle (SEP) events, which can intensify radiation belts, disrupt satellites, and damage spacecraft. Accurate modeling of CME propagation, arrival times, and impacts are thus critical for effective space weather forecasting. A prolonged southward component of the IMF is one of the key factors responsible for most of the intense geomagnetic storms. This depends upon the orientation of the magnetic cloud (MC)/flux rope, associated with a CME. The tilt angle of the CME flux rope observed at 1 AU is generally assumed to remain the same as the one estimated from the polarity inversion line (PIL) at the Sun, if the flux rope is unaffected by the ambient structures due to interactions (Gopalswamy et al., 2022). Therefore, it is important to examine the continuous evolution of the flux rope parameters, in particular the tilt, as the CME propagates from the Sun to the Earth.

Vourlidas et al. (2011) presented the first direct detection of a rapidly rotating CME in the middle corona (5–15 $R_{\odot}$), reporting a rotation rate of 60°/day.

Using simultaneous observations from STEREO/SECCHI and SOHO/LASCO instruments, they reconstructed the 3D structure of a CME observed on 16 June 2010 and found that, despite the rapid rotation, projection effects remained minimal in individual coronagraph views, i.e., different angular width from different viewpoints. The CME originated from a quiet-Sun neutral line with weak low-corona signatures, classifying it as a stealth CME. The study suggests that these rotations, which are possibly a result of footpoint disconnection, could influence space weather forecasting. It can also help to explain the previously observed constancy in CME angular widths beyond 5 $R_{\odot}$.

Kay et al. (2017) studied the deflection and rotation of CMEs that erupted from active region 11158 between 13-16 February, 2011. They used the GCS and Forecasting CME's Altered Trajectory (ForeCAT) models to simulate the nonradial dynamics of CMEs driven by the magnetic forces and reported rotation of the CMEs in the range of 5° to 50° in both clockwise and anticlockwise directions, in the lower corona. Gopalswamy et al. (2022) also analyzed the solar and interplanetary causes of the third largest geomagnetic storm of the solar cycle 24, caused by a CME observed on 26 August 2018. They reported a prolonged acceleration of the associated CME, due to continued magnetic reconnection at the source region. They found multiple coronal holes and high-speed streams near the filament channel of the source region. The combined effect of these processes produced a complex rotation of the CME in the corona and interplanetary medium, resulting in a high-inclination MC with a south-pointing axial magnetic field at L1.

Recently Maharana et al. (2023) reports a case study and investigates how CME–CME and CME–solar wind interactions can significantly alter the geoeffectiveness of CME as it propagates in the heliosphere. Using EUHFORIA 3D MHD simulations, the authors model two successive CMEs launched from NOAA AR 12158 in September 2014. Despite remote observations suggesting strong geoeffectiveness of the second CME, in situ data at 1 AU showed only a weak negative Bz, followed by a prolonged positive Bz. The simulations reveal that

interaction with the preceding CME caused rotation and significant deflection of the second CME, changing its orientation and magnetic structure. The results highlight that CME interactions can produce geoeffective magnetic fields in the sheath region, even when the individual CMEs themselves appear weak.

Accurately predicting the magnetic field configuration within an Earth-directed CME remains a major challenge in space weather forecasting. Palmerio et al. (2018) conducted a study of 20 CMEs by tracking them from the Sun to Earth using heliospheric imaging, comparing their intrinsic flux rope types (orientation and handedness at eruption) with their in-situ counterparts. They found a strict match in only 20% of events, increasing to 55% when intermediate cases of tilt values were included. The study also revealed that flux ropes often undergo significant rotation exceeding 90° in 35% of the events during their propagation. These findings underscore the necessity of capturing CME evolution and including intrinsic flux rope characteristics in forecasting models.

As reported in Chapter 5, out of 15 geoeffective CMEs analysed, a continuous increase in flux rope tilt was observed for two events: 5 October 2012 (Event 7) and 23 May 2017 (Event 12). In this chapter, we present a detailed analysis of these CMEs, which showed a significant rotation in the heliosphere. For the 5 October 2012 event, previous studies reported a significant mismatch between the tilt estimated from the PIL on the solar surface and the MC orientation observed at L1 (Marubashi et al., 2017; Martinić et al., 2022). Marubashi et al. (2017) found a low inclination tilt both near the Sun (based on PIL orientation) and at L1 (via flux rope fitting on the in-situ IMF). In contrast, Martinić et al. (2022) reported a transition from low to high inclination in the coronagraph field of view (from LASCO-C2 to C3), with a high inclination of the MC at L1. We show that this discrepancy can be attributed to the continuous rotation of the CME flux rope during its propagation to Earth. Furthermore, we compare the 5 October 2012 event with the 23 May 2017 CME, highlighting the similarities and differences in their observations and evolution.

6.2 Observations and Analysis

To track the tilt of the CME in the heliosphere we considered the following approach:

1. In the outer corona from COR2 FOV, up to the time when the CME is visible in the HI1 images, we implemented the GCS reconstruction (R$\leq$ 60 $R_{\odot}$), using a newly developed Python module as described Chapter 2, Section 2.3.4.
2. At L1, we fitted the in-situ magnetic field observations from the ACE with the cylinder and torus models developed by Marubashi and Lepping (2007) (discussed in Chapter 2, Section 2.3.4).

In order to understand the overall evolution of these two CMEs in the heliosphere, we compared the near-sun tilt of the flux rope with the tilt of the CME at L1.

The 5 October 2012 CME was observed as a limb CME from STEREO-A (the angle between the STEREO-A and CME was about 94.9°). This offered us a unique opportunity to study the evolution of the width of the CME and also to estimate the heliocentric height at which the flux rope attained maturity. This height is a proxy for the height beyond which CME width is constant, and therefore, the flux rope can be considered as stable (Dagnew et al., 2022). Whereas for the 23 May 2017 CME, the orientation of the spacecraft was not favourable to estimate this parameter (STEREO-A and Sun-Earth line angle was $\approx$ 120°).

To understand the ambient magnetic field and solar wind background of the CME, PFSS extrapolation of the photospheric magnetic field and WSA (Arge et al., 2003; Arge and Pizzo, 2000) models as discussed in Chapter 2.

6.3 5 October 2012 CME

This event has been extensively studied by Nitta and Mulligan (2017). They reported a partial-halo CME observed by LASCO-C2 at 02:48 UT on 5 October 2012, though no obvious eruption signatures were initially seen on the solar disk.

A geomagnetic storm, marked by a storm sudden commencement at 05:16 UT on 8 October 2012 associated with the CME, was recorded, reaching a minimum D_{st} index of ≈ -105 nT. This possible Sun–Earth connection was initially categorized as a problematic event due to the unclear solar origin of the CME. However, a closer inspection of SDO/AIA images revealed strong evidence (coronal dimmings) of an eruption near the PIL in active region AR 11584, located near S20W25, around 02:00 UT on 5 October 2012 (Nitta and Mulligan, 2017). As mentioned in the Introduction section of Chapter 5, it is well known that CMEs can undergo deflection due to ambient magnetic pressure that leads to changes in the direction of their propagation, i.e., changes in latitude (θ) and longitude (ϕ) (Shen et al., 2011), in the lower corona (COR2 FOV). The direction of propagation (as defined by the θ and ϕ of the midpoint of the axis shown) of the 5 October 2012 and 23 May 2017 CME is along the local heliospheric current sheet as shown in Figure 6.1 and Figure 6.5, respectively. Therefore, we expect that the first two parameters of the GCS model fit, θ and ϕ, do not change as these CMEs propagate through the heliosphere, in agreement with Shen et al. (2011).

Moreover, to clearly capture the heliospheric evolution of the CME flux rope, we start the GCS fitting from the time frame that represents a mature CME flux rope. To estimate the corresponding time/height of the CME, we calculate the angular width between the CME legs and the height of the leading edge/tip of the CME from the STEREO-A/COR2 images using the CDAW online measurement tool[1]. Using this tool we estimated the transition height (Hc) as defined by (Dagnew et al., 2022). We found that Hc is ≈ $11R_{\odot}$ for the 5 October 2012 CME. Therefore, we start the GCS fitting of the CME at 7:24 UT after its leading edge crossed Hc, i.e., at $15R_{\odot}$.

At 7:24 UT, the values of best-fit parameters of GCS reconstruction, i.e., half angle, kappa (aspect ratio), latitude, and longitude, tilt are 57°, 0.38, −14°, 14° and 43°, respectively, at 15.8 $R_{\odot}$. The latitude and longitude of the GCS fit

[1] https://cdaw.gsfc.nasa.gov/movie/make_htmem_js.php?step=1&img1=sta_cor2rd&stime=20121005_0000&etime=20121005_1000

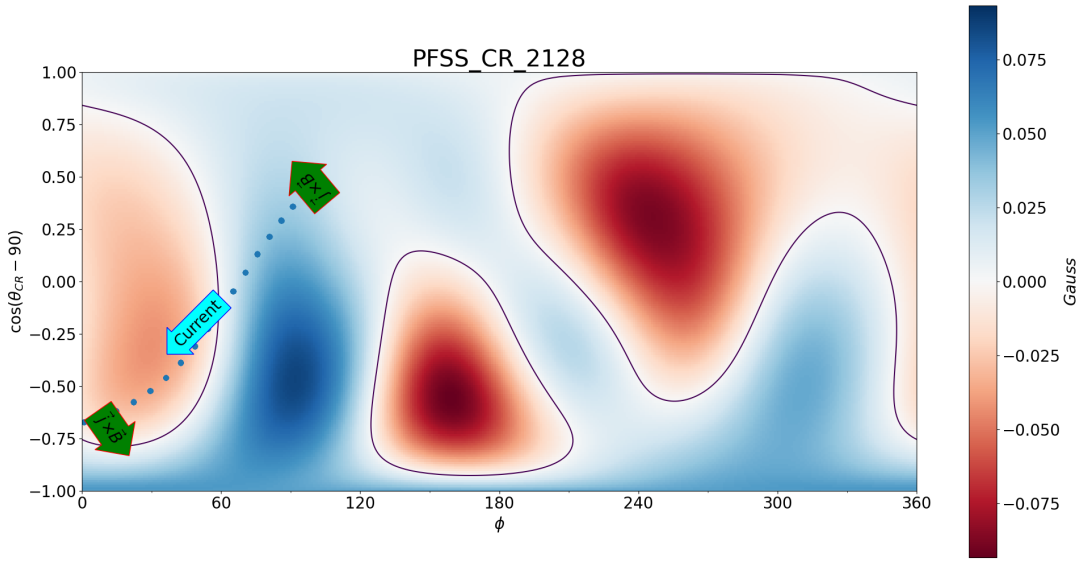

Figure 6.1: Figure shows GCS axis (blue dots) representing current along the axis of CME front projected on the PFSS extrapolated magnetic field at $2.5R_{\odot}$. The cyan color arrow shows the direction of the toroidal current in the CME derived from the flux rope type in Marubashi et al. (2017), Palmerio et al. (2018), and Martinić et al. (2022). The green arrows show the direction of the force on the CME.

are close to the average location of the source region as identified by Nitta and Mulligan (2017). The values of the fitted parameters at 7:24 UT obtained here agree with those reported in Martinić et al. (2022) for the same event.

To look for possible reasons for deflection in the direction of propagation, we examined the ambient magnetic field of the Sun as done by Shen et al. (2011), which can lead to a change in the latitude (θ) and longitude (ϕ) parameters of the GCS reconstruction in the upcoming time steps. For the ambient medium, we used the PFSS extrapolation of the Sun from the GONG synoptic map of CR 2128. This extrapolation is a fairly good approximation of the global magnetic field of the Sun. Then we plotted the axis of the GCS reconstruction of the CME from the first image overlaid on the PFSS extrapolated magnetic field for CR2128 as shown in Figure 6.1, which shows that the direction of propagation (approximate midpoint of the axis) of the CME is in the region of the local HCS/PIL (purple line). Therefore, we do not expect any force that can significantly change the direction of propagation of the CME further (Shen et al., 2011). Based on

the above two analyses (flux rope maturity and CME deflection), we expected the aspect ratio, half angle, latitude (θ), and longitude (ϕ) to remain constant above the transition height, which implies a consistent direction of propagation. We found that after the first fitting at 7:24 UT, good-quality GCS model fits could be obtained by changing the tilt in the upcoming time frames.

Consequently, we followed the evolution of the tilt parameter of the reconstructed CME flux rope. We considered a two-hour interval between each GCS fit to identify significant changes in the tilt parameter. We found a gradual increase in the tilt, which indicates CME rotation in the heliosphere from 15 to 58 $R_{\odot}$. Beyond 58 $R_{\odot}$ it was not possible to visualize the CME clearly in the HI1 FOV; therefore, GCS reconstruction could not be implemented in the HI2 FOV.

We did four independent GCS fittings at all time steps. All four independent GCS fittings clearly showed the increasing tilt of the flux rope, i.e., the rotation of CME in the HI1 FOV. We have plotted the mean values of the CME flux rope tilt obtained from different independent fittings and the standard deviation (SD) as the error in Figure 6.2. This shows a 21° increase in the mean value of the tilt from $44° \pm 3°$ to $65° \pm 7°$ from 7:24 UT to 20:09 UT (approximately height ranging from $15 \pm 1 R_{\odot}$ to $58 \pm 1 R_{\odot}$). We also found that as the structure evolved in the heliosphere, it became fainter and errors in the tilt increased, as shown in Figure 6.2.

Martinić et al. (2022) used the coronagraphic observations from LASCO-C2, COR2 and from LASCO-C3 FOV. Using the GCS method on COR2 FOV and the elliptical fitting method on LASCO-C2 and C3, they reported an increase in tilt, which agrees with our findings. Our approach incorporates continuous tracking of the CME in HI1 FOV and also at L1. This analysis provides clear evidence of the continuous rotation of the CME throughout the heliosphere.

As mentioned earlier, we employed the cylindrical and toroidal flux rope models of Marubashi and Lepping (2007) to fit the observed interplanetary magnetic field (IMF) at L1. Both models are force-free with constant-α and provide the latitude and longitude of the flux rope axis in the GSE coordinate system, which are used to determine the axis tilt.

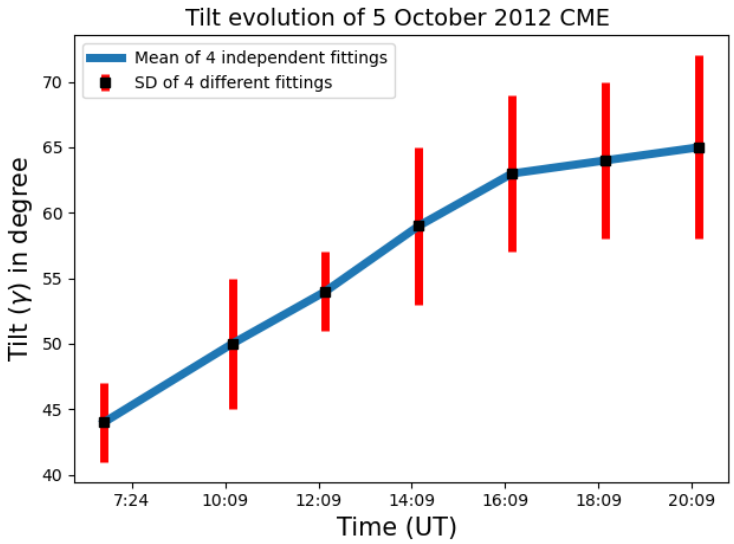

Figure 6.2: Evolution of tilt with respect to the time based on the GCS fitting of the CME of 5 October 2012 in COR2 last frame and in the HI1 FOV. The error bars are incorporated based on independent fittings.

Figure 6.3 (top panel) presents the observed temporal evolution of the solar wind IMF components $|B|$, B_x, B_y, and B_z, along with the bulk solar wind speed (black curves), by ACE. The ICME event spans from 17:22 UT on 8 October to 18:36 UT on 9 October 2012. The leftmost vertical line marks the shock arrival, the region between the left and middle vertical lines indicates the sheath, and the interval between the middle and rightmost vertical lines corresponds to the magnetic cloud (MC). The MC exhibits a clear rotation in the B_y component. The data show a sequence of slow solar wind, a turbulent sheath, and the structured MC, both the sheath and MC displaying an extended southward IMF. Notably, the MC alone maintained a southward IMF for approximately 25.5 hours, leading to a geomagnetic storm with a minimum Dst of -105 nT.

Flux rope tilt angles derived from model fitting are approximately 114° for the cylindrical model and 108° for the toroidal model, giving an average tilt of about 110° at L1. This high inclination is consistent with the observed rotation in B_y and persistent negative B_z throughout the MC.

The upper panel of Figure 6.3 also displays the best-fit toroidal model ($Torus_{M03}$) applied to the MC interval (red line). The lower panel shows the flux rope orientation at L1 based on this fit, with the '+' symbol marking the

spacecraft crossing point through the MC. To compare the tilt of the flux rope near the Sun (from GCS fitting) with that at L1, we measure the tilt at L1 counterclockwise from the negative y-axis of the GSE coordinate system.

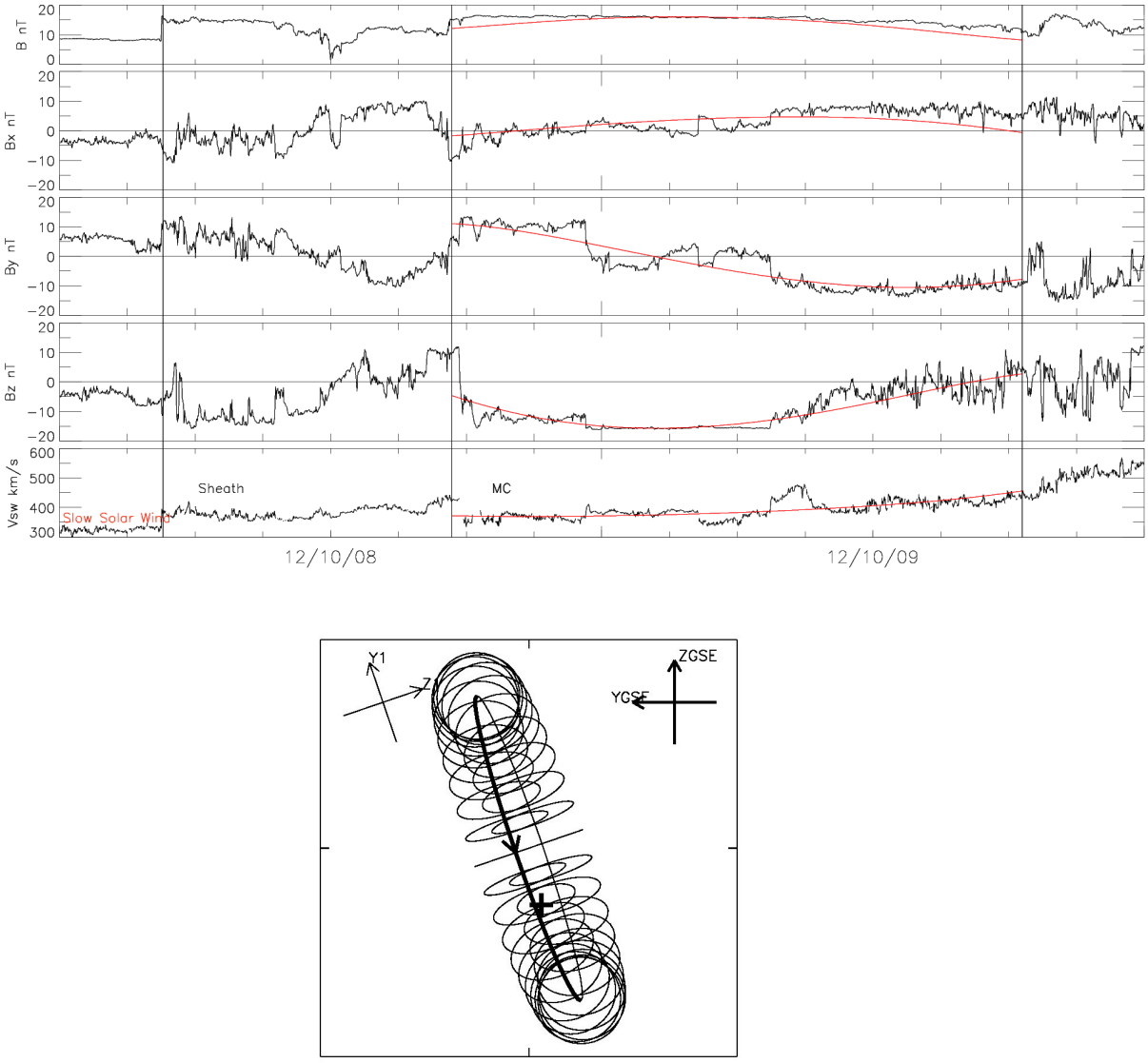

Figure 6.3: Top panel: Marubashi's toroidal model fit ($Torus_{M03}$) to the magnetic cloud (red line), overlaid on the observed solar wind parameters from ACE as a function of time (YY/MM/DD). From top to bottom, the black curves represent the IMF strength $|B|$, components B_x, B_y, B_z, and the bulk solar wind speed (in km/s). Bottom panel: Orientation of the flux rope at L1 as derived from the $Torus_{M03}$ model. The '+' symbol indicates the spacecraft's trajectory through the magnetic cloud. The flux rope tilt angle is measured counterclockwise from the negative y-axis in the GSE coordinate system.

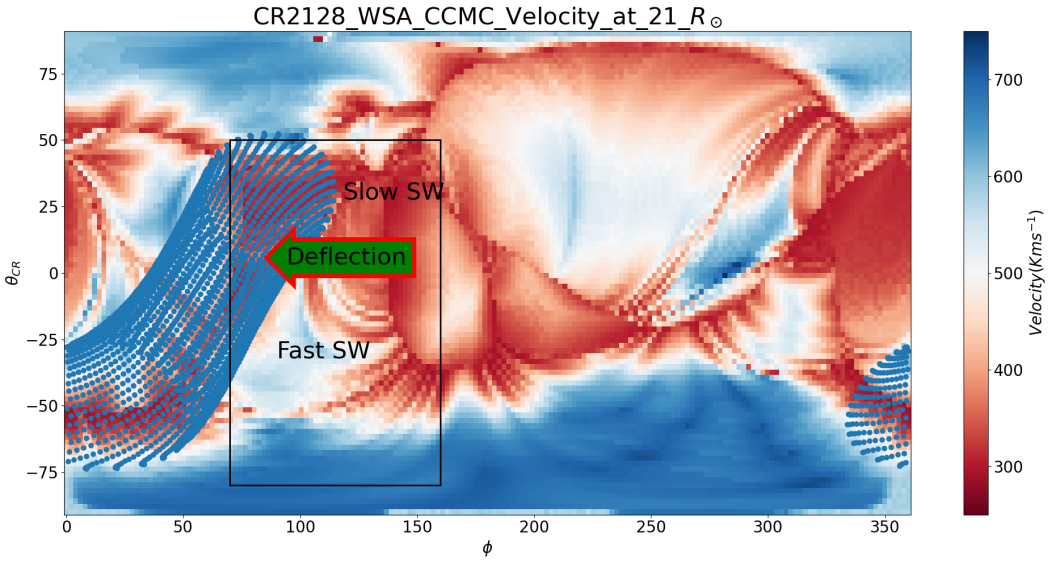

Figure 6.4: This figure shows the WSA velocity background of the CME at $21R_\odot$ from NASA/CCMC. The black rectangle specifies the inhomogeneous velocity background around the CME top front. The green arrow in the lower panel shows the deflection of the upper front of the CME due to interaction with the slow solar wind in front of it.

Our analysis reveals a significant change in orientation, with the tilt increasing by about 66° (from 44° to 110°) in the anticlockwise direction as the CME propagated from 15 $R_\odot$ to L1. Notably, around 30% of the total change in the tilt value occurred within the 60 $R_\odot$, with the remaining 70% taking place over the next 160 $R_\odot$, indicating that the CME underwent continuous rotation throughout its journey in the heliosphere. This gradual rotation ultimately resulted in a highly inclined flux rope at L1, which contributed to a prolonged southward IMF component lasting approximately 25.5 hours, thereby driving a strong geomagnetic storm.

The increase in tilt observed near the Sun can be explained by the force acting on the toroidal current in the CME front (derived from the type of flux rope), by the ambient radial magnetic field of the Sun. Earlier observers reported an ESW type of flux rope near the Sun which had Right-Handed (RH) chirality with axial field pointing southward (Marubashi et al., 2017; Palmerio et al., 2018). The direction of the current derived from the ESW type of flux rope is represented by the cyan color arrow in the bottom panel of Figure 6.1.

For the ambient radial magnetic field, we used the PFSS extrapolation of the photospheric magnetic field up to 2.5 $R_\odot$ from the pfsspy Python code (Stansby, 2019) as shown in Figure 6.1. This extrapolation gives an approximation of the magnetic field polarity and magnitude between 2.5 $R_\odot$ and 21 $R_\odot$. Beyond 2.5 $R_\odot$, nearly radial extrapolation of the field can be approximated from PFSS, retaining polarity and PIL structure. Further, the torque due to the ambient radial magnetic field acts on the CME front, causing the CME to rotate in an anti-clockwise direction (Figure 6.1). However, this sense of rotation may hold good only up to 21 $R_\odot$ because of the dominance of the radial magnetic field within this distance (Schatten, 1972).
The synoptic map of the ambient solar wind for CR2128 at $21R_\odot$, from NASA/CCMC [2], is shown in Figure 6.4. Beyond 21 $R_\odot$, the dynamics of the ambient medium are dominated by the velocity of the solar wind (Riley and Lionello, 2011). Therefore, we conclude that the observed rotation in the heliosphere beyond 21 $R_\odot$ may be due to the interaction of the CME flux rope with the ambient solar wind.

We found a non-uniform solar wind velocity environment in the leading part of this CME as shown in Figure 6.4 (black rectangle). We found a slow solar wind ($\approx$ 300 km/s) flow ahead of the top part of the CME (above the green arrow, Figure 6.4). In contrast, the lower part of the CME faces an overall fast solar wind background in front of it (below the green arrow). The slow solar wind heading the top part of the fast CME ($v \approx 600$ km/s) can deflect the upper part of the CME in the eastward direction due to rotation of the Sun, as shown by the green arrow. Moreover, this kind of deflection is not possible in the lower part of the CME (as shown in the lower half of the black rectangle) because it faces an overall fast solar wind in front of it. This rotates the CME in the same sense in the rest of the heliosphere as provided by the force due to the ambient radial magnetic field on the CME axis, below $21R_\odot$. The slow solar wind ahead of the CME front is further confirmed by the observation of slow solar wind in

[2] https://ccmc.gsfc.nasa.gov/

in-situ observations at L1 by ACE (top panel, Figure 6.3). Earlier studies have shown eastward deflections of fast CMEs propagating in the slow solar wind, these studies did not take into account the latitudinal extension of the CMEs in the heliosphere, whereas we base our arguments on the possibility that different parts of a CME can propagate through different environments, thereby rotating the CME as it propagates (Wang et al., 2004; Gopalswamy et al., 2009). We, therefore, believe that the interaction of the CME with the solar wind in the rest of the heliosphere led to a further increase in the tilt at L1 (Figure 6.3). The analysis also suggests that a favourable solar wind environment can change the orientation, leading to rotation of the CME, resulting in a geoeffective event. A recent study by He et al. (2018) also suggested an increase in the geoeffectiveness of a stealth CME on 8 October 2016, because of its interaction with the ambient solar wind medium. Their study showed that the increased geoeffectiveness was due to the interaction of the CME with a CIR in the ambient solar wind.

6.4 23 May 2017 CME

The source region of the 23 May 2017 CME was very close to the disk center (S01W03) compared to the source region of the 5 October 2012 CME, which was S23W31. The 23 May 2017 CME in its initial evolution near the Sun, i.e., below 10 $R_{\odot}$, was deflected longitudinally from west to east, whereas the 5 October 2012 CME showed no such significant deflection. This may be due to the magnetic pressure force trying to align the 23 May 2017 CME along the PIL. After 10 $R_{\odot}$, neither CME showed any significant change in latitude or longitude.

23 May 2017 (Event 12) CME showed a change in tilt during its propagation in the heliosphere. This CME was relatively slow as compared to the other faster Events 1, 3, 13, and 14, discussed in the previous chapter, with an average velocity of 400 km/s, which showed longitudinal deflection in the heliosphere. We reconstructed the CME from 8:24 UT on 23 May in COR2 FOV to 10:30 UT on 24 May in HI1 FOV. We did not find any significant change in the direction of the propagation of the CME as it propagated from 10 $R_{\odot}$ to 70$R_{\odot}$. However, its tilt increased from 13° at 10 $R_{\odot}$ to 32° at 70 $R_{\odot}$ as it propagated in the

heliosphere. We investigated the ambient magnetic field environment of the

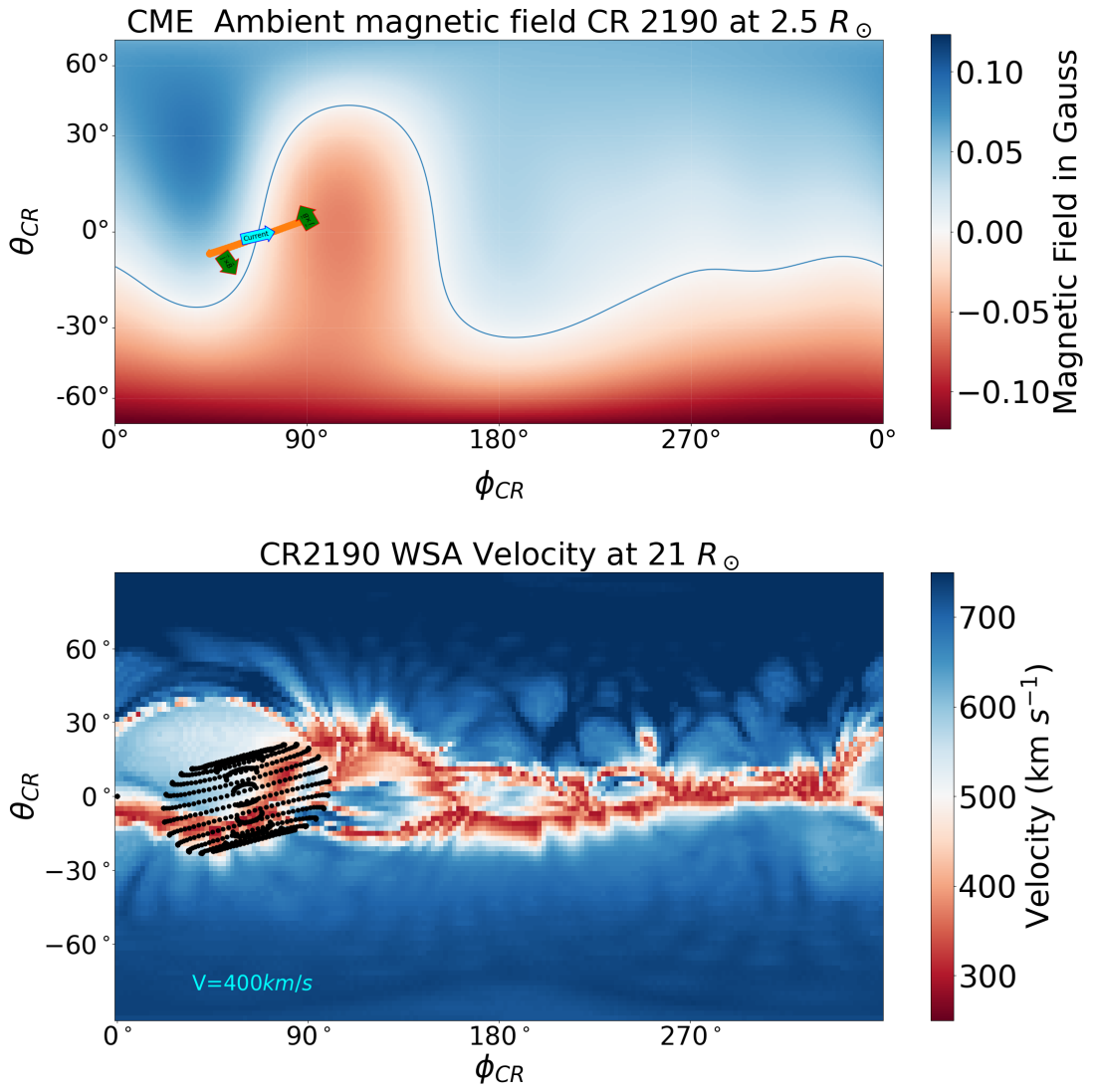

Figure 6.5: Radial magnetic field (top) and solar wind velocity (bottom) environment of the 23 May 2017 CME (Event 12).

CME and found that the direction of propagation is already aligned with the PIL/HCS, i.e., the center of the CME axis shown in the top panel of Figure 6.5. Moreover, there is no noticeable difference between the velocity of the CME (400 km/s) and the ambient solar wind. Therefore, we do not expect a significant deflection assuming that deflection occurs due to magnetic pressure difference or due to drag between the ambient medium and CME, i.e., no change in the θ and ϕ of GCS parameters (Wang et al., 2004; Shen et al., 2011). It is also confirmed from the values of latitude and longitude of CME estimated from GCS

reconstruction that no change in the direction of the propagation of the CME was noted. Using Marubashi toroidal and cylindrical fitting models (Marubashi

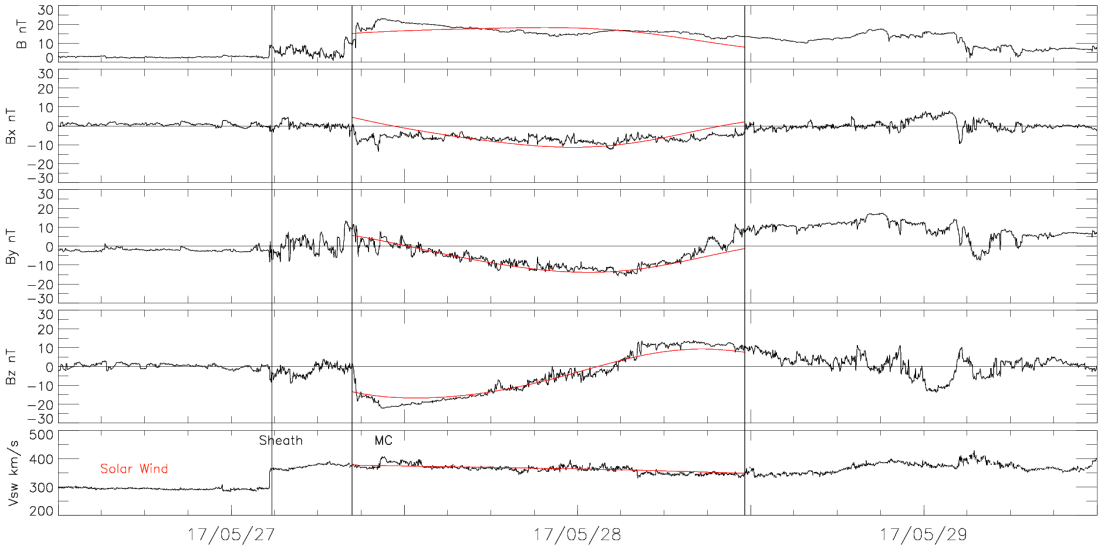

Figure 6.6: Marubashi's toroidal model fit ($Torus_{M03}$) to the magnetic cloud (red line), overlaid on the observed solar wind parameters from ACE for 23 May 2017 CME, as a function of time (YY/MM/DD). From top to bottom, the black curves represent the IMF strength $|B|$, components B_x, B_y, B_z, and the bulk solar wind speed (in km/s).

and Lepping, 2007; Marubashi et al., 2017) to IMF observations at L1, we found a low inclination for the flux rope at L1 for the CME. From the rotation of the Bz in the IMF vectors with prolonged B_y shown in Figure 6.6, we find the signature of a SWN flux rope. Its tilt at the L1 was estimated $\approx 40°$ which is similar to that estimated from the last GCS reconstruction in HI1 FOV, i.e., $\approx 32°$. It suggests that this CME rotated by a smaller angle beyond 70 $R_\odot$, i.e., from 32° to 40°. We investigated the ambient magnetic field using the PFSS model for the 23 May 2017 CME to understand the role of the magnetic field in its propagation. The top panel of Figure 6.5 shows the ambient magnetic field for this CME. As we can see, on the left of the PIL, the magnetic field is directed radially outward in the blue color region, and it is directed radially inward in the red region. Based on the in-situ observations of IMF, we also identified the SWN type of flux rope associated with the CME. The direction of the current in this type of flux rope is from south to north, as shown by the cyan color arrow along the axis of the CME. Green arrows at the end show the direction of torque

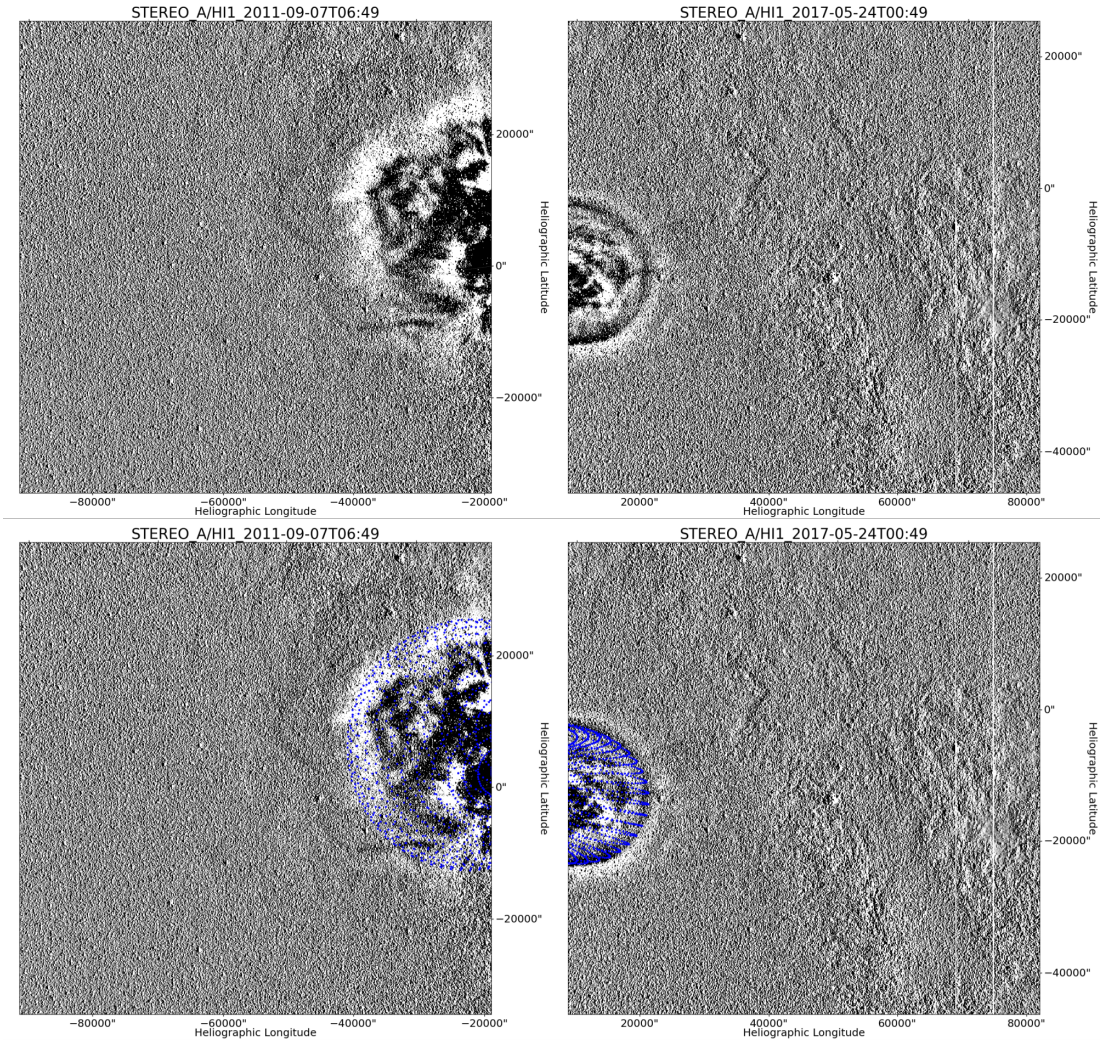

Figure 6.7: The left panels show the 7 September 2011 CME (Event 3) with a velocity of approximately 850 km/s, exhibiting a distorted and non-coherent structure at a heliocentric distance of about 37 $R_\odot$, as estimated from GCS reconstruction. The right panels display the 23 May 2017 CME (Event 12), with a velocity of around 400 km/s, showing a well-defined, coherent circular structure at approximately 48 $R_\odot$ within the HI1 field of view. The top row presents the CME structures without the GCS mesh, while the bottom row shows the same events with the GCS mesh overlaid—highlighting the contrast in the quality of fit between the two cases.

on the CME. The bottom panel of Figure 6.5 shows the solar wind velocity background for the CME. This CME is much less spread in the $\theta - \phi$ plane, i.e., half angle 22°, and there is a smooth, slow, and fast solar wind velocity ahead of the CME front.

Comparison of the two CMEs (Event 7 and Event 12)

For 5 October 2012 CME (Event 7), we observed a continuous rotation of the CME from 44° at around 15 $R_\odot$, approximately 65° at 58 $R_\odot$ and 110° at L1. This rotation was attributed to two factors: the $\vec{J} \times \vec{B}$ torque (Lorentz force) within the flux rope, particularly below 21 $R_\odot$, and interaction with the solar wind above this boundary. The CME was an extended structure in the θ-ϕ plane with a half angle of 52°. Figure 6.4 shows distinct regions of slow and fast solar wind ahead of the CME. A non-uniform velocity profile was noted ahead of the leading edge of the fast CME, with slow solar wind preceding the upper segment and fast solar wind preceding the lower part. Interaction between the slow solar wind and the fast-moving upper segment of the CME caused an eastward deflection due to solar rotation, while the lower segment of the CME faced predominantly fast solar wind. The interaction with the ambient magnetic field and solar wind gave the CME a consistent sense of rotation throughout the heliosphere.

The direction of current ($\vec{J}$) in the 23 May 2017 CME and ambient magnetic field ($\vec{B}$) were both reversed near the Sun in comparison to the 5 October 2012 CME (Figure 6.1). Therefore we found a consistent sense of $\vec{J} \times \vec{B}$ as shown in top panel of Figure 6.5 for both the events, i.e., counterclockwise.

23 May 2017 CME has less angular extent in the $\theta - \phi$ plane as compared to 5 October 2012 CME, i.e., lower half angle (22°), and faced a homogenous/mixed solar wind background ahead of the CME front. Moreover, there is no significant difference between the velocity of the CME (400 km/s) and the ambient medium solar wind velocity. Therefore, we do not expect the same kind of solar wind interaction in the 23 May 2017 CME as observed in the 5 October 2012 CME, i.e., no rotation due to solar wind interaction. Since the solar wind drag acts throughout the heliosphere, we expect the rotation of the 5 October 2012 CME due to drag to be long-lasting as compared to the 23 May 2017 CME, which rotated only because of the magnetic field interaction.

In a recent study, Martinić et al. (2023) estimated the drag parameters (γ) for

the 5 October 2012 and 23 May, 2017 CMEs as, 0.502 and 0.065, respectively using the reverse drag technique (DBEMv3 tool, Čalogović et al. (2021)). The γ parameter in the DBEMv3 model is directly proportional to the cross-sectional area of the CME in the heliosphere. Also, the cross-sectional area increases with aspect ratio and half angle in the GCS model. We obtained a higher half-angle and aspect ratio for the October event (52°, 0.48) than that for the May event (22°, 0.38). Therefore, we expect a lower value of the drag parameter for the May event compared to the October event. Therefore, our results are in agreement with Martinić et al. (2023). This also provides evidence of a weaker drag interaction of the May event with the solar wind as compared to the October event, leading to a higher change in the tilt of the October CME compared to the May CME while propagating in the drag-dominated regime.
Therefore, for 23 May 2017, CME, only the magnetic field environment was in favour of its rotation, whereas for 5 October 2012, both the factors, i.e., magnetic field and ambient solar wind velocity, were in favour of its rotation.
It is worth mentioning that the overall shape of the two CMEs remained consistent and coherent throughout their propagation, which made it possible to implement GCS reconstruction on the CME structure and to estimate the GCS model parameters with less ambiguity. This contrasted with the other faster events analyzed in this work, where such consistency and coherence in CME structure in HI1 images was lacking (Figure 6.7). Furthermore, we observed that the fast CMEs selected in our dataset (Chapter 5) were fitted with larger values of aspect ratio, this agrees with previous studies by Pluta et al. (2019). They reported that the aspect ratio in GCS reconstruction is proportional to the speed of the CMEs. As the aspect ratio increased, we encountered difficulty in distinguishing the quality of GCS fits with different values of tilt in GCS reconstruction. It became challenging to differentiate the projection of the GCS mesh with different tilts for those CMEs that were fitted with higher aspect ratio values.

6.5 Conclusions

Our analysis of the two CMEs, observed on 5 October 2012 and 23 May 2017 in the heliosphere, provides clear evidence of rotation for the CMEs. For the first case (5 October 2012) a continuous increase in tilt from the COR2 FOV (starting at $15R_{\odot}$) to the HI1 FOV (up to $58R_{\odot}$) is reported. Although the CME could not be tracked beyond $58R_{\odot}$ in the HI1 FOV, flux rope fitting to in-situ IMF observations at L1, using both cylindrical and toroidal models (Marubashi and Lepping, 2007), revealed a further increase in tilt compared to the last HI1 frame. This points to a continuous rotation from near the Sun to L1.

Propagating at a moderate speed of 600 km/s near the Sun, the CME underwent a progressive tilt increase while propagating in the heliosphere. This evolution resulted in a prolonged southward magnetic field component, contributing to its increased geoeffectiveness.

Further, our analysis revealed a change of 19° in the tilt of 23 May, 2012 CME in the heliosphere. It is important to note that although the magnetic field configuration for this CME favored an anti-clockwise rotation in the CME flux rope, however the increase in tilt/CME rotation persisted even beyond the magnetically dominated regime, i.e., from 21 $R_{\odot}$ to 70 $R_{\odot}$. We attribute this change to potentially gained angular momentum below 21 $R_{\odot}$.

It is worth pointing out that the height ($\tilde{h}_0$) at which the drag starts to dominate the magnetic interaction (Lorentz force) varies for different CMEs (Sachdeva et al., 2015, 2017; Martinić et al., 2023). Martinić et al. (2023) concluded that the range of $\tilde{h}_0$ can be from 3.5 $R_{\odot}$ to 70 $R_{\odot}$. This range also defines the upper bound of the height up to which magnetic field interactions can influence the CME trajectory. For slower CMEs (speed $\leq$ 900 km/s), this height tends to be higher compared to faster CMEs. In particular, for 5 October 2012 CME, the height $\tilde{h}_0$ was estimated as 31 $R_{\odot}$ by Sachdeva et al. (2017). Although their dataset did not include the 23 May, 2017 event, however, they reported that $\tilde{h}_0$ is up to $\approx$ 47 $R_{\odot}$ for CMEs with speeds comparable to that of the 23 May, 2017 CME (Refer to Tables 1 and 2 in Sachdeva et al. (2017)). The above observations

strongly support the idea that CME rotation due to the Lorentz force is possible even beyond 21 $R_\odot$ for these two CMEs. However, the analysis showed that for 23 May, 2012 CME rotation did not persist in the drag-dominated regime for a longer time, i.e., beyond 70 $R_\odot$. This is evident from the estimated value of tilt at 70 $R_\odot$ ($\approx 32°$) from GCS reconstruction and at L1 ($\approx 40°$) from Marubashi fitting. This contrasts with the behaviour observed for the 5 October 2012 CME, where a continuous rotation from 14 $R_\odot$ to L1 was identified.

A recent simulation study by Koehn et al. (2022) showed that the orientation of the CME flux rope affects its geoeffectiveness. Keeping all the parameters constant in a spheromak model of a CME, they found that a tilt of 180° of the spheromak axis (equivalent to 90° tilt of the CME flux rope as defined in our study) results in a prolonged southward B_z, leading to the most geoeffective case in their study.

Our analysis presented in Chapters 5 and 6, based on a set of 15 events, highlights that CME rotation is a relatively rare occurrence observable in HI1 images. This rarity is partly due to the specific conditions required for a persistent CME rotation. While rotation is more frequently observed in the lower corona, where the ambient magnetic field is dominant, sustained rotation throughout the heliosphere requires favourable conditions in both the magnetic field and solar wind. Additionally, as CMEs propagate and enter the HI1 field of view, they tend to become fainter and more diffuse, complicating the application of GCS model reconstruction. These factors collectively contribute to the rare detection of CME rotation in the heliosphere.

Furthermore, our findings underscore the difficulties in forecasting space weather effects associated with such stealthy CMEs. The study illustrates that predicting the geoeffectiveness of CMEs solely from near-sun observations can be challenging. In this context, HI observations play a vital role in bridging the observational gap between the Sun and Earth, thereby enhancing our understanding of CME propagation through the heliosphere. *The work presented in this chapter has been published in Kumar et al. (2023) and Kumar et al. (2024).*

Chapter 7

CME Deflection and Its Impact on CME Arrival Time Estimation

7.1 Introduction

Earth-directed CMEs interact with the magnetosphere of the Earth, causing a geomagnetic storm that results in adverse space weather effects. CMEs can deflect and rotate in the heliosphere due to various interactions, including those with other CMEs, stream interacting regions, the ambient solar wind, and the magnetic field (Wang et al., 2004; Gui et al., 2011; Wang et al., 2014; Kay et al., 2017; Kumar et al., 2023, 2024). These interactions complicate the estimation of CME properties at L1 based on their near-Sun observations. Therefore, studying propagation of CMEs in the heliosphere is crucial for accurately determining and predicting their geoeffectiveness on Earth. The geoeffectiveness of a CME is determined by several factors, including the strength of the southward component (Bz) of the Interplanetary Magnetic Field (IMF), density, velocity, and the duration of negative Bz. (Tang et al., 1989; Gosling et al., 1990; Echer et al., 2008). The negative Bz component interacts with the magnetopause, causing magnetic reconnection, which causes the exchange of energy between the CME and the magnetosphere of Earth (Dungey, 1961; Gonzalez and Mozer, 1974; Gonzalez et al., 1999) and thus creates a geomagnetic storm, which causes a decrease in the Dst Index. Intense geomagnetic storms having Dst (≤ -100 nT) can cause se-

rious space weather consequences (Cid et al., 2014). Thus, studying these events and improving space weather prediction becomes essential. Apart from studying the properties of the geo-effectiveness of CMEs, there is a need to develop an arrival time prediction model for CMEs to obtain their transit speed to minimise the potential damage caused by the CMEs. The STEREO mission has been providing multiple viewpoints observations of CMEs, enabling estimation of the true CME speeds in the coronagraphic (COR2) and Heliospheric Imager (HI) fields-of-view (FOV). Several 3D reconstruction models have been developed to track the 3-dimensional view of CMEs (e.g., tie-pointing: Inhester (2006); forward modeling: Thernisien et al. (2009); polarisation ratio: Moran and Davila (2004)). However, the true speeds derived in COR2 FOV may not be the actual speed of the CME at 1 AU. This speed may change due to the drag interaction of the CME with the ambient medium, which may accelerate or decelerate the CME (Gopalswamy et al., 2000).

Different space weather models can be used to estimate the time of arrival of the CMEs and their impact parameters. This approach included complete 3D MHD modeling of the ambient solar wind environment with a model of the CME (Kumar et al., 2020), e.g., cone model (Xie et al., 2004), (FRi3D; Isavnin, 2016), and spheromak (Singh et al., 2020). Although these models can estimate and produce the in-situ properties at L1, they are computationally expensive. Given the fact that the physics of the heliosphere is mostly drag-dominated, simple models are also used in the community, which are faster as compared to the full 3D MHD models and provide a reliable estimate of the time of arrival of the CME at L1. These models include Empirical CME Arrival (ECA) by Gopalswamy et al. (2001), which had an error range of 35 hr, Empirical Shock Arrival model (ESA) by Gopalswamy et al. (2005), which is a modified version of ECA where in a CME is considered as a driver of MHD shock. This reduces the error in the arrival time to 30 hr. Previous studies reported on the forecasting of CME arrival time using the empirical relationship between the projected speed of the CME and the arrival time estimation of various events, e.g., (Gopalswamy et al., 2001; Vršnak and Gopalswamy, 2002; Schwenn et al., 2005). The analytical Drag

Based Model (Vršnak and Žic, 2007; Lara and Borgazzi, 2009; Vršnak et al., 2010) and numerical MHD simulation model (Odstrcil et al., 2004; Manchester et al., 2004; Smith et al., 2009) reduced the errors in the arrival time to 10 hr or less (Gopalswamy et al., 2013). The drag-based model estimates the arrival time of the apex of the CME at Earth. Although it considers acceleration or deceleration of the CME due to the drag force, it does not consider the geometry of the CME, which was incorporated in the advanced drag-based model (ADBM). The ADBM considers both the ambient solar wind drag and the geometry of CMEs (Vršnak et al., 2013). One of the major CMEs of SC25 was observed on 21 April 2023, which reached the Earth on 23 April 2023. This CME was a high-speed CME with a projected speed of more than 1000 km/s, leading to a strong geomagnetic storm on 24 April, 2023 with a Dst index of -231 nT (Ghag et al., 2024; Gopalswamy et al., 2024). It originated around 18:00 UT on 21 April 2023 from the AR 13283 near the disc center S21W11, The CME was associated with the M 1.7 flare observed by GOES (Vemareddy, 2024). Gopalswamy et al. (2024), used the cone-based Model (Gopalswamy et al., 2015) to estimate the shock arrival of the CME and suggested a westward deflection of the CME. Ghag et al. (2024), investigated the geomagnetic storm caused by this CME on Earth, where they found a two-step decrease in the Dst index, once during the sheath region and another during the Magnetic Cloud (MC) region of the CME. This CME produced the largest storm of SC 25 to date. Thus, it provided a unique opportunity to understand its propagation in the heliosphere and its impact on the magnetosphere of the Earth. In Chapter 5 and Chapter 6, we show how solar wind interactions with CMEs lead to their deflection and rotation in the heliosphere. In this chapter, we focus on the case study of the 21 April 2023 CME to understand the importance of the deflection of the CME on its arrival time prediction. In this chapter, we revisit the propagation characteristics, including the time of arrival of the 21 April 2023 CME, using 3D GCS reconstruction and multi-point in-situ observations.

7.2 Observations

In order to track the CME of 21 April 2023 near the Sun, we used observations from the SOHO/LASCO-C2 and C3 and STEREO-A/SECCHI-COR2 and HI1 instruments for 3D, GCS reconstruction of the CME.

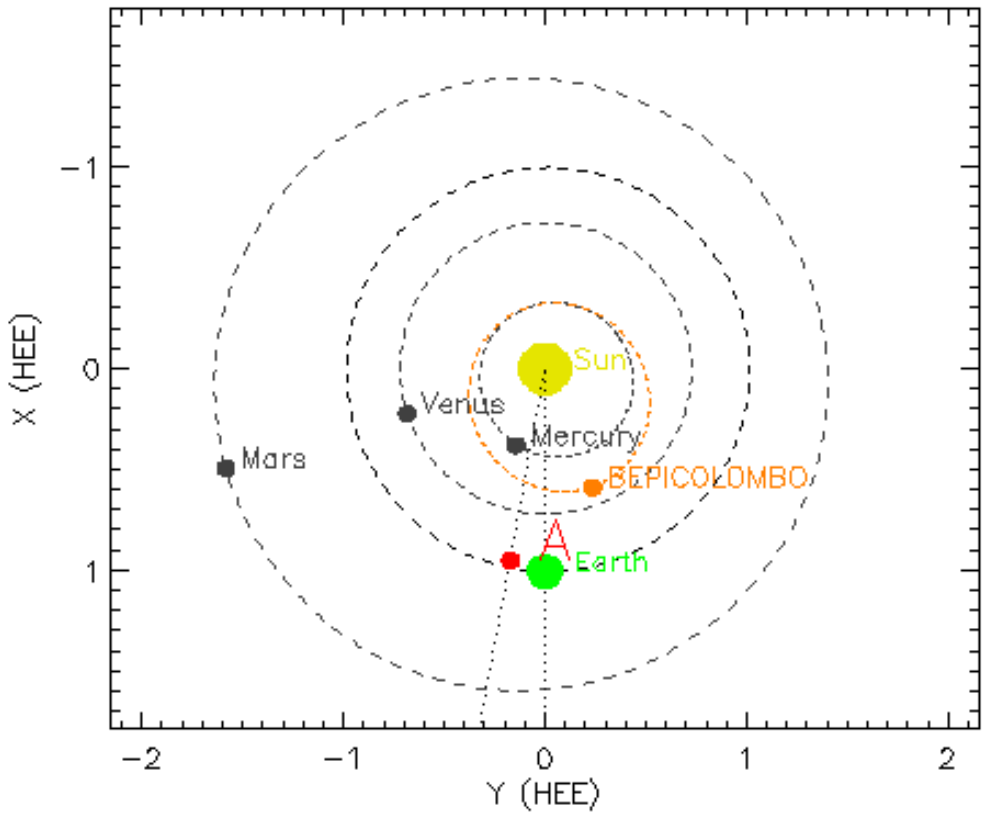

Figure 7.1: The relative orientation and location of different spacecraft, i.e., STEREO-A (red), BepiColombo (orange), and Earth/ACE (green) on 23 April 2023. The angular separation between the ACE and STEREO-A is nearly -10°, and between ACE and Bepicolombo is nearly +22°.

As the 21 April 2023 CME propagated in the heliosphere, it was also observed by different spacecraft located at different heliocentric distances. For example, BepiColombo, situated at ~ 0.63 AU, measured the IMF properties of this CME. Mishra et al. (2021) recently reported that in-situ properties of an ICME may differ at different longitudinal locations in the heliosphere. Therefore, it is crucial to have a multiview point in-situ observation of ICMEs. We used in-situ data from

ACE, STEREO-A, and BepiColombo (Benkhoff et al., 2021) for this particular CME. The solar wind and magnetic field were also recorded at STEREO-A and ACE, which were located $\sim$ 0.96 AU and $\sim$ 0.99 AU, respectively. Figure 7.1 shows the relative orientations and locations of STEREO-A (red), BepiColombo (orange), and Earth/ACE (green) on 23 April 2023. The image was generated by the online tool of Stereo Science Center[1]. The information on the arrival time of different parts of the CME at L1 and at STEREO-A spacecraft was obtained from the HELCAT(WP4) Catalogue[2] (Moestl et al., 2020).

7.3 Analysis

7.3.1 GCS Reconstruction of the CME close to the Sun

The projected speed of the CME in the LASCO FOV was 1284 km/s at 18:12 UT on 21 April 2023 as listed in the CDAW catalogue[3] (Yashiro et al., 2004). The associated halo CME was observed in the images taken by LASCO-C2 and C3 coronagraphs from 18:54 UT to 23:54 UT and also by the COR2 coronagraph between 18:54 UT and 20:08 UT. To derive its deprojected kinematics, we applied a 3D reconstruction using the GCS model for near-Sun observations. The CME was tracked in from C2, COR2, C3 to HI1 FOV, from 18:24 UT to 23:54 UT using an extended version of the Python module (Forstner, 2024; Kumar et al., 2023) mentioned in Chapter 2, which implements GCS reconstruction in C2, C3, COR2, and HI1 images. As mentioned in Chapter 2, Section 2.3.4, the GCS model is described by six parameters: half-angle, kappa, height, latitude, longitude, and tilt. The first three parameters determine the flux rope geometry, while longitude and latitude specify its azimuthal and latitudinal positions, respectively. The tilt defines its orientation relative to the ecliptic plane. As shown in Figure 7.1, a small angular separation of 10° between STEREO-A and Earth may introduce errors in the GCS fitting (Verbeke et al., 2023). Therefore, we performed two independent GCS fittings on the CME images as mentioned below.

[1] https://stereo-ssc.nascom.nasa.gov/cgi-bin/make_where_gif

[2] https://www.helcats-fp7.eu/catalogues/wp4_icmecat.html

[3] https://cdaw.gsfc.nasa.gov/CME_list/UNIVERSAL_ver2/2023_04/univ2023_04.html

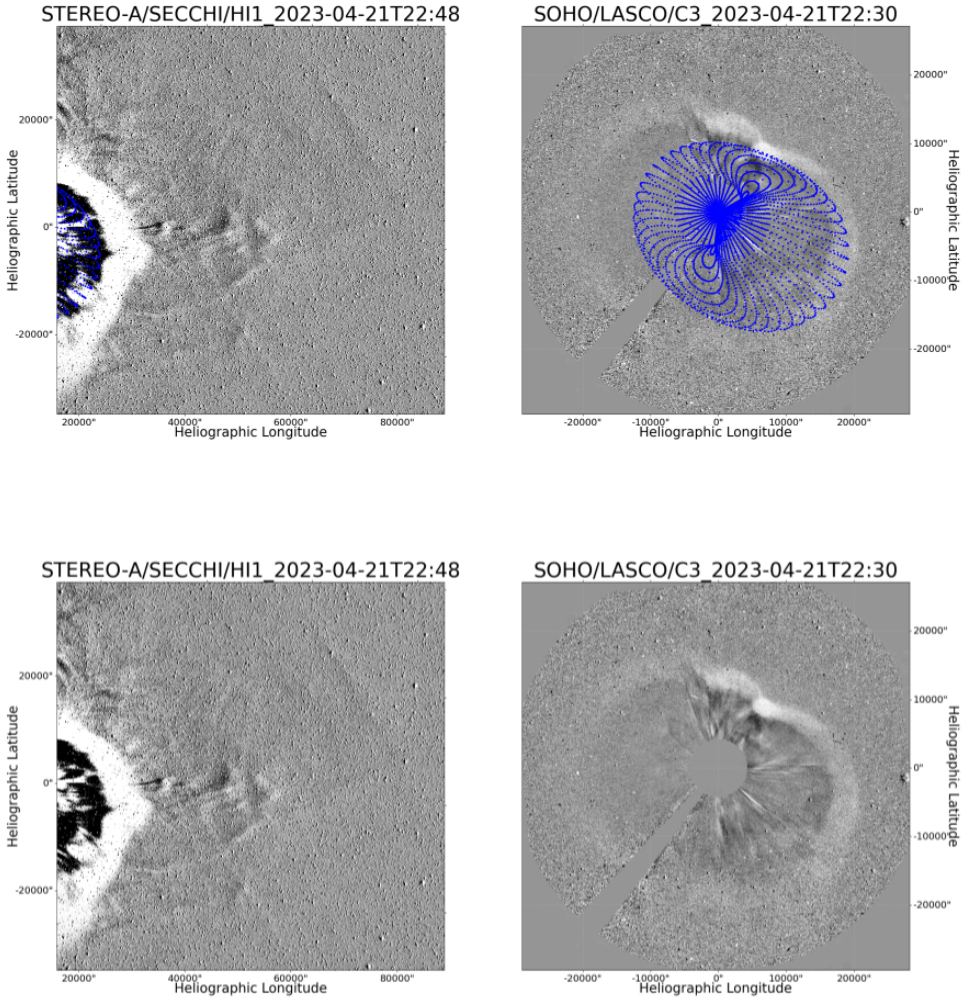

Figure 7.2: GCS reconstruction of the 21 April 2023 CME using observations from two viewpoints of STEREO-A/HI1 and SOHO LASCO-C3. The top panel shows the CME image overplotted with GCS reconstructed mesh. The bottom panel shows a CME image without GCS mesh at 21 April 2023 22:30 UT.

1. In the first GCS fitting of the CME on images from STEREO and SOHO viewpoints, recorded between during 18:24 to 23:54 UT, the longitude of the CME was found to remain constant (nearly +20°) as the CME propagated from COR2 to HI FOV. This suggests a final westward propagation of the CME in the heliosphere at $\approx 38\ R_{\odot}$.

2. In the second GCS fitting, we observed a decrease in longitude(+34 to +0°.) as the CME propagated from COR2 to HI FOV, which corresponds

to deflection towards the east, suggesting a final direction of propagation of the CME along the Sun-Earth line at 42 $R_{\odot}$.

It is important to note there is an agreement on the initial westward propagation of the CME near the Sun (up to 15 $R_{\odot}$), i.e., initial longitudes, both the fittings lie between +20° to +30° in COR2 FOV. This is also in agreement with the longitude of the source region of the CME (S21W11) mentioned in Vemareddy (2024); Gopalswamy et al. (2024).

Based on the above fittings, it is clear that the uncertainty about the estimated final direction of CME is in the HI1 FOV. The range of values in the longitude obtained from two GCS fittings increases more in HI1 FOV, i.e., 0° to +34°. Therefore, whether the CME was propagating along the Sun-Earth line or 20° westward is uncertain.

We further explore the implications of the different directions of propagation of the 21 April 2023 CME on its propagation kinematics and arrival time estimate. For this purpose, we used the ADBM model to estimate the arrival time at different heliocentric distances. We also examined the in-situ observations at different heliocentric distances of different spacecraft and compared our results from the ADBM model, corresponding to inputs from different GCS fittings.

7.3.2 In-situ Observations of the CME

As described in Section 7.2, the CME was intercepted by three spacecraft, Bepi-Colombo, STEREO-A, and ACE, respectively. We have plotted the in-situ data for STEREO-A and ACE spacecraft in Figure 7.3 and 7.4, respectively. In Figure 7.3 and 7.4, the vertical black lines represent the start time of the shock, the start time of the MC, and the end time of the MC, respectively. As reported in the HELCAT catalogue[4], the shock reached BepiColombo on April 22, 2023 at 18:28 UT, which was followed by the arrival of a MC at the spacecraft on 23 April 2023 at 00:11 UT. The MC ended at 07:32 UT on the same day. The CME shock was detected at STEREO-A on 23 April 2023 at 14:29 UT. The MC began at 20:30 UT and ended on 24 April 2023 at 23:25 UT (Figure 7.3).

[4] https://helioforecast.space/icmecat/ICME_BEPI_MOESTL_20230422_01

The ACE spacecraft observed the CME shock on 23 April 2023 at 17:02 UT. The MC passage in ACE was from 24 April 2023 at 01:00 UT to 22:02 UT (Figure 7.4). It is important to mention here that the HELCAT catalogue mentions the ToA in the Wind spacecraft; however, we assumed the same ToA for the ACE spacecraft, because both spacecraft are located at L1. We have tabulated the shock arrival time, MC start, and end time recorded by different spacecraft in Table 7.1. These

Table 7.1: Shock and MC arrival times at different spacecraft (Spc) along with their heliocentric locations in HEE coordinates.. Here, BpC and STA stand for BepiColombo and STEREO-A, respectively. Shock arrival time and MC interval are provided in UT.

Spc	**Location (R, ϕ, θ)**	**Shock Time**	**MC Interval**
BpC	0.631 AU, 21.9°, -3.4°	22 Apr 18:28	23 Apr 00:11 – 07:32
STA	0.963 AU, -10.2°, -5.8°	23 Apr 14:29	23 Apr 20:30 – 24 Apr 23:25
ACE	0.997 AU, -0.1°, -4.9°	23 Apr 17:02	24 Apr 01:00 – 22:02

observations reveal that the MC of the CME, after passing through BepiColombo, reached STEREO-A first and arrived at the ACE spacecraft approximately 3 hrs and 30 minutes later. We want to emphasize the chronology of the arrival of the CME at STEREO-A and Earth, which is crucial for interpreting the results of the ADBM model from two different GCS fittings in the next section. This also improved our understanding of the kinematics of the CME in the heliosphere.

It is interesting to note here that the speed of the solar wind is fast even after the passage of the CME at L1. There is a significant increase in the solar wind speed from before the shock (17:02 UT, 23 April) and after the CME passage (22:02 UT, 24 April). This suggests a transition from slow ($\approx$ 350 km/s) to fast solar wind ($\approx$ 650 km/s) related to Stream Interacting Regions (SIR) around the ICME time.

Moreover, there is a sudden increase in the β parameters at around the same time. All these features indicate the possible presence of sector boundary crossings associated with SIR crossings.

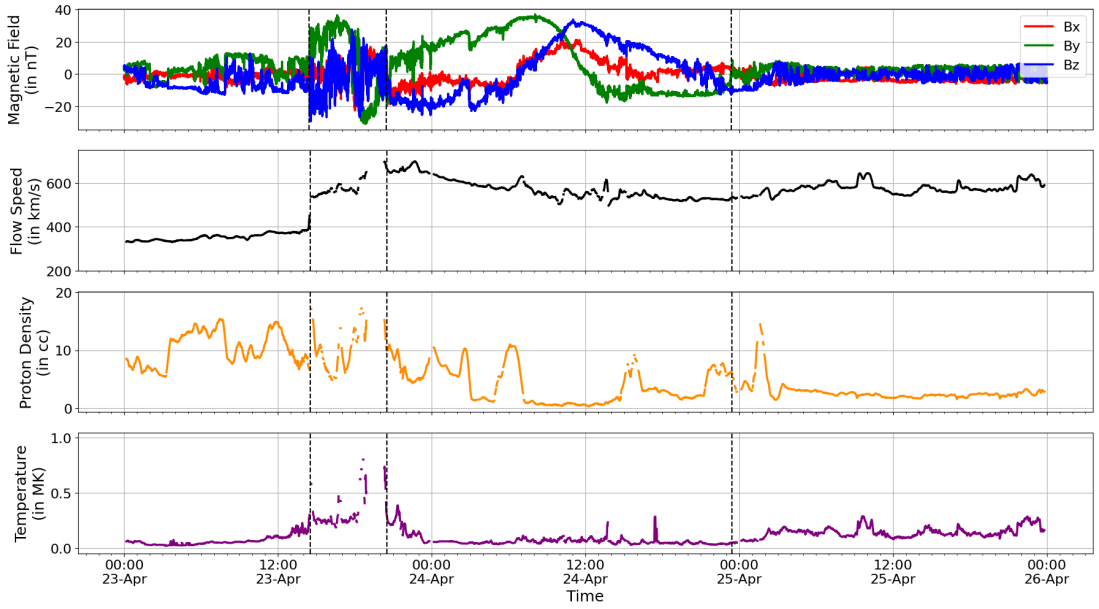

Figure 7.3: In situ observations by the STEREO-A spacecraft from 23 to 26 April 2023 showing, from top to bottom: the IMF vectors, solar wind flow speed, proton density, and proton temperature. The first vertical dashed black line marks the arrival of the CME-driven shock, while the second and third lines indicate the start and end times of the associated magnetic cloud, respectively.

7.4 Results

7.4.1 Time of Arrival (ToA) Estimate

ADBM was implemented to forecast the transit speed and ToA at each spacecraft based on the results of two GCS reconstructions, which are used as input for ADBM. As discussed in the previous section (Section 7.2), two different scenarios of CME longitude estimates were considered in the ADBM model. We then estimated the ToA and impact speed of the CME MC for each scenario and compared these predictions with the actual ToA and impact speeds observed at the respective spacecraft.

The input parameters used in the ADBM model are described below.

1. CME Take-off Date and time: The date/time of the image used for the last GCS fitting of the CME in HI FOV (21 April 2023 23:54 UT) was used as CME take-off time. Since we have used GCS reconstruction upto HI FOV,

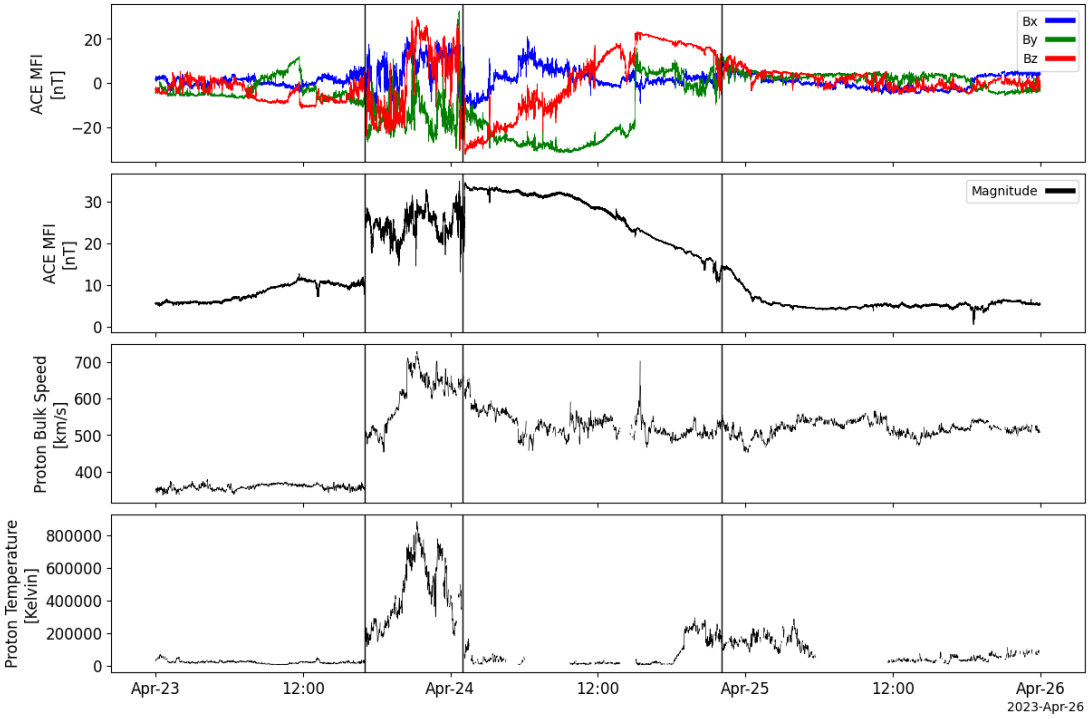

Figure 7.4: In-situ parameters at L1 observed by the ACE spacecraft from 23 to 26 April 2023. IMF vectors, total magnetic field, plasma flow speed and temperature are plotted with time from top to bottom, respectively. The first vertical black line denotes the arrival of the shock of the CME, and the second and third dashed lines represent the start and end of the magnetic cloud, respectively.

it gives an advantage to track the CME to higher heights as compared to previous studies, which use a typical value of 21 $R_{\odot}$ (Martinić et al., 2023) for CME take off distance.

2. Starting Radial Distance of the CME: It is the average of the two true heights of the CME obtained from the last GCS fit in HI1 FOV from two GCS fittings, i.e., approximately 40 $R_{\odot}$, for this particular parameter.

3. Speed of the CME: The true speed of the CME is the speed obtained by taking the average of the speeds in the last GCS fitted frame in HI FOV of the two GCS fittings, which is 1100 km/s.

4. Drag Parameter: It is a variable that ranges from 0.1 to 2 $\times$ 10^{-7}. Different values of the drag parameter within this range are used to improve the ToA and impact speed accuracy. We used an optimum value of the drag =

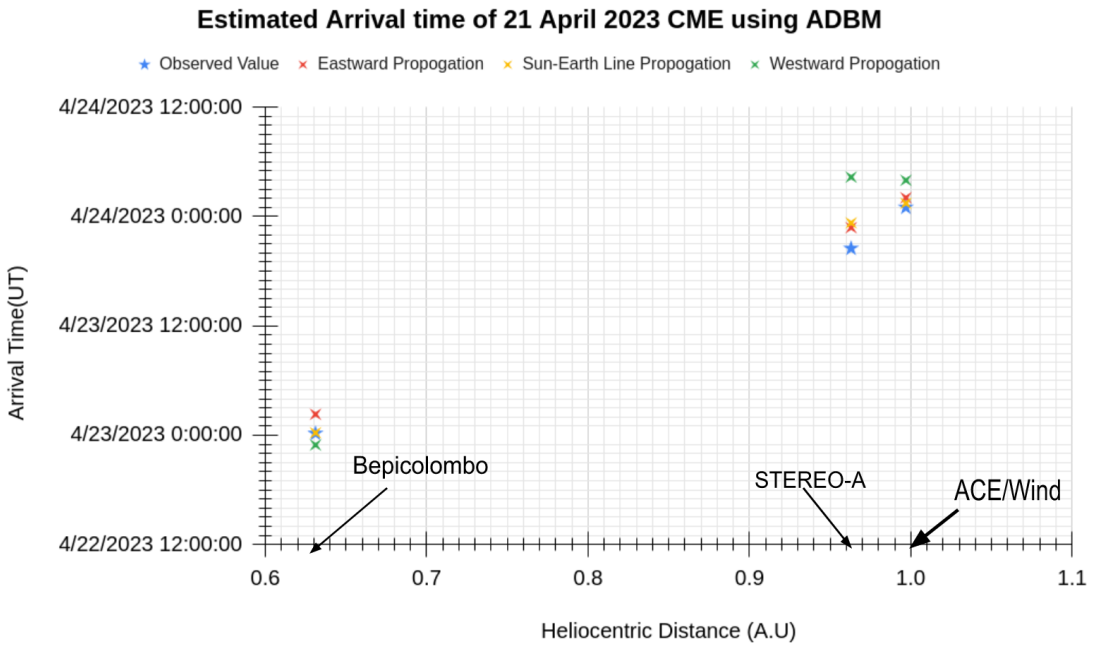

Figure 7.5: Scatter plot of ToA v/s heliocentric distances(AU) of different spacecraft, i.e, BepiColombo, STEREO-A, and ACE, respectively. The blue star represents the observed time of the arrival of the MC at each spacecraft. The red crosses represent the time of arrival of MC estimated considering the case of eastward propagation where the final longitude reaches -10°. The yellow crosses represent the case where the CME is considered to propagate along the Sun-Earth line. The green crosses are the time of arrival estimated by considering the westward propagation of the CME.

0.25×10^{-7}, which provided us with overall better results.

5. Solar Wind Speed: The background solar wind speed is assumed constant and approximately 350 km/s for this CME. This value is taken from the ambient solar wind velocity observed before the CME arrival at L1 (from ACE data).

6. R_{target}: Here, the positions (distance of the spacecraft from the Sun) of the three spacecraft are used, i.e., BepiColombo, STEREO-A, and ACE (as mentioned in Table 7.2).

7. CME Angular Width: The CME angular width in the ecliptic plane. We derived this parameter from the projection of the GCS CME mesh on the ecliptic plane.

8. Earth-target heliocentric angular separation: We have used the angular separation between the Spacecraft and Earth (as mentioned in Table 7.2.).
9. Source region central meridian distance: This corresponds to the longitude of the CME obtained from GCS reconstruction in the last frame in HI FOV.

We have listed all the input parameters in Table 7.3. As the ADBM model estimates the arrival of the MC at different spacecraft, using the parameters mentioned above and two cases of GCS fitting, the ToA and transit speed of the CME at the three spacecraft are forecast and compared with the actual ToA of the CME (start time of MC as mentioned in Table 7.2) in the respective spacecraft. In Figure 7.5, we have plotted the different cases of predicted ToA (marked with

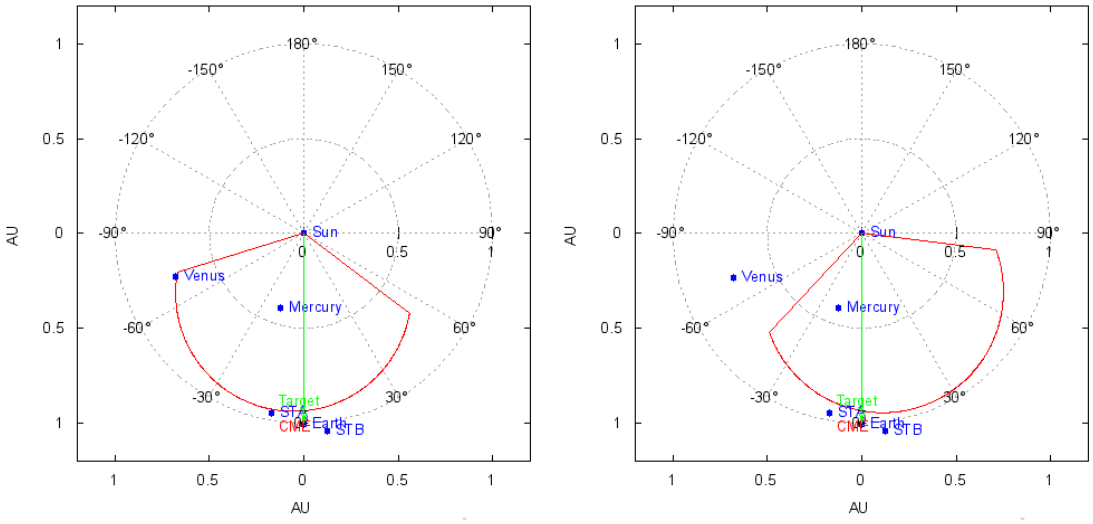

Figure 7.6: CME arrival at different spacecraft based on the two possible cases of the eastward and westward propagation of the CME. The left panel shows a snapshot of the ADBM output for eastward propagation of CME, showing the arrival of the CME first at STEREO-A (blue dot on the left), then at ACE spacecraft (green dot). The right panel shows a snapshot of the ADBM output for the case of westward propagation, showing the arrival of the CME first at ACE and then at the STEREO-A spacecraft.

a cross) and the actual ToA (marked with a star) with the radial position of the spacecraft from the Sun. From Figure 7.5, Table 7.1, and Table 7.3, we can notice that:

1. For the case of GCS fitting corresponding to final Earthward propagation (yellow cross) due to eastward deflection from COR2 to HI FOV in GCS

fitting, the prediction errors of ToA and transit speed of CME are the least for all three spacecraft. Also, the CME arrives in the STEREO-A spacecraft before the ACE spacecraft.

2. For the case of GCS fitting, suggesting no deflection in the CME propagation direction, leading to a final westward propagation (green cross), the errors in ToA ($\geq$3 hr) and transit speed of CME in STEREO-A are high ($\geq$ 50 km/s). Also, the CME arrives in the ACE spacecraft and then at STEREO-A.

Table 7.2: Summary of CME parameters used in the analysis 21 April 2023 CME

Input Parameter	**Value**
CME Take-off Date/Time	21 April 2023 23:54 UT
Starting Radial Distance	$\sim$40 $R_{\odot}$
CME Speed	1100 km/s (from GCS reconstruction)
Drag Parameter (γ)	2.5×10^{-8} (range: 0.1 to 2×10^{-7})
Solar Wind Speed	$\sim$350 km/s
R_{target}	Spacecraft (see Table 7.1)
CME Angular Width (Ecliptic)	derived from GCS fitting projection
Earth-Spacecraft Angular Separation	based on Table 7.1
Source Region Central Meridian Distance	from GCS reconstruction in last HI1 frame

In the case of Earthward propagation, the nose of the CME hits the STEREO-A spacecraft, and thus, the CME appears in STEREO-A first, then at the Wind/ACE spacecraft. In the case of westward propagation, the flank part of the CME appears in the STEREO-A and ACE spacecraft. Thus, the CME appears in ACE first, then at STEREO-A.

It is important to note that in the case of westward propagation of the CME, the errors in ToA are larger in the STEREO-A spacecraft. Moreover, according to ADBM results, CME first arrived at ACE at 3:59 UT on 24 April and then at STEREO-A at 4:20 UT on 24 April, contrary to the actual in-situ observations. The chronology of the arrival of the CME at STEREO-A and ACE matches only

in the cases of Earthward propagation of the CME. In this case, CME first arrives at STEREO-A at 23:18 UT (+2:48 hr of actual ToA) on 23 April and then at ACE at 01:27 UT on 24 April (00:27 hr of actual ToA). Moreover, the ToA estimated for the BepiColombo (00:05) is in very good agreement.

The GCS fitting corresponding to this case suggested the eastward deflection from its initial/first direction of propagation. i.e., the direction of propagation at the height above approx 40 $R_{\odot}$ (insertion time of the input to ADBM model) is Earth-directed (stonyhurst longitude 0°). This suggests a net eastward deflection of the CME from its initial direction of propagation (near the Sun in COR2 FOV) is westward for both the fittings, i.e., longitude positive $\geq 20°$.

Motivated by the above finding, we further increased the input longitude of the CME in the eastward direction in the ADBM to find a better match for the ToA of the CME at STEREO-A and ACE. We used longitude -10°, with speed = 1100 km/s, the starting distance as 40 $R_{\odot}$, and the starting time as 23:54 UT, and the rest of the parameters are the same as the previous two cases. The corresponding values of ToA are plotted in Figure 7.5 with red crosses and tabulated in Table 7.1.

For this case, the arrival of CME at STEREO-A was on 23 April at 22:47 with an error of +02:17 with the actual ToA. Whereas the arrival of the CME at ACE for this case was on 24 April at 02:04 with an error of +01:04 with the actual ToA at ACE. Moreover, this resulted in a difference of ToA for STEREO-A and ACE, approx 03:30, which is very close to the actual difference between ToA, i.e., 03:17, at these two spacecraft.

Therefore, we found that using input longitude -10° in ADBM (nearly the exact longitude as STEREO-A) gave us the best results in the context of the chronology of CME arrival at STEREO-A and Earth.

Thus, using the ADBM model, we inferred that the CME underwent an eastward deflection during its propagation from near the Sun (COR2 FOV) to the heliosphere (HI FOV), and its direction of propagation is along the STEREO-A-Sun line in the heliosphere.

It is important to mention here that due to the assumed shape of the CME in

ADBM and the relative location of STEREO-A and ACE, the chronology of the arrival of the CME at these two spacecraft depends only upon the longitude of the CME in the ADBM. It is also possible that by using individual inputs (speed and height) from GCS for each GCS fitting to ADBM, slightly different results can be obtained for individual spacecraft; however, in this work, we only studied the ADBM parameter that differentiates the chronology of the arrival of the CME at STEREO-A and ACE, i.e., the longitude of the CME. Therefore, in the above analysis, we only discussed the results corresponding to different longitudes of the two GCS fittings and used average values for other ADBM parameters.

Table 7.3: Comparison of arrival time estimate of different cases of the direction of propagation of predicted ToA with the observed ToA of MC at respective spacecraft. The values in brackets represent the errors of the different cases (hh:mm). Here, EW, ERW, and WW show the cases of eastward propagation, Earthward (Sun-Earth line) propagation, and westward propagation of CME, respectively.

Spacecraft	**Obs. ToA (UT)**	**EW (ϕ =-10°)**	**ERW(ϕ=0°)**	**WW (ϕ = 20°)**
BepiColombo	23 April 00:11	23 April 2:18 (+2:07)	23 April 00:16 (+00:05)	23 April 22:55 (-01:16)
STEREO-A	23 April 20:30	23 April 22:47 (+2:17)	23 April:18 (+2:48)	24 April 4:20 (+7:50)
ACE	24 April 1:00	24 April 2:04 (+01:04)	24 April 1:27 (00:27)	24 April 3:59 (+2:59)

7.5 Discussion

This study, based on the 3D reconstruction of the CME on 21 April 2023 close to the Sun and estimation of the ToA using the advanced drag base model (ADBM) model, suggests that the CME, which originated at S21W11, underwent an overall eastward deflection while propagating in the heliosphere till 1 AU. The possible cause of the CME deflection in the heliosphere is also a subject of research that influences the propagation. This needs to be explored using full 3D MHD modeling in the heliosphere.

This eastward deflection can range from a maximum of E10° (20° east, from the source region) to the Sun-Earth line (11° west, from the source region). This happens to be the most favourable scenario for explaining the arrival of the CME in STEREO-A first, then at ACE spacecraft.

We note that Gopalswamy et al. (2024) used a westward propagation direction in the CONE model of the CME and found an error (14 hrs) in the ToA of the shock at the ACE spacecraft when applying an empirical relation for 3D speed. They suggested that assuming a relative westward propagation direction decreases the estimated CME speed in the empirical relation, leading to a longer transit time and reduced errors. They suggested the reason for this westward deflection could be the presence of a nearby coronal hole. In contrast, our approach involves tracking the CME to a larger distance using 3D reconstruction, providing more accurate 3D speed estimates and height in the ADBM model. Furthermore, we extend the analysis to investigate the sequence of the CME arrival at STEREO-A and ACE, which strongly hints towards an eastward deflection of the 21 April 2023 CME in the heliosphere.

It is important to mention here that due to uncertainty in the GCS parameters and different inputs of the ADBM model, one could easily tweak the parameters to find the best arrival estimate closely matching with the observations, individually for ACE or at STEREO, even in the case of the westward direction of propagation of the CME. However, due to the assumed shape of the CME in the ADBM model (circular front), the relative locations of the spacecraft and

relative heliocentric distances, it is impossible to set the chronology correctly for the spacecraft simultaneously for the same input parameter for a westward propagating CME. In addition, our final conclusion about the eastward deflection of this fast CME in the heliosphere agrees with the results of the previous studies by Wang et al. (2004); Wang et al. (2014), which is also in agreement with our findings in Chapter 5. Wang et al. (2004) reported that a fast CME of speed $\approx$ 1100 km/s, while propagating in a slow solar wind of speed $\approx$ 450 km/s (Figure 7 of Wang et al. (2004)), tends to deflect in an eastward direction by $\approx 25°$. This value of longitudinal deflection is comparable with the range of values we observed, i.e., $\approx 20° - 30°$.

This study suggests that using individual simplistic models for CME propagation and tracking might not be sufficient to conclude even about the simple CME parameters, especially when the separation angle between two observing spacecraft is small. It has further implications when used as an input in another model, i.e., ADBM, leading to errors in ToA. Therefore, a more conclusive finding can be made by using multiple techniques (GCS and ADBM) and multiple observations (STEREO-A, ACE, and BepiColombo) to constrain the CME propagation direction.

The in-situ observations of ACE and STEREO-A suggest the passage of a sector boundary with a substantial solar wind speed, which provides us with the possibility of the CME shock interacting with the SIR. Further investigation and analysis are required to establish the CME-SIR interactions.

7.6 Conclusion

In conclusion, this study highlights the challenges in estimating the propagation direction of the 21 April 2023 CME, primarily due to the small separation angle between STEREO-A and SOHO. This limitation affects the accuracy of the time of arrival (ToA) of CME, prediction at Earth, underscoring the complexity of CME propagation in the heliosphere.

The analysis also emphasizes the importance of accurately determining the propagation direction of the CME to improve ToA forecasts. In this chapter, we em-

ployed a simplified yet fast model assuming an isotropic solar wind environment. However, real solar wind conditions are often highly non-uniform, as discussed in Chapter 5 and Chapter 6, necessitating more realistic modeling using fully 3D MHD simulations. Moreover, the observations at L1 suggest the possibility of a non-coherent or deformed CME front, likely caused by the interaction with an inhomogeneous solar wind. This further supports the need for 3D MHD simulations to better understand such distortions during CME propagation.

Therefore, in the next chapter, we separately model the ambient solar wind and the CME using a more realistic approach to better capture the complex dynamics of CME–solar wind interactions.

The work presented in this chapter is under review in ***Journal of Astrophysics and Astronomy****.*

Chapter 8

CME-Solar Wind Modeling

8.1 Introduction

An effective space weather forecasting framework must accurately predict both the arrival time and the intensity of an impact on the geospace. These outcomes are strongly influenced by the global geometry of the CME, internal magnetic structure, and dynamic evolution, which are, in turn, governed by its interaction with the ambient solar wind. The geoeffectiveness of a CME is primarily determined by the strength and duration of the southward component (B_z) of the interplanetary magnetic field (IMF), along with solar wind density and velocity (Tang et al., 1989; Gosling et al., 1990; Echer et al., 2008). A prolonged negative B_z interacts with the magnetopause of the Earth, triggering magnetic reconnection and enabling energy transfer into the magnetosphere (Dungey, 1961; Gonzalez and Mozer, 1974; Gonzalez et al., 1999), often resulting in geomagnetic storms characterized by a decrease in the Dst index. Intense geomagnetic storms (Dst $\leq$ -100 nT) can have severe space weather consequences (Cid et al., 2014), emphasizing the importance of improving prediction capabilities of space weather.

The ADBM, described in Chapter 7, is a simple and fast model that effectively fulfils its core objective of providing quick estimates of CME arrival times at Earth. Its speed and efficiency make it suitable for operational forecasting. However, the model assumes a constant drag coefficient and a uniform solar wind, which limits its ability to represent the full complexity of CME–solar wind

interactions. By treating CMEs as rigid bodies, the ADBM simplifies computations but neglects key physical features such as internal magnetic structure, rotation, and deformation—factors critical for accurate arrival time and geoeffectiveness predictions. Furthermore, it only considers radial propagation, omitting non-radial deflections and shock/sheath formation, which also influence CME evolution. Despite these limitations, ADBM provides useful insights into CME kinematics, particularly at larger heliocentric distances. However, its sensitivity to initial conditions and lack of magnetic force treatment make it inadequate for modeling CME evolution in the low corona, where magnetic forces dominate.

To realistically model CME propagation through the heliosphere, a full 3D extrapolation of the solar wind is necessary (Odstrcil et al., 2004; Pomoell, Jens and Poedts, S., 2018; Kumar et al., 2020; Mayank et al., 2022). This process involves two main components: (i) specifying solar wind boundary conditions from a coronal model in the coronal domain, and (ii) extending this solar wind solution throughout the heliosphere. Several physics-based models, such as the Alfvén Wave Solar Model (AWSoM; van der Holst et al., 2014) and COolfluid COroNa UnsTructured (COCONUT; Perri et al., 2022), have been developed to simulate the solar corona and solar wind. These models solve the full set of 3D MHD equations and incorporate physical processes such as Alfvén wave turbulence, coronal heating, and solar wind acceleration. These models provide self-consistent plasma properties and more accurate heliospheric conditions, but at the cost of significantly higher computational resources as compared to empirical solar wind velocity models, i.e., WS, WSA and DCHB. The empirical models are based on the expansion factor of the coronal magnetic field and footpoint distances to estimate solar wind speed.

These coronal models are combined with heliospheric models/code such as EUHFORIA, ENLIL, or PLUTO (Mignone et al., 2007) to make full heliospheric solar wind modeling frameworks. These solar wind solutions serve as the background medium into which CME models such as the cone model (Xie et al., 2004; Odstrčil and Pizzo, 1999), the FRi3D model (Isavnin, 2016), or the spheromak model (Singh et al., 2020) can be injected to simulate their propagation.

In Chapter 2 and Chapter 3, we used a two-dimensional (2D) extrapolation of the solar wind to compute its velocity in the heliosphere, resulting in a one-dimensional velocity profile at L1. However, to investigate the global heliospheric interaction between a CME and the solar wind—both of which are inherently three-dimensional (3D) structures—a full 3D heliospheric solar wind profile is essential.

Scolini and Palmerio (2024) addressed the limitation of simplistic CME models by implementing a more realistic spheroid CME model within EUHFORIA. This model allows for a non-spherical (croissant-like) front, in line with coronagraph observations, and provides improved forecasts of CMEs for flank encounters that are commonly misclassified by spherical models. Parallel efforts to enhance the magnetic realism of CME simulations are presented by Guo et al. (2024), who implemented a Regularized Biot–Savart Law (RBSL) flux rope model into the newly developed global coronal model, COCONUT. The RBSL framework facilitates the construction of magnetically force-free flux ropes with arbitrary axis shapes, allowing for accurate representation of non-circular and sigmoidal structures observed in the low corona. Their simulation captures the initiation, acceleration, and heliospheric propagation of an S-shaped flux rope in a physically self-consistent manner.

Building on flux rope physics, Singh et al. (2020) proposed a modified spheromak model for CME simulation within the Multi-Scale Fluid-Kinetic Simulation Suite (MS-FLUKSS). Their approach allows for the independent specification of poloidal and toroidal fluxes, as well as the helicity sign of the flux rope, based on observational proxies such as post-eruption arcades and coronal dimming regions.

Apart from the above-mentioned frameworks providing full 3D-MHD treatment for CMEs and the solar wind, there are other simpler models offering a mid-way approach. Sarkar et al. (2020) proposed an observationally constrained analytical model, the INterplanetary Flux ROpe Simulator (INFROS), to predict the magnetic field vectors of ICMEs. INFROS uses near-Sun CME flux rope properties, derived from remote-sensing observations, as inputs and evolves them analytically to estimate the magnetic field at any heliocentric distance. One of

the key features of INFROS is its ability to account for the self-similar expansion of the CME and the time-varying axial magnetic field during its transit over a spacecraft.

Roy and Nandy (2023) presents a computationally efficient, data-driven 3D MHD model, CESSI-STORMI, to simulate the interaction of ICME flux ropes with the magnetosphere of the Earth. Their approach essentially uses a self-similar CME expansion approach in the heliosphere, which provides an input to a magnetospheric MHD model to predict the geoeffectiveness of the CMEs.

Temmer et al. (2023) provides a comprehensive review of the current status and future directions in CME modeling and heliospheric observations. The paper identifies key challenges, including the lack of standardized validation metrics, the need for ensemble modeling frameworks, and the limitations of current observational constraints. It also emphasizes that CME propagation cannot be reliably modeled without accurate solar wind background predictions, which remain a source of considerable uncertainty.

To study CME–solar wind interactions in detail, in this chapter we present different modules of a comprehensive framework of full 3D MHD simulations of the ambient solar wind with a CME model. We aim to demonstrate the initial development toward an integrated CME–solar wind framework. The magnetohydrodynamics (MHD) domain in this chapter employs the PLUTO code to simulate plasma properties in the inner heliosphere. A preliminary assessment of the applicability of PLUTO for solar wind modeling was conducted in a two-dimensional pilot study (Kumar et al., 2020), where the results were compared with those from other extrapolation models based on the WSA (Wang–Sheeley–Arge) relation. In the present chapter a three-dimensional implementation of the WSA relation is adopted. For the coronal magnetic field extrapolation, we utilize the `pfsspy` Python package (Stansby et al., 2020a) described in Chapter 2. We use stereoscopic observations to reconstruct the 3D structure of the CME flux rope near the Sun, enabling its tracking throughout the heliosphere. This reconstructed geometry of the CME flux rope is then used to model the internal magnetic field evolution of the CME during its propagation. All these different modules form a

basis for a grand unified modeling framework for the CME and its propagation in the ambient solar wind from Sun to Earth.

8.2 Solar Wind-CME Simulation Framework Development

To develop a full solar wind-CME framework, we combine the WSA coronal model for solar wind velocity with the PLUTO MHD code (Mignone et al., 2007). It is important to note that in Chapter 2 and Chapter 3, the solar wind velocity profile along the Sun–Earth line (i.e., the sub-Earth point in the ecliptic plane) was considered using the 2D heliospheric extrapolation model HUX. In contrast, the present framework requires a complete specification of the inner heliospheric boundary conditions in the θ–ϕ sphere at some $R = R_{inner}$.

With an aim to incorporate the effects of some of the physical aspects in solar wind extrapolation, we describe a physics-based modeling approach in the heliosphere (from R_{inner} to L1) that involves solving a set of conservative equations using the Godunov scheme-based Eulerian grid code, PLUTO. For this, we assume the solar wind to be hydrodynamic and solve the following set of compressible equations in 3D polar co-ordinates (r, θ,ϕ) :

$$\frac{\partial \rho}{\partial t} + \nabla \cdot (\rho \vec{v}) = 0 \tag{8.1}$$

$$\frac{\partial \rho \vec{v}}{\partial t} + \nabla \cdot (\rho \vec{v}\vec{v} + P\mathcal{I}) = \rho \vec{g} \tag{8.2}$$

$$\frac{\partial E}{\partial t} + \nabla \cdot ((E + P)\vec{v}) = \rho \vec{v} \cdot \vec{g} \tag{8.3}$$

where, ρ is the density of the fluid, P being the isotropic thermal pressure, $\vec{v}$ is the fluid velocity is denoted by $\vec{v}$, $\mathcal{I}$ represents the identity matrix, and the total energy is given by $E = \frac{1}{2}\rho v^2 + \rho\epsilon$, which is the sum of kinetic and internal energy. The gravitational acceleration, defined as $\vec{g} = -GM_{\odot}/r^2$, is neglected in the source term of the conservative momentum equation, i.e., we set $\vec{g} = 0$. A polytropic equation of state is employed with an adiabatic index $\gamma = 1.5$ (Odstrcil et al., 2004; Pomoell and Poedts, 2018).

These equations are solved in a non-inertial reference frame, where the inner radial boundary co-rotates with the Sun at the solar rotation rate. To simplify the

model, the Coriolis and centrifugal forces are omitted, as their influence on the steady-state structure of the solar wind is minimal (Pomoell and Poedts, 2018).

The computational grid is defined in polar coordinates, spanning radially from 0.1 AU to 1 AU, with 256 grid cells. The azimuthal (ϕ) direction is resolved using the same number of grid cells.

At the inner radial boundary ($R_{inner} = 21R_{\odot}$), the radial velocity is specified based on the WSA model mapping (Kumar et al., 2020). It is important to mention here that for simplicity, we are estimating the solar wind velocity profile at 2.5 $R_{\odot}$ and we are using the same profile at R_{inner} without incorporating the SCS model from 2.5 $R_{\odot}$ to 21 $R_{\odot}$ Mayank et al. (2022). This boundary also rotates relative to the computational domain at the solar rotation period of a CR, i.e., 27.3 days. Given that the boundary condition corresponds to a supersonic inflow, all characteristic waves point outward from the boundary. Consequently, in addition to prescribing the solar wind velocity, it is necessary to specify both the density and pressure at the inner radial boundary.

Following Pomoell and Poedts (2018), the number density (n), and pressure are imposed at the inner radial boundary as described below:

$$n(r) = n_0 \left(\frac{v_0}{v_r}\right)^2 \tag{8.4}$$

$$P = P_0 \tag{8.5}$$

where P_0 is set to be a constant value of 3.27 nPa and $n_0 = 150$ cm^{-3}, resulting in a temperature of 1.67 MK. The scaling velocity v_0 is set to be 700 km/s. The outer radial boundary is set to have free-flowing outflow conditions. It is also important to note that the above HD framework can be extended to the MHD framework by providing additional boundary conditions for the magnetic field as (Pomoell and Poedts, 2018):

$$B_r = \mathrm{sgn}(B_{\mathrm{corona}}) B_0 \left(\frac{v_r}{v_0}\right) \tag{8.6}$$

$$B_\phi = -B_r \sin\theta \left(\frac{v_{\mathrm{rot}}}{v_r}\right), \tag{8.7}$$

Here v_{rot} is the rotating speed ($R_{inner} \times \omega$, ω is the angular speed of the inner boundary) of the inner boundary. B_r and B_ϕ are radial and azimuthal compo-

nents of B, B_0, is scaling magnetic field. sgn(B_{corona}) represents the polarity of the magnetic field line at a particular location obtained from PFSS model extrapolation. In the present work, we only show the results corresponding to the HD simulations.

Elliptical Cone Model for CME

CMEs constitute significant global-scale magnetic transient structures in the solar wind. To model their influence on the plasma in the inner heliosphere, we first employ the modified version of the cone CME model, similar to that of Odstrčil and Pizzo (1999). The aim of hydrodynamic implementation of the simplistic CME cone model is to provide a computationally efficient validation of the solar wind background and CME kinematics. The cone model treats the CME as a hydrodynamic cloud exhibiting a simple geometry as the CME evolves in the outer corona, which is characterized by a constant angular width, propagation direction, and speed. The cross-section of the CME is assumed to be circular, and the CME is also homogeneously filled (i.e., density, pressure, and radial speed are constant in the CME).

CME is introduced as a time-dependent boundary condition at the inner radial boundary, i.e., at 0.1 AU. Following the assumption of a circular cross-section, the perturbation on the boundary for the cone model has a circular shape with a radius that varies in time. The speed at which the radius of the circular enhancement increases and decreases is linked to the speed and the shape of the CME. In this work, we set the angular width of the enhancement at 0.1 AU to be sinusoidal in time, which corresponds to pushing a sphere/ellipsoid through a plane at a constant speed for the cone model.

Specifically, the ambient solar wind values for each quantity ϵ ρ, v_r, P are replaced by constant values ρ_{CME}, v_{CME}, P_{CME} for points at r=R_{inner} for which

$$(\theta - \theta_{\text{CME}})^2 + (\varphi - \varphi_{\text{CME}})^2 < \alpha(t)^2 (\text{ Cone model }) \tag{8.8}$$

and for the elliptical cone model:

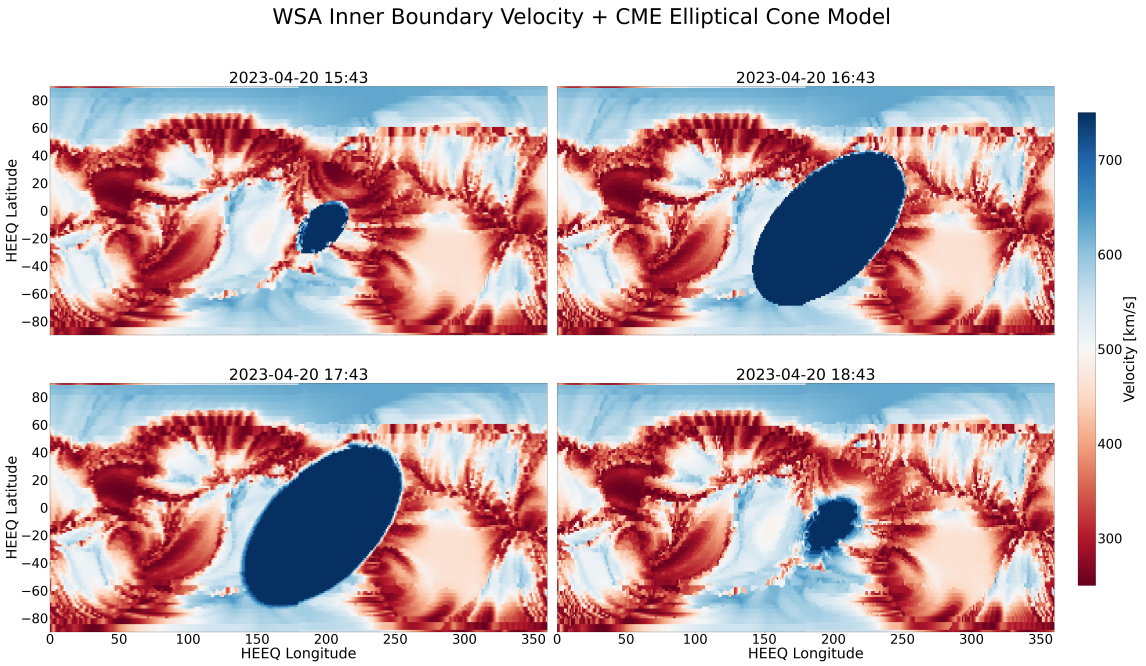

Figure 8.1: Insertion of the elliptical cone CME into the velocity profile at the inner boundary of the computational domain. The four panels show the evolution of the velocity profile at the inner boundary, with a 1-hour time step between each panel. The inserted elliptical CME expands and then gradually decays over time.

$$\frac{(\theta - \theta_{\mathrm{CME}})^2}{a^2} + \frac{(\varphi - \varphi_{\mathrm{CME}})^2}{b^2} < \alpha(t)^2 \tag{8.9}$$

where

$$\alpha(t) = \frac{\omega_{CME}}{2} * sin\left[\frac{\pi}{2}\left(t - t_{onset}\right)/t_{half}\right] \tag{8.10}$$

In the equation, θ_{CME} and ϕ_{CME} are the latitude and longitude of the CME, which are estimated using the GCS reconstruction. t_{onset} is the time when CME reaches R_{inner}, i.e., 0.1AU, and t_{half} is the activation/insertion time period determined by the time taken by the CME to cross the R_{inner}=0.1AU sphere. Since the projection of a CME is not spherical in shape in the $\theta - \phi$ plane, we used a cone model in an elliptical geometry by introducing different extensions of the CME in latitudinal and longitudinal directions, as given in Eq.8.9. It is also important to mention that, for the elliptical cone model, the 3D shape of the CME pushed at the inner boundary is an ellipsoid with a tilt angle with the solar equator, as shown in Figure 8.1. The resultant geometry is closer to the projection of the

most commonly used graduated cylindrical shell model of the CME in the $\theta - \phi$ plane.

8.2.1 HD Simulation of 21 April 2023 CME (CR2270)

To validate the setup of the PLUTO code and the elliptical cone model described in the Section 8.2, we simulated the CME that occurred on 21 April 2023, which is discussed in detail in Chapter 7. The associated halo CME was observed in the images taken by LASCO-C2 and C3 coronagraphs from 18:54 UT to 23:54 UT and also by the COR2 coronagraph between 18:54 UT and 20:08 UT. To derive its deprojected kinematics, we applied the 3D reconstruction using the GCS model for near-Sun observations.

We derived the inner boundary conditions of velocity for this CME from the WSA model, i.e., CR2270 (from 20 April 2023 to 17 May 2023), which is the CR during which this CME occurred. The boundary conditions for density and pressure are specified based on the velocity and derived from equations 8.4 and 8.5. We initially simulated the entire CR during which this CME erupted without including the CME. Once the solution reached a steady-state condition throughout the domain, we introduced the CME into the ambient medium. Using GCS reconstruction (Chapter 7), we estimated the time and velocity of CME when it arrived at the inner boundary of our simulation domain, i.e., at 21 $R_{\odot}$ (0.1 AU). This was done at 20:42 UT on 21 April when the height of the CME estimated from GCS reconstruction was approximately 21 $R_{\odot}$ (0.1 AU). We inserted the CME assuming an elliptical shape using the elliptical cone model with a speed of 1080 km/s in background solar wind at the inner boundaries defined by the WSA model. Input parameters of CME, i.e., CME speed and direction of propagation (latitude $=-17°$ and longitude $=20°$), are derived from GCS reconstruction, which defines the position of insertion (center of ellipsoid) in Figure 8.1. For simplicity, we assume $\rho_{CME} = 600/cc$ and a constant pressure of $\approx$ 10 nP ($\approx$ three times the ambient solar wind pressure). The outer radial boundary of the simulations was set at 1AU with an outflowing boundary.

Figure 8.2 and Figure 8.3 show the heliospheric profiles of the velocity and density,

respectively, in the HEEQ coordinate system at 18:43 UT on 23 April.

Figure 8.4 and Figure 8.5 show the velocity and density profiles obtained from the OMNI database (red dashed line) and the modeled profile (blue dashed line) at L1. We can see that the observed velocity and density profile match the simulated velocity profile using the PFSS+WSA+PLUTO setup. We notice that CME arrival is on time in the velocity profile, as shown by the enhancement in the velocity near the vertical blue line. Similarly, for the density profile in Figure 8.5. The CME cone model does not include the internal magnetic field configuration, which is crucial for assessing the geo-effectiveness of the CME, particularly in predicting the southward Bz component at Earth. Therefore, to model IMF parameters accurately, a model that captures the internal magnetic structure of CME is required.

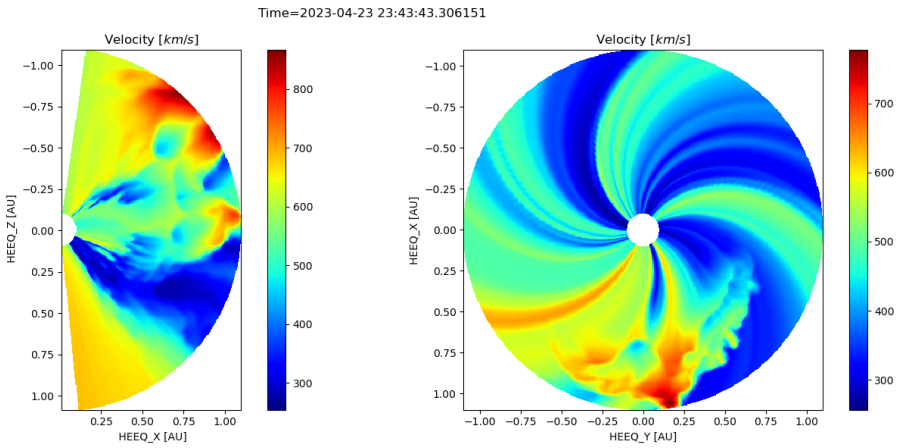

Figure 8.2: Velocity distribution in the heliosphere for 21 April 2023 CME using the elliptical cone model in the PLUTO HD simulation on 23 April 2023. The left and right panels show the velocity profile in the meridional and ecliptic planes, respectively. Note that the Z axis is inverted in the left plot.

The hydrodynamic implementation of the CME cone model provides a computationally efficient approach for validating the solar-wind background and CME kinematics in PLUTO MHD setup. Although magnetic effects are not included at this stage, this step establishes the foundation for it coupling with flux-rope models in the future, as discussed in the following sections. To overcome the limitations inherent in the hydrodynamic PLUTO+WSA+Cone framework, we complement it with the Flux Rope in 3D (FRi3D) model (Isavnin, 2016), which

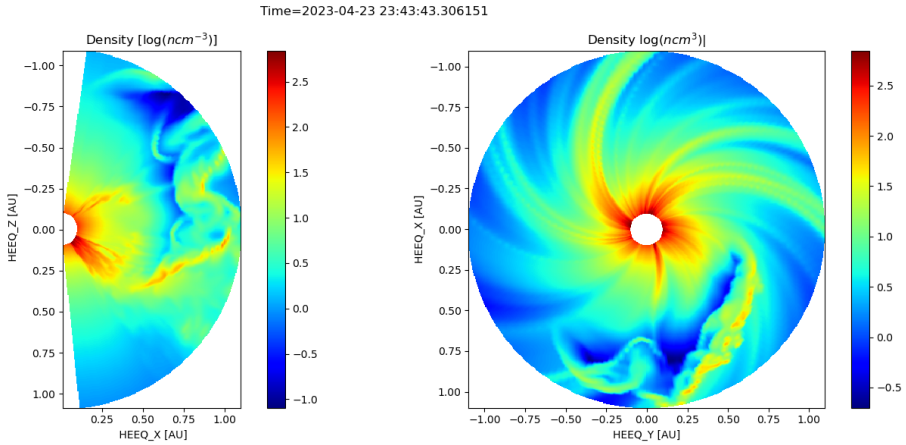

Figure 8.3: Logarithmic density distribution in the heliosphere for 21 April 2023 CME using elliptical cone model in PLUTO HD simulation on 23 April 2023. The left and right panels show the density profile in the meridional and ecliptic planes, respectively. Note that the Z axis is inverted in the left plot.

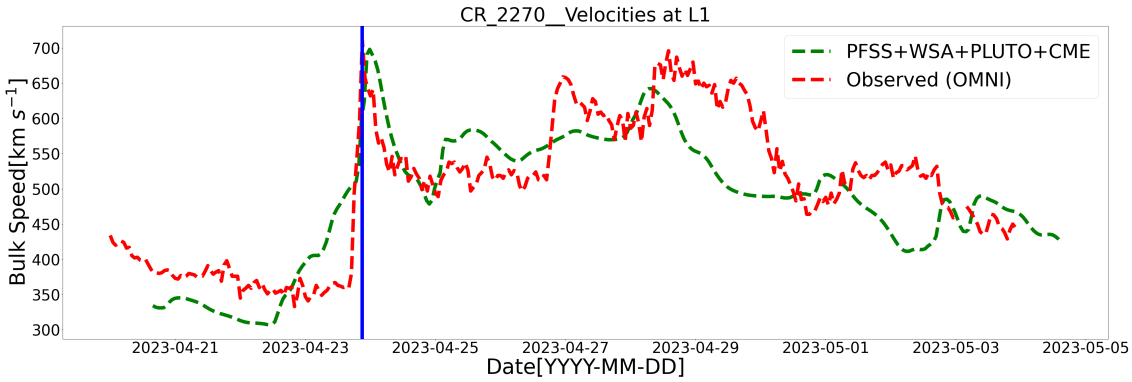

Figure 8.4: Observed solar wind velocity (red dashed line) obtained from OMNI database and modeled (blue dashed line) velocity at L1 for CR2270, with an elliptical cone model in PLUTO HD simulation for 21 April 2023 CME. The blue vertical line marks the arrival time of the CME shock.

incorporates the internal magnetic-field structure of CMEs. While FRi3D is implemented separately in this chapter, our eventual goal is to integrate such flux-rope models into the PLUTO-based MHD framework to achieve a comprehensive heliospheric CME simulations. In the next section, we describe the geometric implementation of the FRi3D model, which offers a self-consistent approach to first track a CME through the heliosphere and subsequently initialize it within the MHD domain using its geometrical and magnetic field description.

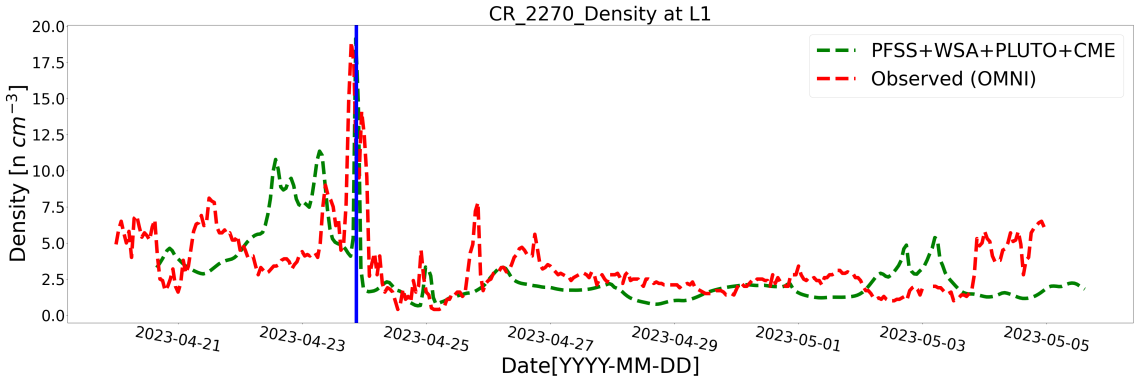

Figure 8.5: Observed (red dashed line) density obtained from OMNI database and modeled (green dashed line) density at L1 for CR2270, with an elliptical cone model in PLUTO HD simulation for 21 April 2023 CME. The blue vertical line marks the arrival time of the CME shock.

8.3 Magnetic Flux rope Modeling

Given the limitations of the cone model particularly its inability to describe the internal magnetic field structure of a CME we employ the Flux Rope in 3D (FRi3D) model (Isavnin, 2016) to track the CME through the heliosphere and study its dynamics. The geoeffectiveness of a CME is influenced by several key parameters, including the impact speed, the IMF component B_z, and the plasma density. Accurate prediction of these parameters is essential for reliable space weather forecasting. The FRi3D model is well-suited for this purpose, as it can be applied in a self-similar expansion framework to predict the IMF conditions at L1. Additionally, it can be used to insert a CME flux rope into an MHD simulation. The FRi3D model offers multiple capabilities:

1. It describes the geometry and internal magnetic structure of a CME close to the Sun, making it suitable for inserting a realistic flux rope into MHD models.
2. It can be used to track the CME from the corona through the heliosphere in the coronagraphic images, allowing for estimation of the propagation direction and analysis of its kinematics.
3. Assuming self-similar expansion of the CME, the model can be extended to predict the magnetic field components of the IMF at L1.

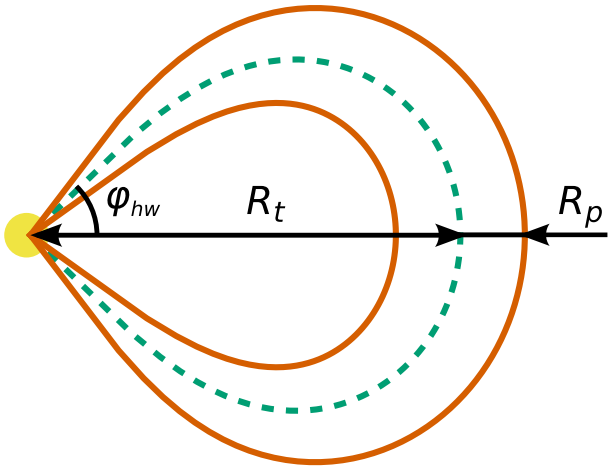

Figure 8.6: The geometrical shape of the CME flux rope according to the FRi3D model(Adapted from (Isavnin, 2016)).

In Sections 8.3.1 and 8.3.2, we provide a detailed description of the implementation of the geometrical and magnetic components of the FRi3D model. We validate our implementation of the FRi3D geometrical and magnetic field model on the CME that occurred on October 5 2012. This particular CME is extensively analyzed in Chapter 6, where we utilize both near-Sun CME tracking and in-situ IMF modeling at L1, applying the Marubashi flux rope model. This makes it an ideal case for validating our FRi3D model implementation.

8.3.1 FRi3D Model: Geometrical Implementation

First, we consider a simplified representation of CME as a bundle of magnetic field lines attached by both ends to the Sun. They form a croissant-like shape as shown in the Figure 8.7. Heliocentric distance to the apex (the furthest point) of the axis of the structure is its toroidal height R_t. This model further assumes the CME has a circular cross-section anywhere perpendicular to its axis. The radius of the cross-section varies proportionally to the heliocentric distance, with the largest in the apex of the structure (referred to as the poloidal height R_p) and tending to zero in the Sun as

$$R(\varphi) = \frac{D(\varphi)}{2} = \frac{R_p}{R_t} r(\varphi), \tag{8.11}$$

where $R(\varphi)$ and $D(\varphi)$ are the radius and diameter of the cross-section, and $r(\varphi)$ describes the axis of the structure in polar coordinates as:

$$r(\varphi) = R_t \cos^n(a\varphi). \tag{8.12}$$

Here, $a = (\pi/2)/\varphi_{hw}$, where φ_{hw} is the angular half-width between the legs of the axis of the structure. The 3D geometry of FRi3D model CME represents a loop structure attached to the Sun by both ends with axis given by Eq. 8.12 and circular cross-section diameter given by Eq. 8.11.

The overall geometry of the FRi3D model is characterized by 9 free parameters: toroidal height R_t, poloidal height R_p, angular half-width φ_{hw}, front flattening coefficient (FFC) n, pancaking angle θ_p, skewing angle φ_s, direction of propagation is defined by latitude θ and longitude φ, and tilt angle γ.

For the sake of simplicity, we implemented the above-mentioned geometrical structure without pancaking and skewing angles. We developed a graphical user interface to implement the FRi3D geometrical model on coronagraphic images obtained from COR2, C3, and HI1 instruments. This allowed us to track the CME and to estimate geometrical parameters, i.e., the direction of propagation and extension of the CME up to 80 $R_\odot$. These parameters can further be used as input in the MHD simulations and in magnetic field modeling of the CME flux rope in the heliosphere. It is important to note that in the geometrical implementation of the FRi3D model, we define a parameter as $n1 = R_p/R_t$ instead of two free values for R_t and R_p, and introduce a new parameter as $H_{apx} = R_t + R_p$. This implementation reduces the parameters from 9 to 7, which makes it simpler to track the CME dynamics beyond $10R_\odot$, where CME is expected to expand self-similarly without any deformation. Figure 8.7 shows a snapshot of the graphical user interface (GUI) developed for the FRi3D geometrical model.

We present a comparison of the implemented FRi3D geometrical model with the GCS reconstruction by applying both models to the coronagraphic images (STEREO-A & B/SECCHI-COR2 and SOHO/LASCO-C3) of the CME that occurred on 5 October 2012, as shown in Figure 8.8. Table 8.1 and Table 8.3 summarize and compare fitted parameters of the two models. By fitting, we found that the FRi3D parameter R_p/R_t and GCS parameter κ are related; both define

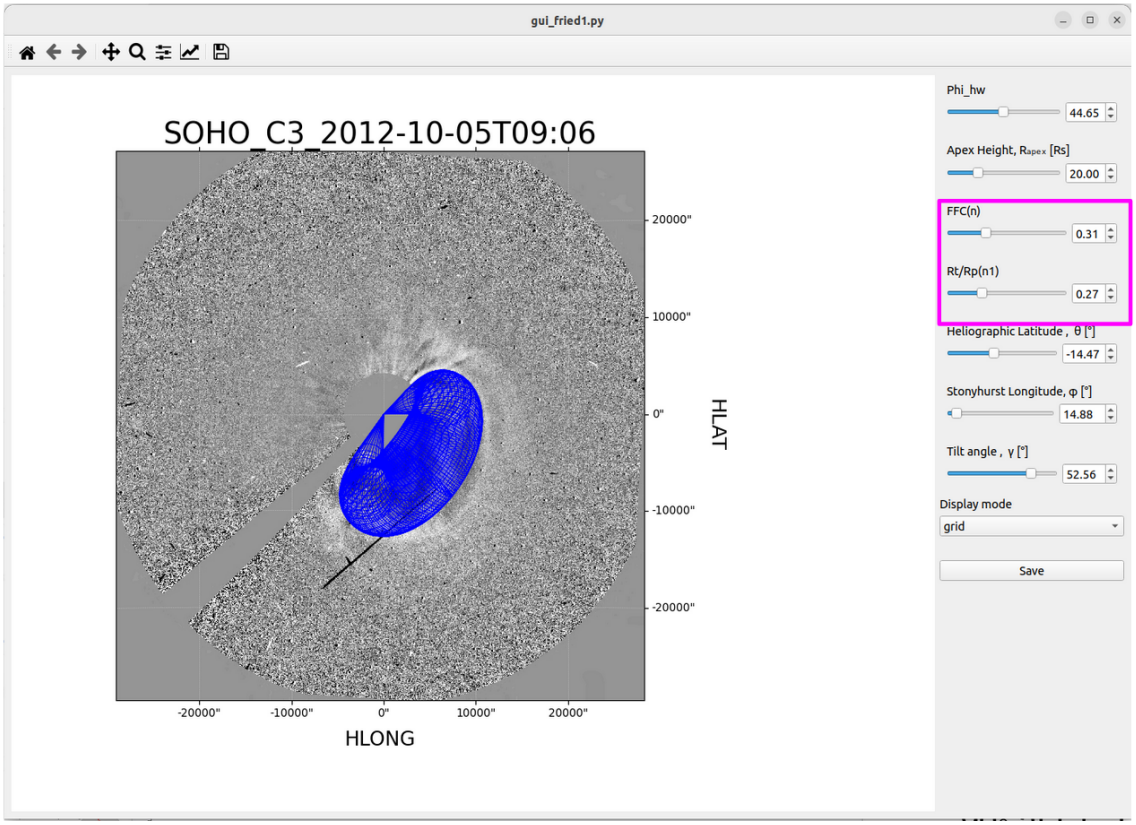

Figure 8.7: Graphical user interface for the geometric implementation of the Flux Rope in 3D (FRi3D) model. The magenta-colored box highlights additional parameters included in the FRi3D model that are not part of the GCS model. The flux rope shown in this figure corresponds to the CME observed on 5 October 2012.

the bulkiness of the flux rope. Moreover, it is essential to mention here that the FRi3D geometrical model is closer to the actual CME structure by introducing the curvature in the CME flux rope legs, unlike the GCS model, which assumes straight conical legs, as shown in Figure 8.8.

Table 8.1: Parameters of the GCS model fits for 5 October 2012 CME shown in Figure 8.8.

	θ (°)	φ (°)	κ	(°)	γ (°)	($R_\odot$)
GCS Parameters	-14	13	0.38	46	54	20

Using the geometrical shape of the CME flux rope implemented in this section, we can track the CME in the heliosphere. The inner morphology of a CME is typically described by a magnetic flux-rope structure. If we describe the magnetic field of the CME flux rope from the FRi3D model, we can also model the observed

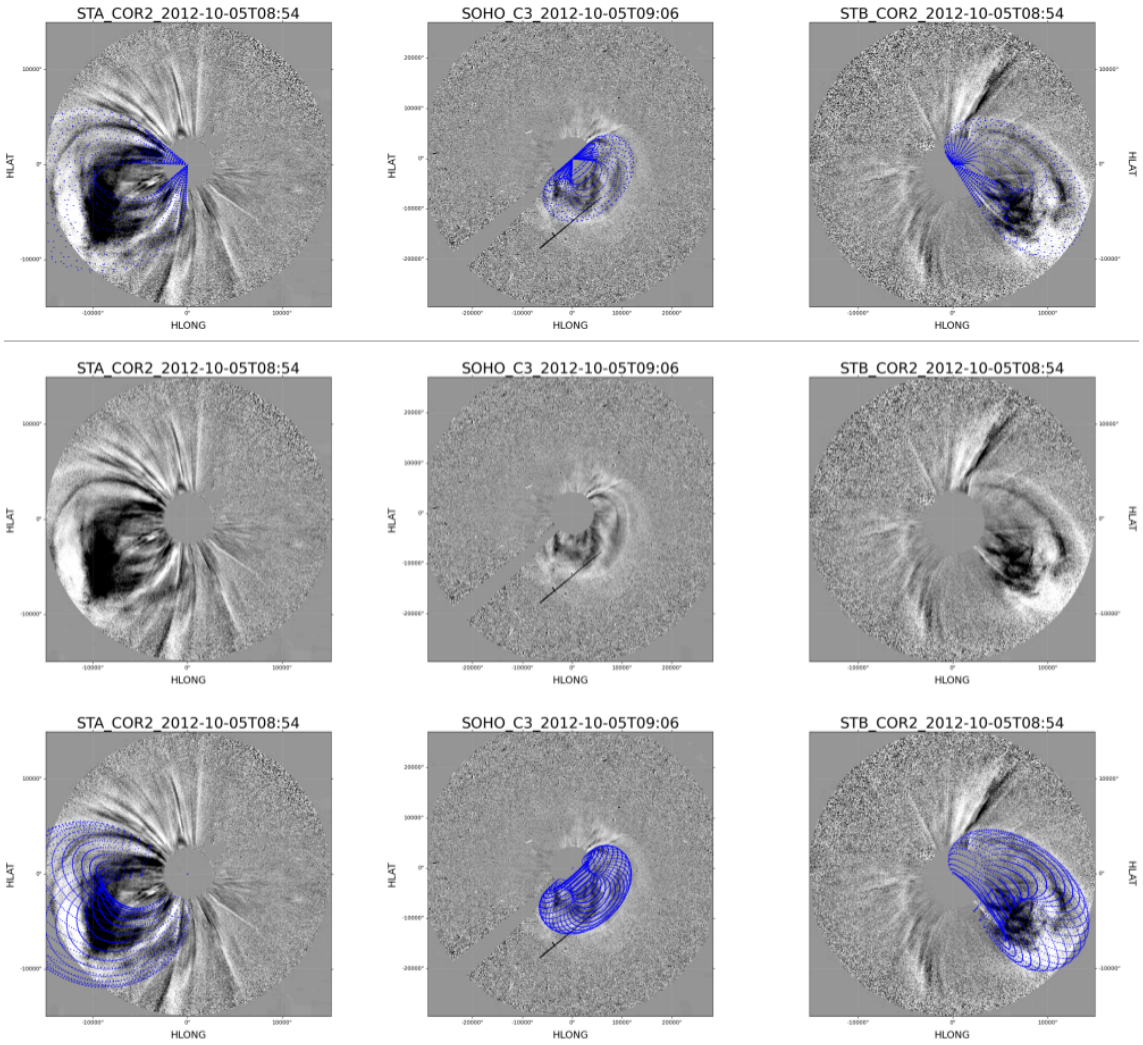

Figure 8.8: Comparison of the FRi3D geometric model with the GCS model for the 5 October 2012 CME. The top row shows the GCS model mesh overlaid on the observed CME structure. The middle row displays the CME structure without any model overlay. The bottom row shows the FRi3D model mesh overlaid on the CME. In each row, images from left to right correspond to observations from STEREO-A/SECCHI-COR2, SOHO/LASCO-C3, and STEREO-B/SECCHI-COR2, respectively.

in-situ parameters. This is discussed in the next section.

8.3.2 FRi3D Model: Magnetic Field Implementation

Classical magnetic flux-rope represents an idealised configuration of magnetic field characterised by the following properties: local cylindrical geometry; helical magnetic field lines with zero twist in the core and increasing to infinity close

to the edge of a flux-rope; maximum magnetic field strength along the axis of the flux-rope (Russell, 1999). Such a configuration is often estimated with the Lundquist model, which describes cylindrical magnetic geometry in a force-free field (Lundquist, 1950). However, recent studies of field line twist and length distributions within magnetic flux ropes in CMEs report inconsistencies with the Lundquist model. Hu et al. (2015) showed that in-situ measurements of interplanetary CMEs are consistent with a flux-rope structure with spiral field lines of constant and low twist. Following Isavnin (2016) we use the constant twist for the construction of the 3D configuration of magnetic field lines for the FRi3D model.

The FRi3D model considers a collection of parallel magnetic field lines contained in a cylinder of unit radius. The direction of the magnetic field is characterized by polarity equal to either $+1$ or -1, which corresponds to the east-west or west-east direction of the core magnetic field of a flux rope. The length of the cylinder is set to the length L of the axis of the CME shell:

$$L = \int_{-\varphi_{hw}}^{\varphi_{hw}} \left[r^2 + \left(\frac{dr}{d\varphi} \right)^2 \right]^{1/2} d\varphi. \tag{8.13}$$

The magnitude of the magnetic field is estimated using the distribution of the magnetic field from the Lundquist model. We can apply twisting deformation with a constant twist τ, tapering deformation according to Eq. 8.11 and bend the structure to the shape defined by Eq. 8.12. The direction of the twist is characterized by chirality that can be equal to $+1$ or -1, which corresponds to right- or left-handedness of a flux-rope, respectively.
The flux conservation is introduced by varying the axial field B_0 so that the total magnetic flux remains unchanged along the axis of the structure, i.e., B_0 is weakest in the apex and most vital in the footpoints.

As a validation of the implementation of the FRi3D magnetic model, we present the results of the observed and predicted IMF by FRi3D model values for the 5 October 2012 CME. On this CME, we have already performed the Marubashi fluxrope fitting at L1 (Chapter 6). Figure 8.9 shows the observed IMF from the ACE spacecraft (solid lines) along with the predicted/modeled values

Table 8.2: Parameters of the FRi3D model fits to coronagraphic image at height=20 $R_{\odot}$ and *in-situ* data at L1, for CME launched on 5 October 2012.

	θ	φ	$n1$	φ_{hw}	γ	n
Near Sun (FRi3D geometrical)	-14	14	0.30	46.0	54	0.30
at L1 (FRi3D magnetic field)	-4	4	0.15	50	95	0.25
$\tau = 1.6$, $\Phi = 3.0 \times 10^{12}$ Wb, $V_{apx} =$ 380 km/s						
Right-handed						

(dashed) obtained from the FRi3D model. We implemented the FRi3D model without pancaking and skewing, assuming a self-similar case of the expansion of CME.

The parameters for the FRi3D model, such as the direction of propagation, were derived from the fitting of the FRi3D mesh on the coronagraphic images near the Sun, i.e., the FRi3D geometrical model. We notice that the predicted IMF matches the observed IMF reasonably well. The input parameters of the FRi3D model for IMF prediction are given in the Table 8.3. These parameters are compared with the near Sun fitted parameters using FRi3D geometrical model.

It is important to emphasize that this approach allows for a direct comparison between the parameters of the geometrical model fitted near the Sun and those of the IMF model at L1. In contrast, our earlier method described in Chapter 6 was limited to comparing only the tilt angle of the CME flux rope at L1 (based on the Marubashi toroidal and cylindrical models), due to the use of different flux rope geometries at different locations, GCS reconstruction near the Sun and the Marubashi model at L1. The current approach is more consistent and logical, as it applies the same flux rope geometry (FRi3D) at both locations, enabling a more meaningful comparison.

From the comparison of the geometrical shape of the flux rope near the Sun (using FRi3D geometrical model) and geometrical parameters of the flux rope fitted on the IMF observations at L1 for the 5 October 2012 CME (using FRi3D magnetic field model), we draw the following conclusions:

Table 8.3: Parameters of the FRi3D geometrical model fits for 5 October 2012 CME shown in the Figure 8.8.

θ (°)	φ (°)	$n1$	φ_{hw} (°)	γ (°)	FFC (n)	Height ($R_\odot$)
-14	14	0.30	46	54.0	0.30	20

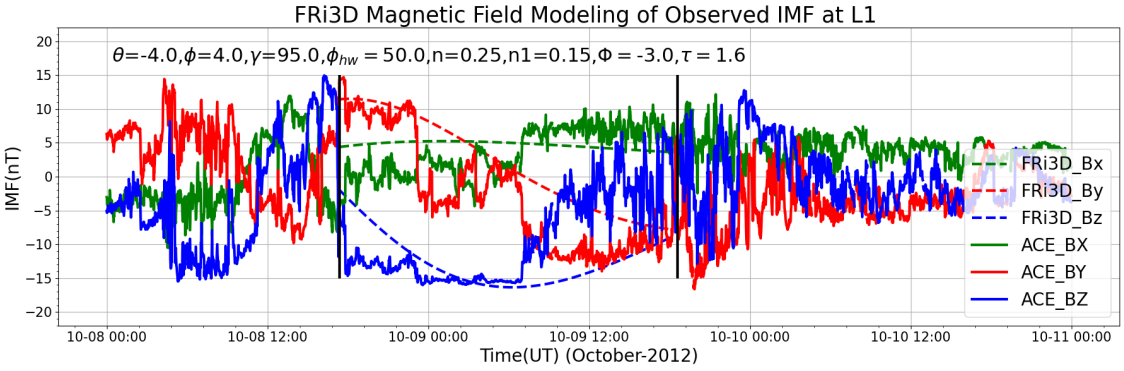

Figure 8.9: Comparison of the observed IMF vectors from ACE spacecraft (solid lines) and predicted IMF (dashed lines) from the FRi3D model for 5 October 2012 CME, at L1. Two vertical black lines mark the boundaries of MC.

1. The tilt of the CME flux rope increased significantly from 54° at 20 $R_\odot$ to approximately 95° at L1. This is in agreement with previous results using the GCS model in HI1 images and flux rope fitting using the Marubashi model at L1 (Chapter 6).

2. The R_p/R_t ratio decreased from 0.30 near the Sun to 0.15 at L1, indicating a reduction in flux rope cross-section. This may be due to magnetic cloud erosion or compression (Dasso et al., 2007; Pal et al., 2021).

3. The estimated CME latitude and longitude show an eastward and equatorward deflection from the Sun to L1.

8.4 Conclusion and Future Scope

In this chapter we demonstrated the various individual model implementations toward building a comprehensive CME–solar wind modeling framework. We first developed and validated a heliospheric modeling framework for solar wind that

incorporates an elliptical cone model for improved CME simulations. Further to model the internal magnetic field structure of the CME and its geometric shape, we successfully implemented the FRi3D magnetic field model along with its geometrical counterpart. We also validated the functionality of the FRi3D GUI, comparing its fitting performance with that of the established GCS GUI.

It is important to mention here that our ability to track the CME up to the HI1 FOV in FRi3D geometrical implementation makes it easier to simulate the CME within the heliospheric domain. Previous studies, such as Singh et al. (2023), tracked the CME only up to the COR2 FOV and then employed a simplistic drag-based model to estimate the CME insertion time at approximately 70 $R_{\odot}$, in the MHD domain. In contrast, our newly implemented framework uses the FRi3D geometrical model, allowing us to track the kinematics up to 80 $R_{\odot}$, and directly insert the CME at higher heights without relying on drag-based approximations.

Moreover, this approach enables us to consistently track the CME using the same geometrical shape that is used as the input for the magnetic field model in the heliospheric simulation. This marks a significant improvement over previous efforts, which involved tracking the CME using the GCS model but injecting it into the heliosphere using a different geometry, such as a cone or spheromak (Mayank et al., 2024; Singh et al., 2023).

By integrating the FRi3D model, including both of its geometrical (to track the CME in the heliosphere) and magnetic field components with near-Sun observations, we can insert a self-consistent CME at the inner boundary of the solar wind module (WSA+PLUTO+FRi3D). This integrated framework can enable more accurate predictions of the IMF at L1. Moreover, the FRi3D model provides us an excellent opportunity to compare the geometric parameters with the same geometrical assumptions near the Sun and at L1. This comparison provides us with more realistic results than comparing different models on remote sensing and in-situ observations, the GCS model on coronagraphic images, and the Marubashi flux rope fitting on in-situ data.

Future work will integrate these model implementations within a single MHD

framework, thereby advancing toward a unified CME propagation and geoeffectiveness prediction model.

Chapter 9

Summary and Future Scope

9.1 Summary

The thesis explores the complex interactions between coronal mass ejections and the ambient solar wind as they propagate through the heliosphere. The research work carried out is structured into two main parts:

In the first part, we focused on the ambient solar wind modeling and optimization. We developed two solar wind forecasting models—

Model1 (PFSS+WSA+HUX) and Model2 (PFSS+SCS+WSA+HUX)— and evaluated their performance over 60 Carrington Rotations spanning SC23 declining and minimum phase and the early ascending phase of SC24. We found that the performance of the framework is significantly improved compared to the previous study by Riley et al. (2015). This study was carried out using standard GONG maps and a conventional value of the source surface height, i.e., 2.5 $R_{\odot}$. However, both models performed poorly during the deep solar minimum of SC23, primarily due to the reduced area of low- and mid-latitude coronal holes, which are key sources of high-speed solar wind. As solar activity increased in the ascending phase of SC24, model performance improved. We suggest using different heights of the source surface or different types of magnetograms as input, which can improve the performance of the framework.

We further examined the impact of varying the source surface height ($R_{\rm ss}$) and the type of input magnetograms on the accuracy of solar wind velocity predictions

at L1 using the PFSS+WSA+HUX modeling framework. By analyzing 16 CRs across different phases of SC24 and SC25, we demonstrate that increasing R_{ss} to 3.0 $R_{\odot}$ significantly improves the correlation between modeled and observed solar wind velocities during solar minimum. Similar results were found when we extended the study from CR2093-CR2272. Additionally, our study highlights the superiority of zero-point corrected maps from GONG over standard GONG synoptic maps, with ZPC maps achieving higher correlation values and better capturing the global magnetic structure when validated against PROBA2/SWAP EUV observations. The findings underscore the importance of dynamic adjustment of R_{ss} with solar cycle phase and advocate for the operational adoption of ZPC maps in solar wind forecasting frameworks. We further extended the analysis with a more refined choice of R_{ss}, using ZPC maps over the entire SC24 and SC25 (CR2093-CR2272). We found similar results from this long-term study. However, a detailed analysis is required with better performance metrics, e.g., Dynamic time warping, to make the conclusions clear.

In the second part, we investigated the role of solar wind interaction in heliospheric propagation of CMEs. We studied Earth-impacting CMEs from 2010 to 2018 observed by STEREO and SOHO spacecraft. We found that roughly half the events follow self-similar expansion, while the rest show deflection or rotation. We found faster CMEs ($\geq$850 km/s) deflected eastward due to interaction with the slow solar wind ahead. Latitudinal deflections toward the heliospheric current sheet in some cases due to the interaction with the ambient magnetic field. We investigated the two rotating CMEs (5 October 2012 and 23 May 2017) using GCS and flux rope models in detail. We attributed the observed rotation to Lorentz forces and solar wind interaction. We found that for the persistence rotation of a CME, specific magnetic field and solar wind conditions of the ambient medium are needed.

As the CME propagation characteristics impact their arrival time prediction at Earth, we analysed the propagation characteristics of a major geoeffective CME on 21 April 2023, which caused a major geomagnetic storm (Dst = -213 nT). We used 3D reconstructions and the Advanced Drag-Based Model (ADBM) to

estimate arrival time. This study highlighted the importance of multi-viewpoint imaging for accurate arrival predictions. It further highlights the role of using multiple models to reduce errors in the direction of propagation of the CME. We further developed and validated a heliospheric modeling framework for solar wind and CME, which incorporates an elliptical cone model for improved CME simulations. Further to model the internal magnetic field structure of the CME and its geometric shape, we successfully implemented the FRi3D model along with its geometrical counterpart.

We also validated the functionality of the FRi3D GUI, comparing its fitting performance with that of the established GCS GUI. A comparative analysis of the flux rope geometry near the Sun and at L1 for the 5 October 2012 CME, using the FRi3D geometrical and magnetic field models, reveals that the flux rope exhibited a significant increase in tilt angle, from near the Sun to L1. It is found to be consistent with our previous findings based on GCS and Marubashi flux rope fitting models (Chapter 6). Additionally, the ratio of poloidal to toroidal radii (R_p/R_t) decreased from 0.30 to 0.15 as the CME propagated in the heliosphere, suggesting a potentially compressed or eroded cross-sectional structure of the magnetic cloud (Pal et al., 2021), potentially attributable to interactions with the solar wind and requiring further refinement in modeling through effects like pancaking. The flux rope also underwent an eastward and equatorward deflection during its heliospheric propagation.

9.2 Future Scope

The first half of the thesis, which is dedicated to improving solar wind velocity forecasting models, has scope for improvement in two key areas. Firstly, the PFSS extrapolation methods used in this thesis employ a uniform $\cos\theta$ grid, which is less accurate than uniform θ grid approaches (Tóth et al., 2005). To improve model performance during deep solar minimum, better polar magnetic field data or alternative extrapolation techniques are recommended (Tóth et al., 2005). Additionally, the HUX model was used for simplicity; its advanced version, HUXt (Barnard and Owens, 2022), includes time-dependent acceleration and may

yield improved results. Further, the optimization approach for the WSA model adopted in our methodology, relying solely on the Pearson coefficient, has its own drawbacks as it disregards other metrics and does not account for overall features. Therefore, advanced metrics, e.g., Dynamic Time warping (Samara et al., 2022) or a combination of metrics, can be used to obtain more robust and conclusive results.

Our study of the heliospheric propagation of the CMEs indicates that the solar wind medium plays a crucial role in the dynamics of the CMEs in the heliosphere. Based on the analysis of Earth-impacting geoeffective CMEs, we reported that CME rotation in the heliosphere is rare. Multi-in-situ and multi-spacecraft measurements studies are required for CMEs, with larger data sets, to further establish and understand the rotations of the CMEs in the heliosphere.

Understanding the conditions that lead to CME rotation in the heliosphere is also crucial. Sachdeva et al. (2017) found that slower CMEs experience Lorentz force dominance up to greater distances, which is a key factor contributing to CME rotation. Interestingly, two cases of CME rotation found in our study were also moderate to slow-speed CMEs, for which the Lorentz force was a common factor for their rotation. It is therefore important to understand the heliospheric regime where Lorentz forces dominate over the drag force. This can be addressed by extending the models (WSA+PLUTO (MHD)) discussed in Chapter 8. In particular, integrating the FRi3D model into full MHD simulations of the ambient solar wind offers a promising approach to better understand CME propagation in the heliosphere.

Bibliography

Alfven, H., 1977. Electric currents in cosmic plasma. Reviews of Geophysics and Space Physics 15, 271–284. doi:10.1029/RG015i003p00271.

Alissandrakis, C.E., 1981. On the computation of constant alpha force-free magnetic field. Astronomy and Astrophysics 100, 197–200.

Antiochos, S.K., DeVore, C.R., Klimchuk, J.A., 1999. A model for solar coronal mass ejections. The Astrophysical Journal 510, 485. URL: https://dx.doi.org/10.1086/306563, doi:10.1086/306563.

Arden, W.M., Norton, A.A., Sun, X., 2014. A "breathing" source surface for cycles 23 and 24. Journal of Geophysical Research: Space Physics 119, 1476–1485. URL: https://agupubs.onlinelibrary.wiley.com/doi/abs/10.1002/2013JA019464, doi:https://doi.org/10.1002/2013JA019464, arXiv:https://agupubs.onlinelibrary.wiley.com/doi/pdf/10.1002/2013JA019464.

Arge, C.N., Odstrcil, D., Pizzo, V.J., Mayer, L.R., 2003. Improved Method for Specifying Solar Wind Speed Near the Sun, in: Velli, M., Bruno, R., Malara, F., Bucci, B. (Eds.), Solar Wind Ten, pp. 190–193. doi:10.1063/1.1618574.

Arge, C.N., Pizzo, V.J., 2000. Improvement in the prediction of solar wind conditions using near-real time solar magnetic field updates. Journal of Geophysical Research 105, 10465–10480. doi:10.1029/1999JA000262.

Badman, S.T., Bale, S.D., Martínez Oliveros, J.C., Panasenco, O., Velli, M., Stansby, D., Buitrago-Casas, J.C., Réville, V., Bonnell, J.W., Case, A.W., Dudok de Wit, T., Goetz, K., Harvey, P.R., Kasper, J.C., Korreck, K.E., Larson, D.E., Livi, R., MacDowall, R.J., Malaspina, D.M., Pulupa, M., Stevens,

M.L., Whittlesey, P.L., 2020. Magnetic Connectivity of the Ecliptic Plane within 0.5 au: Potential Field Source Surface Modeling of the First Parker Solar Probe Encounter. The Astrophysical Journal Supplement Series 246, 23. doi:10.3847/1538-4365/ab4da7, arXiv:1912.02244.

Barnard, L., Owens, M., 2022. HUXt—An open source, computationally efficient reduced-physics solar wind model, written in Python. Frontiers in Physics 10, 1005621. doi:10.3389/fphy.2022.1005621, arXiv:2210.00455.

Baruah, Y., Roy, S., Sinha, S., Palmerio, E., Pal, S., Oliveira, D.M., Nandy, D., 2024. The Loss of Starlink Satellites in February 2022: How Moderate Geomagnetic Storms Can Adversely Affect Assets in Low-Earth Orbit. Space Weather 22, e2023SW003716. doi:10.1029/2023SW003716.

Benkhoff, J., Murakami, G., Baumjohann, W., Besse, S., Bunce, E., Casale, M., Cremonese, G., Glassmeier, K.H., Hayakawa, H., Heyner, D., Hiesinger, H., Huovelin, J., Hussmann, H., Iafolla, V., Iess, L., Kasaba, Y., Kobayashi, M., Milillo, A., Mitrofanov, I.G., Montagnon, E., Novara, M., Orsini, S., Quemerais, E., Reininghaus, U., Saito, Y., Santoli, F., Stramaccioni, D., Sutherland, O., Thomas, N., Yoshikawa, I., Zender, J., 2021. BepiColombo - Mission Overview and Science Goals. Space Sci. Rev. 217, 90. doi:10.1007/s11214-021-00861-4.

Berghmans, D., Hochedez, J., Defise, J., Lecat, J., Nicula, B., Slemzin, V., Lawrence, G., Katsyiannis, A., der Linden, R.V., Zhukov, A., Clette, F., Rochus, P., Mazy, E., Thibert, T., Nicolosi, P., Pelizzo, M.G., Schühle, U., 2006. Swap onboard proba 2, a new euv imager for solar monitoring. Advances in Space Research 38, 1807–1811. URL: https://www.sciencedirect.com/science/article/pii/S0273117705003327, doi:https://doi.org/10.1016/j.asr.2005.03.070. magnetospheric dynamics and the international living with a star program.

Bittencourt, J.A., 2004. Fundamentals of Plasma Physics. Springer Book Archive. 3 ed., Springer, New York, NY. URL: https://doi.org/10.

1007/978-1-4757-4030-1, doi:10.1007/978-1-4757-4030-1. springer Book Archive, Springer Science+Business Media.

Brueckner, G.E., Howard, R.A., Koomen, M.J., Korendyke, C.M., Michels, D.J., Moses, J.D., Socker, D.G., Dere, K.P., Lamy, P.L., Llebaria, A., Bout, M.V., Schwenn, R., Simnett, G.M., Bedford, D.K., Eyles, C.J., 1995. The Large Angle Spectroscopic Coronagraph (LASCO). Sol. Phys. 162, 357–402. doi:10.1007/BF00733434.

Burlaga, L.F., 1995. Interplanetary magnetohydrodynamics. International Series in Astronomy and Astrophysics doi:10.1093/oso/9780195084726.001.0001.

Cargill, P.J., 2004. On the Aerodynamic Drag Force Acting on Interplanetary Coronal Mass Ejections. Sol. Phys. 221, 135–149. doi:10.1023/B:SOLA.0000033366.10725.a2.

Chen, J., 1989. Effects of Toroidal Forces in Current Loops Embedded in a Background Plasma. ApJ 338, 453. doi:10.1086/167211.

Choudhuri, A.R., 1998. The Physics of Fluids and Plasmas: An Introduction for Astrophysicists. Cambridge University Press.

Cid, C., Palacios, J., Saiz, E., Guerrero, A., Cerrato, Y., 2014. On extreme geomagnetic storms. Journal of Space Weather and Space Climate 4, A28. doi:10.1051/swsc/2014026.

Colaninno, R.C., 2012. Investigation of the Forces that Govern the Three-Dimensional Propagation and Expansion of Coronal Mass Ejections from Sun to Earth. Ph.D. thesis. George Mason University, Virginia.

Cranmer, S.R., 2009. Coronal Holes. Living Reviews in Solar Physics 6, 3. doi:10.12942/lrsp-2009-3, arXiv:0909.2847.

Cremades, Bothmer, 2004. On the three-dimensional configuration of coronal mass ejections. A&A 422, 307–322. URL: https://doi.org/10.1051/0004-6361:20035776, doi:10.1051/0004-6361:20035776.

Dagnew, F.K., Gopalswamy, N., Tessema, S.B., Akiyama, S., Yashiro, S., 2022. Effect of the heliospheric state on cme evolution. The Astrophysical Journal 936, 122.

Dasso, S., Nakwacki, M.S., Démoulin, P., Mandrini, C.H., 2007. Progressive Transformation of a Flux Rope to an ICME. Comparative Analysis Using the Direct and Fitted Expansion Methods. Sol. Phys. 244, 115–137. doi:10.1007/s11207-007-9034-2, arXiv:0706.2889.

Domingo, V., Fleck, B., Poland, A.I., 1995. The SOHO Mission: an Overview. Sol. Phys. 162, 1–37. doi:10.1007/BF00733425.

Dungey, J.W., 1961. Interplanetary Magnetic Field and the Auroral Zones. Phys. Rev. Lett. 6, 47–48. doi:10.1103/PhysRevLett.6.47.

Echer, E., Gonzalez, W.D., Tsurutani, B.T., Gonzalez, A.L.C., 2008. Interplanetary conditions causing intense geomagnetic storms (Dst ¡= -100 nT) during solar cycle 23 (1996-2006). Journal of Geophysical Research (Space Physics) 113, A05221. doi:10.1029/2007JA012744.

Eyles, C.J., Harrison, R.A., Davis, C.J., Waltham, N.R., Shaughnessy, B.M., Mapson-Menard, H.C.A., Bewsher, D., Crothers, S.R., Davies, J.A., Simnett, G.M., Howard, R.A., Moses, J.D., Newmark, J.S., Socker, D.G., Halain, J.P., Defise, J.M., Mazy, E., Rochus, P., 2009. The Heliospheric Imagers Onboard the STEREO Mission. Sol. Phys. 254, 387–445. doi:10.1007/s11207-008-9299-0.

Fan, Y., 2005. Coronal Mass Ejections as Loss of Confinement of Kinked Magnetic Flux Ropes. ApJ 630, 543–551. doi:10.1086/431733.

Filippov, B.P., Gopalswamy, N., Lozhechkin, A.V., 2001. Non-radial motion of eruptive filaments. Sol. Phys. 203, 119–130. doi:10.1023/A:1012754329767.

Fisk, L.A., 2003. Acceleration of the solar wind as a result of the reconnection of open magnetic flux with coronal loops. Journal of Geophysical Research (Space Physics) 108, 1157. doi:10.1029/2002JA009284.

Forstner, J.L., 2024. Gcs in python. URL: https://doi.org/10.5281/zenodo.12668802, doi:10.5281/zenodo.12668802.

von Forstner, J.L.F., 2021. johan12345/gcs_python: Release 0.2.2. URL: https://doi.org/10.5281/zenodo.5084818, doi:10.5281/zenodo.5084818.

Foukal, D.P.V., 2004. Radiative Transfer in the Sun's Atmosphere. John Wiley and Sons, Ltd. chapter 2. pp. 35–63. URL: https://onlinelibrary.wiley.com/doi/abs/10.1002/9783527602551.ch2, doi:https://doi.org/10.1002/9783527602551.ch2, arXiv:https://onlinelibrary.wiley.com/doi/pdf/10.1002/9783527602551.ch2.

Fox, N.J., Velli, M.C., Bale, S.D., Decker, R., Driesman, A., Howard, R.A., Kasper, J.C., Kinnison, J., Kusterer, M., Lario, D., Lockwood, M.K., McComas, D.J., Raouafi, N.E., Szabo, A., 2016. The Solar Probe Plus Mission: Humanity's First Visit to Our Star. Space Science Reviews 204, 7–48. doi:10.1007/s11214-015-0211-6.

Geiss, J., Gloeckler, G., von Steiger, R., 1995. Origin of the Solar Wind From Composition Data. Space Sci. Rev. 72, 49–60. doi:10.1007/BF00768753.

Ghag, K., Raghav, A., Bhaskar, A., Soni, S.L., Sathe, B., Shaikh, Z., Dhamane, O., Tari, P., 2024. Quasi-planar ICME sheath: A cause of the first two-step extreme geomagnetic storm of the 25th solar cycle observed on 23 April 2023. Advances in Space Research 73, 6288–6297. doi:10.1016/j.asr.2024.03.011, arXiv:2305.05381.

Gonzalez, W.D., Mozer, F.S., 1974. A quantitative model for the potential resulting from reconnection with an arbitrary interplanetary magnetic field. Journal of Geophysical Research (1896-1977) 79, 4186–4194. URL: https://agupubs.onlinelibrary.wiley.com/doi/abs/10.1029/JA079i028p04186, doi:https://doi.org/10.1029/JA079i028p04186, arXiv:https://agupubs.onlinelibrary.wiley.com/doi/pdf/10.1029/JA079i028p04186

Gonzalez, W.D., Tsurutani, B.T., Clúa de Gonzalez, A.L., 1999. Interplanetary

origin of geomagnetic storms. Space Sci. Rev. 88, 529–562. doi:10.1023/A:1005160129098.

Gopalswamy, N., Akiyama, S., Yashiro, S., Makela, P., Xie, H., 2024. Intense Geomagnetic Storms during Solar Cycles 23-25. arXiv e-prints , arXiv:2401.03524doi:10.48550/arXiv.2401.03524, arXiv:2401.03524.

Gopalswamy, N., Akiyama, S., Yashiro, S., Michalek, G., Lepping, R.P., 2008. Solar sources and geospace consequences of interplanetary magnetic clouds observed during solar cycle 23. Journal of Atmospheric and Solar-Terrestrial Physics 70, 245–253. doi:10.1016/j.jastp.2007.08.070.

Gopalswamy, N., Lara, A., Lepping, R.P., Kaiser, M.L., Berdichevsky, D., St. Cyr, O.C., 2000. Interplanetary acceleration of coronal mass ejections. Geophysical Research Letters 27, 145–148. URL: https://agupubs.onlinelibrary.wiley.com/doi/abs/10.1029/1999GL003639, doi:https://doi.org/10.1029/1999GL003639, arXiv:https://agupubs.onlinelibrary.wiley.com/doi/pdf/10.1029/1999GL003639.

Gopalswamy, N., Lara, A., Manoharan, P.K., Howard, R.A., 2005. An empirical model to predict the 1-AU arrival of interplanetary shocks. Advances in Space Research 36, 2289–2294. doi:10.1016/j.asr.2004.07.014.

Gopalswamy, N., Mäkelä, P., Xie, H., Akiyama, S., Yashiro, S., 2009. CME interactions with coronal holes and their interplanetary consequences. Journal of Geophysical Research (Space Physics) 114, A00A22. doi:10.1029/2008JA013686.

Gopalswamy, N., Makela, P., Xie, H., Yashiro, S., 2009. Cme interactions with coronal holes and their interplanetary consequences. Journal of Geophysical Research 114. doi:10.1029/2008JA013686.

Gopalswamy, N., Mäkelä, P., Xie, H., Yashiro, S., 2013. Testing the empirical shock arrival model using quadrature observations. Space Weather 11, 661–669. URL: https://agupubs.onlinelibrary.wiley.com/doi/

abs/10.1002/2013SW000945, doi:https://doi.org/10.1002/2013SW000945, arXiv:https://agupubs.onlinelibrary.wiley.com/doi/pdf/10.1002/2013SW000945.

Gopalswamy, N., Thompson, B.J., 2000. Early life of coronal mass ejections. Journal of Atmospheric and Solar-Terrestrial Physics 62, 1457–1469. doi:10.1016/S1364-6826(00)00079-1.

Gopalswamy, N., Xie, H., Akiyama, S., Mäkelä, P., Yashiro, S., Michalek, G., 2015. The Peculiar Behavior of Halo Coronal Mass Ejections in Solar Cycle 24. ApJ 804, L23. doi:10.1088/2041-8205/804/1/L23, arXiv:1504.01797.

Gopalswamy, N., Yashiro, S., Akiyama, S., Xie, H., Mäkelä, P., Fok, M.C., Ferradas, C.P., 2022. What Is Unusual About the Third Largest Geomagnetic Storm of Solar Cycle 24? Journal of Geophysical Research (Space Physics) 127, e30404. doi:10.1029/2022JA030404, arXiv:2207.11630.

Gopalswamy, N., Yashiro, S., Kaiser, M.L., Howard, R.A., Bougeret, J.L., 2001. Characteristics of coronal mass ejections associated with long-wavelength type II radio bursts. J. Geophys. Res. 106, 29219–29230. doi:10.1029/2001JA000234.

Gopalswamy, N., Yashiro, S., Michalek, G., Stenborg, G., Vourlidas, A., Freeland, S., Howard, R., 2009. The SOHO/LASCO CME Catalog. Earth Moon and Planets 104, 295–313. doi:10.1007/s11038-008-9282-7.

Gosling, J.T., Bame, S.J., McComas, D.J., Phillips, J.L., 1990. Coronal mass ejections and large geomagnetic storms. Geophys. Res. Lett. 17, 901–904. doi:10.1029/GL017i007p00901.

Gosling, J.T., Thomsen, M.F., Bame, S.J., Zwickl, R.D., 1987. The eastward deflection of fast coronal mass ejecta in interplanetary space. J. Geophys. Res. 92, 12399–12406. doi:10.1029/JA092iA11p12399.

Grimes, E.W., Hatzigeorgiu, N., Lewis, J.W., Russell, C., McTiernan, J.M., Drozdov, A., Angelopoulos, V., 2024. pySPEDAS: Python-based Space Physics En-

vironment Data Analysis Software. Astrophysics Source Code Library, record ascl:2405.005.

Gui, B., Shen, C., Wang, Y., Ye, P., Liu, J., Wang, S., Zhao, X., 2011. Quantitative analysis of cme deflections in the corona. Solar Physics - SOL PHYS 271. doi:10.1007/s11207-011-9791-9.

Guo, J.H., Linan, L., Poedts, S., Guo, Y., Lani, A., Schmieder, B., Brchnelova, M., Perri, B., Baratashvili, T., Ni, Y.W., Chen, P.F., 2024. Modeling the propagation of coronal mass ejections with COCONUT: Implementation of the regularized Biot-Savart law flux rope model. A&A 683, A54. doi:10.1051/0004-6361/202347634, arXiv:2311.13432.

Halain, J.P., Berghmans, D., Seaton, D.B., Nicula, B., De Groof, A., Mierla, M., Mazzoli, A., Defise, J.M., Rochus, P., 2013. The SWAP EUV Imaging Telescope. Part II: In-flight Performance and Calibration. Solar Physics 286, 67–91. doi:10.1007/s11207-012-0183-6, arXiv:1210.3551.

Hamada, A., Asikainen, T., Mursula, K., 2019. New homogeneous dataset of solar euv synoptic maps from soho/eit and sdo/aia. Solar Physics 295. doi:10.1007/s11207-019-1563-y.

Harten, R., Clark, K., 1995. The Design Features of the GGS Wind and Polar Spacecraft. Space Sci. Rev. 71, 23–40. doi:10.1007/BF00751324.

Harvey, J.W., Hill, F., Hubbard, R.P., Kennedy, J.R., Leibacher, J.W., Pintar, J.A., Gilman, P.A., Noyes, R.W., Title, A.M., Toomre, J., Ulrich, R.K., Bhatnagar, A., Kennewell, J.A., Marquette, W., Patron, J., Saa, O., Yasukawa, E., 1996. The Global Oscillation Network Group (GONG) Project. Science 272, 1284–1286. doi:10.1126/science.272.5266.1284.

He, H., Wang, H., Yan, Y., 2011. Nonlinear force-free field extrapolation of the coronal magnetic field using the data obtained by the hinode satellite. Journal of Geophysical Research: Space Physics 116. URL: https://agupubs.onlinelibrary.wiley.com/doi/abs/

10.1029/2010JA015610, doi:https://doi.org/10.1029/2010JA015610, arXiv:https://agupubs.onlinelibrary.wiley.com/doi/pdf/10.1029/2010JA015610.

He, W., Liu, Y.D., Hu, H., Wang, R., Zhao, X., 2018. A stealth cme bracketed between slow and fast wind producing unexpected geoeffectiveness. The Astrophysical Journal 860, 78. URL: https://dx.doi.org/10.3847/1538-4357/aac381, doi:10.3847/1538-4357/aac381.

Hill, F., 2018. The global oscillation network group facility—an example of research to operations in space weather. Space Weather 16, 1488–1497. URL: https://agupubs.onlinelibrary.wiley.com/doi/abs/10.1029/2018SW002001, doi:https://doi.org/10.1029/2018SW002001, arXiv:https://agupubs.onlinelibrary.wiley.com/doi/pdf/10.1029/2018SW002001.

Hoeksema, T., Benevolenskaya, E., Liu, Y., Scherrer, P., Zhao, X., 2006. The sun's polar magnetic flux from 1996-2006 observed with soho/mdi .

van der Holst, B., Sokolov, I.V., Meng, X., Jin, M., Manchester, IV, W.B., Tóth, G., Gombosi, T.I., 2014. Alfvén wave solar model (awsom): Coronal heating. The Astrophysical Journal 782, 81. doi:10.1088/0004-637X/782/2/81.

Howard, R.A., Moses, J.D., Vourlidas, A., Newmark, J.S., Socker, D.G., Plunkett, S.P., Korendyke, C.M., Cook, J.W., Hurley, A., Davila, J.M., Thompson, W.T., St Cyr, O.C., Mentzell, E., Mehalick, K., Lemen, J.R., Wuelser, J.P., Duncan, D.W., Tarbell, T.D., Wolfson, C.J., Moore, A., Harrison, R.A., Waltham, N.R., Lang, J., Davis, C.J., Eyles, C.J., Mapson-Menard, H., Simnett, G.M., Halain, J.P., Defise, J.M., Mazy, E., Rochus, P., Mercier, R., Ravet, M.F., Delmotte, F., Auchere, F., Delaboudiniere, J.P., Bothmer, V., Deutsch, W., Wang, D., Rich, N., Cooper, S., Stephens, V., Maahs, G., Baugh, R., McMullin, D., Carter, T., 2008. Sun Earth Connection Coronal and Heliospheric Investigation (SECCHI). Space Sci. Rev. 136, 67–115. doi:10.1007/s11214-008-9341-4.

Howard, T., 2011. Coronal Mass Ejections: An Introduction. volume 376. Springer. doi:10.1007/978-1-4419-8789-1.

Hu, Q., Qiu, J., Krucker, S., 2015. Magnetic field line lengths inside interplanetary magnetic flux ropes. Journal of Geophysical Research: Space Physics 120, 5266–5283. URL: https://agupubs.onlinelibrary.wiley.com/doi/abs/10.1002/2015JA021133, doi:https://doi.org/10.1002/2015JA021133, arXiv:https://agupubs.onlinelibrary.wiley.com/doi/pdf/10.1002/2015JA021133.

Huang, Z., Tóth, G., Huang, J., Sachdeva, N., van der Holst, B., Manchester, W.B., 2024. Adjusting the Potential Field Source Surface Height Based on Magnetohydrodynamic Simulations. The Astrophysical Journal Letters 965, L1. doi:10.3847/2041-8213/ad3547, arXiv:2403.01712.

Inhester, B., 2006. Stereoscopy basics for the STEREO mission. arXiv e-prints , astro–ph/0612649doi:10.48550/arXiv.astro-ph/0612649, arXiv:astro-ph/0612649.

Isavnin, A., 2016. FRiED: A Novel Three-dimensional Model of Coronal Mass Ejections. ApJ 833, 267. doi:10.3847/1538-4357/833/2/267, arXiv:1703.01659.

Jones, S.R., Barnard, L.A., Scott, C.J., Owens, M.J., Wilkinson, J., 2017. Tracking cmes using data from the solar stormwatch project; observing deflections and other properties. Space Weather 15, 1125–1140. URL: https://agupubs.onlinelibrary.wiley.com/doi/abs/10.1002/2017SW001640, doi:https://doi.org/10.1002/2017SW001640, arXiv:https://agupubs.onlinelibrary.wiley.com/doi/pdf/10.1002/2017SW001640.

Kaiser, M., Kucera, T., Davila, J., St. Cyr, O., Guhathakurta, M., Christian, E., 2008. The stereo mission: an introduction. Space Science Reviews 136, 5–16. doi:10.1007/s11214-007-9277-0.

Kaiser, M.L., Kucera, T.A., Davila, J.M., St. Cyr, O.C., Guhathakurta, M., Christian, E., 2008. The STEREO Mission: An Introduction. Space Sci. Rev. 136, 5–16. doi:10.1007/s11214-007-9277-0.

Kataoka, R., Ebisuzaki, T., Kusano, K., Shiota, D., Inoue, S., Yamamoto, T., Tokumaru, M., 2009. Three-dimensional mhd modeling of the solar wind struc-

tures associated with 13 december 2006 coronal mass ejection. Journal of Geophysical Research-Space Physics 114. doi:10.1029/2009ja014167.

Kay, C., Gopalswamy, N., 2018. The effects of uncertainty in initial cme input parameters on deflection, rotation, bz, and arrival time predictions. Journal of Geophysical Research: Space Physics 123, 7220–7240. URL: https://agupubs.onlinelibrary.wiley.com/doi/abs/10.1029/2018JA025780, doi:https://doi.org/10.1029/2018JA025780, arXiv:https://agupubs.onlinelibrary.wiley.com/doi/pdf/10.1029/2018JA025780.

Kay, C., Gopalswamy, N., Xie, H., Yashiro, S., 2017. Deflection and Rotation of CMEs from Active Region 11158. Sol. Phys. 292, 78. doi:10.1007/s11207-017-1098-z, arXiv:1704.07694.

Kay, C., Opher, M., Evans, R.M., 2015. Global Trends of CME Deflections Based on CME and Solar Parameters. ApJ 805, 168. doi:10.1088/0004-637X/805/2/168, arXiv:1410.4496.

Kilpua, E., Koskinen, H.E.J., Pulkkinen, T.I., 2017. Coronal mass ejections and their sheath regions in interplanetary space. Living Reviews in Solar Physics 14, 5. doi:10.1007/s41116-017-0009-6.

King, J.H., Papitashvili, N.E., 2005. Solar wind spatial scales in and comparisons of hourly Wind and ACE plasma and magnetic field data. Journal of Geophysical Research (Space Physics) 110, A02104. doi:10.1029/2004JA010649.

Koehn, G.J., Desai, R.T., Davies, E.E., Forsyth, R.J., Eastwood, J.P., Poedts, S., 2022. Successive interacting coronal mass ejections: How to create a perfect storm. The Astrophysical Journal 941, 139. URL: https://dx.doi.org/10.3847/1538-4357/aca28c, doi:10.3847/1538-4357/aca28c.

Krista, L.D., 2012. The Evolution and Space Weather Effects of Solar Coronal Holes. arXiv e-prints , arXiv:1210.4475doi:10.48550/arXiv.1210.4475, arXiv:1210.4475.

Kruse, M., Heidrich-Meisner, V., Wimmer-Schweingruber, R.F., Hauptmann, M., 2020. An elliptic expansion of the potential field source surface model. Astronomy And Astrophysics 638, A109. doi:10.1051/0004-6361/202037734, arXiv:2005.12843.

Kumar, Srivastava, Nandita, Talpeanu, Dana-Camelia, Mierla, Marilena, D'Huys, Elke, Dominique, Marie, 2025. On the role of source surface height and magnetograms in solar wind forecast accuracy. J. Space Weather Space Clim. 15, 24. URL: https://doi.org/10.1051/swsc/2025021, doi:10.1051/swsc/2025021.

Kumar, S., Hegde, D.V., Srivastava, N., Pogorelov, N.V., Gopalswamy, N., Yashiro, S., 2023. Rotation of a stealth cme on 2012 october 5 observed in the inner heliosphere. The Astrophysical Journal 958, 103. URL: https://dx.doi.org/10.3847/1538-4357/ad011f, doi:10.3847/1538-4357/ad011f.

Kumar, S., Paul, A., Vaidya, B., 2020. A comparison study of extrapolation models and empirical relations in forecasting solar wind. Frontiers in Astronomy and Space Sciences 7, 92. URL: https://www.frontiersin.org/article/10.3389/fspas.2020.572084, doi:10.3389/fspas.2020.572084.

Kumar, S., Srivastava, N., 2022. A parametric study of performance of two solar wind velocity forecasting models during 2006–2011. Space Weather 20, e2022SW003069. URL: https://agupubs.onlinelibrary.wiley.com/doi/abs/10.1029/2022SW003069, doi:https://doi.org/10.1029/2022SW003069, arXiv:https://agupubs.onlinelibrary.wiley.com/doi/pdf/10.1029/2022SW003069. e2022SW003069 2022SW003069.

Kumar, S., Srivastava, N., Gopalswamy, N., Dash, A., 2024. On the influence of the solar wind on the propagation of earth-impacting coronal mass ejections. The Astrophysical Journal 977, 57. URL: https://dx.doi.org/10.3847/1538-4357/ad8e63, doi:10.3847/1538-4357/ad8e63.

Lamy, P.L., Floyd, O., Boclet, B., Wojak, J., Gilardy, H., Barlyaeva, T., 2019.

Coronal Mass Ejections over Solar Cycles 23 and 24. Space Sci. Rev. 215, 39. doi:10.1007/s11214-019-0605-y.

Lang, K.R., 2006. Sun, Earth and Sky. 2 ed., Springer, New York, NY. doi:10.1007/978-0-387-33365-6. originally published by Springer Heidelberg, 1995.

Lara, A., Borgazzi, A.I., 2009. Dynamics of interplanetary CMEs and associated type II bursts, in: Gopalswamy, N., Webb, D.F. (Eds.), Universal Heliophysical Processes, pp. 287–290. doi:10.1017/S1743921309029421.

Lee, C.O., Luhmann, J.G., Hoeksema, J.T., Sun, X., Arge, C.N., de Pater, I., 2011. Coronal Field Opens at Lower Height During the Solar Cycles 22 and 23 Minimum Periods: IMF Comparison Suggests the Source Surface Should Be Lowered. Sol. Phys. 269, 367–388. doi:10.1007/s11207-010-9699-9.

Li, H., Feng, X., Wei, F., 2021. Comparison of Synoptic Maps and PFSS Solutions for The Declining Phase of Solar Cycle 24. Journal of Geophysical Research (Space Physics) 126, e28870. doi:10.1029/2020JA028870.

Liu, Y., Luhmann, J.G., Bale, S.D., Lin, R.P., 2011. Solar Source and Heliospheric Consequences of the 2010 April 3 Coronal Mass Ejection: A Comprehensive View. ApJ 734, 84. doi:10.1088/0004-637X/734/2/84.

Low, B.C., 1994. Magnetohydrodynamic processes in the solar corona: Flares, coronal mass ejections, and magnetic helicity. Physics of Plasmas 1, 1684–1690. doi:10.1063/1.870671.

Lowder, C., Qiu, J., Leamon, R., 2016. Coronal holes and open magnetic flux over cycles 23 and 24. Solar Physics 292. doi:10.1007/s11207-016-1041-8.

Lowder, C., Qiu, J., Leamon, R., 2017. Coronal Holes and Open Magnetic Flux over Cycles 23 and 24. Solar Physics 292, 18. doi:10.1007/s11207-016-1041-8, arXiv:1612.07595.

Lundquist, S., 1950. Magnetohydrostatic fields. Ark. Fys. 2, 361–365.

Lyot, B., 1939. The study of the solar corona and prominences without eclipses (George Darwin Lecture, 1939). MNRAS 99, 580. doi:10.1093/mnras/99.8.580.

MacNeice, P., Jian, L.K., Antiochos, S.K., Arge, C.N., Bussy-Virat, C.D., DeRosa, M.L., Jackson, B.V., Linker, J.A., Mikic, Z., Owens, M.J., Ridley, A.J., Riley, P., Savani, N., Sokolov, I., 2018. Assessing the quality of models of the ambient solar wind. Space Weather 16, 1644–1667. URL: https://agupubs.onlinelibrary.wiley.com/doi/abs/10.1029/2018SW002040, doi:https://doi.org/10.1029/2018SW002040, arXiv:https://agupubs.onlinelibrary.wiley.com/doi/pdf/10.1029/2018SW002040.

MacQueen, R.M., Hundhausen, A.J., Conover, C.W., 1986. The propagation of coronal mass ejection transients. Journal of Geophysical Research: Space Physics 91, 31–38. URL: https://agupubs.onlinelibrary.wiley.com/doi/abs/10.1029/JA091iA01p00031, doi:https://doi.org/10.1029/JA091iA01p00031, arXiv:https://agupubs.onlinelibrary.wiley.com/doi/pdf/10.1029/JA091iA01p00031.

Maharana, A., Scolini, C., Schmieder, B., Poedts, S., 2023. Rotation and interaction of the CMEs of September 8 and 10, 2014, tested with EUHFORIA. A&A 675, A136. doi:10.1051/0004-6361/202345902, arXiv:2305.06881.

Makela, P., Gopalswamy, N., Xie, H., Mohamed, A., Yashiro, S., 2013. Coronal hole influence on the observed structure of interplanetary cmes. Solar Physics 284. doi:10.1007/s11207-012-0211-6.

Manchester, W.B., Gombosi, T.I., Roussev, I., Ridley, A., de Zeeuw, D.L., Sokolov, I.V., Powell, K.G., Tóth, G., 2004. Modeling a space weather event from the Sun to the Earth: CME generation and interplanetary propagation. Journal of Geophysical Research (Space Physics) 109, A02107. doi:10.1029/2003JA010150.

Martinić, K., Dumbović, M., Temmer, M., Veronig, A., Vršnak, B., 2022. Determination of coronal mass ejection orientation and consequences for

their propagation. A&A 661, A155. doi:10.1051/0004-6361/202243433, arXiv:2204.10112.

Martinić, K., Dumbović, M., Čalogović, J., Vršnak, B., Al-Haddad, N., Temmer, M., 2023. Effects of coronal mass ejection orientation on its propagation in the heliosphere. A&A 679, A97. doi:10.1051/0004-6361/202346858, arXiv:2309.15475.

Marubashi, K., Cho, K.S., Ishibashi, H., 2017. Interplanetary Magnetic Flux Ropes as Agents Connecting Solar Eruptions and Geomagnetic Activities. Sol. Phys. 292, 189. doi:10.1007/s11207-017-1204-2.

Marubashi, K., Lepping, R.P., 2007. Long-duration magnetic clouds: a comparison of analyses using torus- and cylinder-shaped flux rope models. Annales Geophysicae 25, 2453–2477. URL: https://angeo.copernicus.org/articles/25/2453/2007/, doi:10.5194/angeo-25-2453-2007.

Mayank, P., Lotz, S., Vaidya, B., Mishra, W., Chakrabarty, D., 2024. Study of Evolution and Geo-effectiveness of Coronal Mass Ejection–Coronal Mass Ejection Interactions Using Magnetohydrodynamic Simulations with SWASTi Framework. ApJ 976, 126. doi:10.3847/1538-4357/ad8084, arXiv:2409.19943.

Mayank, P., Vaidya, B., Chakrabarty, D., 2022. Swasti-sw: Space weather adaptive simulation framework for solar wind and its relevance to the aditya-l1 mission. The Astrophysical Journal Supplement Series 262, 23. URL: https://dx.doi.org/10.3847/1538-4365/ac8551, doi:10.3847/1538-4365/ac8551.

McComas, D.J., Bame, S.J., Barker, P., Feldman, W.C., Phillips, J.L., Riley, P., Griffee, J.W., 1998. Solar Wind Electron Proton Alpha Monitor (SWEPAM) for the Advanced Composition Explorer. Space Sci. Rev. 86, 563–612. doi:10.1023/A:1005040232597.

McComas, D.J., Elliott, H.A., Schwadron, N.A., Gosling, J.T., Skoug, R.M., Goldstein, B.E., 2003. The three-dimensional solar wind around solar maximum. Geophys. Res. Lett. 30, 1517. doi:10.1029/2003GL017136.

McGregor, S., Hughes, W., Arge, C., Owens, M., 2008. Analysis of the magnetic field discontinuity at the pfss and schatten current sheet interface in the wsa model. J. Geophys. Res. 113. doi:10.1029/2007JA012330.

McGregor, S.L., Hughes, W.J., Arge, C.N., Owens, M.J., 2008. Analysis of the magnetic field discontinuity at the potential field source surface and Schatten Current Sheet interface in the Wang-Sheeley-Arge model. Journal of Geophysical Research (Space Physics) 113, A08112. doi:10.1029/2007JA012330.

Meyer, K.A., Mackay, D.H., Talpeanu, D.C., Upton, L.A., West, M.J., 2020. Investigation of the Middle Corona with SWAP and a Data-Driven Non-Potential Coronal Magnetic Field Model. Solar Physics 295, 101. doi:10.1007/s11207-020-01668-2, arXiv:2007.02668.

Mignone, A., Bodo, G., Massaglia, S., Matsakos, T., Tesileanu, O., Zanni, C., Ferrari, A., 2007. PLUTO: A Numerical Code for Computational Astrophysics. ApJS 170, 228–242. doi:10.1086/513316, arXiv:astro-ph/0701854.

Mignone, A., Zanni, C., Tzeferacos, P., van Straalen, B., Colella, P., Bodo, G., 2012. The PLUTO Code for Adaptive Mesh Computations in Astrophysical Fluid Dynamics. ApJS 198, 7. doi:10.1088/0067-0049/198/1/7, arXiv:1110.0740.

Mishra, W., Dave, K., Srivastava, N., Teriaca, L., 2021. Multipoint remote and in situ observations of interplanetary coronal mass ejection structures during 2011 and associated geomagnetic storms. MNRAS 506, 1186–1197. doi:10.1093/mnras/stab1721.

Mitalas, R., Sills, K.R., 1992. On the Photon Diffusion Time Scale for the Sun. ApJ 401, 759. doi:10.1086/172103.

Moestl, C., Davies, E., Weiler, E., 2020. HELIO4CAST Interplanetary Coronal Mass Ejection Catalog v2.3 URL: https://figshare.com/articles/dataset/HELCATS_Interplanetary_Coronal_Mass_Ejection_Catalog_v2_0/6356420, doi:10.6084/m9.figshare.6356420.v22.

Moore, R.L., Labonte, B.J., 1980. The filament eruption in the 3B flare of July 29, 1973 - Onset and magnetic field configuration, in: Dryer, M., Tandberg-Hanssen, E. (Eds.), Solar and Interplanetary Dynamics, pp. 207–210.

Moran, T.G., Davila, J.M., 2004. Three-Dimensional Polarimetric Imaging of Coronal Mass Ejections. Science 305, 66–71. doi:10.1126/science.1098937.

Narechania, N., Nikolic, L., Freret, L., Sterck, H., Groth, C., 2020. An integrated data-driven solar wind - cme numerical framework for space weather forecasting. Journal of Space Weather and Space Climate 11. doi:10.1051/swsc/2020068.

Newton, H.W., 1943. Solar flares and magnetic storms. MNRAS 103, 244. doi:10.1093/mnras/103.5.244.

Nikolić, L., 2019. On solutions of the pfss model with gong synoptic maps for 2006–2018. Space Weather 17, 1293–1311. URL: https://agupubs.onlinelibrary.wiley.com/doi/abs/10.1029/2019SW002205, doi:https://doi.org/10.1029/2019SW002205, arXiv:https://agupubs.onlinelibrary.wiley.com/doi/pdf/10.1029/2019SW002205.

Nitta, N.V., Mulligan, T., 2017. Earth-Affecting Coronal Mass Ejections Without Obvious Low Coronal Signatures. Sol. Phys. 292, 125. doi:10.1007/s11207-017-1147-7.

Odstrcil, D., Riley, P., Zhao, X.P., 2004. Numerical simulation of the 12 May 1997 interplanetary CME event. Journal of Geophysical Research (Space Physics) 109, A02116. doi:10.1029/2003JA010135.

Odstrcil, D., Riley, P., Zhao, X.P., 2004. Numerical simulation of the 12 may 1997 interplanetary cme event. Journal of Geophysical Research: Space Physics 109. URL: https://agupubs.onlinelibrary.wiley.com/doi/abs/10.1029/2003JA010135, doi:10.1029/2003JA010135, arXiv:https://agupubs.onlinelibrary.wiley.com/doi/pdf/10.1029/2003JA010135.

Odstrčil, D., Pizzo, V.J., 1999. Three-dimensional propagation of coronal mass ejections (cmes) in a structured solar wind flow: 1. cme launched within the streamer belt. Journal of Geophysical Research: Space Physics 104, 483–492. URL: https://agupubs.onlinelibrary.wiley.com/doi/abs/10.1029/1998JA900019, doi:https://doi.org/10.1029/1998JA900019, arXiv:https://agupubs.onlinelibrary.wiley.com/doi/pdf/10.1029/1998JA900019.

Owens, M., Lang, M., Barnard, L., Riley, P., Ben-Nun, M., Scott, C.J., Lockwood, M., Reiss, M.A., Arge, C.N., Gonzi, S., 2020. A computationally efficient, time-dependent model of the solar wind for use as a surrogate to three-dimensional numerical magnetohydrodynamic simulations. Solar Physics 295, 43. URL: https://doi.org/10.1007/s11207-020-01605-3, doi:10.1007/s11207-020-01605-3.

Owens, M., Riley, P., 2017. Probabilistic solar wind forecasting using large ensembles of near-sun conditions with a simple one-dimensional "upwind" scheme: Ensemble solar wind forecasting. Space Weather 15. doi:10.1002/2017SW001679.

Pal, S., Kilpua, E., Good, S., Pomoell, J., Price, D.J., 2021. Uncovering erosion effects on magnetic flux rope twist. A&A 650, A176. doi:10.1051/0004-6361/202040070, arXiv:2104.03569.

Palmerio, E., Kilpua, E.K.J., Möstl, C., Bothmer, V., James, A.W., Green, L.M., Isavnin, A., Davies, J.A., Harrison, R.A., 2018. Coronal magnetic structure of earthbound cmes and in situ comparison. Space Weather 16, 442–460. URL: https://agupubs.onlinelibrary.wiley.com/doi/abs/10.1002/2017SW001767, doi:https://doi.org/10.1002/2017SW001767, arXiv:https://agupubs.onlinelibrary.wiley.com/doi/pdf/10.1002/2017SW001767.

Parker, E.N., 1958. Dynamics of the Interplanetary Gas and Magnetic Fields. ApJ 128, 664. doi:10.1086/146579.

Patsourakos, S., Georgoulis, M.K., Vourlidas, A., Nindos, A., Sarris, T., Anagnostopoulos, G., Anastasiadis, A., Chintzoglou, G., Daglis, I.A., Gontikakis,

C., Hatzigeorgiu, N., Iliopoulos, A.C., Katsavrias, C., Kouloumvakos, A., Moraitis, K., Nieves-Chinchilla, T., Pavlos, G., Sarafopoulos, D., Syntelis, P., Tsironis, C., Tziotziou, K., Vogiatzis, I.I., Balasis, G., Georgiou, M., Karakatsanis, L.P., Malandraki, O.E., Papadimitriou, C., Odstrčil, D., Pavlos, E.G., Podlachikova, O., Sandberg, I., Turner, D.L., Xenakis, M.N., Sarris, E., Tsinganos, K., Vlahos, L., 2016. The Major Geoeffective Solar Eruptions of 2012 March 7: Comprehensive Sun-to-Earth Analysis. ApJ 817, 14. doi:10.3847/0004-637X/817/1/14.

Perri, B., Leitner, P., Brchnelova, M., Baratashvili, T., Kuźma, B., Zhang, F., Lani, A., Poedts, S., 2022. Coconut, a novel fast-converging mhd model for solar corona simulations: I. benchmarking and optimization of polytropic solutions. The Astrophysical Journal 936, 19. doi:10.3847/1538-4357/ac7237.

Pluta, A., Mrotzek, N., Vourlidas, A., Bothmer, V., Savani, N., 2019. Combined geometrical modelling and white-light mass determination of coronal mass ejections. A&A 623, A139. doi:10.1051/0004-6361/201833829.

Pomoell, J., Poedts, S., 2018. EUHFORIA: European heliospheric forecasting information asset. Journal of Space Weather and Space Climate 8, A35. doi:10.1051/swsc/2018020.

Pomoell, Jens, Poedts, S., 2018. Euhforia: European heliospheric forecasting information asset. J. Space Weather Space Clim. 8, A35. URL: https://doi.org/10.1051/swsc/2018020, doi:10.1051/swsc/2018020.

Prabhu, A., Lagg, A., Hirzberger, J., Solanki, S. K., 2020. The magnetic fine structure of the sun´s polar region as revealed by sunrise. A&A 644, A86. URL: https://doi.org/10.1051/0004-6361/202038704, doi:10.1051/0004-6361/202038704.

Reiss, M.A., MacNeice, P.J., Mays, L.M., Arge, C.N., Möstl, C., Nikolic, L., Amerstorfer, T., 2019. Forecasting the ambient solar wind with numerical models. i. on the implementation of an operational framework. The Astrophys-

ical Journal Supplement Series 240, 35. URL: https://doi.org/10.3847%2F1538-4365%2Faaf8b3, doi:10.3847/1538-4365/aaf8b3.

Reiss, M.A., Temmer, M., Veronig, A.M., Nikolic, L., Vennerstrom, S., Schöngassner, F., Hofmeister, S.J., 2016. Verification of high-speed solar wind stream forecasts using operational solar wind models. Space Weather 14, 495–510. URL: https://agupubs.onlinelibrary.wiley.com/doi/abs/10.1002/2016SW001390, doi:10.1002/2016SW001390, arXiv:https://agupubs.onlinelibrary.wiley.com/doi/pdf/10.1002/2016SW001390.

Richardson, I.G., Cliver, E.W., Cane, H.V., 2000. Sources of geomagnetic activity over the solar cycle: Relative importance of coronal mass ejections, high-speed streams, and slow solar wind. Journal of Geophysical Research: Space Physics 105, 18203–18213. URL: https://agupubs.onlinelibrary.wiley.com/doi/abs/10.1029/1999JA000400, doi:10.1029/1999JA000400, arXiv:https://agupubs.onlinelibrary.wiley.com/doi/pdf/10.1029/1999JA000400.

Riley, P., Linker, J.A., Arge, C.N., 2015. On the role played by magnetic expansion factor in the prediction of solar wind speed. Space Weather 13, 154–169. doi:10.1002/2014SW001144.

Riley, P., Linker, J.A., Mikić, Z., 2001. An empirically-driven global mhd model of the solar corona and inner heliosphere. Journal of Geophysical Research: Space Physics 106, 15889–15901. URL: https://agupubs.onlinelibrary.wiley.com/doi/abs/10.1029/2000JA000121, doi:10.1029/2000JA000121, arXiv:https://agupubs.onlinelibrary.wiley.com/doi/pdf/10.1029/2000JA000121.

Riley, P., Lionello, R., 2011. Mapping Solar Wind Streams from the Sun to 1 AU: A Comparison of Techniques. Sol. Phys. 270, 575–592. doi:10.1007/s11207-011-9766-x.

Robbrecht, E., Patsourakos, S., Vourlidas, A., 2009. No Trace Left Behind: STEREO Observation of a Coronal Mass Ejection Without Low Coronal Signatures. ApJ 701, 283–291. doi:10.1088/0004-637X/701/1/283, arXiv:0905.2583.

Roy, S., Nandy, D., 2023. A Time-efficient, Data-driven Modeling Approach for Predicting the Geomagnetic Impact of Coronal Mass Ejections. ApJ 950, L11. doi:10.3847/2041-8213/acd77c, arXiv:2210.00071.

Russell, C.T., 1999. Magnetic stress in solar system plasmas. Australian Journal of Physics 52, 733–751. doi:10.1071/PH98102.

Sachdeva, N., Subramanian, P., Colaninno, R., Vourlidas, A., 2015. CME Propagation: Where does Aerodynamic Drag 'Take Over'? ApJ 809, 158. doi:10.1088/0004-637X/809/2/158, arXiv:1507.05199.

Sachdeva, N., Subramanian, P., Vourlidas, A., Bothmer, V., 2017. CME Dynamics Using STEREO and LASCO Observations: The Relative Importance of Lorentz Forces and Solar Wind Drag. Sol. Phys. 292, 118. doi:10.1007/s11207-017-1137-9, arXiv:1705.04871.

Sakurai, T., 1976. Magnetohydrodynamic interpretation of the motion of prominences. PASJ 28, 177–198.

Samara, E., Laperre, B., Kieokaew, R., Temmer, M., Verbeke, C., Rodriguez, L., Magdalenić, J., Poedts, S., 2022. Dynamic time warping as a means of assessing solar wind time series. The Astrophysical Journal 927, 187. doi:10.3847/1538-4357/ac4af6.

Santandrea, S., Gantois, K., Strauch, K., Teston, F., Proba2 Project Team, Tilmans, E., Baijot, C., Gerrits, D., Proba2 Industry Team, de Groof, A., Schwehm, G., Zender, J., 2013. PROBA2: Mission and Spacecraft Overview. Solar Physics Journal 286, 5–19. doi:10.1007/s11207-013-0289-5.

Sarkar, R., Gopalswamy, N., Srivastava, N., 2020. An Observationally Constrained Analytical Model for Predicting the Magnetic Field Vectors of Interplanetary Coronal Mass Ejections at 1 au. ApJ 888, 121. doi:10.3847/1538-4357/ab5fd7, arXiv:1912.03494.

Schatten, K.H., 1972. Current Sheet Magnetic Model for the Solar Corona. po-

tential formulation for the magnetic fields. (ref: Schatten, wilcox, 1968, a model of...). This current free. volume 308. p. 44.

Schatten, K.H., Wilcox, J.M., 1968. A model for interplanetary and coronal magnetic fields. Solar Physics .

Schatten, K.H., Wilcox, J.M., Ness, N.F., 1969. A model of interplanetary and coronal magnetic fields. Solar Physics 6, 442–455. doi:10.1007/BF00146478.

Scherrer, P.H., Bogart, R.S., Bush, R.I., Hoeksema, J.T., Kosovichev, A.G., Schou, J., Rosenberg, W., Springer, L., Tarbell, T.D., Title, A., Wolfson, C.J., Zayer, I., MDI Engineering Team, 1995. The Solar Oscillations Investigation - Michelson Doppler Imager. Solar Physics 162, 129–188. doi:10.1007/BF00733429.

Scherrer, P.H., Schou, J., Bush, R.I., Kosovichev, A.G., Bogart, R.S., Hoeksema, J.T., Liu, Y., Duvall, T.L., Zhao, J., Title, A.M., Schrijver, C.J., Tarbell, T.D., Tomczyk, S., 2012. The Helioseismic and Magnetic Imager (HMI) Investigation for the Solar Dynamics Observatory (SDO). Solar Physics 275, 207–227. doi:10.1007/s11207-011-9834-2.

Schwenn, R., 2006. Space Weather: The Solar Perspective. Living Reviews in Solar Physics 3, 2. doi:10.12942/lrsp-2006-2.

Schwenn, R., dal Lago, A., Huttunen, E., Gonzalez, W.D., 2005. The association of coronal mass ejections with their effects near the Earth. Annales Geophysicae 23, 1033–1059. doi:10.5194/angeo-23-1033-2005.

Scolini, C., Palmerio, E., 2024. The spheroid CME model in EUHFORIA. Journal of Space Weather and Space Climate 14, 13. doi:10.1051/swsc/2024011.

Seaton, D.B., Berghmans, D., Nicula, B., Halain, J.P., De Groof, A., Thibert, T., Bloomfield, D.S., Raftery, C.L., Gallagher, P.T., Auchère, F., Defise, J.M., D'Huys, E., Lecat, J.H., Mazy, E., Rochus, P., Rossi, L., Schühle, U., Slemzin, V., Yalim, M.S., Zender, J., 2013. The SWAP EUV Imaging Telescope Part

I: Instrument Overview and Pre-Flight Testing. Solar Physics 286, 43–65. doi:10.1007/s11207-012-0114-6, arXiv:1208.4631.

Shen, C., Wang, Y., Gui, B., Ye, P., Wang, S., 2011. Kinematic Evolution of a Slow CME in Corona Viewed by STEREO-B on 8 October 2007. Sol. Phys. 269, 389–400. doi:10.1007/s11207-011-9715-8, arXiv:1101.3205.

Shiota, D., Kataoka, R., Miyoshi, Y., Hara, T., Tao, C., Masunaga, K., Futaana, Y., Terada, N., 2014. Inner heliosphere mhd modeling system applicable to space weather forecasting for the other planets. Space Weather 12, 187–204. URL: https://agupubs.onlinelibrary.wiley.com/doi/abs/10.1002/2013SW000989, doi:https://doi.org/10.1002/2013SW000989, arXiv:https://agupubs.onlinelibrary.wiley.com/doi/pdf/10.1002/2013SW000989.

Singh, T., Benson, B., Raza, S.A.Z., Kim, T.K., Pogorelov, N.V., Smith, W.P., Arge, C.N., 2023. Improving the arrival time estimates of coronal mass ejections by using magnetohydrodynamic ensemble modeling, heliospheric imager data, and machine learning. The Astrophysical Journal 948, 78. URL: https://dx.doi.org/10.3847/1538-4357/acc10a, doi:10.3847/1538-4357/acc10a.

Singh, T., Yalim, M.S., Pogorelov, N.V., Gopalswamy, N., 2020. A Modified Spheromak Model Suitable for Coronal Mass Ejection Simulations. ApJ 894, 49. doi:10.3847/1538-4357/ab845f, arXiv:2002.10409.

Smith, C.W., L'Heureux, J., Ness, N.F., Acuña, M.H., Burlaga, L.F., Scheifele, J., 1998. The ACE Magnetic Fields Experiment. Space Sci. Rev. 86, 613–632. doi:10.1023/A:1005092216668.

Smith, Z.K., Dryer, M., McKenna-Lawlor, S.M.P., Fry, C.D., Deehr, C.S., Sun, W., 2009. Operational validation of HAFv2's predictions of interplanetary shock arrivals at Earth: Declining phase of Solar Cycle 23. Journal of Geophysical Research (Space Physics) 114, A05106. doi:10.1029/2008JA013836.

Spiegel, E.A., Zahn, J.P., 1992. The solar tachocline. A&A 265, 106–114.

Stansby, D., 2019. dstansby/pfsspy: pfsspy 0.1.2. URL: https://doi.org/10.5281/zenodo.2566462, doi:10.5281/zenodo.2566462.

Stansby, D., Yeates, A., Badman, S.T., 2020a. pfsspy: A python package for potential field source surface modelling. Journal of Open Source Software 5, 2732. URL: https://doi.org/10.21105/joss.02732, doi:10.21105/joss.02732.

Stansby, D., Yeates, A., Badman, S.T., 2020b. pfsspy: A python package for potential field source surface modelling. Journal of Open Source Software 5, 2732. URL: https://doi.org/10.21105/joss.02732, doi:10.21105/joss.02732.

Stone, E.C., Frandsen, A.M., Mewaldt, R.A., Christian, E.R., Margolies, D., Ormes, J.F., Snow, F., 1998. The Advanced Composition Explorer. Space Sci. Rev. 86, 1–22. doi:10.1023/A:1005082526237.

Sturrock, P.A., 1989. The Role of Eruption in Solar Flares. Sol. Phys. 121, 387–397. doi:10.1007/BF00161708.

Stys, J.E., Ireland, J., Müller, D., 2015. The Helioviewer Project: Solar and Heliospheric Data Visualization, in: AAS/AGU Triennial Earth-Sun Summit, p. 403.04.

Tang, F., Tsurutani, B.T., Gonzalez, W.D., Akasofu, S.I., Smith, E.J., 1989. Solar sources of interplanetary southward B_z events responsible for major magnetic storms (1978-1979). J. Geophys. Res. 94, 3535–3541. doi:10.1029/JA094iA04p03535.

Temmer, M., Scolini, C., Richardson, I.G., Heinemann, S.G., Paouris, E., Vourlidas, A., Bisi, M.M., writing teams, :, Al-Haddad, N., Amerstorfer, T., Barnard, L., Buresova, D., Hofmeister, S.J., Iwai, K., Jackson, B.V., Jarolim, R., Jian, L.K., Linker, J.A., Lugaz, N., Manoharan, P.K., Mays, M.L., Mishra, W., Owens, M.J., Palmerio, E., Perri, B., Pomoell, J., Pinto, R.F., Samara, E., Singh, T., Sur, D., Verbeke, C., Veronig, A.M., Zhuang, B., 2023. CME

Propagation Through the Heliosphere: Status and Future of Observations and Model Development. arXiv e-prints , arXiv:2308.04851doi:10.48550/arXiv.2308.04851, arXiv:2308.04851.

The SunPy Community, Barnes, W.T., Bobra, M.G., Christe, S.D., Freij, N., Hayes, L.A., Ireland, J., Mumford, S., Perez-Suarez, D., Ryan, D.F., Shih, A.Y., Chanda, P., Glogowski, K., Hewett, R., Hughitt, V.K., Hill, A., Hiware, K., Inglis, A., Kirk, M.S.F., Konge, S., Mason, J.P., Maloney, S.A., Murray, S.A., Panda, A., Park, J., Pereira, T.M.D., Reardon, K., Savage, S., Sipőcz, B.M., Stansby, D., Jain, Y., Taylor, G., Yadav, T., Rajul, Dang, T.K., 2020. The sunpy project: Open source development and status of the version 1.0 core package. The Astrophysical Journal 890, 68–. URL: https://iopscience.iop.org/article/10.3847/1538-4357/ab4f7a, doi:10.3847/1538-4357/ab4f7a.

Thernisien, A., Vourlidas, A., Howard, R.A., 2009. Forward Modeling of Coronal Mass Ejections Using STEREO/SECCHI Data. Sol. Phys. 256, 111–130. doi:10.1007/s11207-009-9346-5.

Thernisien, A.F.R., Howard, R.A., Vourlidas, A., 2006. Modeling of flux rope coronal mass ejections. The Astrophysical Journal 652, 763. URL: https://dx.doi.org/10.1086/508254, doi:10.1086/508254.

Tóth, G., Sokolov, I.V., Gombosi, T.I., Chesney, D.R., Clauer, C.R., De Zeeuw, D.L., Hansen, K.C., Kane, K.J., Manchester, W.B., Oehmke, R.C., Powell, K.G., Ridley, A.J., Roussev, I.I., Stout, Q.F., Volberg, O., Wolf, R.A., Sazykin, S., Chan, A., Yu, B., Kóta, J., 2005. Space weather modeling framework: A new tool for the space science community. Journal of Geophysical Research: Space Physics 110. URL: https://agupubs.onlinelibrary.wiley.com/doi/abs/10.1029/2005JA011126, doi:10.1029/2005JA011126, arXiv:https://agupubs.onlinelibrary.wiley.com/doi/pdf/10.1029/2005JA011126.

Čalogović, J., Dumbović, M., Sudar, D., Vršnak, B., Martinić, K., Temmer, M., Veronig, A.M., 2021. Probabilistic Drag-Based Ensemble Model (DBEM)

Evaluation for Heliospheric Propagation of CMEs. Sol. Phys. 296, 114. doi:10.1007/s11207-021-01859-5, arXiv:2107.06684.

Vemareddy, P., 2024. Filament Eruption from Active Region 13283 Leading to a Fast Halo-CME and an Intense Geomagnetic Storm on 2023 April 23. ApJ 961, 199. doi:10.3847/1538-4357/ad1662, arXiv:2312.08790.

Verbeke, C., Mays, M.L., Kay, C., Riley, P., Palmerio, E., Dumbović, M., Mierla, M., Scolini, C., Temmer, M., Paouris, E., Balmaceda, L.A., Cremades, H., Hinterreiter, J., 2023. Quantifying errors in 3D CME parameters derived from synthetic data using white-light reconstruction techniques. Advances in Space Research 72, 5243–5262. doi:10.1016/j.asr.2022.08.056, arXiv:2302.00531.

Vourlidas, A., Colaninno, R., Nieves-Chinchilla, T., Stenborg, G., 2011. The First Observation of a Rapidly Rotating Coronal Mass Ejection in the Middle Corona. ApJ 733, L23. doi:10.1088/2041-8205/733/2/L23.

Vourlidas, A., Howard, R.A., Esfandiari, E., Patsourakos, S., Yashiro, S., Michalek, G., 2010. Comprehensive Analysis of Coronal Mass Ejection Mass and Energy Properties Over a Full Solar Cycle. ApJ 722, 1522–1538. doi:10.1088/0004-637X/722/2/1522, arXiv:1008.3737.

Vršnak, B., Gopalswamy, N., 2002. Influence of the aerodynamic drag on the motion of interplanetary ejecta. Journal of Geophysical Research (Space Physics) 107, 1019. doi:10.1029/2001JA000120.

Vršnak, B., Žic, T., 2007. Transit times of interplanetary coronal mass ejections and the solar wind speed. A&A 472, 937–943. doi:10.1051/0004-6361:20077499.

Vršnak, B., Žic, T., Falkenberg, T.V., Möstl, C., Vennerstrom, S., Vrbanec, D., 2010. The role of aerodynamic drag in propagation of interplanetary coronal mass ejections. A&A 512, A43. doi:10.1051/0004-6361/200913482.

Vršnak, B., Žic, T., Vrbanec, D., Temmer, M., Rollett, T., Möstl, C., Veronig, A., Čalogović, J., Dumbović, M., Lulić, S., Moon, Y.J., Shanmugaraju, A.,

2013. Propagation of Interplanetary Coronal Mass Ejections: The Drag-Based Model. Sol. Phys. 285, 295–315. doi:10.1007/s11207-012-0035-4.

Žic, T., Vršnak, B., Temmer, M., 2015. Heliospheric Propagation of Coronal Mass Ejections: Drag-based Model Fitting. ApJS 218, 32. doi:10.1088/0067-0049/218/2/32, arXiv:1506.08582.

Wang, J., Hoeksema, J.T., Liu, S., 2020. The deflection of coronal mass ejections by the ambient coronal magnetic field configuration. Journal of Geophysical Research: Space Physics 125, e2019JA027530. URL: https://agupubs.onlinelibrary.wiley.com/doi/abs/10.1029/2019JA027530, doi:https://doi.org/10.1029/2019JA027530, arXiv:https://agupubs.onlinelibrary.wiley.com/doi/pdf/10.1029/2019JA027530. e2019JA027530 10.1029/2019JA027530.

Wang, J., Liu, S., Luo, B., 2023. Analyzing deflection of multiple Solar Coronal Mass Ejections from the same active region. Advances in Space Research 72, 5263–5274. doi:10.1016/j.asr.2022.06.017.

Wang, Y., Shen, C., Wang, S., Ye, P., 2004. Deflection of coronal mass ejection in the interplanetary medium. Sol. Phys. 222, 329–343. doi:10.1023/B:SOLA.0000043576.21942.aa.

Wang, Y., Wang, B., Shen, C., Shen, F., Lugaz, N., 2014. Deflected propagation of a coronal mass ejection from the corona to interplanetary space. Journal of Geophysical Research: Space Physics 119, 5117–5132. URL: https://agupubs.onlinelibrary.wiley.com/doi/abs/10.1002/2013JA019537, doi:https://doi.org/10.1002/2013JA019537, arXiv:https://agupubs.onlinelibrary.wiley.com/doi/pdf/10.1002/2013JA019537.

Wang, Y.M., Sheeley, N. R., J., 1990. Solar Wind Speed and Coronal Flux-Tube Expansion. Astrophysical journal 355, 726. doi:10.1086/168805.

Wang, Y.M., Ye, P.Z., Wang, S., Zhou, G.P., Wang, J.X., 2002. A statistical study on the geoeffectiveness of earth-directed coronal mass ejections from march

1997 to december 2000. Journal of Geophysical Research: Space Physics 107, SSH 2–1–SSH 2–9. URL: https://agupubs.onlinelibrary.wiley.com/doi/abs/10.1029/2002JA009244, doi:https://doi.org/10.1029/2002JA009244, arXiv:https://agupubs.onlinelibrary.wiley.com/doi/pdf/10.1029/2002JA009244.

West, M.J., Seaton, D.B., D'Huys, E., Mierla, M., Laurenza, M., Meyer, K.A., Berghmans, D., Rachmeler, L.R., Rodriguez, L., Stegen, K., 2022. A Review of the Extended EUV Corona Observed by the Sun Watcher with Active Pixels and Image Processing (SWAP) Instrument. Sol. Phys. 297, 136. doi:10.1007/s11207-022-02063-9.

Wiegelmann, T., 2004. Optimization code with weighting function for the reconstruction of coronal magnetic fields. Solar Physics 219, 87–108. doi:10.1023/B:SOLA.0000021799.39465.36, arXiv:0802.0124.

Wu, C.C., Liou, K., Wood, B.E., Plunkett, S., Socker, D., Wang, Y.M., Wu, S.T., Dryer, M., Kung, C., 2020. Modeling inner boundary values at 18 solar radii during solar quiet time for global three-dimensional time-dependent magnetohydrodynamic numerical simulation. Journal of Atmospheric and Solar-Terrestrial Physics 201, 105211. URL: http://www.sciencedirect.com/science/article/pii/S1364682620300316, doi:https://doi.org/10.1016/j.jastp.2020.105211.

Xie, H., Ofman, L., Lawrence, G., 2004. Cone model for halo cmes: Application to space weather forecasting. Journal of Geophysical Research: Space Physics 109. URL: https://agupubs.onlinelibrary.wiley.com/doi/abs/10.1029/2003JA010226, doi:https://doi.org/10.1029/2003JA010226, arXiv:https://agupubs.onlinelibrary.wiley.com/doi/pdf/10.1029/2003JA010226.

Yashiro, S., Gopalswamy, N., Michalek, G., St. Cyr, O.C., Plunkett, S.P., Rich, N.B., Howard, R.A., 2004. A catalog of white light coronal mass ejections observed by the soho spacecraft. Journal of Geophysical Research: Space Physics 109. URL: https://agupubs.onlinelibrary.wiley.com/doi/abs/10.1029/2003JA010282, doi:https://doi.org/10.1029/2003JA010282, arXiv:https://agupubs.onlinelibrary.wiley.com/doi/pdf/10.1029/2003JA010282.

Yoder, C.F., 1995. Astrometric and Geodetic Properties of Earth and the Solar System. American Geophysical Union (AGU). pp. 1–31. URL: https://agupubs.onlinelibrary.wiley.com/doi/abs/10.1029/RF001p0001, doi:https://doi.org/10.1029/RF001p0001, arXiv:https://agupubs.onlinelibrary.wiley.com/doi/pdf/10.1029/RF001p0001.

Zhang, J., Dere, K.P., Howard, R.A., Kundu, M.R., White, S.M., 2001. On the Temporal Relationship between Coronal Mass Ejections and Flares. ApJ 559, 452–462. doi:10.1086/322405.

Zhou, G., He, H.Q., Wan, W., 2020. Effects of Solar Activity on Taylor Scale and Correlation Scale in Solar Wind Magnetic Fluctuations. ApJ 899, L32. doi:10.3847/2041-8213/abaaa9, arXiv:2008.08542.

Zhuang, B., Wang, Y., Shen, C., Liu, S., Wang, J., Pan, Z., Li, H., Liu, R., 2017. The Significance of the Influence of the CME Deflection in Interplanetary Space on the CME Arrival at Earth. ApJ 845, 117. doi:10.3847/1538-4357/aa7fc0.

Zirker, J.B., 1977. Coronal holes and high-speed wind streams. Reviews of Geophysics and Space Physics 15, 257–269. doi:10.1029/RG015i003p00257.

List of Publications

Publications included in the thesis

1. **Sandeep Kumar** & N. Srivastava, "A Parametric Study of Performance of Two Solar Wind Velocity Forecasting Models During 2006–2011", Space Weather,20, e2022SW003069, https://agupubs.onlinelibrary.wiley.com/doi/10.1029/2022SW003069

2. **Sandeep Kumar**, Dinesha V. Hegde, Nandita Srivastava, Nikolai V. Pogorelov, Nat Gopalswamy, and Seiji Yashiro, "Rotation of a Stealth CME on 2012 October 5 Observed in the Inner Heliosphere", The Astrophysical Journal, Volume 958, Number 103, https://iopscience.iop.org/article/10.3847/1538-4357/ad011f

3. **Sandeep Kumar**, Nandita Srivastava, Nat Gopalswamy, and Ashutosh Dash, "On the Influence of the Solar Wind on the Propagation of Earth-impacting Coronal Mass Ejections", The Astrophysical Journal, Volume 977, Number 57, https://iopscience.iop.org/article/10.3847/1538-4357/ad8e63

4. **Sandeep Kumar**,Nandita Srivastava, Dana Camelia Talpeanu, Marilena Mierla, Elke D'Huys and Marie Dominique, "On the role of source surface height and magnetograms in solar wind forecast accuracy", Space Weather and Space Climate, Volume 15, Number 24, https://doi.org/10.1051/swsc/2025021

5. **Sandeep Kumar**, Nandita Srivastava, Parthib Banerjee, Nat Gopalswamy, "Propagation Characteristics of April 21, 2023, CME" (Under Revision in

JAA).

6. **Sandeep Kumar,** Nandita Srivastava and Dana-Camelia Talpeanu, "On the variation of source surface height in WSA model in SC23, SC24 and SC25". (under preparation)

7. **Sandeep Kumar** and Nandita Srivastava, "Investigating CME-Solar wind interaction in the heliosphere with MHD simulations and Heliospheric CME tracking". (under preparation)

Contributed

1. S. S. Rao, Nandita Srivastava, Monti Chakraborty, **Sandeep Kumar**, D. Chakrabarty, "Observations of Geomagnetic Crochet at high-latitudes due to X1.5 Class Solar Flare on 3 July 2021", Space Weather DOI:10.1029/2023SW003719, 2023.

Awards/Honors

1. Awarded PROBA2/SWAP guest investigator grant of 5000 Euros for the proposal **"Using SWAP Observations for Optimising The Magnetic Field Extrapolation and Solar Wind Velocity Prediction Models"**, in Royal Observatory of Belgium, 2023.

2. Work on CME rotation (paper 2 and 4) was highlighted in Solar Nugget (**Unveiling CME Dynamics: Rare Rotations of CMEs in the Heliosphere**, Dec 2024.)

Presentations at International Conferences/Meetings

1. Oral presentation (online) on **"On the Role of Source Surface Height Optimisation and Magnetogram Impact in Improving Solar Wind Forecasting Models"** was given in the **9th Parker Solar Probe (PSP) Scholar Meeting on 21 May 2025**.

2. Poster presentation on **"Improving Solar Wind Forecasting Models Over the Phase of Solar Cycle: Source Surface Height Optimization and Magnetogram Impact"** in **Sun, Space Weather and Solar-Stellar Connections meeting (Jan 20–25, 2024) (An international conference commemorating 125 years of Kodaikanal Solar Observatory, India)**, presented by Prof. Nandita Srivastava.

3. Solicited Talk on **"Improving Solar Wind Forecasting Models Over the Phase of Solar Cycle: Source Surface Height Optimization and Magnetogram Impact"** in an **international conference on "Solar cycle variability: From understanding to making prediction"** presented on October 14–18, 2024, at ARIES Nainital, India.

4. Oral presentation (online) on **"On the influence of the solar wind on the propagation of Earth-impacting Coronal Mass Ejections"** was given in the **7th PSP Scholar Meeting on 28 May 2024**

5. Oral presentation (online) on **"Rotation of a Stealth CME on 5 October 2012 Observed in the Inner Heliosphere"** was given in the **5th Parker Solar Probe (PSP) Scholar Meeting on 3 May 2023**.

6. A seminar on **"A Parametric Study of Performance of Solar Wind Velocity Forecasting Models During 2006–2011"** was given in the **Royal Observatory of Belgium on July 13, 2023.**

7. **Poster presentation in 5th ISEE Symposium** on "A parametric study of the performance of solar wind velocity forecasting models during 2006 to 2011" on 16 Nov 2022.

National

1. Co-Author in a presentation **"Geomagnetic signatures at high latitudes during the X1.5 class solar flare of 3 July 2021"** presented in **National Space Science Symposium 2024 held at Goa University, Goa from 26th February-1 March 2024**, presented by **S S Rao**

2. Oral presentation on the **"Influence of solar wind medium on the propagation of Earth impacting Coronal Mass Ejections"** was given in **Workshop 3 on CME propagation in the interplanetary space to predict Bz in Astronomical Society of India (ASI)** 2024, on 31 Jan 2024.

3. Poster presentation on **"Continuous Rotation of a Stealth CME Observed in the Heliosphere on 5 October 2012 and Its Space Weather Impact"** in **Astronomical Society of India (ASI) 2024 (Jan 31-Feb 5, 2024)**.

4. Oral presentation in online mode entitled **"Using In-situ and Heliospheric Observations for Continuous Tracking of a Stealth CME Observed on 5 October 2012"** in the **"2nd Indian Space Weather Conference (ISWC-2)"** , 19-20 October 2023.

5. Poster presentation in **Science from In-situ Measurements of Aditya-L1 (SIMA-01)** meeting on **"Using In-situ and Heliospheric Observations for Continuous Tracking of a Stealth CME Observed on 5 October 2012."** on April 11-13, 2023.

6. Poster presentation in **Solar Physics Workshop [USPW-2023]** on **"Multi-scale Phenomena on the Sun: Present Capabilities and Future Challenges"** during April 3-5, 2023 , on "A parametric study of performance of solar wind forecasting models during 2006 to 2011".

7. Co-Author in a poster on **"Variation of Geomagnetic field components at high latitudes during X1.5 class solar flare of July 3, 2021"**, presented in **USO Solar Physics Workshop-2023 organized by Udaipur Solar Observatory/Physical Research Laboratory Udaipur during April 3-5, 2023**. presented by **S S Rao**

8. Oral presentation on **"A parametric study of performance of solar wind forecasting models during 2006 to 2011" at the ASI-2022 workshop at IIT Roorkee on 25th March 2022**.

9. Oral presentation on **"A parametric study of performance of solar wind forecasting models during 2006 to 2011"** at the **Indian Space Weather Conference (ISWC)-2022 conference in PRL on 11-12 January 2022.**

Outreach Talks/ Tutorials

1. A hands-on session for UN school students (in online mode) on The Arrival of Interplanetary Coronal Mass ejections using an Advanced Version of the Drag Based Model. on Sep. 4, 2024

2. **A hands-on session for UN school students (in online mode)** on **The Arrival of Interplanetary Coronal Mass ejections using an Advanced Version of the Drag Based Model. on May 23, 2023**

3. An outreach talk on, **"Origin of Stellar Energy"**, was given in the **Krea University**, 11 Jan, 2024.

4. **A practical session for UN school students (in online mode)** on **The Arrival of Interplanetary Coronal Mass ejections using an Advanced Version of the Drag Based Model** on March 9, 2022.

5. Co-Author in a talk on **"India-Uzbekistan Collaboration in Astronomy: From medieval to recent times" in the International Conference on "Ali Qushji – An outstanding ambassador of the scientific school of Ulugh Beg"** celebrating the 620th anniversary of Ali Qushji's birth and the 80th anniversary of the **Uzbekistan Academy of Sciences, September 21-22, 2023** (online presented by **Prof. Nandita Srivastava**)

Publications attached with the thesis

1. **Sandeep Kumar** & N. Srivastava, A Parametric Study of Performance of Two Solar Wind Velocity Forecasting Models During 2006–2011, Space Weather,20, e2022SW003069, https://agupubs.onlinelibrary.wiley.com/doi/10.1029/2022SW003069

2. **Sandeep Kumar**, Dinesha V. Hegde, Nandita Srivastava, Nikolai V. Pogorelov, Nat Gopalswamy, and Seiji Yashiro, Rotation of a Stealth CME on 2012 October 5 Observed in the Inner Heliosphere, The Astrophysical Journal, Volume 958, Number 103, https://iopscience.iop.org/article/10.3847/1538-4357/ad011f

3. **Sandeep Kumar**, Nandita Srivastava, Nat Gopalswamy, and Ashutosh Dash, On the Influence of the Solar Wind on the Propagation of Earth-impacting Coronal Mass Ejections, The Astrophysical Journal, Volume 977, Number 57, https://iopscience.iop.org/article/10.3847/1538-4357/ad8e63

4. **Sandeep Kumar**,Nandita Srivastava, Dana Camelia Talpeanu, Marilena Mierla, Elke D'Huys and Marie Dominique, On the role of source surface height and magnetograms in solar wind forecast accuracy, Space Weather and Space Climate, Volume 15, Number 24, https://doi.org/10.1051/swsc/2025021

Space Weather

RESEARCH ARTICLE
10.1029/2022SW003069

Special Section:
Understanding the interconnected sun-heliospheric-planetary system during solar minimum

A Parametric Study of Performance of Two Solar Wind Velocity Forecasting Models During 2006–2011

Sandeep Kumar[1,2] **and Nandita Srivastava**[1]

[1]Udaipur Solar Observatory, Physical Research Laboratory, Udaipur, India, [2]Indian Institute of Technology Gandhinagar, Palaj, Gujarat, India

Abstract There is an increasing need for the development of a robust space weather forecasting framework. State-of-the-art MHD space weather forecasting frameworks are based upon the Potential Field Source Surface (PFSS) and Schatten Current Sheet (SCS) extrapolation models for the magnetic field using synoptic magnetograms. These models create a solar wind (SW) background for the simulations using empirical relations of Wang, Sheeley and Arge (WSA), at the inner boundary of heliosphere and have been used to simulate coronal mass ejections for specific cases in previous studies. Besides these MHD frameworks, the Heliospheric Upwind eXtrapolation (HUX) technique can extrapolate SW from inner heliospheric boundaries to L1 and can give a reliable estimate of the SW velocity at L1 comparable to MHD models but in a short computational time. We carried out an extensive parametric study of the performance of the Model1 (PFSS+WSA+HUX) and Model2 (PFSS+SCS+WSA+HUX) for SW velocity prediction at L1. We implemented this framework on 60 Carrington Rotations from CR2047 to CR2107 during 2006–2011, covering the descending and deep minimum phase of solar cycle (SC) 23, and the ascending phase of SC 24. Our results show an unexpected decrease in the performance of the framework during the deep minimum phase of cycle 23, which is attributed to the decrease in the observed coronal hole area. As SC 24 began, this decreasing trend vanished due to an increase in the coronal hole (CH) area at the low and mid-latitudes, suggesting a good correlation between the performance of the framework and the variation in the CH area.

Plain Language Summary We carried out a parametric study of solar wind (SW) velocity forecasting models on 60 Carrington Rotations during the time period 2006–2011, spanning the descending and deep minimum phases of SC 23 and the ascending phase of SC 24. The overall performance of the framework shows an average *cc* of 0.65 for the Model1 and 0.63 for Model2 between observed and simulated SW velocity at L1. We report a correlation between the framework performance and the observed low and mid-latitude coronal hole area.

Key Points:

- A study of implementation of solar wind velocity forecasting models on 60 Carrington Rotations during the time period 2006–2011
- The framework performance shows an average *cc* between observed and modeled velocities, 0.65 for Model1 and 0.63 for Model2
- We report a correlation between the performance of framework and the observed low and mid-latitude coronal hole area

Correspondence to:
S. Kumar,
ssandeepsharma201@gmail.com

Citation:
Kumar, S., & Srivastava, N. (2022). A parametric study of performance of two solar wind velocity forecasting models during 2006–2011. *Space Weather*, *20*, e2022SW003069. https://doi.org/10.1029/2022SW003069

Received 19 FEB 2022
Accepted 23 AUG 2022
Corrected 7 FEB 2024

This article was corrected on 7 FEB 2024. See the end of the full text for details.

Author Contributions:
Conceptualization: Sandeep Kumar
Formal analysis: Sandeep Kumar
Investigation: Sandeep Kumar
Methodology: Sandeep Kumar
Resources: Nandita Srivastava
Supervision: Nandita Srivastava
Writing – original draft: Sandeep Kumar, Nandita Srivastava

1. Introduction

We live in a space technology-driven era, where most of our gadgets rely on satellite-based data. Moreover, communication satellites are prone to space weather. Therefore extreme space weather events can directly affect human activities on the Earth. Predicting the impact of space weather is thus a critical task. In particular, explosive events on the Sun that include solar flares, coronal mass ejections (CMEs) and solar energetic particles (SEPs) play a crucial role in influencing space weather (Schwenn, 2006). The ambient solar wind (SW) being the medium in which the CMEs propagate, also plays a significant role in influencing space weather, particularly, high speed SW streams which contribute to about 70% of geomagnetic activity outside of the solar maximum phase (Richardson et al., 2000). When a fast SW stream takes over a slow SW stream it creates a high density region co-rotating with the Sun called co-rotating interacting region (CIR). The ambient SW containing CIRs also plays important role in space weather. These CIRs and high speed streams are responsible for space weather events as they enhance energetic particle fluxes up-to relativistic energy in the radiation belt (Blake et al., 1997).

A state-of-the-art space weather forecasting framework combines the coronal magnetic field reconstruction models with the heliospheric model of SW to estimate the SW parameters at L1 which is required to study space weather impacts of CMEs on the Earth. These models work on a background steady state SW provided by empirical SW models. Kinematic extrapolation methods that also incorporate stream interactions rely on 1D stream propagation like Heliospheric Upwind eXtrapolation (HUX; Riley & Lionello, 2011) and its time dependent variant HUXt (Owens et al., 2020) provides a computationally efficient solution of SW velocity without providing much of physical insight for other parameters (like temperature, pressure and magnetic field) as done

Writing – review & editing: Sandeep Kumar, Nandita Srivastava

by the 3D MHD physics based frameworks like Wang Sheeley and Arge (WSA)-ENLIL (Odstrcil et al., 2004) and EUHFORIA (Pomoell & Poedts, 2018). As discussed earlier, understanding and predicting the key properties of the ambient SW plays a crucial role in space weather modeling. The development of the empirical relations to predict SW velocity at L1 was initiated by Wang and Sheeley (WS Model) who discovered a simple inverse correlation between expansion factor (f_s) and the SW velocity at L1 (Wang & Sheeley, 1990). The expansion factor represents the magnetic flux loss from the photosphere to a reference height along a magnetic field line. Some of the simple assumptions in coronal environment made it possible to extrapolate the photospheric magnetic field of the Sun outward (Schatten & Wilcox, 1968) and to calculate the expansion factor. Later, it was realized, that it is better to compute the SW velocity at some inner reference surface and then extrapolate it in the heliosphere to compare with the SW velocity at L1. WS model later evolved into an improved WSA model which incorporates another property of the magnetic field lines denoted by the parameter θ_b, which is defined as the minimum angular distance of the footpoint of the fieldline from its nearest coronal hole (CH) boundary (Arge et al., 2003). Further improvements to the WSA model were made to incorporate more parameters in its functional form (Riley et al., 2015). Distance from CH Boundary (DCHB) model also depends upon the properties of magnetic field lines in a way that it relates the SW velocity with the perpendicular distance of the footpoint of the field line from the CH and propagates it to the outer boundary of coronal region along the field lines (Riley et al., 2001).

Other than the SW forecasting models mentioned above, which depend upon the properties of the magnetic field lines in the corona, there are statistical-based SW forecasting models which use the previously observed data of SW parameters to create an ensemble. This data is then used to predict the SW parameters including SW velocity in a given fixed time window in the future by identifying the most similar windows of velocity in the past data with respect to the most recent past window (Owens & Riley, 2017). These models often outperform the model based on the magnetic field extrapolation on an operational level but do not provide any physical insight and sudden changes in the environment (MacNeice et al., 2018).

A parametric study of 14 selected CRs, covering a time period of 200 Carrington Rotations (CRs), from CR 1900 to 2100, for empirical SW velocity models (WS, WSA, and DCHB) using HUX, was carried out by Riley et al. (2015) to investigate the role of expansion factor in SW velocity prediction. This study did not incorporate the Schatten Current Sheet (SCS) model (Schatten, 1972) for magnetic field extrapolation. The results show a poor performance of WS model from mid-2007 to 2009 which was attributed to the presence of pseudo-streamers in this period. The overall results shows that the mean value of the WS correlation coefficient was 0.27, while the mean values of WSA coefficients was 0.39.

The performances of the empirical models (WSA or WS) are often related to the curvature of the Polarity Inversion Line (PIL) on the source surface (the outer boundary of the Potential Field Source Surface (PFSS) across which the radial component of the magnetic field changes its sign) (McGregor et al., 2008). A significant curvature of the PIL near the sub-Earth point is often related to the minimum error in the predictions made by the empirical models like WSA.

Although the solar community uses a fixed value of PFSS surface (2.5 $R_\odot$), however there might be change of values of reference radius of the source surface with the phase of SC. It has been shown that during the solar minimum a lower source surface radius gives better magnetic field extrapolation (Lee et al., 2011). Therefore the optimum parameters of WSA might change with the reference radius of the PFSS model, that is, source surface. Our focus is to study the overall performance of the framework with the SC phase by implementing the methodology with a fixed source surface radius (2.5 $R_\odot$) and also to incorporate the SCS model. Our approach is to select the values of input parameters on the basis of the best performance of the models over a range of a reasonable set of values of parameters.

The paper is organized as follows: the details of the method adopted and values of parameters for the forecasting framework are described in Section 2. The best results from models adopted in Section 2 and set of values of parameters for forecasting of SW velocity for the 60 selected CRs and the statistical assessment of their accuracy are discussed in Section 3. We compare the framework performance using two different approaches: PFSS + WSA + HUX (referred to as Model1) and PFSS + SCS + WSA + HUX (referred to as Model2). Finally, Section 4 discusses possible explanation for the trend of the performances of the framework in the chosen time period. A comparison of the performance of the framework is also done with the low and mid latitude CH area observed from SOHO/EIT synoptic maps.

2. Methodology

We separate the region between the solar photosphere and the Lagrangian point L1 into two domains. First domain includes the inner coronal region extending from the photosphere up to 2.5 $R_\odot$ or 5 $R_\odot$, where $R_\odot$ is the solar radius. Second domain extends from 5 $R_\odot$ up-to the L1 point. Data driven prediction of SW velocity at L1 point involves the following steps:

- To calculate the magnetic field in the coronal region (in the first domain) through various extrapolation methods like PFSS and SCS, by using the observed photospheric magnetic field as input.
- To apply the empirical velocity relation based on the magnetic field line properties, obtained from extrapolation at the outer boundary of the coronal region.
- To extend the velocity estimates from the outer boundary of the coronal region (first domain) up-to L1.

In Section 2.1 we describe the magnetic field extrapolations methods. Section 2.2 describes the empirical SW formulation used in this work. Section 2.3 describes our SW extrapolation technique in the heliosphere. In Section 2.4 different SW prediction models are discussed, defined as a combination of magnetic field extrapolation methods (PFSS or PFSS + SCS) and SW extrapolation method (HUX). We also describe the parametric space explored in our study to find the optimum parameters for each Carrington Rotation (CR). In Section 2.5 we discuss the statistical methods used to quantify the performance of the framework.

2.1. Magnetic Field Extrapolation

Forecasting SW throughout the heliosphere requires accurate magnetic field solutions extrapolated from the photosphere to the outer boundaries of the coronal domain (2.5 or 5 $R_\odot$). In the current work, we extrapolated the magnetic field up to a distance of 5 $R_\odot$. The inner boundary conditions for the magnetic fields at the solar surface are specified by the input magnetograms (synoptic magnetic maps) taken from the Global Oscillation Network Group (GONG) (https://gong.nso.edu/data/magmap/crmap.html). To extrapolate magnetic field from photosphere to 2.5 $R_\odot$ we use the potential field formulation for the magnetic fields ($\nabla^2\Psi = 0$ where $\vec{B} = -\nabla\Psi$) (Schatten & Wilcox, 1968), by assuming current-free environment. The outer boundary sphere of 2.5 $R_\odot$ is known as the *source surface*. The magnetic fields inside the source surface can be solved using the PFSS model (Altschuler & Newkirk, 1969; Mackay & Yeates, 2012). We used an open-source Python module pfsspy (Stansby, 2019) (Version 0.2.1), which is a finite difference PFSS solver for the PFSS solution.

Current-free approximation does not hold good in the region outside the source surface (2.5 $R_\odot$). Beyond the source surface, a thin current sheet separates positive and negative polarity magnetic field lines. Therefore, in this region, the magnetic field needs to be extrapolated in a unipolar manner in their respective polarity regions. We used the SCS model with same resolution (180 × 360) as that of the output from *pfsspy*, to calculate the magnetic field beyond PFSS (Schatten, 1972). This model incorporates the existence of the current sheet in the system. The SCS model extends the magnetic fields from the source surface to a distance of $5R_\odot$, that is, the outer boundary of the coronal domain. SCS is a pseudo potential field extrapolation model which requires a radially outward polarity as an input. Therefore, the input to the SCS model is the re-oriented output from *pfsspy*, that is, if $B_r \geq 0$, the field remains unchanged, but if $B_r \leq 0$, then B_r, B_θ, B_ϕ are replaced by $-B_r$, $-B_\theta$, $-B_\phi$. In this fashion, all the field lines are made to point radially outward before giving input to the SCS model. The detailed method of magnetic field extrapolation can be found in Kumar et al. (2020).

Two sets of magnetic field lines were traced using the magnetic field extrapolation models discussed above. One set of field lines was traced from the photosphere to the outer boundary of the coronal domain to create a map of the footpoints of open and closed magnetic field lines. Those field lines that could reach the source surface were marked as open, and others which were traced back to the photosphere were marked as the closed field lines. The second set of field lines was traced from sub-Earth points at the outer boundary of the coronal domain to the photosphere to find the properties of sub-Earth field lines. This was done to relate the SW velocities at the outer boundary of the coronal domain with the properties of the field lines (f_s and θ_b) using empirical models like WSA as discussed in Section 2.2.

Extrapolated source surface magnetic fields and input magnetic fields for CR2051, CR2088, and CR2105 are shown in Figure 1. These three CRs correspond to the descending, deep minimum phase of the SC 23 and ascending phase of the SC 24, respectively. This is also evident from their input and source surface magnetic field.

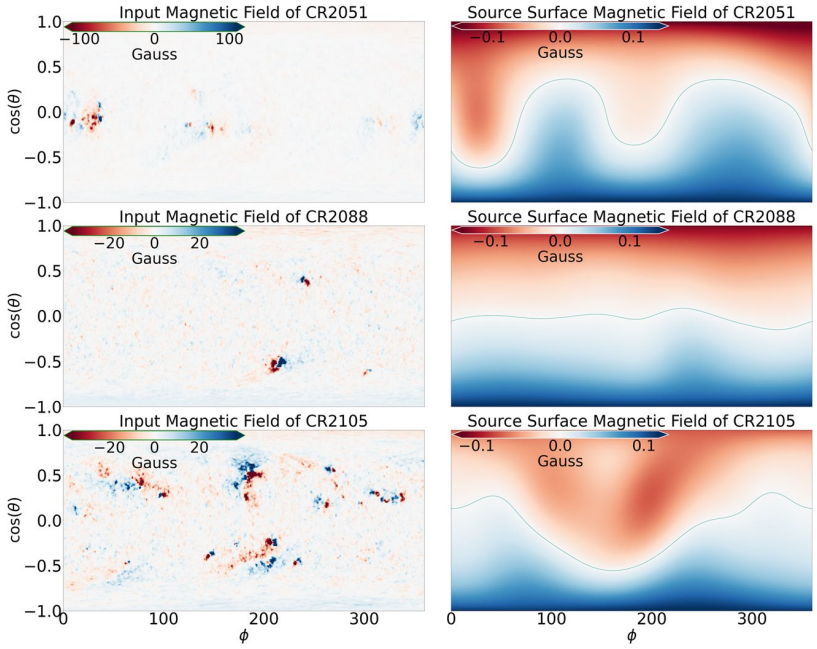

Figure 1. Input (left column) and extrapolated (right column) magnetic field at 2.5 $R_{\odot}$ in Gauss displayed for three Carrington Rotations (CRs). Top: CR2051, middle: CR2088, and bottom: CR2105. Here $\theta = 90 - \theta_{cr}$, where θ_{cr} is the Carrington Latitude.

CR2051 displays a higher range of input magnetic field in the active regions (ARs) and a more corrugated pattern of the PIL (shown by the blue line in Figure 1) in the source surface magnetic field as compared to CR2088 and CR2105 which corresponds to the deep minimum phase of cycle 23 and ascending phase of the cycle 24, respectively. For CR2088 the PIL is close to the equator representing the bipolar symmetry of CHs and absence of low latitude CHs during the deep minimum phase of the SC 23.

2.2. Empirical Velocity Relation in the Coronal Domain Using HUX

Extrapolated magnetic field lines up to the source surface give a skeleton of the magnetic field line in the inner corona because in low plasma β environment, the magnetic pressure dominates the dynamics and plasma parcels are forced to move along the magnetic field lines. Empirical SW velocity relations like WSA, WS, and DCHB give the velocity at the outer boundary (2.5 or 5 $R_{\odot}$) of the inner corona, based on the properties of the open magnetic field line (Arge et al., 2003; Riley et al., 2001). In this parametric study, we chose the best performing and well developed WSA empirical model as compared to other empirical models to estimate the SW velocity in the coronal domain (Riley et al., 2015).

The Wang-Sheeley-Arge model incorporates the effect of minimum angular distance of foot point of the field line from CH boundary, along with the expansion factor (f_s) (Arge et al., 2003). Further, it is well known that CHs produce fast streams of SW, therefore, the position of the foot point of the field line in CH plays a significant role in estimating SW velocity at outer boundary of coronal model (PFSS or SCS). The empirical relation from the WSA model (Riley et al., 2015) is used in the present work

$$v_{sw}^{wsa}(f_s, \theta_b) = v_{slow} + \frac{v_{fast} - v_{slow}}{(1 + f_s)^{\alpha}} \left(\beta - \gamma e^{-(\theta_b/w)^{\delta}}\right)^{3.5} \quad (1)$$

Here the parameters v_{slow} and v_{fast} correspond to the velocity of slowest and fastest SW stream. θ_b is the minimum angular distance for the foot point of the field line from a CH boundary at the solar surface. f_s is the expansion factor of the field line. We are calculating the expansion factor (f_s) based on flux tube expansion only to the source surface for both the magnetic field extrapolation methods. α, β, γ, δ, and w are the tunable parameters of the model Riley et al. (2015).

2.3. Extrapolation Into the Heliospheric Domain

As discussed earlier, the WSA model provides us the SW velocity maps at the outer boundary of the coronal domain, that is, at 2.5 $R_\odot$ or 5 $R_\odot$ based on the choice of magnetic field extrapolation method. For comparison with the observed SW velocities at L1 point by the in-situ spacecraft, it is required to extrapolate these velocities into the inner heliosphere. This requires coupling of the coronal velocity models (like WSA) with heliospheric velocity extrapolation models. We have employed one such model called Heliospheric Upwind eXtrapolation (HUX) (Riley & Lionello, 2011) to extrapolate from the outer boundary of the coronal domain to L1. The HUX model assumes the SW flow at the outer boundary of the coronal domain to be time-stationary. The extrapolation of the SW velocities in an r-ϕ grid can then be kinetically approximated using

$$v_{r+1,\phi} = v_{r,\phi} + \frac{\Delta r \Omega_\odot}{v_{r,\phi}} \left(\frac{v_{r,\phi+1} - v_{r,\phi}}{\Delta \phi} \right) \tag{2}$$

where, Δr and $\Delta \phi$ represent the grid spacing in r and ϕ directions respectively. $\Omega_\odot$ is the angular velocity of the Sun calculated assuming a rotation time period of 27.3 days. The HUX is essentially a 1D extrapolation model that neglects the effects of magnetic fields, pressure gradients and gravity. The advantage being that such an extrapolation method is computationally inexpensive as compared to state-of-the-art 3D MHD models, which makes it suitable for our parametric study.

2.4. Model Definitions and Parametric Space

Our framework uses two different approaches: PFSS + WSA + HUX referred as **Model1** and PFSS + SCS + WSA + HUX referred as **Model2**, with the difference being whether or not the coronal model includes a SCS model. Velocity extrapolation in the heliosphere in both the models are done using the HUX model. It is important to mention that our Model1 is similar to one of the models used in Riley et al. (2015).

We applied this framework to 60 CRs spanning the declining and minimum phase of SC 23 and the ascending phase of the SC 24. We define our parametric space to find the best parameter of WSA model for each CR as described in Table 1. Here our goal is to study the overall best performance of the framework in our parametric space (defined in the next section). Our choice of parameters values are around those obtained in previous studies on individual CRs (Kumar et al., 2020; Pomoell & Poedts, 2018; Riley et al., 2015). It is done to cover any solar cycle dependency of parameters in the model. We have broadened the range of sample space of the parameters to look for the best possible set of parameters for every CR under consideration. We have also provided practical solution for the choice of possible parameters, for example, β should be greater than γ in order to avoid mathematical errors in Equation 1. We compute the velocity profile for each possible set of combination of parameters in the WSA model in Equation 1.

For each CR we tried 23,040 ($V_{slow} \times V_{fast} \times \alpha \times \beta \times w \times \gamma \times \delta = 3 \times 3 \times 8 \times 4 \times 5 \times 4 \times 4$) combinations of set of solutions constituting all the points in our parametric space of seven parameters, that is, V_{slow}, V_{fast}, α, β, γ, δ and w, to find the optimum set of parameter values for both the models.

Table 1
Parametric Space to Find the Best Parameters of Wang Sheeley and Arge Model

V_{slow}	200–300 km s^{-1}, 3 points
V_{fast}	850–950 km s^{-1}, 3 points
α	0.1 to 0.25 step of 0.05 and 0.3 to 0.6 step of 0.1
β	1, 1.25, 1.5, and 1.75, 4 points
ω	0.01, 0.02, 0.03, 0.04, and 0.05, 5 points
γ	0.6, 0.7, 0.8, and 0.9, 4 points
δ	1, 1.25, 1.5, and 1.75, 4 points

2.5. Statistical Measures of Forecast Performance

The performance of a forecast can be assessed by comparing the forecast outcome of continuous variables (e.g., SW velocity) with the observed values. We used the OMNI data base (https://omniweb.gsfc.nasa.gov/form/dx1.html) for the observed SW velocity profiles at L1. We calculated several scalar measures of forecast accuracy which have previously been used to determine forecast performances by Reiss et al. (2016) and Wu et al. (2020). Given a set of modeled values m_n and a set of corresponding observed values o_n, Mean Absolute Percentage error (MAPE) is one such measure which is given by

$$MAPE = \frac{100}{N} \sum_{n=1}^{N} \left| \left(\frac{m_n - o_n}{o_n} \right) \right| \tag{3}$$

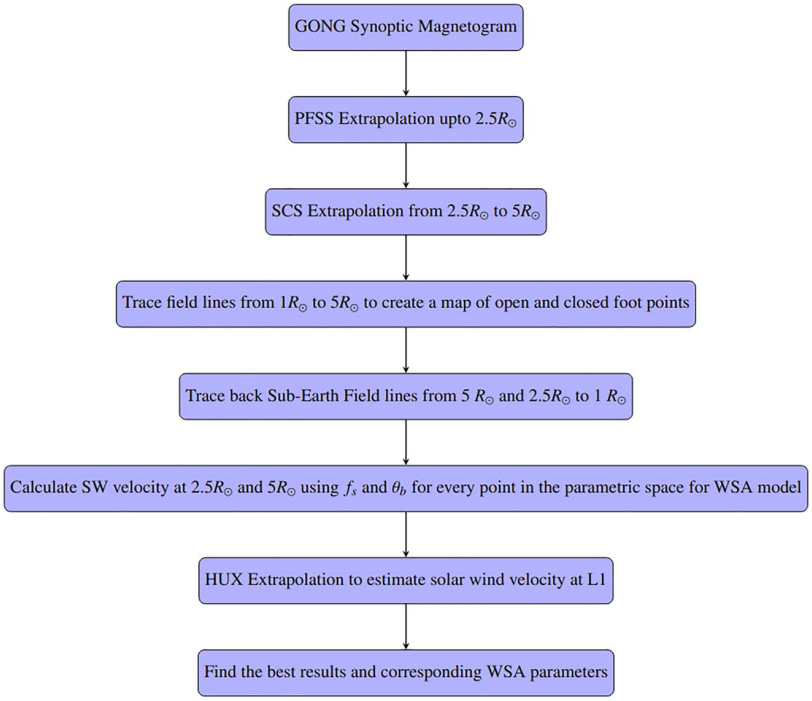

Figure 2. Flow chart explaining the steps of framework adopted in this work.

The Root Mean Square Error or RMSE is also used sometimes as a performance statistic for a model and is given by

$$RMSE = \sqrt{\frac{1}{N}\sum_{n=1}^{N}(m_n - o_n)^2} \tag{4}$$

Another important measure in determining the forecast performance is the Pearson Correlation Coefficient (cc) which can be used to estimate the correlation between the observed and the model values. In addition to this, another measure is the standard deviation (SD) of the difference between observed and simulated velocity profile.

After tracing sub-Earth field lines (from outer boundary of PFSS or SCS to photosphere to find f_s and θ_b) for each CR, we optimized the performance of the two models based on the above four quantities, by iterating the WSA parameter values from the parametric space discussed in Section 2.4. The steps adopted in the framework are explained in the flow chart shown in Figure 2.

We have done a two way analysis of the framework. In the first case, we analyzed the framework performance solely based on the cc values, that is, we estimated the highest cc in the parametric space for every CR. Next we looked for the corresponding values of the other metrices (RMSE, MAPE, and SD) as shown in the middle panels of Figure 8.

In the second case, we tried to optimize metrics other than cc. Although it is very unlikely to find a single set of the WSA parameter that can optimize all the metrics simultaneously. Moreover, some of the parameters of the WSA model (like δ and β) do not have much effect on cc, but they can alter the other metrics significantly. In addition to this, it was observed that overall lower values of RMSE, MAPE, and SD were related to higher cc values.

We put a maximum threshold tolerance equal to minimum value of each metrics (MAPE, RMSE, and SD) in the parametric space, around the minimum of MAPE and RMSE and SD for every CR. We found a common set from above individual reduced sets of metrics that are centered around the minimum of each metrics. Then we chose the highest cc from the above common set of parametric combinations. Therefore, the tolerance around the best values of the metrics and the fact that overall lower values of RMSE, MAPE, and SD were related to higher cc

values, provided us a reasonable optimization of the other metrics. This helped us to arrive at the "optimized/best" parameters in a very close proximity of highest *cc* (first method) for every CR as shown in the three panels of Figure 8.

The discussion on the optimized parameters of WSA in Section 3.2 is based on our second optimization method. Although there is no significant difference between our "optimized *cc*" along with other metrics (RMSE, MAPE, and SD), and our first method, but the values for the other metrics are significantly improved shown in the middle and bottom panels of Figure 8 for the second method. We also need to mention here that our tolerance values for RMSE, MAPE, and SD are arbitrary. Increasing their values will shift our optimized *cc* toward highest *cc*, which will lead to a significant poor optimization for other metrics as compared to our second method. This is very clear from the relative comparison of the middle and bottom panels of Figure 8. Following a more practical approach, our notion of "Model/framework performance" is exclusively based only on the values of Pearson Correlation Coefficient as shown in Figure 8 for both the methods of optimization.

3. Results on the Performance of the Framework

3.1. Case Studies of CR

In this section, we present our results of SW velocity estimation using the method described in Section 2 for CRs spanning the declining phase of cycle 23, near the solar minimum and the rising phase of SC 24. Specifically, we discuss three CRs, that is, CR2051 (from 12 December 2006 to 8 January 2007), CR2061 (from 10 September 2007 to 8 October 2007) and CR 2105 (from 24 October 2010 to 20 January 2011) as representatives of different phases of SC, in order to show the applicability of the framework for the three different phases of SC. We also discuss the limitations of the framework in view of the obtained results. This is important and holds relevance for the main conclusion of the study as discussed in Section 4.

3.1.1. CR2051

CR2051 represents a relatively quiet phase of the Sun during the decline of the SC 23. The source surface extrapolation is shown in top right panel of Figure 1. Although it shows an overall bipolar nature of the field but its PIL (shown by blue color line) which represents the location of the heliospheric current sheet (HCS) is corrugated. There are two small ARs at low latitudes during this time as shown in top-left panel of Figure 1. However, the field strength of ARs of CR2051 are much higher than the ARs shown in the CR2088 and CR2105. The source surface magnetic fields of these three CRs represent the typical evolution of cycle 23 (year 2007 and 2009) and ascending phase of cycle 24 (starting of 2011), respectively.

We present the modeled SW profile for the same period. One can easily notice that in Figure 3 the simulated/modeled SW velocity profile matches well with the observed velocity with $cc = 0.68$ for Model1 and 0.67 for Model2. Bottom panel of Figure 3 shows that our simulated velocity pattern deviates from the observed profile, only in the initial time period of the Carrington rotation. It is also worth pointing out that during this Carrington rotation, three CMEs reached at the Earth on 14, 15, and 16 December, in the beginning of this CR where the modeled values do not match with the observed values.

Furthermore, the middle and bottom panels of Figure 3 reveal that the overall observed velocity pattern matches with the θ_b profile in the inner boundary of heliosphere. This suggests that θ_b plays a relatively dominant role in the SW velocity prediction at L1 compared to the expansion factor (f_s). Moreover θ_b and f_s are inversely correlated to each other as shown in the top and middle panel of Figure 3. This is consistent with the findings of Riley et al. (2015), and implies that the field lines originating from deep within the CH having higher θ_b are expected to have a lower expansion factor (f_s).

Although the field line parameters (f_s and θ_b) for the two different models, corresponding to two different inner heliospheric boundaries follow similar trend, however small shifts in the pattern is noticeable at few instances. One of the possible reason for the shift observed could be due to the acceleration of the SW in between the space of PFSS and SCS boundaries (Riley et al., 2015).

3.1.2. CR2061 and CR2105

To discuss the applicability of our framework further to different phases of the SC, we select two Carrington rotations CR2061 and CR2105. The variation in the expansion factor for CR2061 is less as compared to the CR2051

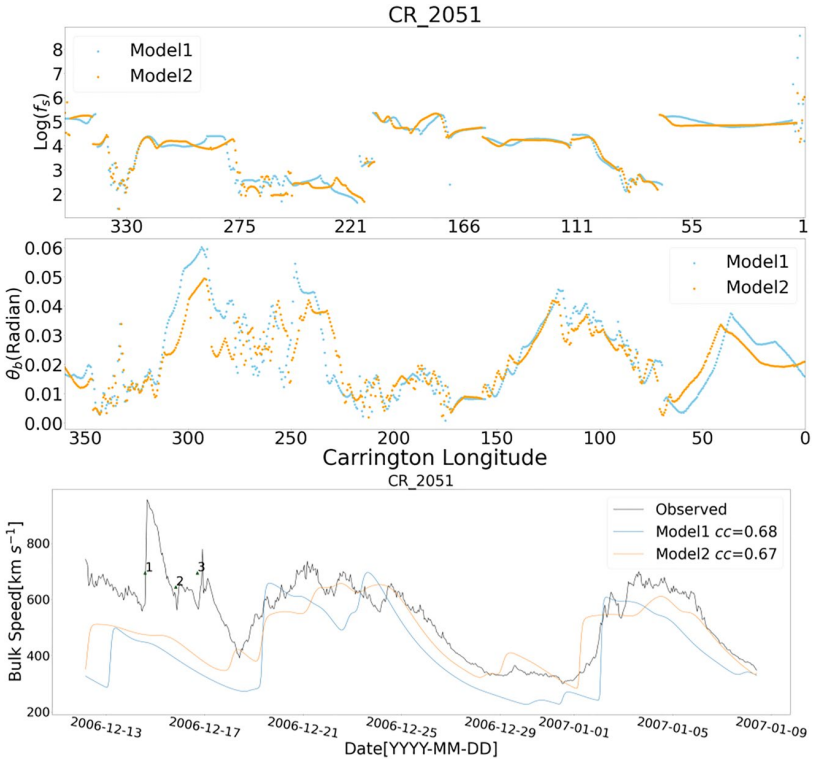

Figure 3. Plots of expansion factor (f_s) and θ_b with the Carrington longitude for CR2051 are shown in the top and middle panels, respectively. The bottom panel shows the observed velocity profile at L1 and the simulated velocity profiles obtained using two different models. Here 1, 2, and 3 mark the arrival times of coronal mass ejections.

(as shown in the top panel of Figure 4). Here, again θ_b shows an inverse correlation with f_s, this inverse correlation is found to be less as compared to the CR2051. The overall velocity pattern appears to be dominated by the profile of θ_b at the inner heliosphere. This is also expected from Equation 1 where θ_b is in the exponential term.

Our simulated and observed velocity profiles for CR2061 are shown in the third panel (from top) of Figure 4. Model1 and Model2 show a correlation of 0.75 and 0.73, respectively, with the observed SW velocity at L1. Here again, Model1 and Model2 show a similar velocity pattern. However, the deviation of the two models for the simulated velocities are larger as compared to CR2051 as shown by two simulated profiles in CR2061 (skyblue and orange curves). MAPE, RMSE, and SD values for Model2 for CR2061 are 14, 83 km s^{-1} and 96 km s^{-1} respectively, which are better than those for CR2051, that is, 14, 102 km s^{-1} and 114 km s^{-1} for MAPE, RMSE, and SD respectively.

Despite a good match of the observed and simulated velocity profiles in the later part of the velocity profile of CR2051, the statistical quantities are poorer as compared to CR2061, because of strong signatures of CMEs which occurred in the initial phase. Our simulated velocity profiles at L1 are smoother than the observed because of the fact that the HUX extrapolation method ignores pressure gradient term along with the gravity. One expects to get results that match better, if one incorporates 2D pressure gradient term (Kumar et al., 2020).

For the sake of completeness, we have also shown the velocity profile for CR2105 in the bottom panel of Figure 4, which corresponds to the ascending phase of cycle 24. This CR shows better results with $cc = 0.81$ and 0.85 for Model1 and Model2, respectively, thereby suggesting a good match of model estimates of SW velocity with that of the observed values.

3.2. Parameter Optimization for Different CRs

We tested every possible combination of the parametric space discussed in Section 2.4. The distribution of values among the final set of the best performing parameters, are provided in Figure 5 and Figure 6, for 60 CRs from

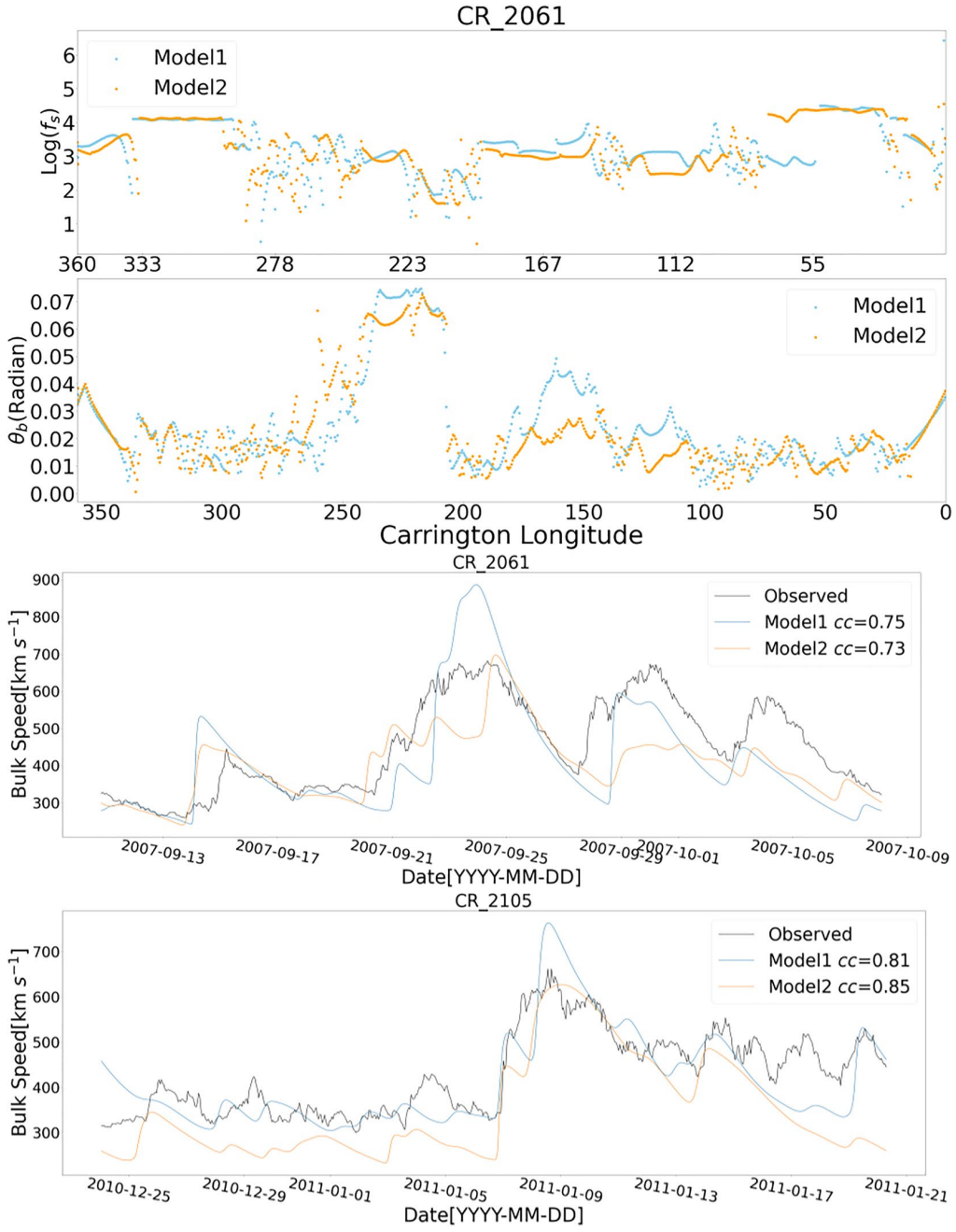

Figure 4. Plots of f_s and θ_b with the Carrington longitude for CR2061 are shown in the top first and second panel respectively. The bottom two panels show the observed velocity profile at L1 and the simulated velocity profiles obtained using two different models for CR2061 and CR2105, respectively.

CR2047 to CR2107 (excluding CR2096 with problematic SW velocity data). Although it is to be noted that our final choice of parameters for each CR is according to the second method of Section 2.5. We also would like to mention that the *cc* values obtained from two methods do not differ significantly and the overall trend of performance is same. However, the second method shows a significant improvement in metrics other than *cc* as shown in Figure 8.

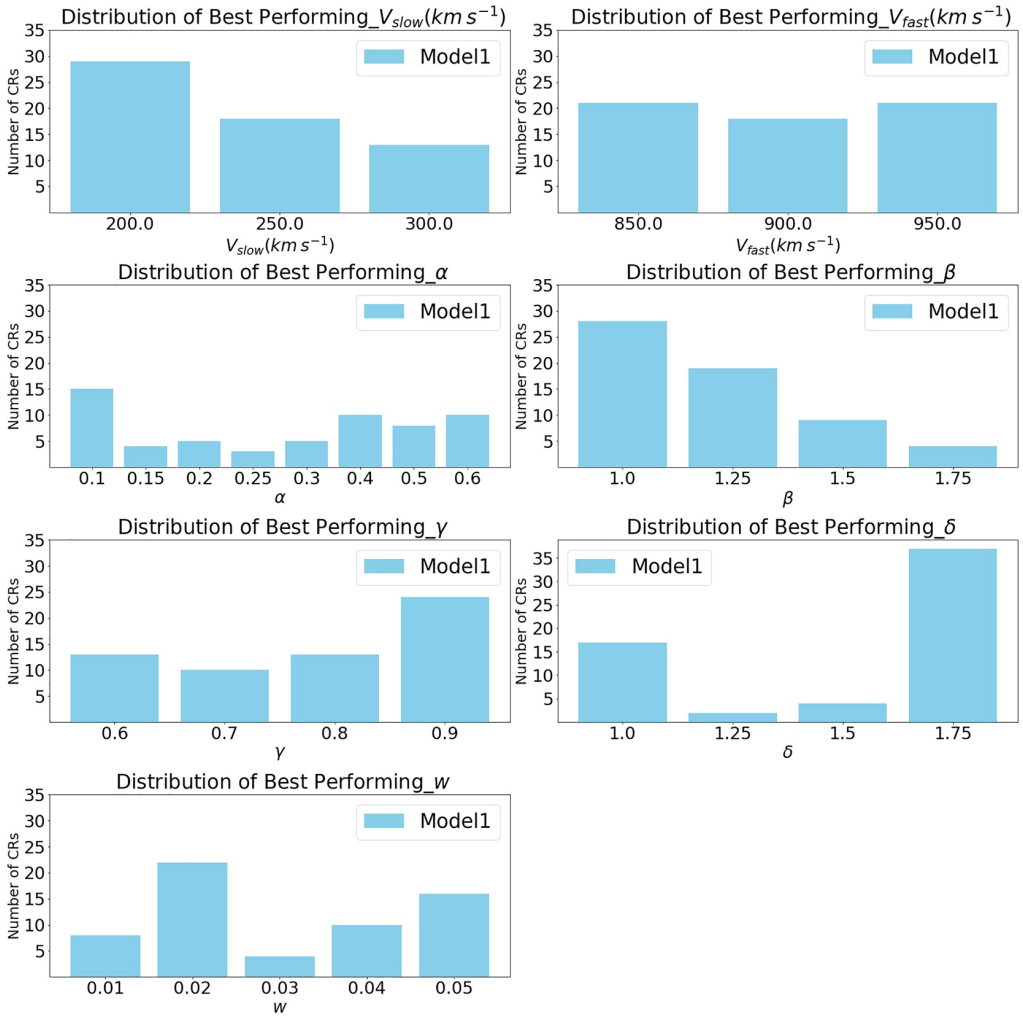

Figure 5. The distribution of values of best-performing parameters of the Wang Sheeley and Arge model among the 60 Carrington Rotations (CRs) for Model1. This is the distribution of values among the set of final best working parameters of all the CRs which give the optimized *cc* as shown in Figure 8.

Our final distribution of values of the velocity parameters (V_{slow} and V_{fast}) among the set of best working parameters for all 60 CRs show a uniform distribution as compared to other parameters for both the models, as shown in Figures 5 and 6. For both Model1 (PFSS + WSA + HUX) and Model2 (PFSS + SCS + WSA + HUX), the β parameter did not change much for the set of combinations of the best-performing parameters. It also supports the constant value of $\beta = 1$, generally used by the community (Arge et al., 2003). Further, same trend is observed for the parameter δ, as $\delta = 1.75$ is the best working value as compared to 1.0, 1.25, and 1.5.

We also note that there is a spread of values for α, γ, and w for both the models among the CRs. γ tends to be more distributed around the extreme end values (0.6 and 0.9) for Model2 as compared to Model1. Since, for both the models, w values are spread over the range of 0.01–0.05, it suggests that the performance (and the velocity values) are more sensitive to this parameter as compared to the other parameters. It is also evident from the fact that w appears in the exponential term of Equation 1.

Figure 7 shows the distribution of model performance (correlation coefficient of the modeled and simulated velocity profile) for all the CRs with those with optimum WSA parameters (second method of optimization). It is to be noted that Model1 gives better results in the sense that it results with higher *cc* (0.8–1.0) for a larger number of CRs as compared to Model2. Whereas Model2 performs reasonably well having larger number of CRs with

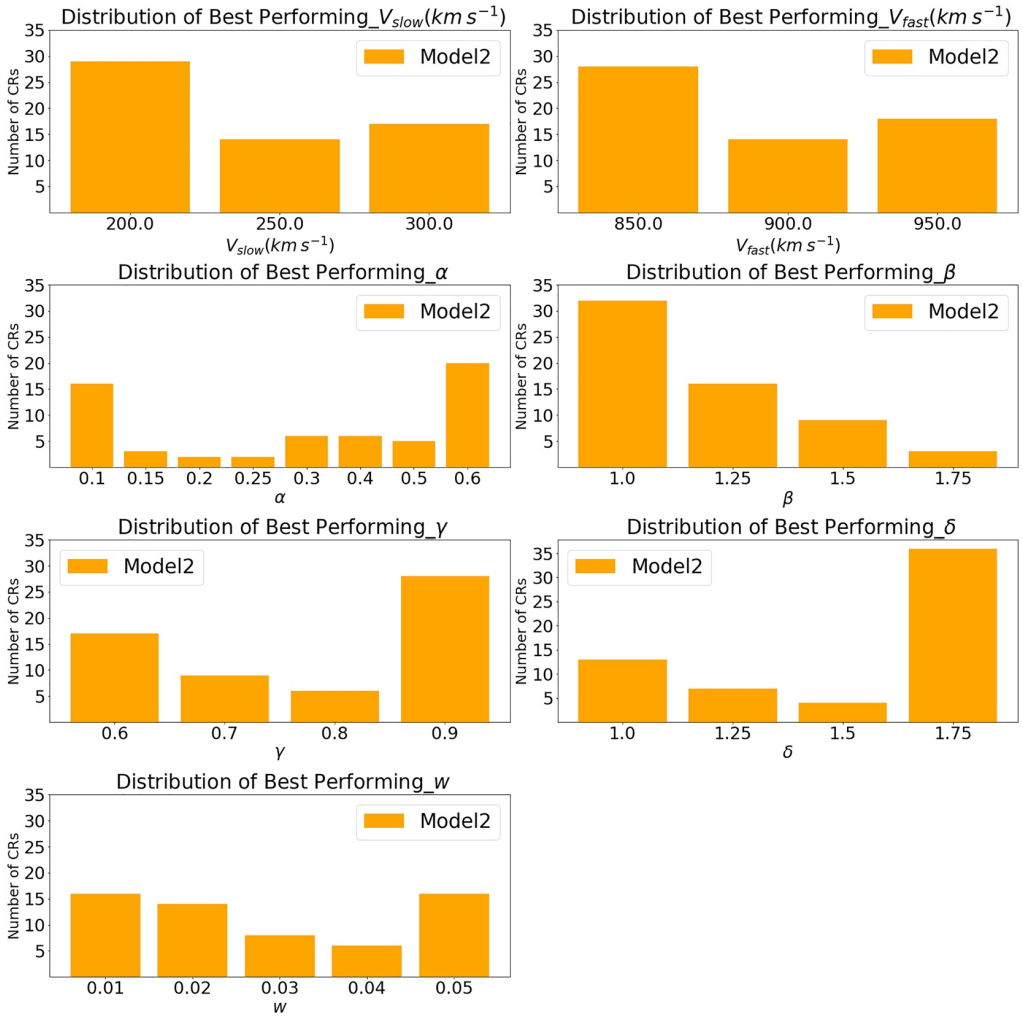

Figure 6. Same as Figure 5 for Model2.

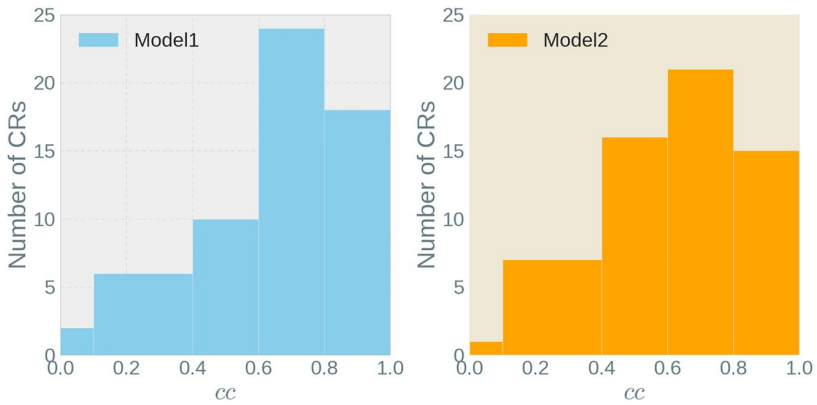

Figure 7. Histogram showing the distribution of framework performance (final best *cc* with optimum parameters) for all the Carrington Rotations (CRs). Left plot shows the distribution of *cc* (between modeled and observed SW velocity) among all the CRs for Model1 (PFSS + WSA + HUX). Right plot is a similar plot for Model2 (PFSS + SCS + WSA + HUX).

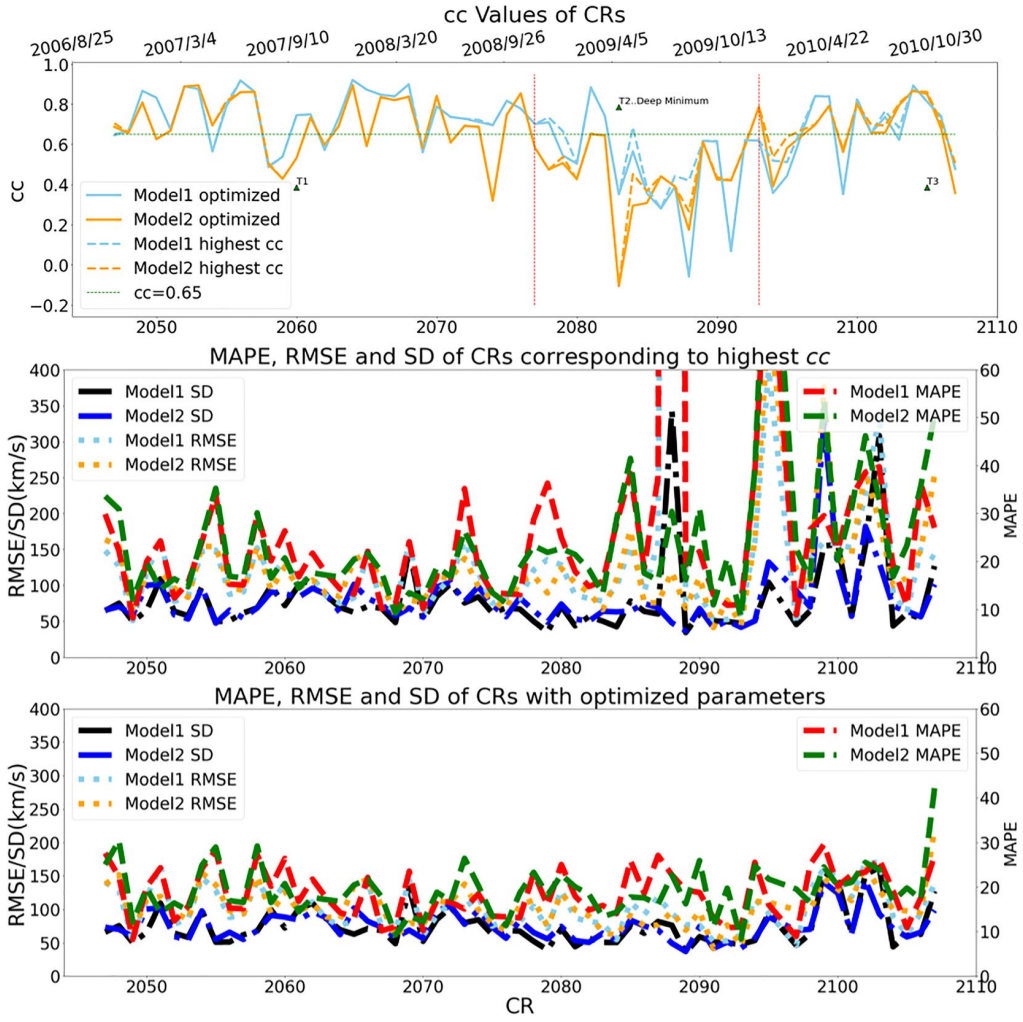

Figure 8. Top panel shows the highest *cc* (dotted lines) and optimized *cc* (solid lines) along with other metrices, for Model1 and Model2. The horizontal green dotted line corresponds to $cc = 0.65$. Middle panel shows the Mean Absolute Percentage error (MAPE), Root Mean Square Error (RMSE), and standard deviation (SD) corresponding to those highest *cc* (the dotted lines of top panel). Bottom panel shows the optimized MAPE, RMSE and SD corresponding to the solid line in the top panels.

moderate *cc* (0.4–0.8) as compared to Model1. Moreover, the average performances (*cc*) of Model1 and Model 2 are 0.65 and 0.63, respectively.

These results confirm that the final set of the values of parameters chosen are the best performing parameters. The overall trend for both the model performance (*cc* values) agrees in general with the trend obtained by Riley et al. (2015) for the period common to both the studies that is from CR2047 to CR2107. Moreover, we have also optimized other quantities like SD, MAPE, and RMSE. Our study shows that for around 60% of CRs framework performances are in the range between $0.6 < cc < 1.0$ as compared to the 37% of CRs with $cc > 0.5$ in Riley et al. (2015) for one of their best model with WSA. The improved performance reported in our study could be explained by the fact that we have optimized the parameters for each CR. Another factor that could result in better performance is that we incorporated SCS magnetic field extrapolation in our Model2.

Possible reasons for the higher correlation obtained from our analysis could be due to shorter period selected in our study or wider range of parameters, optimization of parameters for every CR or the incorporation of the SCS model in our framework in case of Model2.

Table 2
Comparison of Two Methods of Optimization (Average Values of Metrics)

Metrics	Model1	Model2
*cc*1	0.68	0.64
*cc*2	0.65	0.63
MAPE1	36.0	24.0
MAPE2	19	19
RMSE1	164	123
RMSE2	101	103
SD1	81	79
SD2	74	75

Note. Here suffix of the metric corresponds to our method of optimization.

For a comparison of two methods of optimization for *cc*, MAPE, RMSE, and SD, we have mentioned the mean values for each quantity for all the CRs in Table 2. Clearly, our second method gives an overall better optimisation for MAPE, RMSE, and SD, compared to our first method.

4. Discussion and Analysis

In this parametric study of empirical models for SW velocity prediction at L1, we have made an attempt to understand the factors affecting the performances of the empirical models namely PFSS + WSA + HUX (Model1) and PFSS + SCS + WSA + HUX (Model2). We optimized the WSA parameters for each CR. We divided the time period of our study into three parts: T1) from CR2047 to CR2077 (August 2006 to November 2008), T2) from CR2078 to CR2093 (December 2008 to January 2010) and T3) from CR2094 to CR2107 (February 2010 to December 2010). These time periods correspond to the descending, deep minimum phase of SC 23 and ascending phase of SC 24, respectively. We notice that the *cc* values for both the models (Model1 and Model2) follow a similar trend in all the three time periods without any significant deviation from each other as shown in Figure 8. Further the following important points about our framework can be highlighted.

1. In the first (T1) and third (T3) period, our framework performed significantly better as compared to the time period T2. The average *cc* of Model1 for time period T1, T2, and T3 were 0.75, 0.48, and 0.63, respectively. Performance of Model1 in T2 is less than overall average 0.65 (represented by the green dotted line in Figure 8), as the time period T2 corresponds to the deep minimum phase of the cycle 23. In case of Model2 average *cc* for T1, T2, and T3 are 0.70, 0.43, and 0.66, respectively, which shows a similar trend as Model1.
2. There are some CRs in the three time periods for which the performance of both the models is poor. For example, CR2058, CR2059, CR2068 and CR2069 in the T1, CR2083 in the T2, and CR2099 in the T3 period for which performance of our both the models (Model1 and Model2) are relatively poor as compared to the neighboring CRs.

It may be noted that time period T2 corresponds to the deep minimum phase of SC 23 where CHs are known to be located at the polar regions and thus away from the sub-Earth points (Lowder et al., 2016).

For a better interpretation, it may be important to highlight the following points about our framework

1. The HUX model extrapolates SW velocities under a steady state assumption (Riley et al., 2015).
2. The input magnetograms to the models are unreliable near the polar regions (Hoeksema et al., 2006; Prabhu et al., 2020).
3. The steady state models used in this framework are limited in the sense that they can not be used to replicate CMEs as shown in Figure 3. In the initial phase of CR, the simulated SW velocity deviates from the observed values because of velocity enhancement due to occurrence of CMEs (Kataoka et al., 2009).

The overall decreased performance in T2 can be explained on the basis of the point 2 mentioned above. To discuss it further, we calculated the observed low and mid latitudes CH (LMCH) area during the time period of our study. For our analysis we used SOHO/EIT synoptic maps. We used 19.5 nm channel images which is the most reliable for CH detection (http://satdat.oulu.fi/solar_data/). The detailed procedure for making these synoptic maps can be found in Hamada et al. (2019). We extracted the CH area of low and mid latitudes (from 60° South to 60° North) from the synoptic maps where the magnetic field measurements are most reliable in the magnetograms. We have removed 6 CRs from our data set for the present analysis for which available CH data was less than 90%. We found that during the time period T2, CH area at low and mid latitudes decreased significantly (around 50%) as shown by the red curve in Figure 9. The overall variation in LMCH area agrees with Lowder et al. (2016), during the time period coinciding with our study. CH area at low and mid latitudes, and running average of the performances of the framework (orange curve for Model2 and skyblue for Model1) are found to be correlated with each other as shown in Figure 9. All the three curves follow a similar trend. Moreover, for our second method of optimization, the performances of Model2 and Model1 show a *cc* of 0.61 and 0.33, respectively, with LMCH area. For our first method of optimization (only highest *cc* of every CR) the performances of Model2 and Model1

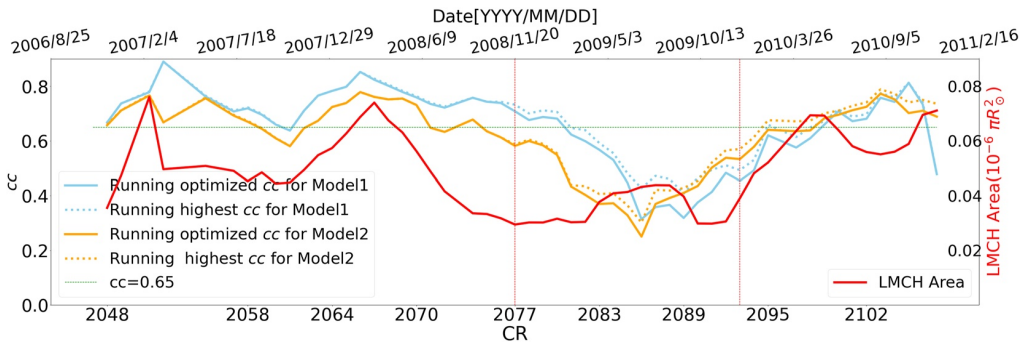

Figure 9. Running average of latitudes coronal hole (LMCH) area of six Carrington Rotations (CRs), derived from SOHO/EIT 19.5 nm channel synoptic maps (shown in Red) and running average of *cc*, of simulated solar wind velocity with the observed solar wind velocity, for Model1 (Sky Blue) and Model2 (Orange).

show a *cc* of 0.67 and 0.39, respectively, with LMCH area. Therefore, our both the methods of optimizations are consistent with the overall trend.

The performance of the empirical frameworks have been studied earlier. One such study by McGregor et al. (2008) suggested that the performance of these empirical frameworks depends upon the curvature of the current sheet near sub-Earth points, resulting in the uncertainties in determining footpoints of the sub-Earth field lines.

Based on the results of our study we suggest that significantly small, LMCH area also affected the performance of the framework in the deep minimum phase of cycle 23. Since, low and mid latitude CHs are the source regions of the SW at the Earth and mainly responsible for the SW velocity pattern at the Earth. In the case of significantly small area of LMCH (time period T2), the overall velocity pattern will be entirely governed by the polar CHs (from 60° to 90° in North and South). Further polar regions are the regions where magnetograms are mostly unreliable and their signature in the PFSS extrapolation based on these magnetograms will be erroneous leading to a poor performance of the framework. As the LMCH area starts increasing in the ascending phase of cycle 24 the overall trend of the performances of the models improves and is represented by increased average *cc* in the time period T3 as shown in Figure 9.

The common extrapolation methods of PFSS and SCS used in the present study is based on a regular $\cos\theta$ grid for solutions of the magnetic field in the region. This method is regarded erroneous as compared to a scheme based on a re-meshed magnetograms on a regular θ grid (Tóth et al., 2005).

Therefore we suggest that the framework performance can be improved for the deep minimum case if reliable observations of the magnetic field near the poles can be obtained or by using an extrapolation method on regular θ grid for PFSS and SCS. Further, relative contributions of various factors affecting the framework performance need to be explored for the deep minimum period, that is, curvature of PIL, CH area at low-mid latitudes, and the errors in the magnetic field extrapolation method.

Data Availability Statement

The authors have used Potential Field Source Surface (Altschuler & Newkirk, 1969), pfsspy (Stansby, 2019), Schatten Current Sheet (Schatten, 1972), Wang Sheeley and Arge (Riley et al., 2015), and Heliospheric Upwind eXtrapolation (Riley et al., 2001) models. The data used in this study are all publicly available. For the coronal hole data on (http://satdat.oulu.fi/solar_data/), the authors want to acknowledge Hamada, A., Asikainen, T., Virtanen, I., and Mursula, K. We want to acknowledge the Global Oscillation Network Group for magnetic synoptic maps available on https://gong.nso.edu/data/magmap/crmap.html. Solar wind velocity data are available on https://omniweb.gsfc.nasa.gov/form/dx1.html.

Acknowledgments
The authors would like to express their gratitude to the reviewers for their insightful comments and suggestions. The authors gratefully acknowledge the computational facilities of HPC Vikram-100, provided by Physical Research Laboratory Ahmedabad.

References

Altschuler, M. D., & Newkirk, G. (1969). Magnetic fields and the structure of the solar corona. I. Methods of calculating coronal fields, (Vol. *9*(1), pp. 131–149). https://doi.org/10.1007/BF00145734

Arge, C. N., Odstrcil, D., Pizzo, V. J., & Mayer, L. R. (2003, September). Improved method for specifying solar wind speed near the Sun. In M. Velli, R. Bruno, F. Malara, & B. Bucci (Eds.), *Solar wind ten*, (Vol. 679, pp. 190–193). https://doi.org/10.1063/1.1618574

Blake, J. B., Baker, D. N., Turner, N., Ogilvie, K. W., & Lepping, R. P. (1997). Correlation of changes in the outer-zone relativistic-electron population with upstream solar wind and magnetic field measurements. *Geophysical Research Letters*, *24*(8), 927–929. https://doi.org/10.1029/97GL00859

Hamada, A., Asikainen, T., & Mursula, K. (2019). New homogeneous dataset of solar EUV synoptic maps from SOHO/EIT and SDO/AIA. *Solar Physics*, *295*, 2. https://doi.org/10.1007/s11207-019-1563-y

Hoeksema, T., Benevolenskaya, E., Liu, Y., Scherrer, P., & Zhao, X. (2006). The sun's polar magnetic flux from 1996-2006 observed with SOHO/MDI.

Kataoka, R., Ebisuzaki, T., Kusano, K., Shiota, D., Inoue, S., Yamamoto, T., & Tokumaru, M. (2009). Three-dimensional MHD modeling of the solar wind structures associated with 13 December 2006 coronal mass ejection. *Journal of Geophysical Research*, *114*(A10). https://doi.org/10.1029/2009ja014167

Kumar, S., Paul, A., & Vaidya, B. (2020). A comparison study of extrapolation models and empirical relations in forecasting solar wind. *Frontiers in Astronomy and Space Sciences*, *7*, 92. https://doi.org/10.3389/fspas.2020.572084

Lee, C. O., Luhmann, J. G., Hoeksema, J. T., Sun, X., Arge, C. N., & de Pater, I. (2011). Coronal field opens at lower height during the solar cycles 22 and 23 minimum periods: IMF comparison suggests the source surface should be lowered. *Solar Physics*, *269*(2), 367–388. https://doi.org/10.1007/s11207-010-9699-9

Lowder, C., Qiu, J., & Leamon, R. (2016). Coronal holes and open magnetic flux over cycles 23 and 24. *Solar Physics*, *292*. https://doi.org/10.1007/s11207-016-1041-8

Mackay, D. H., & Yeates, A. R. (2012). The sun's global photospheric and coronal magnetic fields: Observations and models. *Living Reviews in Solar Physics*, *9*(1), 6. https://doi.org/10.12942/lrsp-2012-6

MacNeice, P., Jian, L. K., Antiochos, S. K., Arge, C. N., Bussy-Virat, C. D., DeRosa, M. L., et al. (2018). Assessing the quality of models of the ambient solar wind. *Space Weather*, *16*(11), 1644–1667. https://doi.org/10.1029/2018SW002040

McGregor, S., Hughes, W., Arge, C., & Owens, M. (2008). Analysis of the magnetic field discontinuity at the PFSS and Schatten current sheet interface in the WSA model. *Journal of Geophysical Research*, *113*(A8). https://doi.org/10.1029/2007JA012330

Odstrcil, D., Riley, P., & Zhao, X. P. (2004). Numerical simulation of the 12 May 1997 interplanetary CME event. *Journal of Geophysical Research*, *109*(A2). https://doi.org/10.1029/2003JA010135

Owens, M., Lang, M., Barnard, L., Riley, P., Ben-Nun, M., Scott, C. J., et al. (2020). A computationally efficient, time-dependent model of the solar wind for use as a surrogate to three-dimensional numerical magnetohydrodynamic simulations. *Solar Physics*, *295*(3), 43. https://doi.org/10.1007/s11207-020-01605-3

Owens, M., & Riley, P. (2017). Probabilistic solar wind forecasting using large ensembles of near-sun conditions with a simple one-dimensional "upwind" scheme: Ensemble solar wind forecasting. *Space Weather*, *15*(11), 1461–1474. https://doi.org/10.1002/2017SW001679

Pomoell, J., & Poedts, S. (2018). EUHFORIA: European heliospheric forecasting information asset. *Journal of Space Weather and Space Climate*, *8*, A35. https://doi.org/10.1051/swsc/2018020

Prabhu, A., Lagg, A., Hirzberger, J., & Solanki, S. K. (2020). The magnetic fine structure of the sun´s polar region as revealed by sunrise. *A&A*, *644*, A86. https://doi.org/10.1051/0004-6361/202038704

Reiss, M. A., Temmer, M., Veronig, A. M., Nikolic, L., Vennerstrom, S., Schöngassner, F., & Hofmeister, S. J. (2016). Verification of high-speed solar wind stream forecasts using operational solar wind models. *Space Weather*, *14*(7), 495–510. https://doi.org/10.1002/2016SW001390

Richardson, I. G., Cliver, E. W., & Cane, H. V. (2000). Sources of geomagnetic activity over the solar cycle: Relative importance of coronal mass ejections, high-speed streams, and slow solar wind. *Journal of Geophysical Research*, *105*(A8), 18203–18213. https://doi.org/10.1029/1999JA000400

Riley, P., Linker, J. A., & Arge, C. N. (2015). On the role played by magnetic expansion factor in the prediction of solar wind speed. *Space Weather*, *13*(3), 154–169. https://doi.org/10.1002/2014SW001144

Riley, P., Linker, J. A., & Mikić, Z. (2001). An empirically-driven global MHD model of the solar corona and inner heliosphere. *Journal of Geophysical Research*, *106*(A8), 15889–15902. https://doi.org/10.1029/2000JA000121

Riley, P., & Lionello, R. (2011). Mapping solar wind streams from the Sun to 1 AU. *A Comparison of Techniques*, *270*(2), 575–592. https://doi.org/10.1007/s11207-011-9766-x

Schatten, K. H. (1972). Current sheet magnetic model for the solar corona. In C. P. Sonett, P. J. Coleman, & J. M. Wilcox (Eds.) (Vol. 308, p. 44). *Potential formulation for the magnetic fields. (ref: Schatten, wilcox, 1968, a model of…)*. NASA Special Publication.

Schatten, K. H., & Wilcox, J. M. (1968). A model for interplanetary and coronal magnetic fields. *Solar Physics*.

Schwenn, R. (2006). Space weather: The solar perspective. *Living Reviews in Solar Physics*, *3*(1), 2. https://doi.org/10.12942/lrsp-2006-2

Stansby, D. (2019). *dstansby/pfsspy: pfsspy 0.1.2*. Zenodo. https://doi.org/10.5281/zenodo.2566462

Tóth, G., Sokolov, I. V., Gombosi, T. I., Chesney, D. R., Clauer, C. R., De Zeeuw, D. L., et al. (2005). Space weather modeling framework: A new tool for the space science community. *Journal of Geophysical Research*, *110*(A12), A12226. https://doi.org/10.1029/2005JA011126

Wang, Y. M., Sheeley, J., & , N., R. (1990). Solar wind speed and coronal flux-tube expansion. *The Astrophysical Journal*, *355*, 726. https://doi.org/10.1086/168805

Wu, C.-C., Liou, K., Wood, B. E., Plunkett, S., Socker, D., Wang, Y. M., et al. (2020). Modeling inner boundary values at 18 solar radii during solar quiet time for global three-dimensional time-dependent magnetohydrodynamic numerical simulation. *Journal of Atmospheric and Solar-Terrestrial Physics*, *201*, 105211. https://doi.org/10.1016/j.jastp.2020.105211

Erratum

In the originally published version of this article, a second affiliation for author Sandeep Kumar was omitted. The affiliation "Indian Institute of Technology Gandhinagar, Palaj, Gujarat, India" has been added, and this may be considered the authoritative version of record.

The Astrophysical Journal, 958:103 (8pp), 2023 December 1 https://doi.org/10.3847/1538-4357/ad011f

Rotation of a Stealth CME on 2012 October 5 Observed in the Inner Heliosphere

Sandeep Kumar[1,2], Dinesha V. Hegde[3,4], Nandita Srivastava[1], Nikolai V. Pogorelov[3,4], Nat Gopalswamy[5], and Seiji Yashiro[5]

[1] Udaipur Solar Observatory, Physical Research Laboratory, Udaipur, 313001, India
[2] Discipline of Physics, Indian Institute of Technology Gandhinagar, Palaj, Gandhinagar-382 355, Gujarat, India
[3] Department of Space Science, The University of Alabama in Huntsville, AL 35805, USA
[4] Center for Space Plasma and Aeronomic Research, The University of Alabama in Huntsville, AL 35805, USA
[5] NASA Goddard Space Flight Center, Greenbelt, MD 20771, USA
Received 2023 May 9; revised 2023 October 4; accepted 2023 October 5; published 2023 November 16

Abstract

Coronal mass ejections (CMEs) are subject to changes in their direction of propagation, tilt, and other properties. This is because CMEs interact with the ambient solar wind and other large-scale magnetic field structures. In this work, we report on the observations of the 2012 October 5 stealth CME using coronagraphic and heliospheric images. We find clear evidence of a continuous rotation of the CME, i.e., an increase in the tilt angle, estimated using the graduated cylindrical shell (GCS) reconstruction at different heliocentric distances, up to 58 $R_{\odot}$. We find a further increase in the tilt at L1 estimated from the toroidal and cylindrical flux rope fitting on the in situ observations of interplanetary magnetic field (IMF) and solar wind parameters. This study highlights the importance of observations of Heliospheric Imager (HI), on board the Solar Terrestrial Relations Observatory. In particular, the GCS reconstruction of CMEs in the HI field of view promises to bridge the gap between the near-Sun and in situ observations at the L1. The changes in the CME tilt have significant implications for the space weather impact of stealth CMEs.

Unified Astronomy Thesaurus concepts: Solar coronal mass ejections (310); Heliosphere (711)

Supporting material: animation

1. Introduction

Coronal mass ejections (CMEs) are the magnetic and kinetic storms in the heliosphere. CMEs are one of the mechanisms through which energy is released into the heliosphere. CME studies are of interest from both scientific and societal points of view. Scientifically, CMEs provide an excellent opportunity to understand the energy buildup and removal processes in the corona (Low 1996). CMEs are the primary cause of severe intense geomagnetic storms and solar energetic particles (SEPs). Geomagnetic storms can result in the enhancement of radiation belt particles that affect satellites in various ways. SEPs can also directly damage spacecraft. Thus, understanding CMEs and predicting their trajectory, time of arrival, and their impact on Earth are important for space weather forecasts.

Propagation of CMEs through the interplanetary medium is quite complex, involving expansion, rotation, and deflection due to various processes. MacQueen et al. (1986) reported that CMEs generally tend to deflect toward the equator from their respective source region near the solar minimum. Their study was based on 29 events observed by the Skylab coronagraph, which suggested that the overall bipolar magnetic field of the Sun during solar minimum may be responsible for this deflection. Deflections of a larger magnitude (≈30°) were recognized by comparing the position angles of the CME leading edge and the associated prominence core (Gopalswamy & Thompson 2000; Gopalswamy et al. 2000; Filippov et al. 2001). Cremades & Bothmer (2004) suggested deflections of CMEs by 20° toward lower latitudes due to fast solar wind flow from the polar coronal holes during solar minimum, i.e., 1996–1998. Such deflections can explain why CMEs originating at higher latitudes (up to 50°) were observed as magnetic clouds (MCs) at 1 au (Gopalswamy et al. 2008) during the rising phase of solar cycle 23. In contrast, no such deflections were observed for the events near the solar maximum, i.e., 1999–2002. Magnetic fields in low-latitude coronal holes that occur predominantly in the declining phase of the solar cycle deflect CMEs away or toward the Sun–Earth line depending on their relative location (Gopalswamy et al. 2008, 2009, 2010).

Shen et al. (2011) studied the kinematic evolution of a slow CME observed on 2007 October 8. They found that the gradient of radial field energy in the $\theta - \phi$ (heliographic latitude and longitude) sphere (constant R) pushed this CME in the regions of lower energy density, i.e., the region of the heliospheric current sheet (HCS). After its alignment with the HCS, the CME propagated almost radially. Gui et al. (2011) studied the propagation of 10 CMEs observed during 2007–2008 by applying the method of Shen et al. (2011) and found that the deflection in eight of the CMEs are consistent in strength and direction with the gradient of the magnetic energy density. An east–west asymmetry in the distribution of the sunspots related to geomagnetic storms has been known for a long time (Newton 1943) and has been confirmed using modern data by Wang et al. (2002). The east–west asymmetry of the Earth encountering halo CMEs has been found to be dependent upon the speed of the CMEs with respect to ambient solar wind speed. The source distribution of fast CMEs was found to be shifted toward the west limb of the Sun, whereas source distribution of slow CMEs was shifted toward the East limb. This asymmetry was related to the longitudinal deflection of the CMEs by the solar wind in interplanetary space (Gosling et al. 1987; Wang et al. 2004).

A CME on 2008 September 12 was studied by Wang et al. (2014) confirming the deflection of the CME not only in the

corona but also in the heliosphere. Kay et al. (2017) studied the deflection and rotation of CMEs that erupted from active region 11158 between 2011 February 13 and 16. They used the graduated cylindrical shell (GCS) and Forecasting CME's Altered Trajectory (ForeCAT) models to simulate the nonradial dynamics of CMEs driven by the magnetic forces and reported rotation of the CMEs in the range of 5°–50° in both clockwise and counterclockwise directions. Gopalswamy et al. (2022) also analyzed the solar and interplanetary causes of the third largest geomagnetic storm of the solar cycle 24. They reported a prolonged acceleration of the associated CME, which occurred on 2020 August 18, due to continued magnetic reconnection at the source region. They found multiple coronal holes and high-speed streams near the filament channel. The combined effect of these processes produced a complex rotation of the CME in the corona and interplanetary medium, resulting in a high-inclination MC with a south-pointing axial magnetic field.

When a CME is shock-driving (super-Alfvénic), it is surrounded by a shock sheath discernible in coronagraph images, first demonstrated by Sheeley et al. (2000) using the images from Large Angle and Spectrometric Coronagraphs (LASCO; Brueckner et al. 1995) on board the Solar and Heliospheric Observatory (SOHO). As a single view is insufficient to estimate the three-dimensional (3D) shapes of CMEs, a full 3D reconstruction based on geometric modeling (Thernisien et al. 2006) became possible after the advent of the Solar Terrestrial Relations Observatory (STEREO) mission (Kaiser et al. 2008).

Researchers generally use the images of COR1 and COR2 coronagraphs of the Sun–Earth Connection Coronal and Heliospheric Investigation (Howard et al. 2008) on board STEREO and LASCO/C2 and C3 on board SOHO for estimating the 3D structure, direction of propagation, and kinematics of the CMEs. Mishra & Srivastava (2014) utilized *J*-maps made from Heliospheric Imager (HI1 and HI2) observations on board STEREO to study interacting CMEs and the change in their dynamics. Their study showed that interaction between CMEs in the heliosphere could sometimes alter the kinematics of the CMEs. We present a detailed analysis of the CME observed on 2012 October 5. This CME was interesting because it led to a strong geomagnetic storm during 2012 October 8–9. The Dst profile showed a two-step decrease, first up to −95 nT in the sheath region and second up to −105 nT in the MC region. Our motivation to investigate this event is stipulated by a significant mismatch between the tilt of the CME estimated from the polarity inversion line on the solar surface and those of the MC, observed at L1 (Marubashi et al. 2017; Martinić et al. 2022). We demonstrate that this discrepancy can be explained by a continuous rotation of the CME flux rope between the Sun and Earth, resulting in a high-inclination MC at L1.

2. Observations and Analysis

The near-Sun observations of the 2012 October 5 CME have been studied in detail by Nitta & Mulligan (2017). Using the percent difference technique, they identified the source region of the CME and the tilt of the initial polarity inversion line (PIL) on the Sun. However, near the Sun, this CME was deemed to be a stealth CME making it difficult to capture the signatures of the eruption on the disk. When it appeared in the LASCO/C2 field of view (FOV) it was observed as a partial halo CME. The CME was initially seen to accelerate slowly. Nitta & Mulligan (2017) also proposed three possible source regions for the CME. These regions were not directly associated with CME, but might have contributed to the destabilization of the flux rope. Based on their analysis, they concluded that the average location of the CME source region was S25W13.

A prolonged southward component of the interplanetary magnetic field (IMF) is one of the key factors responsible for most of the intense geomagnetic storms. This depends upon the orientation of the MC associated with a CME. The tilt angle of the CME flux rope observed at 1 au is generally assumed to remain the same as the one estimated from the PIL at the Sun, if the flux rope is unaffected by the ambient structures due to interactions (Gopalswamy et al. 2022). Therefore, it is important to examine the continuous evolution of the flux rope parameters, in particular the tilt as the CME propagates from the Sun to the Earth. For this purpose, we considered the following approach:

1. In the outer corona from COR1 FOV, up to the time when the CME is visible in the HI1 images, we implemented the GCS reconstruction ($R \leqslant 60\,R_{\odot}$), using a newly developed Python module. The GCS reconstruction is a forward modeling technique to describe the self-similar expansion of a CME (Thernisien et al. 2006). GCS reconstruction model fit a flux rope to a CME defined by six parameters: latitude (θ) and longitude (ϕ) of the axis of the flux rope representing the direction of propagation of the CME; the half angle (α) representing the width of the CME between the conical legs; the tilt (γ) representing the orientation of the flux rope with respect to the ecliptic plane; the height (h) of the flux rope from the Sun and the aspect ratio (κ) show the bulkiness of the flux rope around the GCS axis.
2. At L1, we fitted the in situ magnetic field observations with the cylinder and torus models developed by Marubashi & Lepping (2007).

Figure 1 shows images of the 2012 October 5 CME at 9:54 UT with the GCS flux rope superposed. We performed the GCS fittings starting from 07:24 UT (last frame of COR2) to 20:09 UT (last HI1 frame with clear CME signature), i.e., for approximately 13 hr.

The existing open-source Python module for GCS reconstruction uses images only up to COR2 and C3 FOV (von Forstner 2021). We enhanced this existing Python module to incorporate HI1 level2 images,[6] and were able to continuously track the CME structure up to ≈58 $R_{\odot}$ (Figure 1).

In order to understand the overall evolution of this CME in the heliosphere, we compared the near-Sun tilt of the flux rope with the tilt of the CME at L1 by fitting the flux rope to the observed IMF vectors recorded by the ACE spacecraft (Stone et al. 1998).

The direction of propagation (defined by the latitude (θ) and longitude (ϕ) of the midpoint of the axis shown) of the 2012 October 5 CME is along the local HCS as shown in Figure 2. Therefore, we expect that the first two parameters of the GCS model fit, latitude (θ) and longitude (ϕ), do not change as the CME propagates through the heliosphere, an agreement with Shen et al. (2011). This will be further discussed in the next section.

[6] https://stereo-ssc.nascom.nasa.gov/data/ins_data/secchi/secchi_hi/L2_11_25/

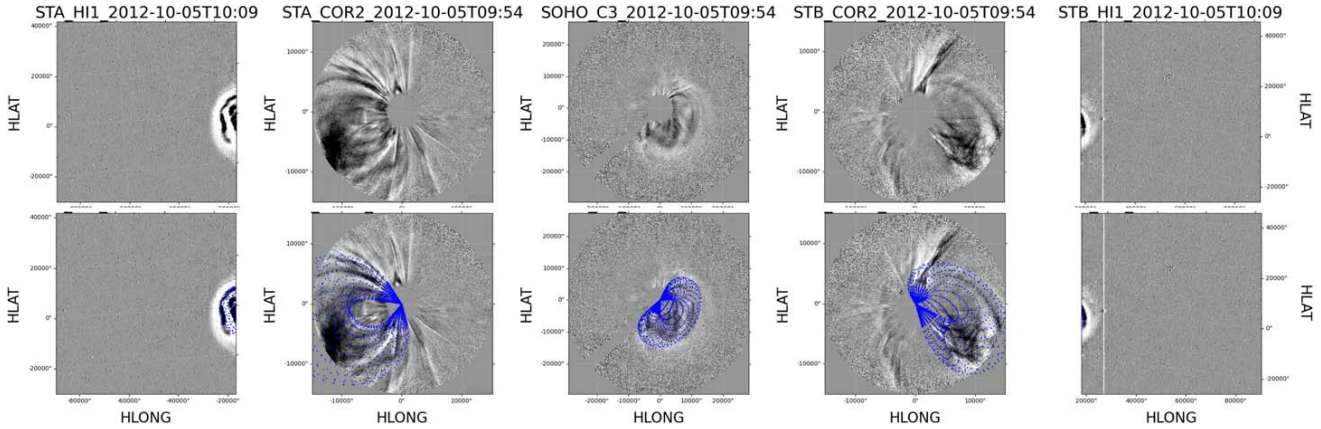

Figure 1. Snapshots of the 2012 October 5 CME in FOV of coronagraphs and heliospheric imager (upper panel) with the corresponding GCS fits (lower panel). STEREO/A (STA) HI1, COR2, respectively are shown on the left; STEREO/B (STB) COR2, HI1 on the right; and SOHO/LASCO/C3 in the middle. HI1 images are obtained at 10:09 UT and COR2 and C3 images at 9:54 UT. Here HLAT and HLONG represent heliographic latitude and longitude, respectively. The animation runs from 07:30 UT to 19:54 UT and loops three times for illustration.

(An animation of this figure is available.)

Further, we estimated the heliocentric distance where the CME attains a constant width. This height is a proxy for the height beyond which CME width is constant, and therefore, flux rope can be considered as stable (Dagnew et al. 2022). The CME was observed as a limb CME from STEREO-A (the angle between the STEREO-A and CME was about 94°.9). This offered a good opportunity to study the evolution of the width of CME and also to estimate the heliocentric height at which the flux rope attained maturity.

To understand the ambient magnetic field and solar wind background of the CME, we also used *pfsspy* (Stansby et al. 2020) for potential field source surface (PFSS) extrapolation of the photospheric magnetic field of the Sun up to 2.5 $R_{\odot}$; PFSS extrapolation also gives us an idea of the overall structure of the magnetic field even above 2.5 $R_{\odot}$. We also used Wang–Sheeley–Arge (WSA; Arge & Pizzo 2000; Arge et al. 2003) code for solar wind velocity background at 21 $R_{\odot}$ from NASA/CCMC.[7]

3. Results and Discussion

3.1. CME Orientation near the Sun

As mentioned in the Introduction, it is well known that CMEs can undergo deflection due to ambient magnetic pressure that leads to changes in the direction of their propagation, i.e., changes in latitude (θ) and longitude (ϕ) (Shen et al. 2011), in the lower corona (COR2 FOV). Moreover, continued magnetic reconnection can lead to an increase in the width and magnetic flux of CME, i.e., an increase in half angle and κ. These simultaneous changes can also lead to errors in the flux rope fitting of the CME flux using GCS model in the COR2 FOV, particularly in the shape and orientation of the CME flux rope. Therefore, to clearly capture the heliospheric evolution of the CME flux rope, we start the GCS fitting from the time frame that represents a mature CME flux rope. In order to estimate the corresponding time/height of the CME, we calculate the angular width between the CME legs and the height of the leading edge/tip of the CME from the STEREO-A/COR2 images using the CDAW online measurement tool.[8] As mentioned earlier, this was a limb event in the STEREO-A view, so we can neglect the projection effects and consider the plane-of-sky measurements as the true measurement. The top panel of Figure 2 shows the plot of angular width as a function of heliocentric distance (CME height). Here the height of the CME corresponding to the matured flux rope is referred to as the transition height (*Hc*) as defined by Dagnew et al. (2022). Figure 2 shows that *Hc* is $\approx$11 $R_{\odot}$. Therefore, we start the GCS fitting of the stable CME after its leading edge crosses *Hc*. We choose $Hc \sim 15$ $R_{\odot}$ and start the GCS model fitting at 7:24 UT.

At 7:24 UT the values of best-fit parameters of GCS reconstruction, i.e., half angle, κ, latitude, and longitude, tilt are 57°, 0.38, −14°, 14°, and 43°, respectively, at 15.8 $R_{\odot}$. The latitude and longitude of the GCS fit are close to the average location of the source region as identified by Nitta & Mulligan (2017). The values of the fitted parameters at 7:24 UT obtained here agree with those reported in Martinić et al. (2022) for the same event.

In order to study the evolution of the CME in the upcoming frames and to look for possible reasons for deflection in the direction of propagation, we examined the ambient magnetic field of the Sun as done by Shen et al. (2011). They reported that the CMEs can be deflected in the PIL region by the magnetic pressure gradient. This deflection can result in a change in the latitude (θ) and longitude (ϕ) parameters of the GCS reconstruction in the upcoming time steps. For the ambient medium, we used the PFSS extrapolation of the Sun from the GONG synoptic map of Carrington Rotation 2128. This extrapolation is a fairly good approximation of the overall magnetic field of the Sun. Then we plotted the GCS axis of the first GCS reconstruction overlaid on the PFSS extrapolated magnetic field for Carrington Rotation 2128 (CR2128) as shown in Figure 2 (bottom panel), which shows that the direction of propagation (approximate midpoint of the axis) of the CME is in the region of the local HCS/PIL (purple line). Therefore, we do not expect any force that can significantly change the direction of propagation of the CME further

[7] https://ccmc.gsfc.nasa.gov/results/index.php

[8] https://cdaw.gsfc.nasa.gov/movie/make_htmem_js.php?step=1&img1=sta_cor2rd&stime=20121005_0000&etime=20121005_1000

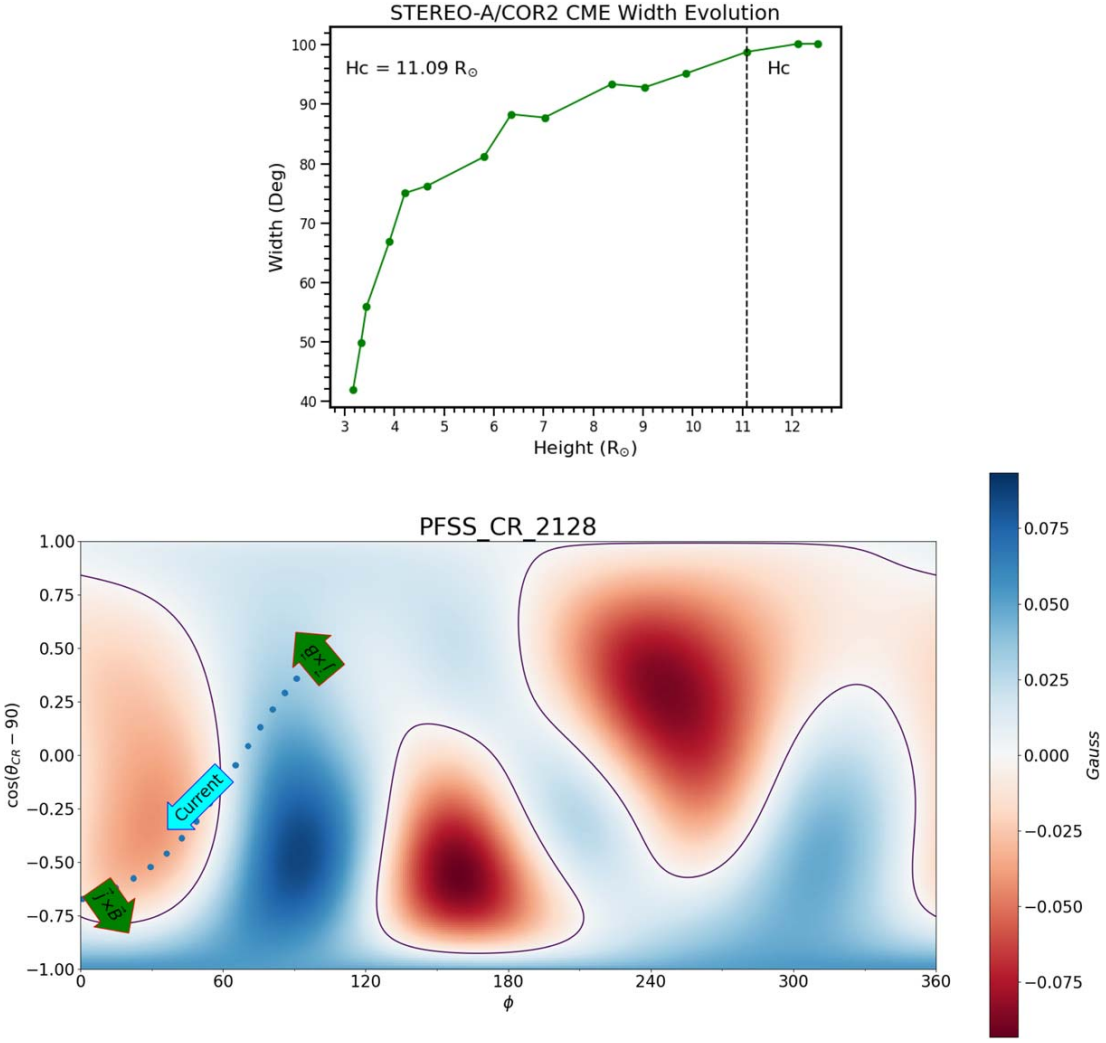

Figure 2. Top panel shows the angular width of 2012 October 5 CME in STEREO-A plotted with respect to height; here, *Hc* represents the transition height. Bottom panel shows GCS axis (blue dots) representing current along the axis of CME front projected on the PFSS extrapolated magnetic field at 2.5 $R_{\odot}$. The cyan color arrow shows the direction of the toroidal current in the CME derived from the flux rope type in Marubashi et al. (2017), Palmerio et al. (2018), and Martinić et al. (2022). The green arrows show the direction of the force on the CME.

(Shen et al. 2011). Based on the above two analyses, we expected the κ, half angle, latitude (θ), and longitude (ϕ) to remain constant above the transition height, which implies a consistent direction of propagation. We found that after the first fitting at 7:24 UT, good quality fits were obtained by changing the tilt in the upcoming time frames.

Consequently, we followed the evolution of the tilt parameter of the reconstructed CME flux rope. We considered a 2 hr interval between each GCS fit to identify significant changes in the tilt parameter. We found a gradual increase in the tilt which indicates CME rotation in the heliosphere from 15 to 58 $R_{\odot}$. Beyond 58 $R_{\odot}$ it was not possible to visualize the CME clearly in the HI1 FOV; therefore, GCS reconstruction could not be implemented in the HI2 FOV.

We also examined the effect of change in the values of other GCS parameters on the values of the tilt. This was done by four independent GCS fittings at all time steps. The independent fittings also demonstrate that the latitude and longitude are the two parameters that vary the least, i.e., not more than 3°. Therefore, we can safely consider the CME propagation direction to be constant. However, to examine a different scenario, in two of these fittings, we changed all the parameters, which showed an increase in tilt by approx 14° in HI1 FOV. In the other two independent fittings, the half angle and κ were assumed to be constant after the flux rope attained maturity, which showed a larger increase in tilt values, i.e., mean ≈28°. These independent fittings suggest that a small increase in the tilt of the flux rope could result in a corresponding increase either in κ or half angle, as compared to the constant κ and half-angle method of fitting. Therefore, an assumption of constant half angle and κ can alter the tilt values. However, it is important to mention that in two of our fittings, we consider the values of half angle and κ to be constant based on the abovementioned analysis. All four independent GCS fittings clearly show the increasing tilt of the flux rope, i.e., the rotation of CME in the HI FOV. The overall trend of the increase in tilt is clearly noticeable in the animated version of Figure 1 made from one of our independent fittings, showing ≈30° of gradual increase in tilt. This animated figure also clearly demonstrates the rotation of the fitted CME flux rope.

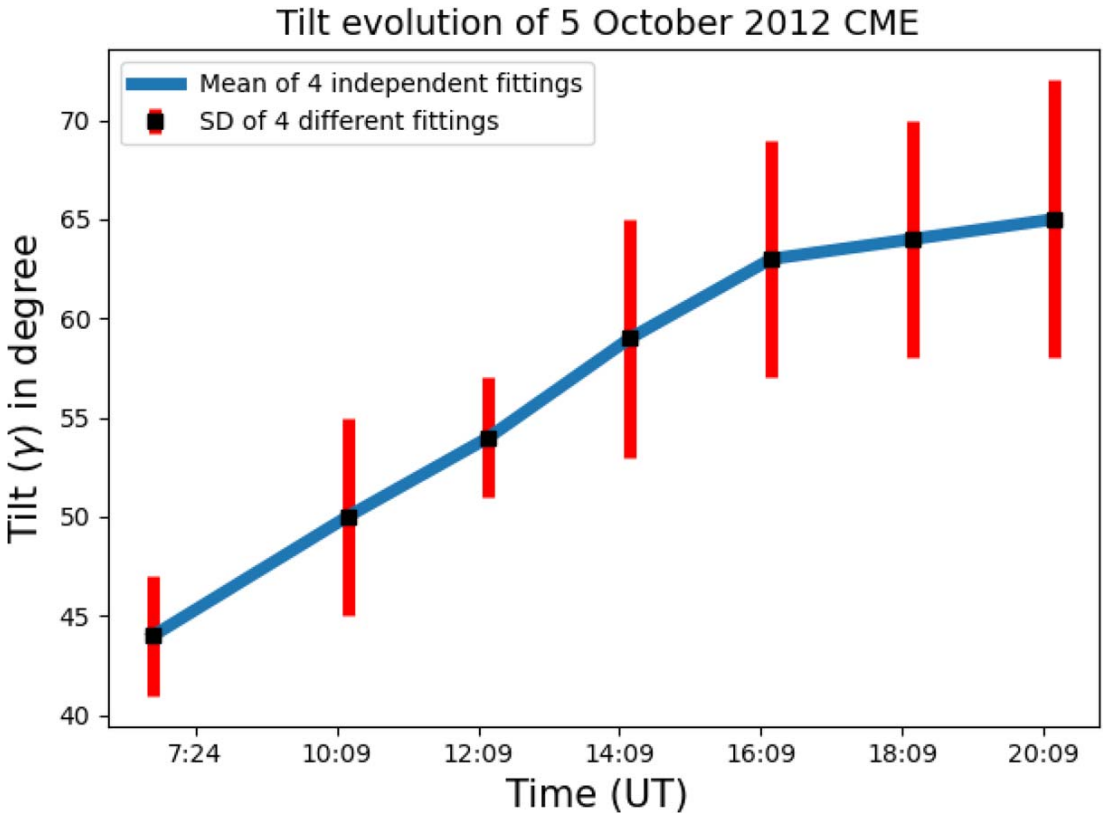

Figure 3. Evolution of tilt with respect to time of GCS fitting of the CME of 2012 October 5 in COR2 last frame and in the HI FOV. The error bars are incorporated based on four independent fittings.

(Please note that we changed the size and representations of labels in Figure 1 for a better representation, as compared to the labels in animation.) We have plotted the mean values of the CME flux rope tilt obtained from four independent fittings and the standard deviation (SD) as the error in Figure 3. This shows a 21° increase in the mean value of the tilt from $44° \pm 3°$ to $65° \pm 7°$ from 7:24 UT to 20:09 UT (approximately height ranging from 15 ± 1 $R_\odot$ to 58 ± 1 $R_\odot$). We also found as the structure evolved in the heliosphere became fainter, errors in the tilt increased as shown in the Figure 3.

Martinić et al. (2022) used the coronagraphic observations from LASCO/C2 FOV, COR2 FOV, and from LASCO/C3 FOV. Using the GCS method in COR2 FOV and the elliptical fitting method in C2 and C3 FOV, the increase in tilt reported by them agrees with our findings. Our approach incorporates continuous tracking of the CME in HI FOV and also at L1. This analysis provides clear evidence of the continuous rotation of the CME throughout the heliosphere.

3.2. CME Orientation at L1

As mentioned earlier, we used the cylindrical and toroidal models of Marubashi & Lepping (2007) to fit the flux rope to the observed IMF at L1. These two models are force-free constant-α models, providing the latitude and longitude of the flux rope axis in GSE coordinates, which can be used to derive the tilt of the axis. Figure 4 (top panel) shows the observed time evolution of solar wind IMF parameters $|B|$, B_x, B_y, and B_z, and bulk solar wind velocity (black curves). The plot shows the passage of the ICME from 17:22 UT on 2012 October 8 to 18:36 UT on October 9. It includes the shock arrival marked by the leftmost vertical line, followed by the sheath region between the left and middle vertical lines. The region between the middle and rightmost vertical lines represents the MC interval. The MC exhibits rotation in the B_y component. This shows a slow solar wind, turbulent sheath region, and the MC region. The sheath region and MC showed a prolonged southward IMF. The MC alone showed southward IMF for almost 25.5 hr, which caused a geomagnetic storm of Dst −105 nT. Based on the cylindrical flux rope fitting (tilt ≈114°) and the fitting of the toroidal flux rope (tilt ≈108°), we estimate the tilt of the flux rope at L1 to be ≈110°. This high-inclination flux rope is also consistent with the rotation observed in the B_y and negative B_z throughout the MC.

The upper plot of Figure 4 shows the Marubashi fitting of toroidal model $\text{Torus}_{\text{M03}}$ (our best fit to the observed solar wind parameters) to the MC (red line). The bottom panel of Figure 4 shows the orientation of the fitted flux rope at L1 for this model. Here the + sign shows the position of the spacecraft crossing the MC. In order to compare the tilt of the flux rope obtained by GCS fit near the Sun with that estimated at L1, we measure the tilt angle at L1, in the counterclockwise direction from the negative y-axis of the GSE coordinate system.

An earlier study by Marubashi et al. (2017) reported that the tilt of the PIL associated with this CME was around 30°. We observed a large change in orientation, i.e., in the tilt value, ≈66° (110° − 44°) in the counterclockwise direction of the CME from 15 $R_\odot$ to L1. The analysis further suggests that ≈30% of the total change in the tilt occurred below 60 $R_\odot$ and the rest in the remaining 160 $R_\odot$, thereby suggesting a

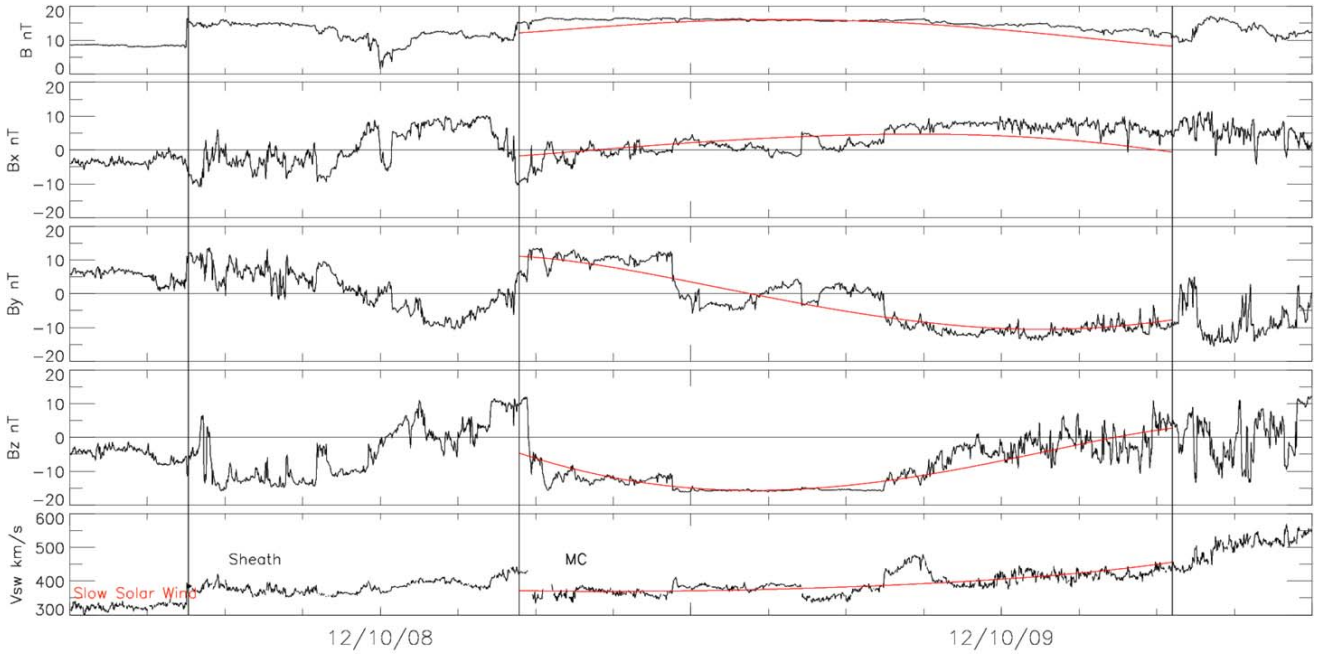

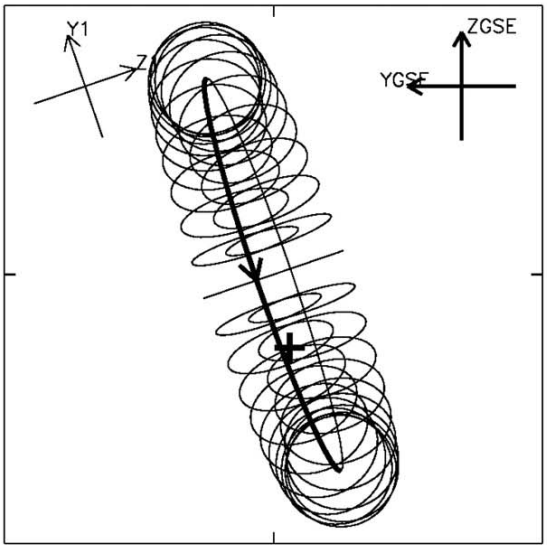

Figure 4. Top panel shows the Marubashi fitting of toroidal model ($\text{Torus}_{\text{M03}}$) with solar wind parameters in the magnetic cloud (red line) and observed solar wind parameters from ACE plotted with respect to time (YY/MM/DD), i.e., $|B|$, B_x, B_y, B_z, of IMF and bulk solar wind velocity in kilometers per second from top to bottom respectively (black curve). The bottom panel shows the orientation of the fitted flux rope at L1 for $\text{Torus}_{\text{M03}}$. Here, + sign shows the position of the spacecraft crossing the magnetic cloud. We measured the tilt angle counterclockwise from the negative y-axis of the GSE coordinate system.

continuous rotation throughout the heliosphere. Further, we note that this rotation resulted in a highly inclined flux rope at L1, leading to a prolonged (≈25.5 hr) southward component of IMF, resulting in an intense geomagnetic storm.

The increase in tilt observed near the Sun can be justified by the force acting on the toroidal current in the CME front (derived from the type of flux rope), by the ambient radial magnetic field of the Sun. Earlier observers reported an ESW type of flux rope near the Sun that had right-handed chirality with the axial field pointing southward (Marubashi et al. 2017; Palmerio et al. 2018). The direction of the current derived from the ESW type of flux rope is represented by the cyan color arrow in bottom panel of Figure 2. For ambient radial magnetic field, we used PFSS extrapolation of the photospheric magnetic field up to 2.5 $R_\odot$ from the *pfsspy* Python code (Stansby 2019) as shown in the bottom panel of Figure 2. This extrapolation gives an approximation of the magnetic field polarity and magnitude between 2.5 and 21 $R_\odot$. Beyond 2.5 $R_\odot$, nearly radial extrapolation of the field can be approximated from PFSS retaining polarity and PIL structure. Further, the torque due to the ambient radial magnetic field is acting on the CME front, making the CME rotate in a counterclockwise direction

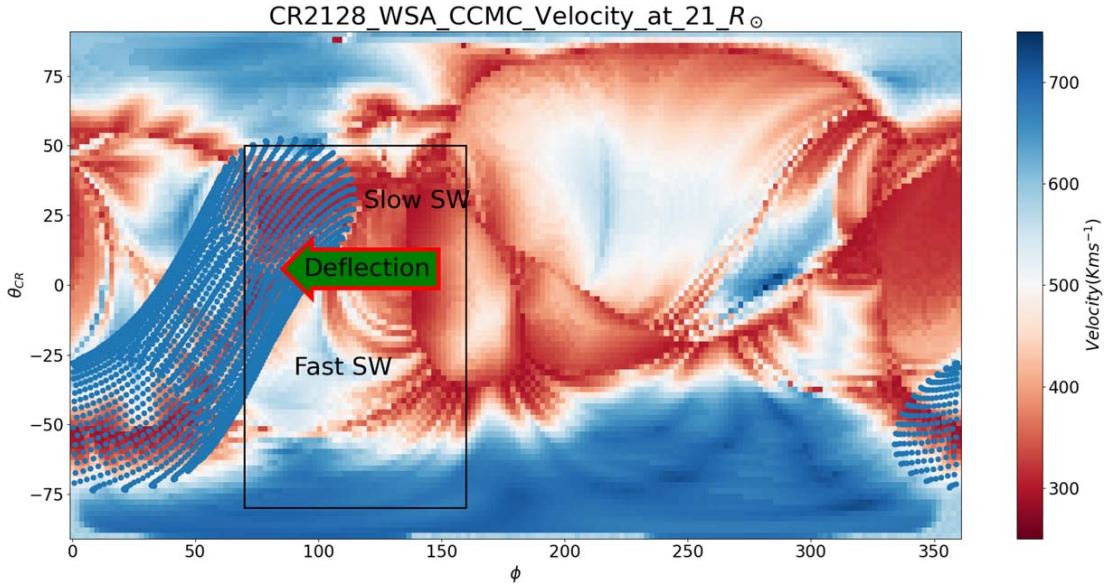

Figure 5. This figure shows the WSA velocity background of the CME at 21 $R_\odot$ from NASA/CCMC. The black rectangle specifies the inhomogeneous velocity background around the CME top front. The green arrow in the lower panel shows the deflection of the upper front of the CME due to interaction with the slow solar wind in front of it.

(Figure 2 bottom). However, this sense of rotation may hold good only up to 21 $R_\odot$ because of the dominance of the radial magnetic field within this distance (Schatten 1972).

The synoptic map of the ambient solar wind for CR2128 at 21 $R_\odot$, from NASA/CCMC,[9] is shown in the bottom panel of Figure 5. Beyond 21 $R_\odot$, the dynamics of the ambient medium are dominated by the velocity of the solar wind (Riley & Lionello 2011). Therefore, we conclude that the observed rotation in the heliosphere beyond 21 $R_\odot$ may be due to the interaction of the CME flux rope with the ambient solar wind.

We found a nonuniform solar wind velocity environment in the leading part of this CME as shown in Figure 5 (black rectangle). We found a slow solar wind ($\approx$300 km s^{-1}) flow ahead of the top part of the CME (above the green arrow, Figure 5). In contrast, the lower part of the CME faces an overall fast solar wind background in front of it (below the green arrow). The slow solar wind heading the top part of the fast CME ($v \approx 600$ km s^{-1}) can deflect the upper part of the CME in the eastward direction due to rotation of the Sun, as shown by the green arrow. Moreover, this kind of deflection is not possible in the lower part of the CME, as shown in the lower half of the black rectangle, because it faces an overall fast solar wind in front of it. This rotates the CME in the same sense in the rest of the heliosphere as provided by the force due to the ambient radial magnetic field on the CME axis, below 21 $R_\odot$. The slow solar wind ahead of the CME front is further confirmed by the slow solar wind velocity observed in in situ observations at L1 by ACE (top panel, Figure 4). Earlier studies have shown eastward deflections of fast CMEs propagating in the slow solar wind, these studies did not take into account the latitudinal extension of the CMEs in the heliosphere, whereas we base our arguments on the possibility that different parts of a CME can propagate through different environments, thereby rotating the CME as it propagates (Wang et al. 2004; Gopalswamy et al. 2009). We, therefore, believe that the interaction of the CME with the solar wind in the rest of the heliosphere led to a further increase in the tilt at L1 (Figure 4). The analysis suggests that a favorable solar wind environment can change the orientation leading to rotation of the CME, resulting in a geoeffective event. A recent study by He et al. (2018) also suggested an increase in the geoeffectiveness of a stealth CME on 2016 October 8, because of its interaction with ambient solar wind medium. Their study showed the increased geoeffectiveness was due to the interaction of the CME with the corotating interacting region in the ambient solar wind. Our study further supports the role of interaction of the ambient solar wind with the stealth CME, enhancing its geoeffectiveness at the Earth.

[9] https://ccmc.gsfc.nasa.gov/

4. Conclusions

1. The study of the evolution of 2012 October 5 CME in the heliosphere shows clear evidence of rotation of the CME as indicated by a continuous increase in the tilt from COR2 FOV, starting from 15 $R_\odot$ to HI1 FOV (up to 58 $R_\odot$). Although it was not possible to track the CME in the HI FOV beyond 58 $R_\odot$, the flux rope fitting implementation to in situ observations using the cylindrical and toroidal model of flux rope by Marubashi & Lepping (2007) resulted in an increased value of the tilt at the L1 point as compared to that measured in the last frame of HI1. This suggests a continuous increase in tilt from near-Sun to L1.
2. The 2012 October 5 CME did not leave any low coronal signatures on the disk, making it difficult for forecasters to assess its impact on Earth. The CME propagated at a moderate speed of 600 km s^{-1} near the Sun. However, it experienced a continuous increase in its tilt due to its propagation from the Sun to the Earth. This led to a prolonged southward component of the flux rope, which was responsible for its enhanced geoeffectiveness. Our

results further highlight the challenges in space weather forecasting of such stealthy CMEs. Our study demonstrates that it may be difficult sometimes to forecast the geoeffectiveness of the CMEs on the basis of the near-Sun observations alone. In this regard, HI observations prove to be crucial and bridge the gap between the near-Sun and near-Earth observation, thereby providing an improved understanding of CME propagation in the heliosphere.

Acknowledgments

We thank the reviewer for the constructive comments to improve the manuscript. We thank and acknowledge K. Marubashi for providing us the flux rope fitting code in IDL. We also acknowledge the use of ACE magnetic field and velocity data (https://izw1.caltech.edu/ACE/ASC/level2/lvl2DATA_MAG.html) and GONG program for the synoptic map data (https://gong.nso.edu/data/magmap/crmap.html). We acknowledge the use of the GCS and *pfsspy* code. We acknowledge the sunpy community (The SunPy Community et al. 2020). We acknowledge the NASA/CCMC program for providing us the WSA velocity map at 21 $R_{\odot}$. Coronagraphic images are used from Helioviewer and HI1 images from the site (https://stereo-ssc.nascom.nasa.gov/data/ins_data/secchi/secchi_hi/L2_11_25/). This work was carried out under the Indo-U.S. Science and Technology Forum (IUSSTF) Virtual Network Center project (Ref. No. IUSSTF/JC-113/2019). S.K. acknowledges the support from IUSSTF and the University of Alabama in Huntsville (UAH) for the visit to UAH during which this work was initiated. N.G. is supported by NASA's STEREO project and Living With a Star program. The work of D.V.H. was supported by NASA FINESST grant 80NSSC22K0058. N.P. was supported, in part, by NSF/NASA Space Weather with Quantified Uncertainty grant 2028154.

ORCID iDs

Sandeep Kumar https://orcid.org/0000-0002-3902-5526
Dinesha V. Hegde https://orcid.org/0000-0002-6055-1192
Nandita Srivastava https://orcid.org/0000-0002-0452-5838
Nikolai V. Pogorelov https://orcid.org/0000-0002-6409-2392
Nat Gopalswamy https://orcid.org/0000-0001-5894-9954
Seiji Yashiro https://orcid.org/0000-0002-6965-3785

References

Arge, C. N., Odstrcil, D., Pizzo, V. J., & Mayer, L. R. 2003, in AIP Conf. Ser. 679, Solar Wind Ten, ed. M. Velli et al. (Melville, NY: AIP), 190
Arge, C. N., & Pizzo, V. J. 2000, JGR, 105, 10465
Brueckner, G., Howard, R., Koomen, M., et al. 1995, SoPh, 162, 357
Cremades, H., & Bothmer, V. 2004, A&A, 422, 307
Dagnew, F. K., Gopalswamy, N., Tessema, S. B., Akiyama, S., & Yashiro, S. 2022, ApJ, 936, 122
Filippov, B. P., Gopalswamy, N., & Lozhechkin, A. V. 2001, SoPh, 203, 119
Gopalswamy, N., Akiyama, S., Yashiro, S., Michalek, G., & Lepping, R. P. 2008, JASTP, 70, 245
Gopalswamy, N., Hanaoka, Y., & Hudson, H. S. 2000, AdSpR, 25, 1851
Gopalswamy, N., Mäkelä, P., Xie, H., Akiyama, S., & Yashiro, S. 2010, in AIP Conf. Ser. 1216, Twelfth Int. Solar Wind Conf., ed. M. Maksimovic et al. (Melville, NY: AIP), 452
Gopalswamy, N., Mäkelä, P., Xie, H., & Yashiro, S. 2009, JGR, 114, A00A22
Gopalswamy, N., & Thompson, B. J. 2000, JASTP, 62, 1457
Gopalswamy, N., Yashiro, S., Akiyama, S., et al. 2022, JGRA, 127, e30404
Gosling, J. T., Thomsen, M. F., Bame, S. J., & Zwickl, R. D. 1987, JGR, 92, 12399
Gui, B., Shen, C., Wang, Y., et al. 2011, SoPh, 271, 111
He, W., Liu, Y. D., Hu, H., Wang, R., & Zhao, X. 2018, ApJ, 860, 78
Howard, R. A., Moses, J. D., Vourlidas, A., et al. 2008, SSRv, 136, 67
Kaiser, M. L., Kucera, T. A., Davila, J. M., et al. 2008, SSRv, 136, 5
Kay, C., Gopalswamy, N., Xie, H., & Yashiro, S. 2017, SoPh, 292, 78
Low, B. C. 1996, SoPh, 167, 217
MacQueen, R. M., Hundhausen, A. J., & Conover, C. W. 1986, JGRA, 91, 31
Martinić, K., Dumbović, M., Temmer, M., Veronig, A., & Vršnak, B. 2022, A&A, 661, A155
Marubashi, K., Cho, K. S., & Ishibashi, H. 2017, SoPh, 292, 189
Marubashi, K., & Lepping, R. P. 2007, AnGeo, 25, 2453
Mishra, W., & Srivastava, N. 2014, ApJ, 794, 64
Newton, H. W. 1943, MNRAS, 103, 244
Nitta, N. V., & Mulligan, T. 2017, SoPh, 292, 125
Palmerio, E., Kilpua, E. K. J., Möstl, C., et al. 2018, SpWea, 16, 442
Riley, P., & Lionello, R. 2011, SoPh, 270, 575
Schatten, K. H. 1972, in Solar Wind, ed. C. P. Sonett, P. J. Coleman, & J. M. Wilcox (Washington, DC: NASA), 44
Sheeley, N. R., Hakala, W. N., & Wang, Y. M. 2000, JGR, 105, 5081
Shen, C., Wang, Y., Gui, B., Ye, P., & Wang, S. 2011, SoPh, 269, 389
Stansby, D. 2019, dstansby/pfsspy: pfsspy v0.1.2, Zenodo, doi:10.5281/zenodo.2566462
Stansby, D., Yeates, A., & Badman, S. T. 2020, JOSS, 5, 2732
Stone, E. C., Frandsen, A. M., Mewaldt, R. A., et al. 1998, SSRv, 86, 1
Thernisien, A. F. R., Howard, R. A., & Vourlidas, A. 2006, ApJ, 652, 763
The SunPy Community, Barnes, W. T., Bobra, M. G., et al. 2020, ApJ, 890, 68
von Forstner, J. L. F. 2021, johan12345/gcs_python: Release v0.2.2, Zenodo, doi:10.5281/zenodo.5084818
Wang, Y., Shen, C., Wang, S., & Ye, P. 2004, SoPh, 222, 329
Wang, Y., Wang, B., Shen, C., Shen, F., & Lugaz, N. 2014, JGRA, 119, 5117
Wang, Y. M., Ye, P. Z., Wang, S., Zhou, G. P., & Wang, J. X. 2002, JGRA, 107, 1340

The Astrophysical Journal, 977:57 (10pp), 2024 December 10 https://doi.org/10.3847/1538-4357/ad8e63

On the Influence of the Solar Wind on the Propagation of Earth-impacting Coronal Mass Ejections

Sandeep Kumar[1,2], Nandita Srivastava[1], Nat Gopalswamy[3], and Ashutosh Dash[4]
[1] Udaipur Solar Observatory, Physical Research Laboratory, Udaipur, 313001, India
[2] Discipline of Physics, Indian Institute of Technology Gandhinagar, Palaj, Gandhinagar-382 355, Gujarat, India
[3] NASA Goddard Space Flight Center, Greenbelt, MD 20771, USA
[4] Central University of Haryana, Jant-Pali, Mahendergarh Haryana, India
Received 2024 July 20; revised 2024 October 28; accepted 2024 November 2; published 2024 December 3

Abstract

Coronal mass ejections (CMEs) are subject to changes in their direction of propagation, tilt, and other properties as they interact with the variable solar wind. We investigated the heliospheric propagation of 15 Earth-impacting CMEs observed during 2010 April to 2018 August in the field of view (FOV) of the Heliospheric Imager (HI) on board the STEREO. About half of the 15 events followed self-similar expansion up to 40 $R_{\odot}$. The remaining events showed deflection either in latitude, longitude, or a tilt change. Only 2 events showed significant rotation in the HI1 FOV. We also use toroidal and cylindrical flux rope fitting on the in situ observations of interplanetary magnetic field and solar wind parameters to estimate the tilt at L1 for these 2 events. Although the sample size is small, this study suggests that CME rotation is not very common in the heliosphere. We attributed the observed deflections and rotations of CMEs to a combination of factors, including their interaction with the ambient solar wind and the influence of the ambient magnetic field. These findings contribute to our understanding of the complex dynamics involved in CME propagation and highlight the need for comprehensive modeling and observational studies to improve space weather prediction. In particular, HI observations help us to connect observations near the Sun and near the Earth, improving our understanding of how CMEs move through the heliosphere.

Unified Astronomy Thesaurus concepts: Solar coronal mass ejections (310); Heliosphere (711); Solar wind (1534); Solar storm (1526)

1. Introduction

Coronal mass ejections (CMEs) are magnetized plasmas with high kinetic and magnetic energies in the heliosphere. Understanding the trajectory of CMEs through the heliosphere and their interaction with the surrounding solar wind helps to determine their impact on the Earth. This essentially requires multipoint remote-sensing observations of CMEs.

Previous studies of CMEs based on the observations made by the Large Angle and Spectrometric Coronagraph (LASCO; G. E. Brueckner et al. 1995) field of view (FOV) on board the Solar and Heliospheric Observatory (SOHO) mission (V. Domingo et al. 1995) suggested that CMEs follow a three-step evolutionary phase (J. Zhang et al. 2001). This includes an initiation phase, an impulsive acceleration phase, and a propagation phase. In the propagation phase, most CMEs are expected to maintain a constant direction of propagation in the heliosphere (A. Vourlidas et al. 2010). However, in some cases, CMEs are also known to get deflected in the lower corona toward the heliospheric current sheet (HCS) region due to the interaction with the ambient magnetic field of the Sun. Near the solar minimum, the HCS generally lies along the equator; during that time, CMEs are deflected toward the equator due to the bipolar structure of the magnetic field (R. M. MacQueen et al. 1986; N. Gopalswamy & B. J. Thompson 2000; B. P. Filippov et al. 2001; N. Gopalswamy et al. 2008; C. Kay et al. 2015). Using a coronal hole influence parameter (CHIP; N. Gopalswamy et al. 2009a), P. Makela et al. (2013) suggested that CMEs can be deflected by nearby coronal holes toward the polarity inversion line (PIL); they also studied the influence of coronal hole magnetic fields on magnetic cloud (MC) and non-MC-associated events. Based on the events with CHIP values larger than 2.6 G, P. Makela et al. (2013) reported that non-MC events were deflected away from the Sun–Earth line, whereas MC events were deflected toward the Sun–Earth line. Their finding supported the idea that all ICMEs are MC/flux rope, and those events that are observed as non-MC at 1 au were deflected away from the Sun–Earth line by nearby coronal holes. Based on a study of 36 CMEs observed during 2007 and 2010, S. R. Jones et al. (2017) found that 28 of the CMEs were deflected toward the HCS region. Their findings also suggest that the magnitude of deflection is directly proportional to the latitudinal distance of the CME from the HCS.

CMEs are also known to deflect in the longitudinal direction due to their interaction with the ambient solar wind. Earlier studies show that eastward heliospheric deflection of fast CMEs propagating in the slow solar wind is due to interaction with Parker spiral in the heliosphere (J. T. Gosling et al. 1987; Y. Wang et al. 2004). Such deflection leads to an asymmetry in the source region of Earth-impacting fast CMEs around the disk center of the Sun, i.e., the distribution is more biased toward the west limb of the Sun for fast CMEs. Apart from the deflection in the latitudinal and longitudinal directions, CMEs are also reported to undergo rotation in the corona and heliosphere. A rapidly rotating CME ($60^{\circ}\,\mathrm{day}^{-1}$) in the lower corona (below 5 $R_{\odot}$) was reported by A. Vourlidas et al. (2011). Previous studies have highlighted a significant disparity in the tilt of CMEs estimated near the Sun, inferred from source regions, and the tilt estimated at L1 based on in situ data (E. Palmerio et al. 2018; H. Xie et al. 2021). This observed mismatch suggests a rotation of the CME in the heliosphere. Although a few studies on CME propagation have been reported based on continuous

stereoscopic reconstruction of CMEs in the heliosphere (T. Amerstorfer et al. 2018; C. R. Braga et al. 2020; C. R. Braga & A. Vourlidas 2021; N. Gopalswamy et al. 2022), only a few of them report on the CME orientation, i.e., the tilt in HI1 images (S. Kumar et al. 2023).

Continuous tracking and stereoscopic reconstruction can help us bridge the gap between the near-Sun observations and the observations at L1. In our previous study, we reported on the continuous rotation of the 2012 October 5 CME by tracking it up to heliospheric distances of 58 $R_\odot$ using HI1 images (S. Kumar et al. 2023). A pertinent question following this finding is whether CME rotation is a rare phenomenon or not during its propagation. A single case study of the CME in the heliosphere using HI1 images is not sufficient to understand the complex dynamics and factors affecting the CME trajectory. Therefore, it is necessary to extend such a study to several cases to enhance our understanding of CME propagation in the heliosphere.

In the present work, we analyze 15 geoeffective (Dst $\leqslant -75$ nT) CMEs observed during 2010 April to 2018 August using graduated cylindrical shell (GCS) reconstruction in the corona and heliosphere. We continuously track each CME to study its trajectory in the heliosphere. We investigate and correlate the observed changes in the trajectories of the CME with the ambient medium of the CME, i.e., solar wind and magnetic field conditions of the ambient medium.

2. Observations and Analysis

2.1. Data Selection

We selected Earth-impacting CMEs that occurred between 2010 April and 2018 August and were associated with geomagnetic storms with a Dst index less than −75 nT. These events were further filtered based on the availability of data from various coronagraphs, i.e., LASCO-C2 and C3 on board SOHO and SECCHI/COR2 (R. A. Howard et al. 2008) and HI1 (C. J. Eyles et al. 2009) on board the STEREO spacecraft (M. L. Kaiser et al. 2008), allowing maximum possible viewpoints for stereoscopic reconstruction. Finally, we had 15 events, fulfilling the selection criteria. Table 1 provides a summary of these events, including the date and time of the first detection of CMEs in LASCO-C2 images. The source location mentioned in the table is taken from the CDAW Data Center, SOHO/LASCO CME catalog (https://cdaw.gsfc.nasa.gov/CME_list/; S. Yashiro et al. 2004; N. Gopalswamy et al. 2009b). We used the coronagraphic images from LASCO-C2 and C3, SECCHI/COR2, and HI1 to extend CME trajectory tracking in the FOV of HI1, i.e., up to 80 $R_\odot$. We also used the interplanetary magnetic field (IMF) data taken by the Advanced Composition Explorer (ACE; E. C. Stone et al. 1998) to model the CME flux rope at L1. We used the standard synoptic magnetic maps of the Sun from the Global Oscillation Network Group website[5] to investigate the ambient magnetic field of the Sun (F. Hill 2018). We also employed the Wang–Sheeley–Arge (WSA) model from NASA CCMC (C. N. Arge et al. 2003) to estimate the background solar wind velocity at 21 $R_\odot$.

2.2. CME Flux Rope Model in the Corona and Heliosphere

The GCS reconstruction (A. F. R. Thernisien et al. 2006) is a framework to illustrate the self-similar expansion of a CME. This model is characterized by two conical legs and a GCS representing the CME flux rope. This model has six parameters, i.e., latitude (θ) and longitude (ϕ) of the axis, the half-angle between conical legs (α), the tilt of the model axis with the ecliptic plane (γ), the axis height (h), and the aspect ratio (κ).

The initial two parameters, θ and ϕ, estimate the direction of CME propagation. The last four parameters, α, γ, h, and κ, collectively provide a description of the overall geometric configuration of the fitted CME.

We implemented the GCS reconstruction model on the images from the SOHO/LASCO-C2 and C3 and STEREO/COR2 running difference images to track the CME in the heliosphere using a module in Python[6] (J. L. F. von Forstner 2021). We enhanced the existing Python module to incorporate HI1 level2[7] images and were able to continuously track the CME structure in the HI1 FOV. A similar approach was followed by N. Gopalswamy et al. (2022), who incorporated GCS reconstruction in the HI1 images of the 2018 August 21 CME. The continuous tracking of GCS parameters allowed us to effectively fit the model to observational data up to approximately 70 $R_\odot$ (for Event 12 in Table 1).

It is important to note that for events until 2014 October, we had observations available from three viewpoints up to the LASCO-C3 FOV, i.e., STEREO-A, STEREO-B, and SOHO. For these events, we utilized data from both COR2 and HI1 and LASCO-C2 and C3. However, for events that occurred after 2014 October, we were limited to only two viewpoints up to the LASCO-C3 FOV: SECCHI/COR2 and HI1 on STEREO-

Table 1
List of 15 Earth-impacting Events Selected for Our Study

Event	Date	Time (UT)	Source Location	Dst (nT)
1[YL]	2010-04-03	10:33	S25E00	−81
2	2010-05-23	18:06	N16W10	−80
3[KG]	2011-09-06	23:05	N14W18	−75
4[SP]	2012-03-07	01:30	N15E26	−145
5	2012-07-03	21:25	N14W23	−78
6[KG]	2012-09-28	00:12	N09W31	−122
7*SK	2012-10-05	02:48	S23W31	−105
8	2013-06-02	16:25	N14W25	−78
9	2015-12-28	12:12	S23W11	−116
10	2016-01-14	23:24	S22W11	−93
11	2016-10-09	02:24	S02E39	−110
12	2017-05-23	05:00	S03W01	−125
13	2017-09-04	20:36	S10W16	−122
14	2017-09-06	12:24	S08W33	−109
15[NG]	2018-08-20	21:24	N21W08	−175

Note. Event 7 has been studied in detail by S. Kumar et al. (2023). Events with superscripts YL, KG, SP, and NG were reported in Y. Liu et al. (2011), S. Patsourakos et al. (2016), C. Kay & N. Gopalswamy (2018), and N. Gopalswamy et al. (2022a), respectively.

[5] https://gong.nso.edu/data/magmap/crmap.html

[6] https://github.com/johan12345/gcs_python

[7] https://stereo-ssc.nascom.nasa.gov/data/ins_data/secchi/secchi_hi/L2_11_25/

A and SOHO/LASCO-C2 and C3. For all events beyond the LASCO-C3 FOV, we were restricted to observations from the HI1 (STEREO-A and STEREO-B) instruments alone. Moreover, since most of the events are Earth directed within ±30° of the Sun–Earth line, the actual trackable distances using 3D GCS reconstruction of these CMEs in the LASCO-C2 and C3 FOV is larger than the normal FOV of LASCO-C2 and C3 due to projection effects.

Along with the GCS reconstruction in the HI1 FOV, we employed the cylindrical and toroidal flux rope models developed by K. Marubashi & R. P. Lepping (2007) and K. Marubashi et al. (2017) to fit IMF data at L1 observed by ACE. Both models are characterized as force-free constant-α models, offering the latitude and longitude of the flux rope axis in the Geocentric Solar Ecliptic coordinates. These coordinates, in turn, enable the estimation of the tilt of the axis of the flux rope.

2.3. Ambient Solar Wind and Magnetic Field Environment

To understand the ambient magnetic field and solar wind of the CME, we used pfsspy (D. Stansby 2019) for potential field source surface (PFSS) extrapolation of the photospheric magnetic field of the Sun up to 2.5 $R_\odot$; PFSS extrapolation also gives us an idea of the overall structure of the magnetic field even above 2.5 $R_\odot$. We also used the Wang–Sheeley–Arge (C. N. Arge & V. J. Pizzo 2000; C. N. Arge et al. 2003) code for solar wind velocity background at 21 $R_\odot$ from NASA/CCMC.[8]

3. Results and Discussion

3.1. GCS Reconstruction

Each CME selected for our analysis was tracked from the LASCO-C2, COR2, and LASCO-C3 FOV up to the last frame/time in the HI1 images. Considering uncertainties in the GCS fitting, we focused on events that exhibited a change greater than 10° in latitudes and longitudes, i.e., difference of initial and final GCS reconstruction. Our threshold for tilt change is almost twice compared to the latitude and longitude because errors in tilt can be much larger than those in latitude or longitude (S. Kumar et al. 2023). The list of selected events that showed significant change is given in Table 2. All the changes observed and listed for each case in the table were in the same direction, i.e., continuously increasing or decreasing. Note that for each event, we selected the time for the first GCS reconstruction when the CME was fully visible and the flux rope structure was well developed in the COR2 and C2 FOV. This choice was made to capture the flux rope at its mature stage. The initial height for the GCS reconstruction ranged between 6 and 14 $R_\odot$ for all events. Additionally, the final height of the GCS reconstruction was determined by the time at which the CME structure remained clearly visible and intact in the HI1 FOV. Although some faster CMEs were observable at higher distances, their features became too distorted at those heights to accurately implement the GCS model. We also estimated the average true velocity. Based on the height–time analysis of the 15 events, we conclude the following:

1. A total of 7 out of 15 CMEs did not exhibit any significant deviations from self-similar expansion, i.e., changes in the values of latitude, longitude, or tilt, indicating that CMEs reach a steady self-similar expansion state above $\approx 10 R_\odot$, as shown by A. Vourlidas et al. (2010).
2. Six events displayed significant deflection ($\geqslant 10°$) in either longitude or latitude.
3. Only two events (2012 October 5 and 2017 May 23) showed an increase in tilt, as mentioned in Table 2.
4. Two CMEs (Event 2 and 6) were latitudinally deflected toward the equator (EqW). Longitudinal deflections were observed in four events (Events 1, 3, 13, and 14) in the eastward (EW) direction.

[8] https://ccmc.gsfc.nasa.gov/results/index.php

Table 2
Summary of the Events that Showed Significant Changes in GCS Parameters

Event	First Fitted Height/Last Fitted Height	Change Observed	Velocity (km s^{-1})
1	6 $R_\odot$/49 $R_\odot$	Long. 10° EW	800
2	8 $R_\odot$/34 $R_\odot$	Lat. 10° EqW	450
3	9 $R_\odot$/54 $R_\odot$	Long. 11° EW	850
6	6 $R_\odot$/54 $R_\odot$	Lat. 10° EqW	850
7*	7 $R_\odot$/58 $R_\odot$	Tilt 21° counterclockwise	600
12	10 $R_\odot$/70 $R_\odot$	Tilt 19° counterclockwise	400
13	13 $R_\odot$/42 $R_\odot$	Long. 25° EW	1800
14	14 $R_\odot$/35 $R_\odot$	Long. 13° EW	1450

Note. Here, EW refers to eastward deflection, and EqW is Equatorward deflection, based on first independent fitting. Events 7 and 12 are the cases of CME rotation, and the asterisk denotes the event reported in S. Kumar et al. (2023).

As reported in our previous study (S. Kumar et al. 2023), GCS parameters have uncertainties associated with them (C. Verbeke et al. 2023). We also found that latitude and longitude vary the least based on the results of four independent fittings (S. Kumar et al. 2023). Therefore, to confirm the changes in latitudes and longitudes for six events (2, 6, 1, 3, 13, and 14), two independent fittings were performed by the coauthors for the events showing latitudinal and longitudinal deflection: the first fitting was done with a cadence of 1 hr, (the estimated heights from this fit are shown in Table 2, column 2), and the second independent fitting was done for the first and last images of the first independent fitting to confirm the change in the first set of fitting. As a part of the second independent fitting for the four cases of longitudinal deflection (Events 1, 3, 13 and 14) and two cases of latitudinal deflection (Events 2 and 6), we implemented GCS reconstruction on the CME structure at a time prior to the first fitting based on the well-developed CME feature. From the two independent fittings on well-developed CME features, we found similar results for latitudinal and longitudinal deflecting CMEs from two independent fittings. However, for the case of Event 12, which showed a change in tilt, three independent fittings were performed on images taken at a cadence of 1 hr, and all three fittings showed similar results. The estimated changes in the values of tilt are (i) 21° (24°–45°), (ii) 19° (13°–32°), and (iii) 20° (15°–35°).

3.2. Ambient Environment Investigation

We examined the ambient magnetic field and solar wind speed to understand the possible reasons for the deflection of the CMEs listed in Table 2.

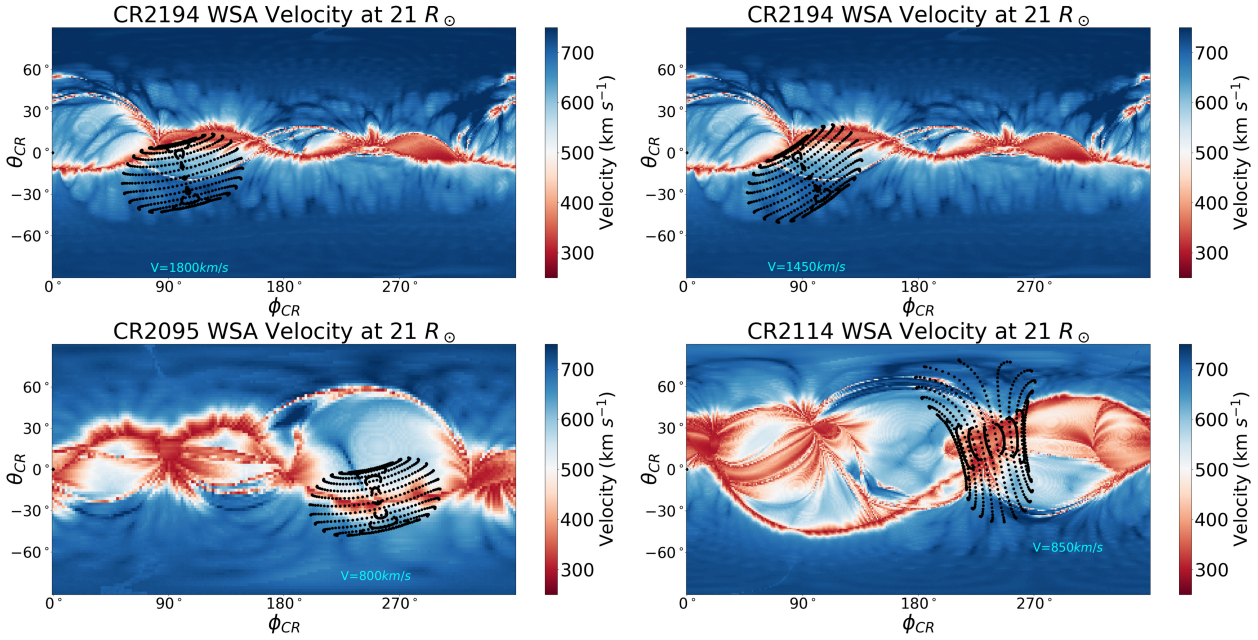

Figure 1. Solar wind velocity background at 21 $R_\odot$ of the events showing the longitudinal deflection. The top left and right panels show the background for Events 13 and 14, respectively. The bottom left and right panels show the background for Events 1 and 3, respectively. The black dotted mesh shows the position of the CME and GCS mesh, and velocities are indicated near the mesh. Events 13 and 14 are plotted with a lower half-angle and kappa than what was used in GCS fitting to show their propagation direction properly. θ_{CR} and ϕ_{CR} represent Carrington latitude and longitude, respectively.

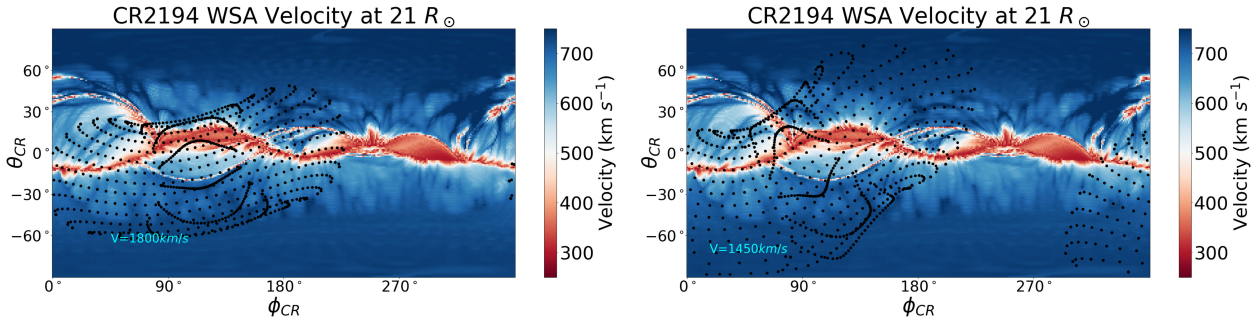

Figure 2. Solar wind velocity background of Events 13 and 14 at 21 $R_\odot$, respectively, from left to right, plotted with the actual fitted parameters of GCS reconstruction.

Figure 1 shows the solar wind background at $\approx 21 R_\odot$ for the longitudinally deflected events.

All four CMEs (Event 1, 3, 13, and 14) propagated in a slow solar wind relative to their own speeds, as illustrated in Figure 1. In this figure, Events 13 and 14 are plotted with a smaller half-angle and kappa than the actual GCS fitting to show their direction of propagation properly. In Figure 2, Events 13 and 14 are replotted with the actual GCS parameters to present the real extension of CMEs in the solar wind environment. The two fast events, 13 and 14, with average speeds of 1800 and 1450 km s^{-1}, respectively, occurred within two days and were longitudinally deflected in the eastward direction toward the Sun–Earth line.

The deflection due to solar wind drag depends on the cross-section area of CME and the difference in the speed of CME and ambient solar wind, CME density, and mass (P. J. Cargill 2004). For CMEs traveling in a similar ambient medium maintaining similar extension/shape in the heliosphere, their relative deflection depends upon their average speeds. Our analysis confirms this. For instance, fast Events 13 and 14 with velocities of 1800 and 1450 km s^{-1} were deflected by 25° and 13°, respectively. They were extremely fast events fitted with higher kappa (0.67 and 0.79, respectively) and half-angles (72° and 78°, respectively) in GCS (see Figure 2). These events propagated in nearly identical solar wind backgrounds, as shown in Figure 1 (top panel) and in Figure 2. Events 1 and 3, with near identical velocities of 800 and 850 km s^{-1}, respectively, exhibited similar magnitude of deflection ≈10°. Moreover, the dependence between the magnitude of deflection and velocities is evident when we compare Events 1 and 3 (with average velocity ≈825 km s^{-1} and average deflection 10.5°) with Events 13 and 14 (with average velocity ≈1625 km s^{-1} and average deflection 19°). For the faster events, i.e., Events 13 and 14, the solar wind drag is expected to dominate over the magnetic field interaction at lower heights, i.e., 3.4 to 4 $R_\odot$ (N. Sachdeva et al. 2017). These heights are lower than the height at which we begin the first GCS fitting, i.e., ≈ 6 $R_\odot$. Therefore, we expect the solar wind

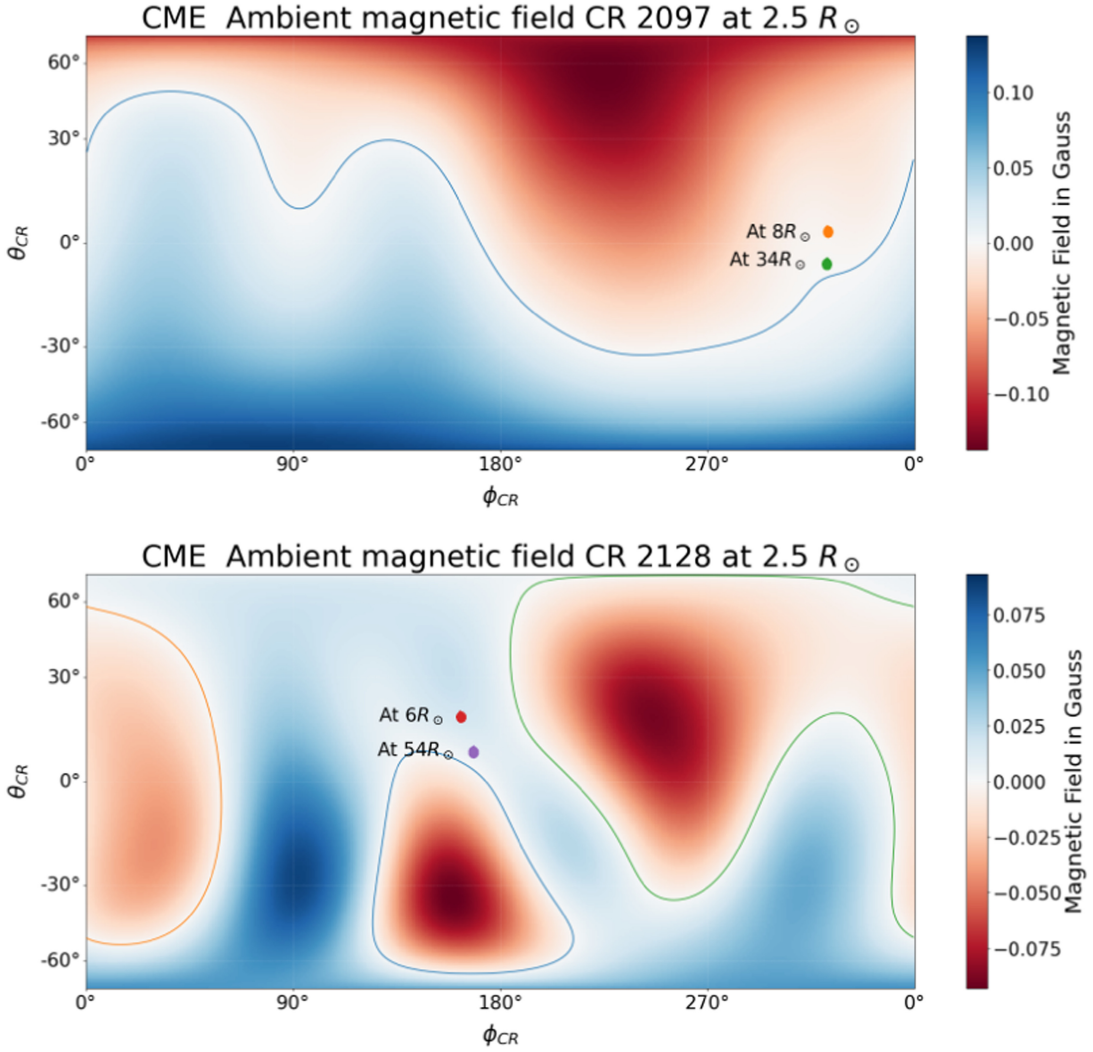

Figure 3. Magnetic field environment of the events showing the latitudinal deflection inferred from PFSS extrapolation of respective Carrington magnetic field maps. The top panel shows the 2010 May 23 CME (Event 2), and the bottom panel shows the 2012 September 28 (Event 6) CME. The color bar shows the magnetic field in Gauss. θ_{CR} and ϕ_{CR} represent Carrington latitude and longitude, respectively.

drag for Events 13 and 14 to play a significant role compared to the magnetic field in the domain of GCS reconstruction beyond 6 $R_\odot$. We investigated the magnetic field environment for Event 1 and 3 (not included in the manuscript). As these events are slower than Events 13 and 14, the ambient magnetic field environment may have influenced their propagation. However, we found that the ambient magnetic field did not influence the CME propagation for Events 1 and 3.

Figure 3 shows the magnetic field environment (extrapolated using PFSS) of the latitudinally deflected Event 2 as it propagated from 8 to 34 $R_\odot$ and Event 6 as it propagated from 6 to 54 $R_\odot$. The initial and final positions of the two CMEs indicate that they were deflected toward the HCS region. Both CMEs experienced deflection from high-magnetic-pressure regions to the low-magnetic-pressure regions toward the current sheet. Figure 3 shows the total deflection of CMEs estimated from the GCS fit to the first and last sets of images.

It has been previously reported that during solar minima, CMEs are observed to be deflected toward the equator (N. Gopalswamy & B. J. Thompson 2000; H. Cremades & V. Bothmer 2004). Studies by N. Gopalswamy et al. (2009a) and C. Shen et al. (2011) showed that the magnetic field is responsible for CME deflection. Since during the solar minimum ambient magnetic field is bipolar in nature, most of the CMEs tend to deflect latitudinally toward the equator or HCS regions, e.g., in Event 2. This deflection is from a higher-magnetic-pressure (far from HCS/PIL) region to a lower-magnetic-pressure region (near the HCS/PIL). Moreover, the deflection in Event 6 also agrees with this finding because it was deflected toward the PIL from the region that was far from PIL.

Event 2 had a speed of 450 km s^{-1} and showed a latitudinal shift due to magnetic field interaction. For this CME, magnetic field interaction is expected to dominate the drag up to 30 $R_\odot$, as reported by N. Sachdeva et al. (2017) for events with similar speeds. Interestingly, this height is very close to the height up to which this CME was tracked, i.e., 34 $R_\odot$. Therefore, for Event 2, only magnetic field interaction is expected to be dominant in the domain of CME tracking, which suggested a latitudinal deflection. Therefore, the solar wind interaction is

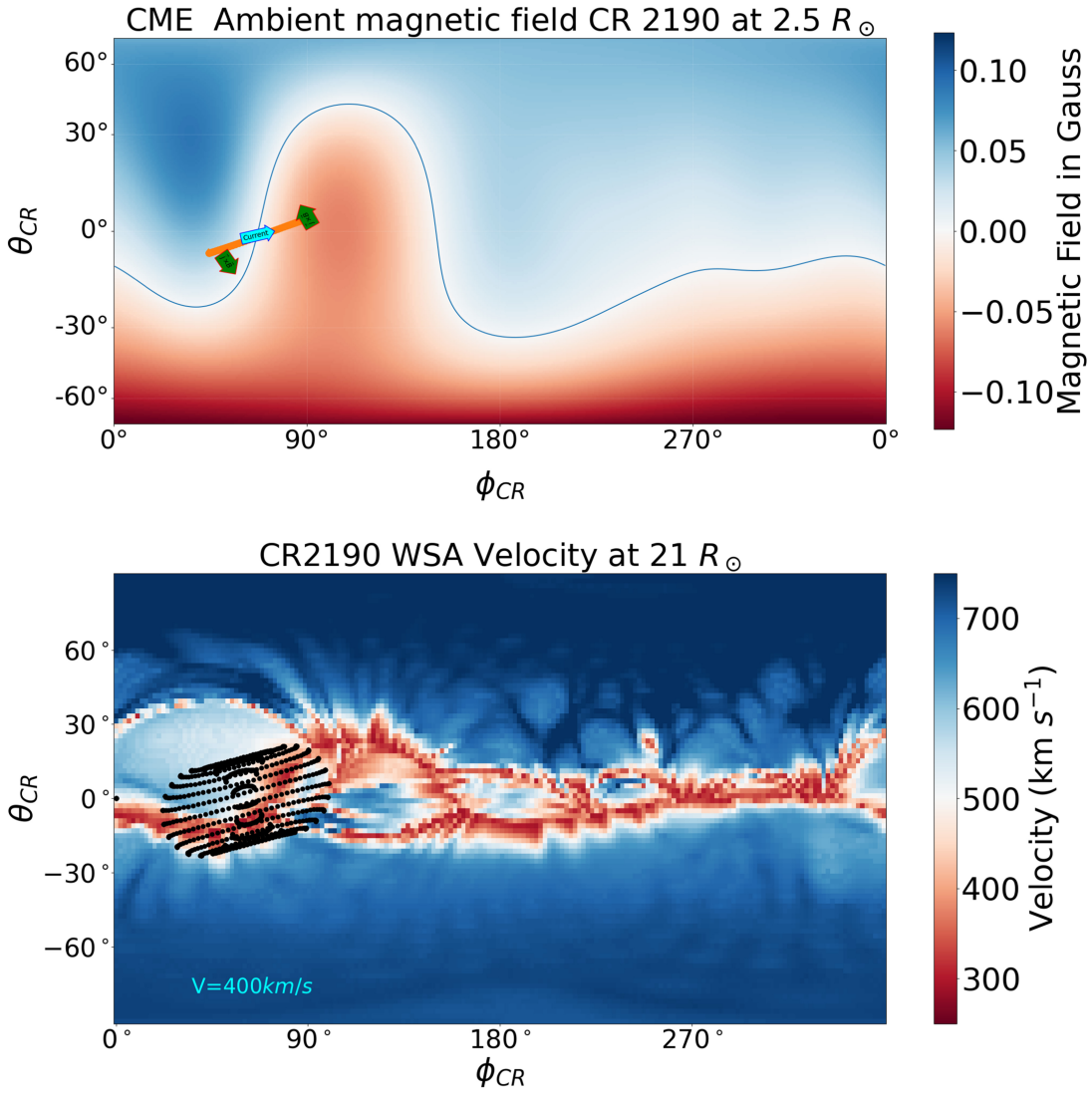

Figure 4. Radial magnetic field (top) and solar wind velocity (bottom) environment of the 2017 May 23 CME (Event 12).

not expected to play a significant role in its propagation at these heights.

We investigated the solar wind environment of Event 6 and found that it did not influence the CME propagation. Since Event 6 is a fast CME, it is expected that drag will dominate at lower heights. Therefore, the latitudinal deflection observed after 6 $R_\odot$ (on the fully developed CME feature) can also occur due to the magnetic field interaction even below the height of the first GCS reconstruction. From GCS reconstruction in the second independent fitting at lower heights, we found the latitude was higher for Events 2 and 6 at this time. This suggests that these CMEs had undergone a larger latitudinal deflection before the CME was well developed in the COR2 FOV. This kind of behavior was not observed for events that showed deflection in longitude, i.e., their latitude and longitude remained unchanged compared to the original GCS fitting on well-developed CMEs (≈6 $R_\odot$). Therefore, Event 6, despite being a fast event, retained its momentum for deflection in latitude from below 6 $R_\odot$. However, this was not the case with the other faster events with similar speeds, i.e., Events 1, 3, 13, and 14.

3.3. Events Showing Tilt Change/CME Rotation

In this section, we discuss the CME on 2017 May 23 (Event 12), which showed a change in tilt during its propagation in the heliosphere. This CME was relatively slow as compared to the other faster Events 1, 3, 13, and 14, with an average velocity of 400 km s^{-1}, which showed longitudinal deflection in the heliosphere. We reconstructed the CME from 8:24 UT on May 23 in the COR2 FOV to 10:30 UT on May 24 in the HI1 FOV. We did not find any significant change in the direction of the propagation of the CME as it propagated from 10 to 70 $R_\odot$. However, its tilt increased from 13° at 10 $R_\odot$ to 32° at 70 $R_\odot$ as it propagated in the heliosphere.

We investigated the ambient magnetic field environment of the CME and found that the direction of propagation is already aligned with the PIL/HCS, i.e., the center of the CME axis shown in the top panel of Figure 4. Moreover, there is no noticeable difference between the velocity of the CME (400 km s^{-1}) and the ambient solar wind. Therefore, we do not expect a significant deflection assuming that deflection

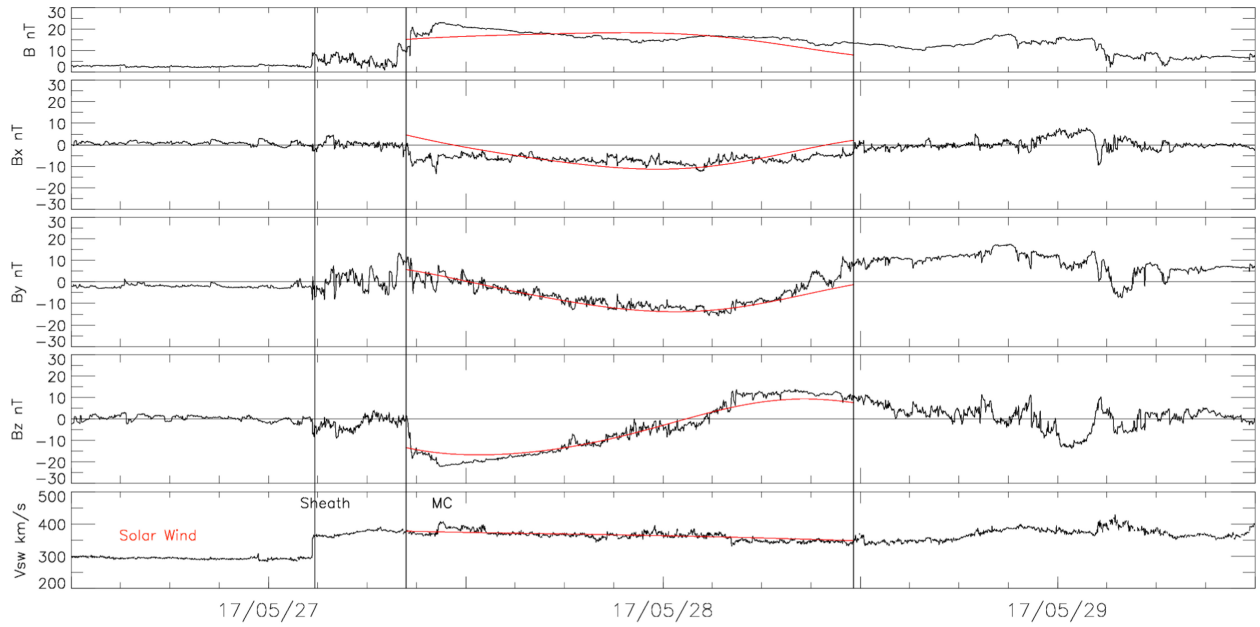

Figure 5. Fitting of the toroidal model with solar wind parameters in the MC (red line) and observed solar wind parameters from ACE plotted with respect to time (YY/MM/DD), i.e., B, B_x, B_y, and B_z, of IMF and bulk solar wind velocity in km s^{-1} from top to bottom (black curve).

occurs due to magnetic pressure difference or due to drag between ambient medium and CME, i.e., no change in the θ and ϕ of GCS parameters (Y. Wang et al. 2004; C. Shen et al. 2011). It was also evident from the values of the latitude and longitude of the CME estimated from GCS reconstruction, i.e., we did not find any significant change in the direction of the propagation of the CME.

Using Marubashi toroidal and cylindrical fitting models (K. Marubashi & R. P. Lepping 2007; K. Marubashi et al. 2017), we found a low inclination for the flux rope at L1 for the 2017 May 23 CME. It is also evident from the rotation of the B_z in the IMF vectors with prolonged B_y shown in Figure 5, i.e., the signature of the south–west–north (SWN) flux rope. Its tilt at the L1 was estimated ≈40°, which is similar to that estimated from the last GCS reconstruction in the HI1 FOV, i.e., ≈32°. It suggests that this CME rotated by a smaller angle beyond 70 $R_\odot$, i.e., from 32° to 40°.

We investigated the ambient magnetic field using the PFSS model for the 2017 May 23 CME to understand the role of the magnetic field in its propagation. The top panel of Figure 4 shows the ambient magnetic field for the 2017 May 23 CME. As we can see, on the left of the PIL, the magnetic field is directed radially outward in the blue color region, and it is directed radially inward in the red region. Based on the in situ observations of the IMF, we also identified the SWN type of flux rope associated with the CME. The direction of the current in this type of flux rope is from south to north, as shown by the cyan color arrow along the axis of the CME. Green arrows at the end show the direction of the torque on the CME. The bottom panel of Figure 4 shows the solar wind velocity background for the 2017 May 23 CME. This CME is much less spread in the θ–ϕ plane, i.e., half-angle 22°, and there is a smooth, slow, and fast solar wind velocity ahead of the CME front.

In our previous study of the 2012 October 5 CME (Event 7), we observed a continuous rotation of the CME from 44° at around 15 $R_\odot$, approximately 65° at 58 $R_\odot$, and 110° at L1. This rotation was attributed to two factors: the $\boldsymbol{J} \times \boldsymbol{B}$ torque (Lorentz force) within the flux rope, particularly below 21 $R_\odot$, and interaction with the solar wind above this boundary. The CME was an extended structure in the θ–ϕ plane with a half-angle of 52°. Figure 5 in S. Kumar et al. (2023) showed distinct regions of slow and fast solar wind ahead of the CME. A nonuniform velocity profile was noted ahead of the leading edge of the fast CME, with slow solar wind preceding the upper segment and fast solar wind preceding the lower part. Interaction between the slow solar wind and the fast-moving upper segment of the CME caused an eastward deflection due to solar rotation, while the lower segment of the CME faced predominantly fast solar wind. The interaction with the ambient magnetic field and solar wind gave the CME a consistent sense of rotation throughout the heliosphere.

The direction of the current ($\boldsymbol{J}$) in the 2017 May 23 CME and ambient magnetic field ($\boldsymbol{B}$) were both reversed near the Sun in comparison to the 2012 October 5 CME (bottom panel of Figure 2 in S. Kumar et al. 2023). Therefore, we found a consistent sense of $\boldsymbol{J} \times \boldsymbol{B}$, as shown in top panel of Figure 4 for both the events, i.e., counterclockwise.

The 2017 May 23 CME is much less spread in the θ–ϕ plane as compared to the 2012 October 5 CME, i.e., lower half-angle (22°), and there is a homogeneous/mixed solar wind background ahead of the CME front. Moreover, there is no significant difference between the velocity of the CME (400 km s^{-1}) and the ambient medium solar wind velocity. Therefore, we do not expect the same kind of solar wind interaction in the 2017 May 23 CME as observed in the 2012 October 5 CME, i.e., no rotation due to solar wind interaction. Since the solar wind drag operates throughout the heliosphere, we expect the rotation of Event 7 due to drag to be long-lasting as compared to Event 12, which rotated only because of the magnetic field interaction.

In a recent study, K. Martinić et al. (2023) estimated the drag parameters (γ) for the 2012 October 5 CME and 2017 May 23 CME as 0.502 and 0.065, respectively, using the reverse drag

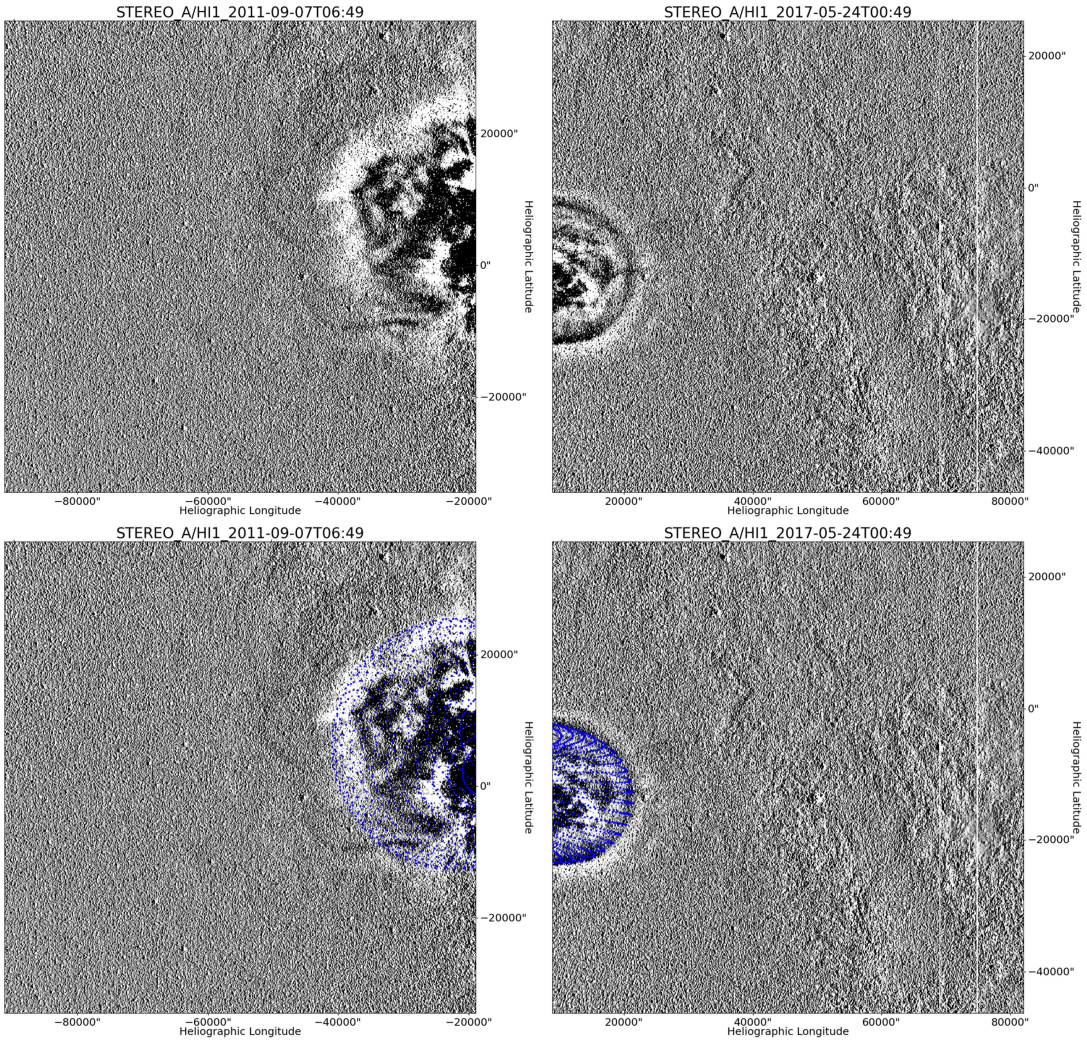

Figure 6. The 2011 September 7 CME (Event 3) with velocity ≈850 km s^{-1} on the left showing a disturbed, noncoherent structure at the heliocentric distance of ≈37 $R_{\odot}$ estimated from GCS reconstruction. The 2017 May 23 CME (Event 12) on the right with velocity ≈400 km s^{-1} showing a coherent circular structure at ≈48 $R_{\odot}$ in the HI1 FOV. The top panel shows the CME structure without the GCS mesh, and the bottom panel shows the CME with the GCS mesh overplotted on it (one can clearly notice the differences in the quality of fit between the two cases).

technique (DBEMv3 tool; J. Čalogović et al. 2021). The γ parameter in their model is directly proportional to the cross-sectional area of the CME in the heliosphere. Also, the cross-sectional area increases with kappa and half-angle in the GCS model. Therefore, our results are in agreement with K. Martinić et al. (2023) as we obtained a higher half-angle and kappa for the October event (52°, 0.48) than that of the 2017 May 23 event (22°, 0.38). A lower value of drag parameter for the 2017 May 23 CME compared to the 2012 October 5 CME provides evidence of a weaker drag interaction of the 2017 May 23 CME with the solar wind as compared to the 2012 October 5 CME. This is confirmed by the higher change in the tilt of the 2012 October 5 CME compared to the May CME while propagating in the drag-dominated regime.

Therefore, for the 2017 May 23 CME, only the magnetic field environment was in favor of its rotation, whereas for 2012 October 5, both the factors, i.e., magnetic field and ambient solar wind velocity, were in favor of its rotation.

It is worth mentioning that the overall shape of the two CMEs that rotated remained consistent and coherent throughout their propagation, which made it possible to implement GCS reconstruction on the CME structure and to estimate the GCS model parameters with less ambiguity. This contrasted with the other faster events analyzed in this paper, where such consistency and coherency in CME structure in HI1 images were lacking (Figure 6). Furthermore, we observed that the fast CMEs in our data set were fitted with larger values of kappa, which agrees with previous studies by A. Pluta et al. (2019). As kappa increased, we encountered difficulty in distinguishing the quality of GCS fits with different tilts on the images. It became challenging to differentiate the projection of the GCS mesh with different tilts for those CMEs that were fitted with higher kappa values.

4. Conclusions

An analysis of 15 geoeffective CMEs observed by SOHO/LASCO-C2 and C3, STEREO/SECCHI COR2, and HI1 reveals that CME propagation can be influenced by ambient

J. Space Weather Space Clim. 2025, **15**, 24

https://doi.org/10.1051/swsc/2025021

JSWSC

Available online at:
www.swsc-journal.org

RESEARCH ARTICLE OPEN ACCESS

On the role of source surface height and magnetograms in solar wind forecast accuracy

Sandeep Kumar[1,2,*], Nandita Srivastava[1], Dana-Camelia Talpeanu[3], Marilena Mierla[3,4], Elke D'Huys[3], and Marie Dominique[3]

[1] Udaipur Solar Observatory, Physical Research Laboratory, Udaipur 313001, Rajasthan, India
[2] Discipline of Physics, Indian Institute of Technology Gandhinagar, Palaj, Gandhinagar 382 355, Gujarat, India
[3] Solar-Terrestrial Centre of Excellence – SIDC, Royal Observatory of Belgium, 1180 Brussels, Belgium
[4] Institute of Geodynamics of the Romanian Academy, Str. Jean-Louis Calderon 19–23, 020032 Bucharest, Romania

Received 24 October 2024 / Accepted 8 May 2025

Abstract – Many operational space weather forecasting frameworks are based on the Potential Field Source Surface (PFSS) model of the magnetic field. The output of PFSS serves as input in many heliospheric models that provide solar wind velocity predictions at L1. Previous studies in the context of prediction of open magnetic flux observed at L1 have suggested different source surface heights (R_{ss}) for the PFSS model at different phases of the solar cycle (SC). We investigate the effects and necessity of optimizing the R_{ss} in the PFSS model in the context of its use in the popular Wang-Sheeley-Arge (WSA) model for solar wind velocity prediction. We used Heliospheric Upwind Extrapolation (HUX) to extrapolate solar wind velocity in the heliosphere. We performed a study of 16 Carrington Rotations (CR) at different phases of the SC24 and SC25, using different types of magnetograms and WSA model parameters. We combine the coronal models (PFSS+WSA) with the heliospheric model (HUX) to predict solar wind velocity at L1 in our framework, i.e., PFSS+WSA+HUX. Our study suggests that using a higher R_{ss} (3.0 $R_{\odot}$) compared to the conventional R_{ss} (2.5 $R_{\odot}$) near the solar minimum, results in an improvement in the average Pearson's correlation coefficient (*cc*) from 0.61 to 0.75 between the observed and modeled values of solar wind velocity profile at L1. We found that the performance of the framework improved by using zero-point corrected (ZPC) maps in comparison to the standard (STD) Carrington maps from GONG, as demonstrated by an increase in the correlation coefficient from 0.31 to 0.51. We also found that the improved performance of the framework for ZPC maps as compared to the STD full Carrington maps, can be attributed to its capability to capture the global magnetic field. This was further confirmed by comparing the extrapolated global magnetic field structures with the large-scale corona observed in the extended field of view of the PROBA2/SWAP images. Our work is a first step in the direction of improving the WSA model and points out the potential ways to enhance the PFSS+WSA framework of solar wind forecasting at L1.

Keywords: Solar wind / Potential field source surface / Magnetograms / Heliosphere / Wang-Sheeley-Arge

1 Introduction

Many of the semi-empirical physics-based operational space weather forecasting frameworks, such as Wang-Sheeley-Arge (WSA)-ENLIL (Arge & Pizzo, 2000; Odstrcil et al., 2004), European heliospheric forecasting information asset (EUHFORIA; Pomoell & Poedts, 2018), and Space Weather Adaptive Simulation Framework for Solar Wind (SWASTi; Mayank et al., 2022), are based on magnetic field extrapolation models. These frameworks combine the coronal magnetic field and heliospheric models to forecast the solar wind properties at L1. Generally, the Potential Field Source Surface (PFSS; Schatten et al., 1969) extrapolation model, which provides an overall magnetic field environment, is used as an input in empirical solar wind models. PFSS is the first-order and lowest-energy approximation of the magnetic field of the Sun as compared to other computationally expensive and more advanced magnetic field models like Nonlinear Force-Free Field (NLFFF; Wiegelmann, 2004; He et al., 2011) and Linear Force-Free Field (LFFF; Alissandrakis, 1981) models. Further, there is a class of models providing full 3D MHD treatment to the coronal domain, such as Alfvén Wave Solar Model (AWSoM; van der Holst et al., 2014) and data-driven COolfluid COroNa UnsTructured (COCONUT; Perri et al., 2022) model. The quick

*Corresponding author: ssandeepsharma201@gmail.com

computation time makes PFSS a suitable choice for use in operational space weather forecasting frameworks. The magnetic field from PFSS is used as an input in empirical solar wind models like Wang-Sheeley (WS; Wang & Sheeley, 1990), Distance from Coronal Hole Boundary (DCHB; Riley et al., 2001), and the Wang-Sheeley-Arge (WSA; Arge et al., 2003).

The main PFSS parameter is the height of the source surface, and it is crucial for the extrapolation of the field above the photosphere. Kruse et al. (2020) also investigated the effects of changing the shape of the source surface from a sphere to an ellipsoid. The source surface height (R_{ss}) in the PFSS model defines the upper boundary where the magnetic field lines are open and radial in the heliosphere. This parameter has two physical effects. First, R_{ss} controls the open flux in the heliosphere. Second, this height also changes the overall magnetic field structure and connectivity of the Sun to the Earth.

Due to the change in the state of the solar magnetic field structure with the phase of the solar cycle (SC), the source surface height is expected to change accordingly (Schatten et al., 1969). This change in source surface height can be studied through various observable outputs provided by the PFSS model. These outputs include the open flux at L1, which can be compared with interplanetary magnetic field (IMF) data from in situ observations. The PFSS model can also be used to estimate the photospheric footpoints of the open field lines. These footpoints can then be compared to coronal hole (CH) locations in different wavelengths in synoptic images (Lowder et al., 2017).

Recently, Meyer et al. (2020) used a global non-potential coronal magnetic field model to estimate the global magnetic field structure, which was compared with the features observed in Sun Watcher using Active Pixel System Detector and Image Processing (SWAP; Berghmans et al., 2006) images, onboard Project for On-Board Autonomy 2 (PROBA2; Santandrea et al., 2013) to study the short-term evolution of the solar magnetic field over the maximum of the SC24. However, their global coronal magnetic field model is computationally expensive to apply over the entire SC compared to PFSS.

Several attempts have been made to assess the change of source surface height in the PFSS model with the phase of the SC. For example, using photospheric magnetic synoptic maps from Mount Wilson Observatory (MWO), Lee et al. (2011) reported that the R_{ss} of 1.9 $R_\odot$ and 1.8 $R_\odot$ produced the best results for the modeled IMF at L1 for the minimum periods of SC22 and SC23, respectively. Moreover, they found that 1.5 $R_\odot$ and 1.8 $R_\odot$ provided the best IMF during the SC23 maximum and minimum, respectively, in Figure 6 of Lee et al. (2011). A study by Arden et al. (2014) using synoptic maps from Solar and Heliospheric Observatory's Michelson Doppler Imager (SOHO/MDI; Scherrer et al., 1995) and Solar Dynamics Observatory's Helioseismic and Magnetic Imager (SDO/HMI; Scherrer et al., 2012) showed that raising R_{ss} by 15–30% (2.88–3.28 $R_\odot$) during the SC 23 minimum as compared to the conventional R_{ss} (2.5 $R_\odot$) better reproduces the observed open flux at L1. Therefore, both studies using different magnetic maps reported an increase in the source surface height during the SC minimum compared to the maximum. A study by Nikolić (2019) suggested a lower source surface height (1.5–2.0 $R_\odot$) as compared to the conventional source surface height during the maximum phase of the SC24. The above-mentioned three studies disagree with each other in terms of the best absolute values of the source surface heights. However, they agree in terms of the relative changes in the best source surface heights with the phase of the SC, i.e., to use a higher source surface height during solar minimum as compared to solar maximum. A recent study by Huang et al. (2024) showed that slightly lower and higher values compared to the conventional value of R_{ss} = 2.5 $R_\odot$, at SC minimum and maximum, respectively, provide better values of unsigned open flux at L1. Similarly, Badman et al. (2020), based on the Parker Solar Probe (PSP; Fox et al., 2016) IMF observations during the October–November 2018 period, showed that reduced source surface height improves accuracy of the predicted IMF on specific days (2018-10-20 and 2018-10-29) at PSP located at 0.5 AU. It is important to mention that the two studies focused on distinct selective time periods, whereas the findings of Lee et al. (2011) and Nikolić (2019) are based on long-term analysis for R_{ss} in a different context.

One of the important aspects of R_{ss} optimization is in the context of the use of PFSS in solar wind velocity prediction models at L1. Forecasting solar wind throughout the heliosphere requires accurate magnetic-field extrapolation from the photosphere to the outer boundaries of the coronal domain and, after that, tracing of the magnetic field lines in the coronal domain. Using the properties of the traced field lines in the coronal domain, empirical solar wind models, like WSA, provide the solar wind velocity profile at the outer boundary of the coronal domain. Further, to predict solar wind velocity at L1, extrapolation of the velocity in the heliosphere is required using sophisticated MHD codes or simple 1D ballistic extrapolation. Riley & Lionello (2011) proposed a simple model called Heliospheric Upwind eXtrapolation (HUX), which is computationally cheaper than sophisticated MHD codes and incorporates more physics than a simple 1D ballistic extrapolation, and can be used for more reliable solar wind velocity estimates at L1.

Currently, the community uses a constant source surface radius (2.5 $R_\odot$) for PFSS in the WSA model with the standard synoptic magnetic maps from the Global Oscillation Network Group (GONG) network (Riley et al., 2015; Reiss et al., 2019; Kumar et al., 2020; Narechania et al., 2021; Kumar & Srivastava, 2022; Mayank et al., 2022). As reported by Lee et al. (2011), a small change in the R_{ss} can change the degree of agreement between the modeled and observed values of IMF at L1. In an earlier study, we have shown that the performance of solar wind velocity forecasting models decreased significantly during the deep solar minimum of SC23 (Kumar & Srivastava, 2022). This study considered a fixed source surface radius in the PFSS model. Since previous studies suggested that R_{ss} changes with the phase of the SC, therefore, one of the reasons for the decreased performance of the framework in our study can also be attributed to the usage of a fixed source surface radius (R_{ss}), i.e., 2.5 $R_\odot$.

The output of the WSA model changes with the source surface radius because changing R_{ss} affects the overall simulated magnetic field structure of the Sun, leading to changes in the connectivity of sub-Earth field lines. Thus, there is a clear need to optimize R_{ss} and the WSA parameters for solar wind forecasting at L1.

In this work, we optimize R_{ss} in the PFSS model with the phase of the SC to be used in the WSA model. We evaluated

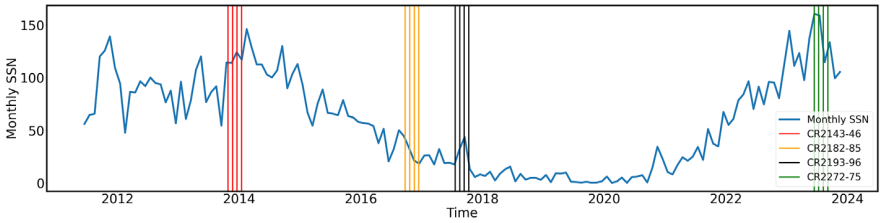

Figure 1. Monthly sunspot numbers (blue line) plotted with time, indicating different phases of solar activity cycle 24 and 25. Vertical lines mark the CRs selected for analysis at different phases of the SC.

the performance of the solar wind velocity prediction framework (PFSS+WSA+HUX) at L1 using different R_{ss}, for 16 Carrington Rotations (CRs) selected at different phases of SC24 and SC25 as shown in Figure 1. Section 2 describes the data selected and the methodology, consisting of the extrapolation method for the magnetic field and the estimation of solar wind velocity in the heliosphere. Section 2.1 provides details about the models used in the framework and the parametric space for the source surface radius in the WSA model. In Section 3, we discuss the main results and their interpretations. Finally, in Section 4, we present our main conclusions.

2 Data and methodology

We consider the space between the Sun and the Lagrangian point L1 as two distinct regions. The first region extends from the photosphere to the source surface. The second region extends from the source surface to the L1 point. We use a combination of different models, PFSS+WSA+HUX, in the framework to estimate the solar wind velocity at L1.

The input magnetograms for PFSS specify the inner boundary conditions for the magnetic field at the solar surface. Our approach is solely based on the magnetic field extrapolation, which is sensitive to the magnetic field inputs provided to the model. Therefore, we explore the use of the three different types of magnetic field maps, taken from the Global Oscillation Network Group (GONG)[1]. Out of the three types of magnetic maps, two are full (CR) synoptic maps commonly used by the community: standard magnetic ("mrmqs" in the GONG file name) and integral zero-point corrected (ZPC) maps ("mrnqs" in the GONG file name). Due to differences in location and observing conditions between the various sites of the GONG network, strong background variations were observed in the standard magnetic GONG maps (Hill, 2018). These so-called zero point errors reached amplitudes of the order of 10 G, but were reduced to 1G with an automated comparison between sites and day-to-day variations, resulting in the ZPC map. We also used the hourly updated ZPC (HU ZPC) synoptic maps ("mrzqs" in the GONG file name) at an interval of 5 h. The HU ZPC maps were chosen to provide an updated representation of the magnetic field of the Sun.

Monthly sunspot data were obtained from the SILSO website[2] to identify different phases of the SC and select different time periods of study. Further, we used the in-situ observations of hourly averaged solar wind velocity recorded at L1 in the OMNI database[3] to compare with modeled solar wind velocity profiles at L1.

Since we aim to optimize the source surface height at different phases of the SC, we therefore selected CRs at different phases of the SC. We selected in total 16 CRs: four consecutive CRs at the maximum phase of the SC24 (CR2143 – CR2146, October 2013–January 2014), 8 CRs in the declining and minimum phase of the SC24 (CR2182 – CR2185, September–December 2016 and CR2193 – CR2196, July–October 2017), and 4 CRs at the maximum phase of the SC25 (CR2272–CR2275, January–September 2023), as shown by red, yellow, black, and green vertical lines, respectively, in Figure 1.

Predicting solar wind velocity at the L1 point for these 16 CRs and selecting the best R_{ss} among three choices, i.e., 2.0 $R_\odot$, 2.5 $R_\odot$, and 3.0 $R_\odot$, for each type of input magnetic map in the framework involves the following steps:

1. Calculate the coronal magnetic field in the coronal domain up to R_{ss}, using the PFSS extrapolation with a Python module pfsspy (Stansby et al., 2020). We use three different values of R_{ss} (2.0 $R_\odot$, 2.5 $R_\odot$, and 3.0 $R_\odot$) for each of the three different types of input synoptic magnetic maps.
2. Trace the magnetic field lines starting from the photosphere to create a map of open and closed field lines with 1° resolution (Sect. 2.2).
3. Trace the sub-Earth field lines from R_{ss} to the photosphere (Sect. 2.2).
4. Utilize the WSA empirical velocity relation to estimate solar wind velocity profile at R_{ss}, based on the magnetic field line properties, using:
   (a) default WSA parameters;
   (b) a parametric space of WSA parameters. Using parametric space involves a range of values of WSA parameters to conclude independently of the choice of parameters (Sect. 2.3).
5. Extrapolate velocity estimates from the outer boundary of the coronal domain (R_{ss}) up to the L1 point using the HUX extrapolation (heliospheric domain) (Sect. 2.1).
6. Apply the first three steps for each value of R_{ss}, with default WSA parameters and for parametric space (Table 1) for each type of magnetic map, and calculate the performance matrix defined by Pearson's correlation coefficient between the modeled and observed solar wind velocity values at L1 to find the best R_{ss} (Sect. 2.3).

[1] https://gong.nso.edu/data/
[2] https://www.sidc.be/SILSO/
[3] https://omniweb.gsfc.nasa.gov/form/dx1.html

Table 1. Parametric space used for WSA model.

Parameter	Range	No. of points
V_{slow}	200–300 km/s	3 points
V_{fast}	600–800 km/s	5 points
α	0.1–0.3	6 points
β	1.00–1.75	4 points
w	0.01–0.05 radian	5 points
γ	0.6–1.0	3 points
δ	0.8–1.5	3 points

Finally, in order to compare the quality of the extrapolation of PFSS close to the Sun using different synoptic magnetic maps as inputs, we used observations from the Sun Watcher using Active Pixel System Detector and Image Processing instrument, which is an EUV imager with a passband centered at 174 Å onboard Project for Onboard Autonomy 2 mission (Berghmans et al., 2006; Santandrea et al., 2013; Halain et al., 2013; Seaton et al., 2013; West et al., 2022). SWAP images the solar corona at a cadence of 110 s. This passband provides an excellent opportunity to observe features like active regions (ARs), streamers, and coronal fans that dominate the large-scale structure of the lower corona. Even though 174 Å is not an ideal wavelength for observing coronal holes and filaments, they are still visible and traceable in SWAP images. All these features have a direct connection with the overall magnetic field configuration of the corona. SWAP has a wide field of view (FOV) spanning 54′, and using the off-pointing capability of PROBA2, the SWAP FOV can be shifted in any direction in order to track coronal features of interest up to more than 2 $R_{\odot}$. This extended FOV is large enough to observe the lower corona and is well within the domain of PFSS extrapolation.

We used observations from special observational campaigns to extend the FOV of SWAP by putting the Sun at the corner of the FOV and recording 30-second exposure images in 174 Å every minute. Finally, we created a single mosaic image by stacking these off-limb images for one hour by keeping the Sun at the center of the mosaic to combine the signal (median of the photon count). This resulted in better visibility of limb features compared to the normal image of the SWAP at larger heights due to increased signal in the overlapped FOV of individual images in the stack. Specifically, we used mosaics reconstructed from the special campaigns on 20 August 2017 and 7 August 2023. These mosaics result in a larger FOV (up to 2.5 $R_{\odot}$ on the side and 3.0 $R_{\odot}$ on the corners) as compared to a standard SWAP image centered at the Sun (up to 1.7 $R_{\odot}$ on the side and 2.5 $R_{\odot}$ on the corners). It is important to mention here that the mosaics obtained using this approach are suitable only for the study of stable and long-lived features in the corona because short-lived features are smeared out over the time span of an hour. However, this method is suitable for the comparison of SWAP images with the PFSS extrapolated global magnetic field structure.

To be noted that CRs 2194 and 2274 and their neighbouring CRs during the maximum phase of SC25 and the declining phase of SC24 were mainly chosen for this study to include the period for which the extended FOV PROBA2/SWAP mosaic images were available. This was required to compare the SWAP images with the PFSS extrapolation around the time of the optimization of the WSA model. Moreover, we selected a relatively stable period during the SC24 maximum, when the HUX model is expected to give better results since it is essentially a steady-state extrapolation model.

The following sections explain the empirical formulation for solar wind velocity, the extrapolation technique in the heliosphere, and the parametric space of the WSA model, as well as methods of assessment of the framework.

2.1 Coronal and heliospheric model

Using the PFSS model, we first extrapolate the magnetic field in the coronal domain, then we trace the magnetic field lines from the photosphere to the R_{ss}. It provides a map of the footpoints of open and closed field lines on the Sun. We also traced the sub-Earth field lines (field lines corresponding to the sub-Earth points in the CR frame of reference) from R_{ss} to the photosphere to calculate parameters of the field lines. The particular form of the WSA model equation used in our framework is given by Riley et al. (2015):

$$v_{sw}^{wsa}(f_s, \theta_b) = v_{slow} + \frac{v_{fast} - v_{slow}}{(1+f_s)^{\alpha}} \left(\beta - \gamma e^{-(\theta_b/w)^{\delta}}\right)^{3.5}. \quad (1)$$

Here, the expansion factor (f_s) is the magnetic flux ratio for a field line between the photosphere and R_{ss}, and θ_b is the angular distance of field line footpoints to the nearest CH boundary, v_{slow} and v_{fast} represent the tunable slowest and fastest solar wind velocities at R_{ss}, with default values set as v_{slow} = 250 km/s and v_{fast} = 750 km/s. Parameters α, β, γ, δ, and w are tunable in the model, with default values set as α = 1.5/9, β = 1.0, γ = 1.0, δ = 1.5 and w = 0.01. These values provide overall optimal results for the time periods analyzed, but they are not necessarily the best values for each CR. The use of the parametric space, i.e., the range of the values for each parameter, makes the final results independent of the choice of the WSA parameters (Sect. 2.3).

Comparing the estimated solar wind velocity with that observed by spacecraft at the L1 point requires connecting solar wind velocity obtained from the WSA model with heliospheric velocity extrapolation models. As mentioned earlier, we use the HUX Riley & Lionello (2011) model. HUX is better than the simple 1D ballistic approximation as it incorporates a stream interaction term in the momentum equation, and it is faster than the full MHD approximation, providing very similar results for solar wind velocity at L1 when compared with MHD results (cc = 0.98) as reported by Riley & Lionello (2011). We used HUX extrapolation with 0.55° (≈1 h in CR time period) resolution to compare with hourly average data at L1. The same resolution is also used for tracing the sub-Earth field lines from R_{ss} to the solar surface.

After the extrapolation of the solar wind velocity profile from R_{ss} at L1 using HUX, we compared the values of estimated solar wind velocity with the observed values at L1. We use Pearson's Correlation Coefficient (cc) to assess the performance of the framework, which has values between [−1, 1], with 1 indicating a direct linear correlation and −1 an inverse correlation. Since we aim to find a modeled solar wind profile that closely matches the observed profile, for our study, a cc value close to 1 is desirable, and lower values of cc, including negative ones, may be considered as poor correlation. We also

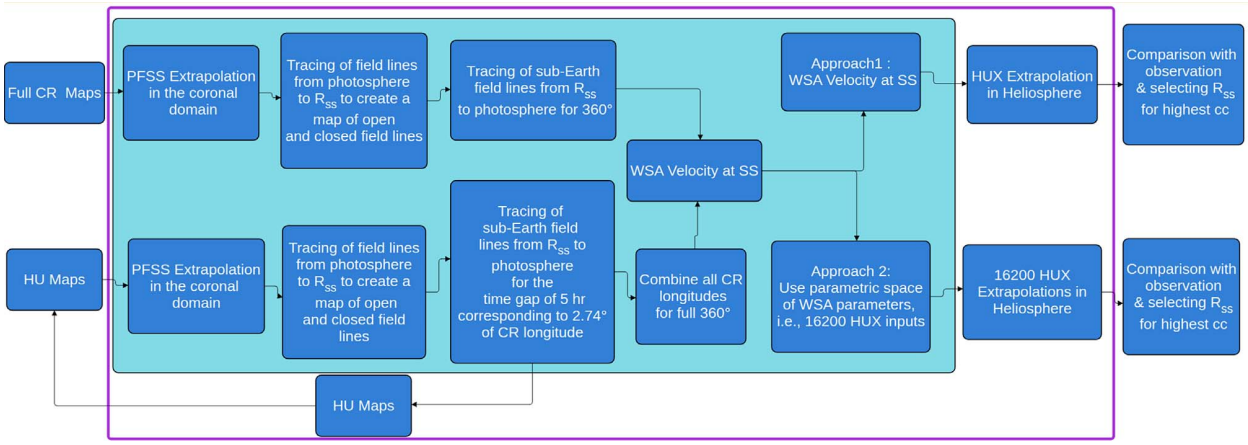

Figure 2. Flow chart of the methodology adopted in this work to find optimal R_{ss}. Steps mentioned in the magenta colour box are repeated for all three choices of R_{ss}, i.e., 2.0 $R_{\odot}$, 2.5 $R_{\odot}$, and 3.0 $R_{\odot}$.

calculate other metrics, such as Mean Absolute Percentage Error (MAPE) and Standard Deviation (SD), as discussed in Kumar & Srivastava (2022). For a set of N modeled values (m_i) and a corresponding observed values (o_i), the MAPE can be given by

$$\mathrm{MAPE} = \frac{100}{N}\sum_{i=1}^{N}\left|\left(\frac{m_i - o_i}{o_i}\right)\right|. \quad (2)$$

For the sake of simplicity, the assessment of the performance of the framework in this work is solely based on the maximum values of *cc*. However, we will discuss the results based on the values of MAPE and SD in the specific case of SC25 maximum phase (see Sect. 3).

2.2 Field line tracing approaches corresponding to different types of GONG maps

As mentioned earlier, we have used three types of magnetic maps. Two out of the three maps are full CR maps, i.e., ZPC and standard maps (STD), giving us an idea about the overall magnetic field over 27.27 days (Carrington Rotation time period). We also used hourly updated zero point corrected (HU ZPC) maps to provide a more updated version of the magnetic field. Therefore, we have two types of magnetic maps, i.e., full CR maps and hourly updated synoptic maps. Further, we use two different extrapolation schemes for these three types of maps while tracing the sub-Earth field lines.

For both full (ZPC and STD) and HU ZPC synoptic maps obtained from the GONG network, we traced field lines all over the photosphere to create a map of footpoints of open (field lines reaching at R_{ss}) and closed field lines (field lines closing back to the photosphere) used for the calculation of θ_b.

In the case of full CR maps, we created a 360° (corresponding to full CR) input for the HUX model and then calculated f_s and θ_b (parameters for the WSA model) for all sub-Earth field lines from Carrington longitude 0° to 360° by tracing all sub-Earth field lines from R_{ss} to the photosphere from a single CR map.

Each HU ZPC map corresponds to a specific central Carrington longitude for a given Carrington rotation based on the observation time. It also represents a full rotation with updated observations for the next 60° of the upcoming Carrington longitude, as described on the GONG website[4]. Further, tracing the sub-Earth field lines for 129 HU ZPC maps selected at the interval of 5 h, for a CR involves the following steps:

1. For a given HU map of a given time, trace the field lines all over the photosphere with 1° resolution, from the photosphere to R_{ss} to create a map of the footpoints of open and closed field lines at the photosphere. This step is vital for the calculation of θ_b using an updated magnetic map.
2. Trace the sub-Earth field lines, from R_{ss} to the photosphere (to calculate f_s and θ_b), corresponding to the 5-hr time gap between the two maps. It corresponds to tracing the field line for the Carrington longitudinal gap of ≈2.74°. Therefore, each HU map is used to create an HUX input for ≈2.74° only.
3. Repeating the above two steps for all the HU maps for a given CR to create a full 360° input for the HUX model.

This approach provides an updated view of the coronal magnetic field than a single full CR map. Detailed explanations about the tracing of field lines can be found in Reiss et al. (2019). Figure 2 shows the flowchart of the overall methodology adopted for the two kinds of magnetic maps and the two approaches used in this work.

2.3 Optimization of the source surface height using two approaches

We applied two different approaches for each type of magnetic map used as input (STD, ZPC, and HU ZPC) to find the best R_{ss} for each CR. In our first approach, following Kumar & Srivastava (2022), we used default parameters

[4] https://gong.nso.edu/data/

(v_{slow} = 250 km/s, v_{fast} = 750 km/s, α = 1.5/9, β = 1.0, w = 0.01, γ = 1.0, and δ = 1.5) in the WSA model for every CR. For each of the three values of R_{ss} (2.0 $R_\odot$, 2.5 $R_\odot$, and 3.0 $R_\odot$), the velocity profile at the outer boundary of the coronal domain was obtained. This was provided as input to the HUX model to give us velocity output at L1. We then compared these values with the observed solar wind profile at L1 from the OMNI database and estimated Pearson's correlation coefficient (*cc*). The R_{ss} corresponding to the maximum *cc* was selected as the best performing for each CR.

In the second approach, we use various combinations of WSA parameters with values around the default values mentioned in Table 1 to estimate the maximum value of the *cc* for each R_{ss}. This involves creating 16,200 velocity profiles using an automated Python code at each source surface height, which corresponds to a combination in the parametric space covering V_{slow}, V_{fast}, α, β, γ, δ, and w (16,200 = 3 × 5 × 6 × 4 × 5 × 3 × 3, see Table 1). For a given R_{ss}, it further involves extrapolation of each velocity profile (corresponding to each parametric combination) up to L1 using HUX, and calculating *cc* for each extrapolated velocity profile with the observed in-situ solar wind profile at L1. Thereafter, R_{ss} corresponding to the highest *cc* (among the three values of R_{ss}) is selected as the best R_{ss} for every CR. Therefore, using parametric space enables us to estimate the best performing R_{ss} independent of the choice of WSA parameters.

3 Results and discussion

We used two approaches to estimate the optimized value of R_{ss} for 16 CRs selected at three different phases, i.e., 8 CRs at the minimum of SC24 and 4 CRs each at the maximum of SC24 and SC25, as shown in Figure 1. In our first approach, we used default WSA parameters, and in the second, we used the parametric space for each R_{ss} (as explained in Sect. 2.3). For both approaches, we also used three different magnetic maps as input (as mentioned in Sect. 2). Therefore, we have a total of 24 (4 × 2 × 3), 48 (8 × 2 × 3), and 24 (4 × 2 × 3) different instances (no. of CRs × no. of methods × no. of maps) to evaluate the best performing R_{ss} at each phase of the SC24 maximum, SC24 declining/minimum phase, and SC25 maximum, respectively. In Section 3.1, we discuss our results obtained from the two approaches and the statistical results based on the above mentioned different instances. In Section 3.2, we discuss how different values of R_{ss} affect the modeled solar wind profile at L1, specifically for CR2143 and CR2183. In Section 3.3, we compare the extrapolated magnetic field structures using different magnetic maps with the observed large-scale structures in PROBA2/SWAP images with extended FOV.

3.1 Source surface height optimization at different phases of SC24 and SC25

Figure 3 depicts the performance of the framework in terms of Pearson's *cc* obtained between the observed and modeled values of solar wind velocity at L1 for different CRs with different R_{ss} based on default WSA parameters, for all three kinds of maps used. In this figure, blue, orange, and green dots represent the performance of the framework (*cc*), for R_{ss} of 2.0 $R_\odot$, 2.5 $R_\odot$, and 3.0 $R_\odot$, respectively, for each CR. Horizontal dashed lines show the average performance in the respective phase for each R_{ss} and all CRs. The annotated value shows the average value of *cc* for each input map and SC phase for all three R_{ss} (dashed lines). From Figure 3, we can clearly draw the following conclusions:

1. The overall performance during the declining phase of SC24 (cc_{avg} = 0.45 averaged over all R_{ss}, CRs, and maps) is better compared to the performance during the maximum of SC24 (cc_{avg} = 0.38).
2. The framework performed best for R_{ss} = 3.0 $R_\odot$ (green dots) in the declining/minimum phase of SC24 for most of the cases (17/24 combined for all the maps). The orange dashed lines show the average *cc* for R_{ss} = 2.5 $R_\odot$, which is estimated to be 0.61 for ZPC maps and 0.52 for HU ZPC maps. The green dashed lines show the average *cc* for R_{ss} = 3.0 $R_\odot$, which is estimated to be 0.75 for ZPC maps and 0.61 for HU ZPC maps. These values show clear improvement using R_{ss} = 3.0 $R_\odot$ in comparison to R_{ss} = 2.5 $R_\odot$, for both the maps. In contrast, the STD maps do not show a significant improvement in performance when using R_{ss} = 3.0 $R_\odot$ as compared to R_{ss} = 2.5 $R_\odot$.
3. During the SC24 maximum phase, the average performance of the framework for all 4 CRs is the best for either R_{ss} = 2.5 $R_\odot$ or R_{ss} = 2.0 $R_\odot$ for all three types of magnetic maps (blue and orange dashed lines). It is also important to note that, in none of the maps, the average performance reaches its highest value at R_{ss} = 3.0 $R_\odot$.
4. The overall performance using full ZPC maps is found to be better than standard CR maps at the SC24 maximum and declining phases, and for all three values of R_{ss}. This is highlighted by the increase in the average *cc* during the minimum phase of the SC24 from 0.31 (for STD maps) to 0.51 (for ZPC maps), and from 0.22 to 0.47 during the maximum phase of the SC24. We also note that the performance using hourly updated ZPC and full CR ZPC maps is similar.
5. Average *cc* was consistently negative (cc_{avg} = −0.11) during the SC25 maximum when default WSA parameters were used with all magnetic maps, indicating the poor performance of the framework for this time period.

Figure 4 displays the performance of the framework for different CRs with different R_{ss} based on optimized *cc*, by using the parametric space of WSA parameters. Each dot represents the highest *cc* in the parametric space for every R_{ss}.

It is important to note that during SC25 maximum, *cc* optimization showed unrealistic improvement in *cc* (Fig. 4) as compared to other phases, i.e., average *cc* increased from negative values to significant positive values for all the maps. In such a case, it becomes important to check the values of the other metrics as well to examine whether this improvement represents a better match or not. Interestingly, we found that other metrics, such as the average MAPE, increased significantly for the SC25 maximum. In this time period, average MAPE increased from approximately 20–22% (for all maps), to 58%, 114%, and 39% for STD, ZPC, and HU ZPC maps, respectively (Figs. A1 and A2 in Appendix). Physically, MAPE represents the mean of the absolute percentage difference between each

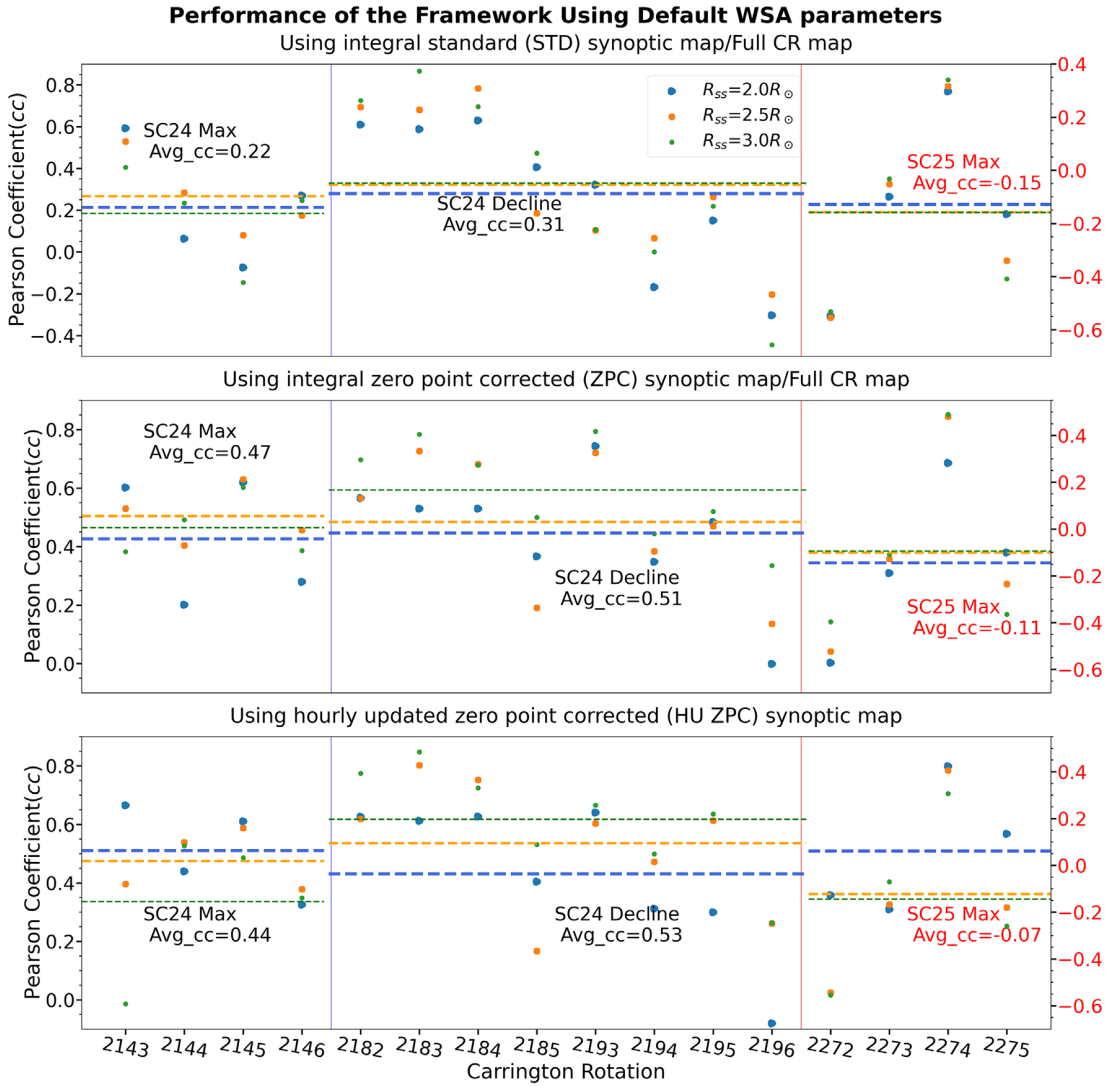

Figure 3. The performance of the framework (*cc*) for different CRs with different R_{ss} based on default WSA parameters. For SC24, refer to the left *y*-axis, whereas for SC25 maximum, refer to the right *y*-axis in red. The top panel shows the result using standard Carrington maps (STD), the middle panel is for the zero-point corrected Carrington maps (ZPC), and the bottom panel is for hourly updated zero-point corrected maps (HU ZPC). Blue, orange, and green dots represent the performance of the framework, i.e., *cc*, for R_{ss} of 2.0 $R_\odot$, 2.5 $R_\odot$, and 3.0 $R_\odot$, respectively. Horizontal dashed lines show the average performance in the respective phase for each R_{ss} and all CRs. The annotated value shows the average value of *cc* for each input map and SC phase for all three R_{ss} (dashed lines).

point in the time series of the modeled and observed solar wind velocity profile for a given CR, and it should be lower for a better match. Similarly, a considerable increase in SD also occurred during the maximum phase of SC25 in ZPC maps, rising from 93 km/s to 160 km/s as a result of *cc* optimization. Therefore, despite the increase in average *cc* during the SC25 maximum phase through optimization of WSA parameters, it does not represent an improved match in the solar wind velocity at L1 because of the increase in errors. On the other hand, during the maximum and declining phases of SC24, the default WSA parameters yielded better performance compared to the SC25 maximum, even without optimization. Furthermore, optimization of the *cc* parameter during the SC24 declining and maximum phase did not result in a significant increase ($\leq$40%) in MAPE and SD, as compared to the increase in the MAPE (up to 200%) and SD (up to 70%) in the case of the SC25 maximum.

Although we used the parametric space (second approach) to obtain the best R_{ss}, independent of WSA parameters, however, during the declining phase of the SC24, both approaches led to R_{ss} = 3.0 $R_\odot$ as the best performing R_{ss}. Moreover, during the SC24 maximum, either R_{ss} = 2.0 $R_\odot$ or 2.5 $R_\odot$ outperformed R_{ss} = 3.0 $R_\odot$ for our second approach by using HU ZPC and STD maps.

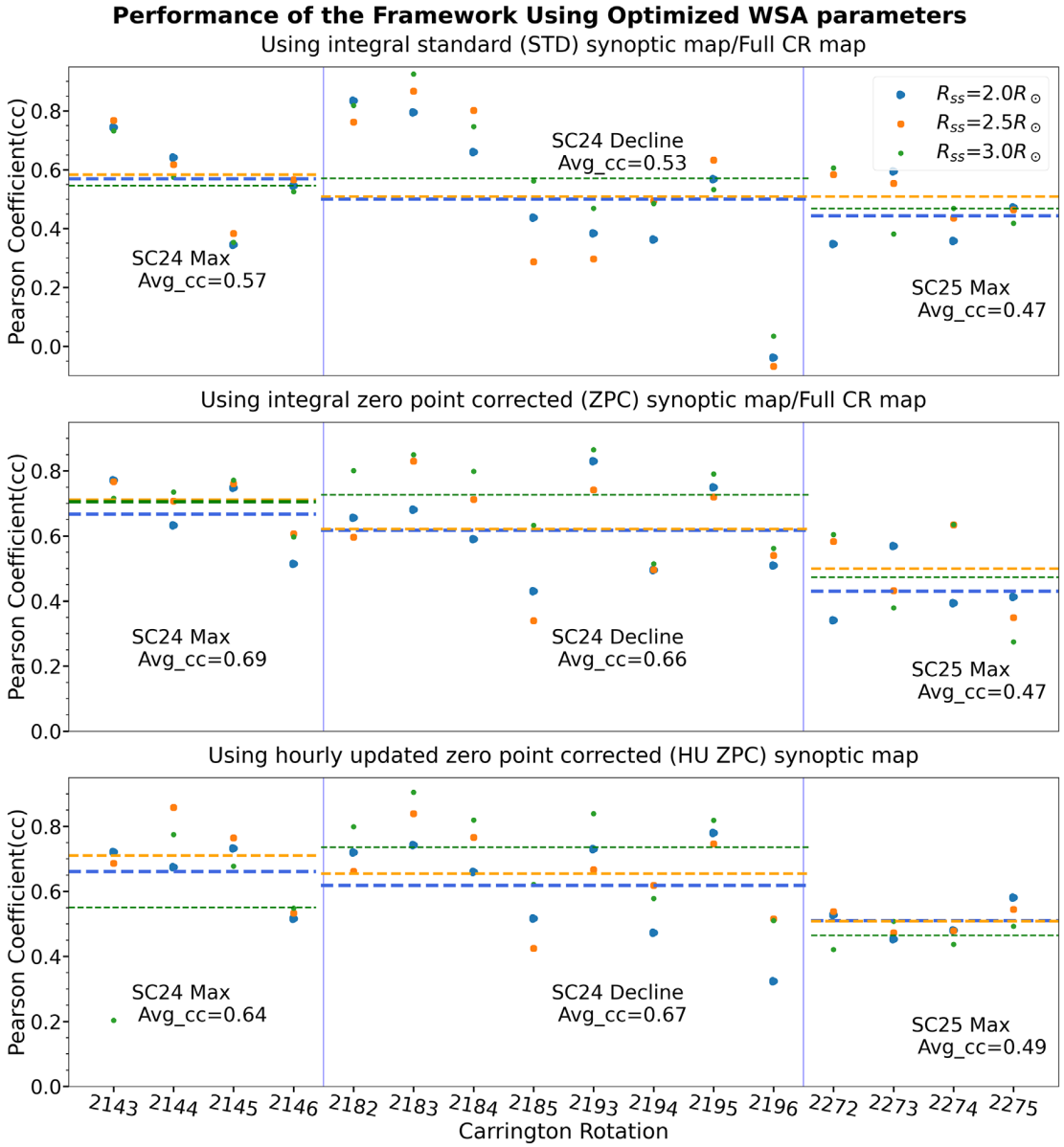

Figure 4. Similar to Figure 3 for optimised WSA parameters.

The trend of the best-performing source surface heights at each phase, as mentioned earlier, remains the same even after using parametric space for three types of input magnetic maps. Therefore, the improvement in performance on using the higher values of R_{ss} in every CR is independent of the choice of the different maps and the WSA parameters. We can make the following inferences from Figure 4:

1. Optimization of WSA parameters significantly increased the *cc* for every CR and at every R_{ss} (when compared with Fig. 3).
2. The overall trend of the performance in the declining/minimum phase of the SC24 remains the same, as it was for the default WSA parameters approach, for different R_{ss}, i.e., the best performing R_{ss} in most cases (18/24 combined for all the maps) is 3.0 $R_\odot$ (green dots). The average *cc* values for R_{ss} = 2.5 $R_\odot$ (orange dashed lines) corresponding to the STD, ZPC, and HU ZPC maps have been determined to be 0.49, 0.61, and 0.64, respectively. The average *cc* values for R_{ss} = 3.0 $R_\odot$ (green dashed lines) corresponding to STD, ZPC, and HU ZPC maps have been estimated as 0.55, 0.72, and 0.72, respectively. These values demonstrate clear improvement in framework performance for all the three maps when using R_{ss} = 3.0 $R_\odot$ as compared to R_{ss} = 2.5 $R_\odot$.
3. During the SC24 maximum phase, the average performance of the framework is the best for either R_{ss} = 2.5 $R_\odot$ or 2.0 $R_\odot$ for all maps (orange and blue dashed lines). The relative increase in average performance is not as significant as it is during the minimum phase.

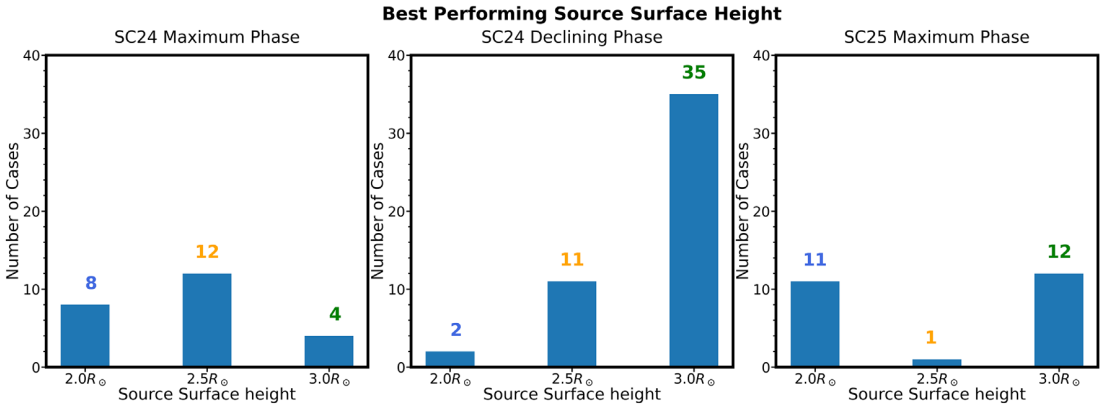

Figure 5. Number of cases for different R_{ss} in the best-performing scenario during the selected phase of the SC. Note, as explained in Section 3, the framework performed poorly for the SC25 maximum phase. Therefore, the results from the right panel are inconclusive.

As mentioned at the beginning of this section, we have a total of 24, 48, and 24 different instances to evaluate the best performing R_{ss} at the SC24 maximum, SC24 declining/minimum phase, and SC25 maximum, respectively. Figure 5 shows a histogram indicating when different values of R_{ss} were found to be the best choice at different phases of SC24 and SC25 (please note that CR2182 – CR2185 and CR2193 – CR2196 are in SC24 declining phase). An important inference from this bar graph is that R_{ss} = 3.0 $R_\odot$ is the most suitable choice for the maximum number of CRs (35/48) during the declining/minimum phase (middle panel Fig. 5).

Moreover, it may be safe to mention that the number of cases of best performance at lower R_{ss} is larger during the maximum of SC24 ((8+12)/24, Fig. 5), as compared to SC24 minimum ((11+2)/48, Fig. 5) leading to an average best performance at R_{ss} = 2.5 $R_\odot$ or 2.0 $R_\odot$ (orange and blue dashed lines in Figs. 3 and 4). Based on this, we can say that lower R_{ss} (2.0 $R_\odot$ or 2.5 $R_\odot$) might be a preferable choice for the SC24 maximum (left panel Fig. 5), however with a very small improvement in the average performance as compared to the SC minimum.

Furthermore, as the average performance of the overall framework increases from SC25 maximum, SC24 maximum to SC24 declining phase in our first approach (Fig. 3), the distinction of the best performing R_{ss} becomes more obvious in Figure 5. Based on Figure 5, it is difficult to comment conclusively on the best-performing R_{ss} during SC25 maximum, given the fact that for half of the cases framework performed poorly (corresponding to default WSA parameters with negative *cc*) and after optimization, it led to a drastic increase in MAPE.

In summary, during the declining phase, R_{ss} = 3.0 $R_\odot$ was found to be the optimal source surface height. Similar results during the SC minimum were reported in the context of observed open flux at L1 by Arden et al. (2014). They found that increasing the R_{ss} by 15-30% as compared to conventional R_{ss} (2.5 $R_\odot$) during the minimum phase gives a better estimate of open flux at L1. Our study shows that during the SC24 maximum, either R_{ss} = 2.0 $R_\odot$ or R_{ss} = 2.5 $R_\odot$ are preferable, as seen in the left panel of Figure 5. Here, observed skewness toward R_{ss} = 2.0 $R_\odot$ at SC24 maximum can be explained based on the findings of Nikolić (2019), which reported a lower source surface height at the solar maximum as compared to the conventional R_{ss}. However, it differs in the absolute values, which could be due to a shorter time period, a smaller number of choices of R_{ss} or different maps and methodologies adopted in our study. Moreover, the results at the SC25 maximum remained inconclusive due to increased activity and, therefore, poorer performance of the framework. The improvement in the performance of the framework using optimized R_{ss} proved to be consistent irrespective of the choice of the magnetic synoptic maps and for all CRs and choice of WSA parameter settings. It has been shown earlier by Lee et al. (2011) that PFSS extrapolation itself is not a good approximation during periods of high solar activity. To investigate the possible reasons for the poor performance of the framework during CR2272–CR2275, we investigated the Carrington rotation movies[5] of SWAP during this period. We compared it with the period of CR2143–CR2146, where the framework performed relatively better. We noted that the CRs during SC25 maximum (CR2272–CR2275), for which the framework performed very poorly, exhibited a more active corona, a larger number of active regions evolving more rapidly, and a complex magnetic corona compared to the CRs selected during the SC24 maximum period. This suggests a more dynamic solar corona with stronger currents in the corona, which challenges the assumptions of the PFSS model during CR2272–CR2275 compared to the period of CR2143–CR2146.

3.2 Case studies of selected Carrington rotations at SC maximum and minimum/declining phases

In this section, we discuss the effect of varying R_{ss} on the profile of the modeled solar wind velocity at L1 at different phases of the SC. We present the results of solar wind velocity estimation using the method described in Section 2 for CRs during the maximum phase of the SC24 and the declining phase of SC24. Specifically, we select two CRs; CR2143, spanning October–November 2013, and CR2183, spanning October–November 2016, as representatives of the maximum and declining phases of SC24, respectively, to show the applicability of the framework for different phases of the SC.

[5] http://proba2.sidc.be/swap/data/mpg/movies/carrington_rotations/

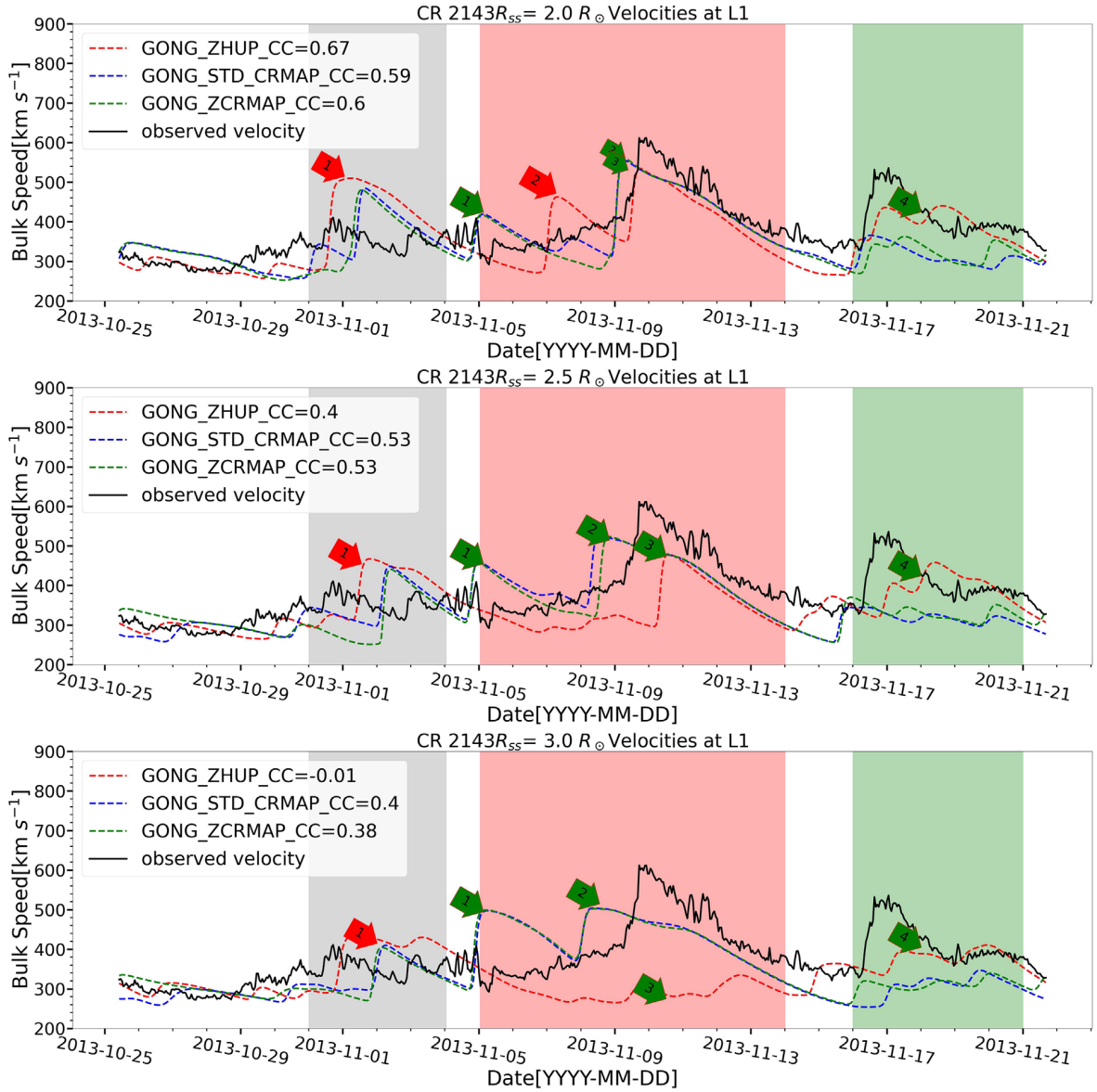

Figure 6. Plots of modeled (PFSS + WSA + HUX) and hourly averaged observed solar wind velocity from OMNI database at L1 (solid black line) with time for CR2143 for different R_{ss}, i.e., for R_{ss} = 2.0 $R_\odot$ (top panel), for R_{ss} = 2.5 $R_\odot$ (middle panel) and R_{ss} = 3.0 $R_\odot$ (bottom panel). The red, blue, and green dashed lines show the velocity profiles using HU ZPC, STD, and full ZPC maps, respectively. Green arrows show the time period around which R_{ss} optimization improves the match between the modeled and observed profile as R_{ss} decreases. The red arrows show the time period around which the prediction does not improve as R_{ss} decreases. The shaded regions show the time period where varying R_{ss} significantly changes the modeled velocity profile.

3.2.1 CR2143 (SC24 maximum phase)

Figure 6 shows the observed velocity profile taken from the OMNI database (black solid curve) and the modeled solar wind velocity profile using different synoptic magnetic maps (shown by colored dashed curves). The top, middle, and bottom panels show the velocity profile for R_{ss} = 2.0 $R_\odot$, R_{ss} = 2.5 $R_\odot$, and R_{ss} = 3.0 $R_\odot$, respectively. The blue dashed line shows the velocity profile using STD maps obtained from GONG. The red and green dashed lines show the velocity profile using HU ZPC and full ZPC maps, respectively. Figure 6 shows the velocity profiles estimated using default WSA parameters as inputs in the model framework.

The green and red shaded areas show the region where using lower R_{ss} improved the solar wind velocity prediction. Green arrows in Figure 6 show the approximate position of the features which matched better with the measurements using lower R_{ss} as compared to higher R_{ss}. As we decrease the R_{ss} from 3.0 $R_\odot$ to 2.0 $R_\odot$ (from bottom panel to top panel), the modeled velocity profile (colored dashed curves) matches better around the green arrows with the measured velocity profile in the red and green shaded areas for all the different maps.

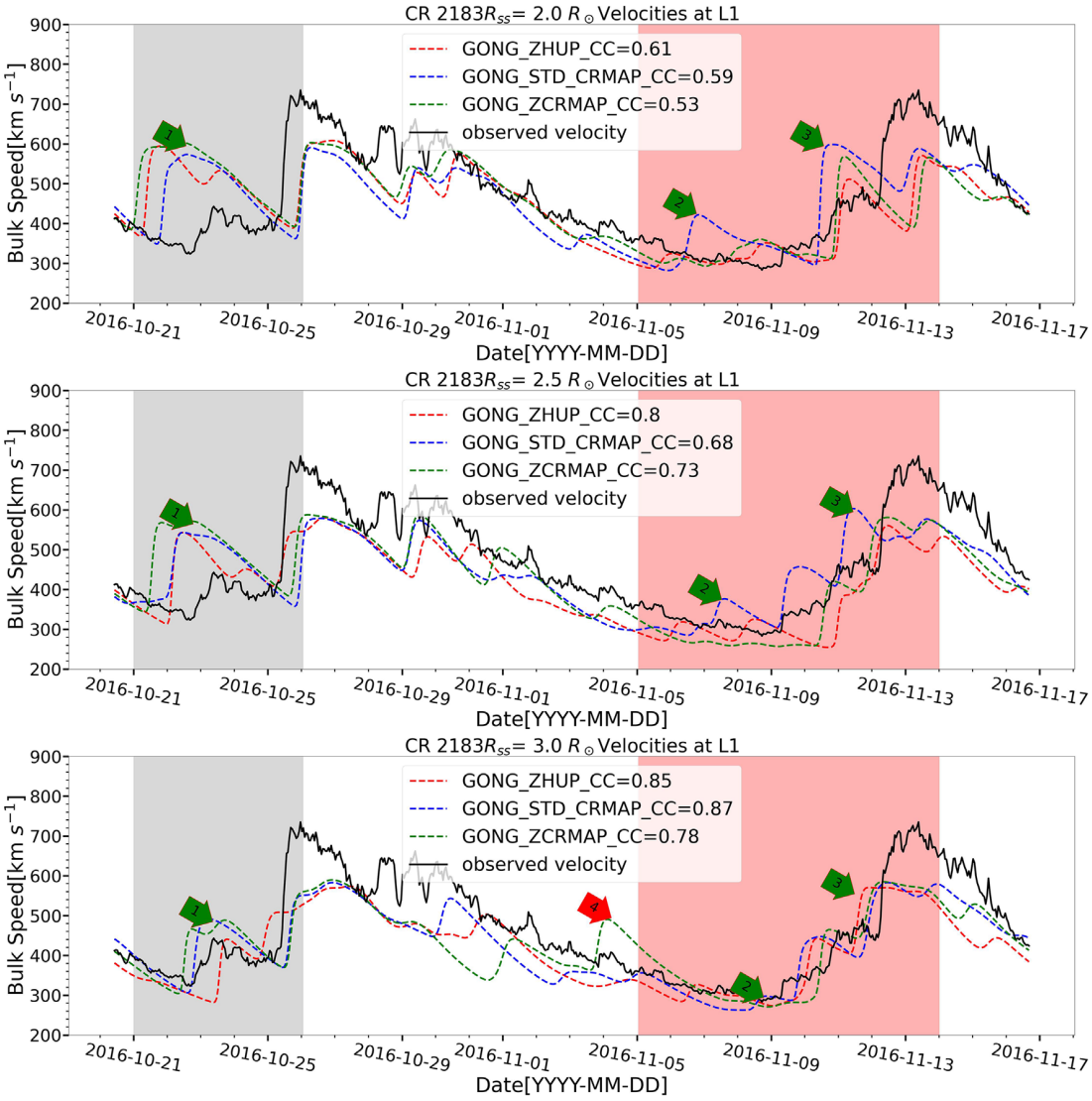

Figure 7. Plots of modeled (PFSS+WSA+HUX) and hourly averaged observed solar wind velocity from OMNI database at L1 with time for CR2183 for different R_{ss}, i.e., for R_{ss} = 2.0 $R_\odot$ (top panel), for R_{ss} = 2.5 $R_\odot$ (middle panel), and R_{ss} = 3.0 $R_\odot$(bottom panel). The red, blue, and green dashed lines show the velocity profile using HU ZPC, STD, and full ZPC maps, respectively. Green arrows show the time period around which R_{ss} optimization improves the match between the modeled and observed profile as R_{ss} increases. The red arrows show the time period around which the prediction does not improve as R_{ss} increases. The shaded regions show the time period where R_{ss} significantly changes the modeled velocity profile.

The red arrows show the features that matched better with the observation while using higher R_{ss} as compared to lower R_{ss}. However, the overall performance, as indicated in terms of *cc*, increases as R_{ss} is decreased. For example, for ZPC maps, *cc* increases from 0.38 to 0.53 and then to 0.6, as R_{ss} decreases from 3.0 $R_\odot$ to 2.5 $R_\odot$ and then to 2.0 $R_\odot$, respectively, as shown in Figure 6. Similar trends can be observed for other maps as well.

It is important to note that although CR2143 shows that the performance improves with decreasing R_{ss}, this does not hold good for all the CRs during the SC24 maximum. However, by examining the average performance based on all the CRs, we can see that lower R_{ss} values (2.0 $R_\odot$ and 2.5 $R_\odot$) perform better than 3.0 $R_\odot$ during SC24 maximum (Fig. 5).

3.2.2 CR2183 (SC24 declining phase)

R_{ss} optimization during the CR2183 gave us better and clearer results about the effects of R_{ss} on the modeled solar wind profile at L1 than CR2143. This is because the PFSS extrapolation during this phase is more reliable than the maximum phase of the SC. Figure 7 shows the modeled (dashed red, green, and blue curves) and observed solar wind velocity profiles (solid black curve) during CR2183.

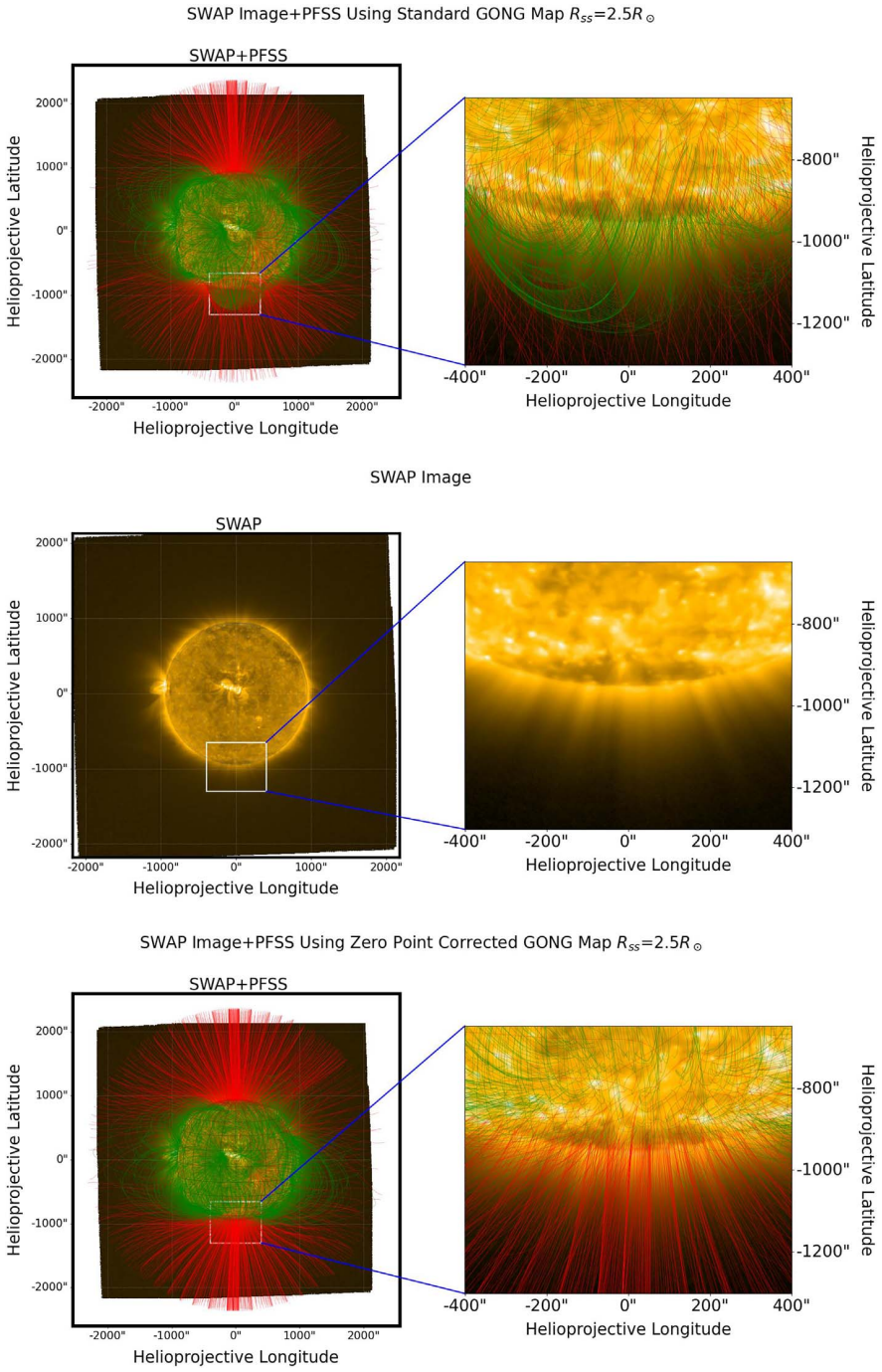

Figure 8. PFSS extrapolated magnetic field lines overlaid on the SWAP (top and bottom panel) image of 20 August 2017, 10:45 UT. The middle panel shows the SWAP mosaic without PFSS extrapolation. The top left panel shows PFSS extrapolation with HU STD map, and the bottom left panel with HU ZPC map (on 20 August 2017, 12:14 UT). The right column shows the zoomed-in version of the white rectangle on the left panels.

One can see that increasing the values of the R_{ss} (from top to bottom panels) suppresses most of the additional peaks, as shown by the green arrows, in the modeled solar wind velocity profile, resulting in a better match of the modeled solar wind velocity profile (red, blue and green curves) with the observed profile (black curve). For example, for ZPC maps, *cc* increases from 0.53 to 0.73 and then to 0.78, as R_{ss} increases from 2.0 $R_\odot$ to 2.5 $R_\odot$ and then to 3.0 $R_\odot$, respectively, as shown in Figure 7. Similar trends can be observed for other maps as well.

The white region between grey and red shaded areas shows a very minute improvement at lower R_{ss}. This is very small in comparison to the improvement at higher R_{ss} in the red and grey-shaded regions. Therefore, the framework performed better at higher R_{ss}, i.e., R_{ss} = 3.0 $R_\odot$.

3.3 Comparing PFSS extrapolation with PROBA2/SWAP observations

In Section 3.1, we observed that using ZPC maps improved the overall performance (averaged over all the three R_{ss} and all CRs) of the framework. This improvement with ZPC maps, compared to STD maps, is evident from the increase in the average *cc*, computed for all three values of R_{ss}. During the minimum phase of SC24, the average *cc* increases from 0.31 (for STD maps) to 0.51 (for ZPC maps), and during the maximum phase of SC24, it rises from 0.22 to 0.47, using the default WSA parameters. Similar results for optimized WSA parameters were found, as discussed above, i.e., an increase in average *cc* from 0.57 to 0.69 during SC24 maximum and an increase in average *cc* from 0.53 to 0.66 during SC24 minimum (for full CR maps).

This indicates that PFSS extrapolations from ZPC maps are likely to provide a more accurate representation of the magnetic field structure of the Sun compared to the extrapolation from STD GONG maps.

Therefore, we compare the overall large-scale coronal structure during the minimum and maximum phases of the SC with the PFSS extrapolated structure from HU STD and ZPC maps. For this purpose, we used the SWAP mosaics reconstructed from the special observational campaign (discussed in Sect. 2) on 20 August 2017 (CR2194, SC24 minimum) and 7 August 2023 (CR2274, SC25 maximum).

Figure 8 illustrates the observed global coronal structure of the Sun from the PROBA2/SWAP during the minimum of the SC24 on August 20, 2017, 10:45 UT (average time of mosaic). We overlaid magnetic field lines obtained from the PFSS extrapolation using the HU STD map (August 20, 2017, 12:14 UT, top panel) and HU ZPC map (August 20, 2017, 12:14 UT, bottom panel). While the overall structure of the extrapolated field lines obtained from both extrapolations is similar, notable differences can be seen near the south pole (in the zoomed-in panel). In this region, the PFSS extrapolation using the HU ZPC map indicates open field lines (red color field lines), whereas the HU STD map show closed fields (green lines). Upon closer inspection in this region, we can identify a coronal hole in the SWAP images, which agrees with the PFSS extrapolation in the HU ZPC map, indicating open field lines (red color).

Similarly, we compared the extended FOV of SWAP with PFSS extrapolation near the maximum of the SC25 on 7 August 2023 (20:37 UT) (Fig. 9, zoomed-in panels). We can see multiple coronal loop structures all over the western limb in the middle panel of Figure 9. The features in the northwest and southwest limb match better with the PFSS extrapolation with the HU ZPC map in the bottom panel of Figure 9 compared to the HU STD GONG map (top panel of Fig. 9). PFSS extrapolation with HU ZPC map (bottom panel) shows multiple local coronal loops, which are closer to the observations in the middle panel compared to more global coronal loops with HU STD map (top panel). Moreover, near the south pole (zoomed-in panel), the PFSS extrapolation from HU ZPC map exhibits more closed field lines (bottom panel) compared to the HU STD map (top panel). Upon closer examination of the SWAP mosaic (middle panel), a coronal cavity is observed at the south-west limb of the Sun. This rules out the presence of open field lines in this region. The closed field lines are not very prominent in the extrapolation from the HU STD map, where the field lines connect to a larger coronal loop structure/streamer (top panel). The overlying closed loops are distinctly visible in the extrapolation from the HU ZPC map (bottom panel).

Consequently, from the comparison with SWAP observations, we found that HU ZPC map are a better choice for both the SC minimum, i.e., August 2017, and as well as for the SC maximum, i.e., August 2023, implying that HU ZPC map yield more accurate results in PFSS extrapolation, matching the coronal structure observed in 174 Å. This further resulted in accurate solar wind velocity prediction at L1. Studies by Nikolić (2019) and Li et al.(2021) demonstrated that standard GONG maps used in space weather prediction have shown a decline in accuracy over time because of the PFSS solutions derived from GONG maps, particularly in the polar regions. As mentioned in Section 2, HU ZPC GONG maps mitigate the zero-point inaccuracies. Our analysis of the 16 CRs at different phases of the SC shows that these inaccuracies are crucial in estimating the solar wind velocity of the WSA model at L1. Therefore, we suggest ZPC maps should be used as input in space weather prediction models.

4 Conclusions

In the present study, we estimated the optimal value of R_{ss} for modeling solar wind velocity by using three different types of magnetic maps as inputs for 16 CRs selected at different phases of the SC. We employed two approaches, one using default WSA parameters and the other using a range of WSA parameters to find the best values of R_{ss} among 2.0 $R_{\odot}$, 2.5 $R_{\odot}$, and 3.0 $R_{\odot}$. During the declining phase of the SC24, the model framework performed overall (average *cc*) better compared to the maximum phases of the SC24 and SC25.

Given the complexity of the solar wind velocity prediction problem at L1, we have attempted to assess the change in the source surface height (R_{ss}) and the impact of the usage of different types of GONG maps and WSA model parameters for different phases of the SC. Our results suggest using a higher surface height (3.0 $R_{\odot}$) in the WSA model during SC minimum as compared to the conventional R_{ss} (2.5 $R_{\odot}$). In contrast, during maximum phase of SC24, either R_{ss} = 2.0 $R_{\odot}$ or R_{ss} = 2.5 $R_{\odot}$ are found to be preferable. During the SC25 maximum, our results are inconclusive because of the poor performance of the framework.

The results agree with those obtained in previous studies (Lee et al., 2011; Arden et al., 2014), in terms of the relative changes in the best source surface heights with the phase of the SC. Previous studies were based on open magnetic flux estimation at L1. We also want to emphasize that our finding for the SC maximum should be carefully interpreted, keeping in mind the applicability of PFSS during the SC maximum as discussed by Lee et al. (2011).

Our previous study (Kumar & Srivastava, 2022) showed that adding the Schatten Current Sheet (SCS; Schatten, 1971) model to the approach provides a similar performance of the framework. Current work hints towards the need for optimization of source surface height in the PFSS model in the context of its use in the WSA model. At the same time, the study highlights the difficulties due to the limitations of the PFSS model

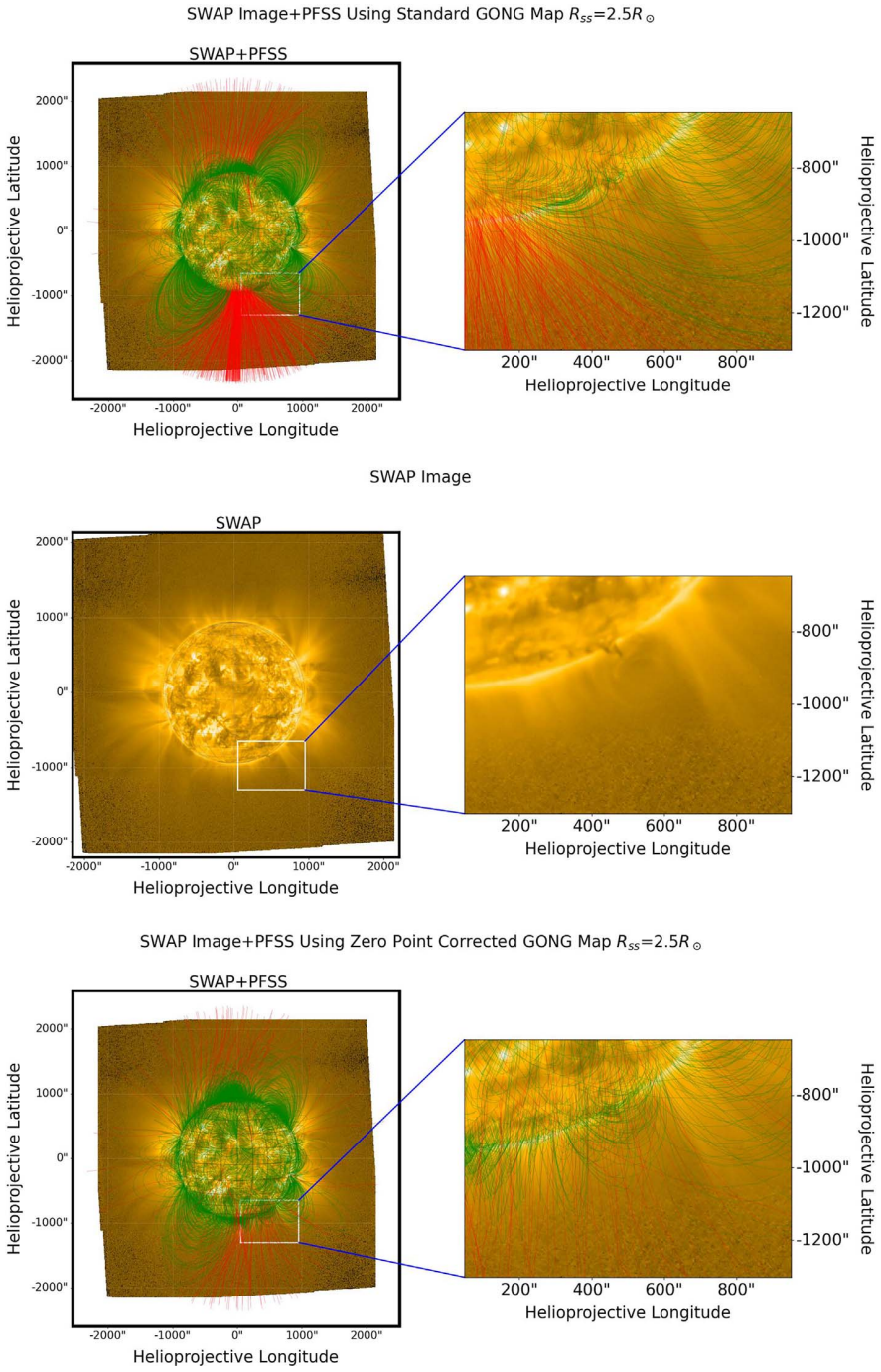

Figure 9. PFSS extrapolated magnetic field lines overlaid on PROBA2/SWAP images recorded on 7 August 2023, 20:37 UT. The top panel shows PFSS extrapolation with HU STD maps, and the bottom panel with HU ZPC maps. The middle panel shows the SWAP mosaic without PFSS extrapolation. The right panel shows the zoomed-in version of the white rectangle on the left panel.

during the solar maximum and uncertainties in the magnetic field measurements at the poles.

We want to mention here that standard magnetic maps from GONG have been used extensively by the community in solar wind velocity forecasting frameworks, e.g., Shiota et al. (2014); Pomoell & Poedts (2018); Nikolić (2019); Narechania et al. (2021); Kumar & Srivastava (2022); Mayank et al. (2022). They are also used in operational WSA-ENLIL simulations. However, we found substantial improvement in the performance of the solar wind forecasting framework while using ZPC magnetic maps compared to STD maps, which is further confirmed by the comparison of PFSS extrapolation with the near-Sun observations obtained from the SWAP instrument. It thus establishes a link between the quality of near-Sun PFSS

extrapolation and the quality of solar wind velocity prediction at L1. Therefore, we strongly advocate the use of ZPC magnetic maps from GONG in space weather prediction models instead of standard maps. A previous study by Narechania et al. (2021) supported the use of ZPC maps compared to the STD GONG maps based on a single case study using MHD simulations.

Our study further supports their results based on a more robust and long-term analysis at different phases of the SC. Moreover, we validated the superiority of ZPC maps over standard GONG maps in both PFSS extrapolations compared with near-Sun observations, and as input in solar wind velocity prediction models at L1. A recent study by Li et al. (2021) based upon open flux and polarity of the IMF at L1 reported that ZPC maps outperformed standard GONG maps significantly. However, they also found that HMI maps ($cc = 0.71$) performed slightly better than ZPC maps ($cc = 0.70$) when compared with observed open flux. A more recent study by Mayank et al. (2022) reported that in the context of solar wind prediction at L1, GONG standard maps outperformed the HMI maps for CR2104 (ascending phase of the SC24). They did not use ZPC GONG maps in their study. Therefore, further investigation is required to compare the impact of different magnetic maps in the context of solar wind velocity prediction.

Our study used discrete sets of 4 CRs (in total 16 CRs) at different SC phases and three distinct values of R_{ss}. Our work is the first step and points out the potential ways to improve the framework. Therefore, to further verify the applicability of the results over the entire phases of the SC, a long-term continuous study is required with a more refined choice of R_{ss}.

It is also important to mention that we used the HUX model for solar wind velocity extrapolation for simplicity. However, a slightly advanced version of this model, i.e., HUXt (Barnard & Owens, 2022), could be used in future work to provide a more realistic framework. This model introduces an explicit time dependence in the solar wind extrapolation by introducing a residual acceleration in the solar wind. Further, the optimization approach relying solely on Pearson's coefficient has its own drawbacks as it disregards other metrics and does not account for overall features. Therefore, advanced metrics, e.g., Dynamic Time warping (Samara et al., 2022) or a combination of metrics, can be used to obtain more robust and conclusive results.

Badman et al. (2020) suggested the use of lower surface height (1.3–1.5 $R_\odot$) to reproduce the radial component of the magnetic field observed at PSP located at 0.5 AU on specific days (2018-10-20 and 2018-10-29), which depends upon the connectivity of the magnetic field lines and the local magnetic field distribution. Our approach in the current work is to optimize the source surface height, i.e., R_{ss} for the entire CR and compare observed and modeled solar wind velocity at L1 for each CR. It may be noted that in our study during solar minimum, for some specific short time periods (during individual CRs), we found that the modeled solar wind velocity profile for lower R_{ss} values matches better with the observed profile (Sect. 3.2). Nevertheless, a higher R_{ss} (3.0 $R_\odot$) was found to perform better for the entire CR as inferred from the *cc* value. And the opposite was observed during SC maximum.

The study by Huang et al. (2024) suggested a slightly lower R_{ss} than 2.5 $R_\odot$ during a solar minimum, by comparing the unsigned, open flux at L1. It assumes an isotropic magnetic field in the heliosphere. This approach is sensitive to the area of coronal holes only, whereas our study is complex in the sense that our final modeled output, the velocity at L1, is related to the overall area of the coronal holes, the overall structure, and connectivity of sub-Earth field lines on the solar surface. Moreover, we use a more sophisticated extrapolation (HUX) method in the heliosphere than previous studies. Therefore, our study highlights the challenges and intricacy of the problem in optimising the source surface height in the PFSS model while using different approaches.

Based on the encouraging results of the current study, which was limited by the availability of the SWAP mosaic data collected during two phases (CR2194, Aug 2017 and CR2274, Aug 2023) of the recent SC, the PROBA2 team has scheduled special observational campaigns every month since. These will be used to test and validate future data sets for more quantitative comparisons.

In summary, the present work is a first step in the direction of improving the WSA model and points out the potential ways to enhance the PFSS+WSA framework of solar wind forecasting at L1. For this purpose, we explore the use of different values of the source surface height (R_{ss}) and different kinds of maps in the PFSS model during selected time periods. This knowledge can contribute to refining predictions of solar wind velocity, as well as for operational space weather frameworks.

Acknowledgements

We thank the reviewers and the editor for the constructive comments to improve the manuscript. The authors have used pfsspy (Stansby et al., 2020). The data used in this study are all publicly available. We want to acknowledge the GONG group for magnetic synoptic maps available on https://gong2.nso.edu/archive/patch.pl?menutype=zeroPoint#step2. Solar wind velocity data is available on https://omniweb.gsfc.nasa.gov/form/dx1.html. The sunspot data is courtesy of WDC-SILSO, Royal Observatory of Belgium, Brussels. We acknowledge the Sunpy community (The SunPy Community et al., 2020). SK and NS want to express their gratitude for the support received through the PROBA2 Guest Investigator program grant. S.K and N.S. also want to express special thanks to the PROBA2 operational team for conducting a special campaign of SWAP observations to have an extended FOV. SWAP is a project of the Centre Spatial de Liége and the Royal Observatory of Belgium, funded by the Belgian Federal Science Policy Office (BELSPO). The ROB team thanks the Belgian Federal Science Policy Office (BELSPO) for the provision of financial support in the framework of the PRODEX Programme of the European Space Agency (ESA). The editor thanks Eleanna Asvestari and an anonymous reviewer for their assistance in evaluating this paper.

References

Alissandrakis CE. 1981. On the computation of constant alpha force-free magnetic field. *A&A* **100(1)**: 197–200.

Arden WM, Norton AA, Sun X. 2014. A "breathing" source surface for cycles 23 and 24. *J Geophys Res Space Phys* **119(3)**: 1476–1485. https://doi.org/10.1002/2013JA019464.

Arge CN, Odstrcil D, Pizzo VJ, Mayer LR. 2003. Improved method for specifying solar wind speed near the sun. In: *Solar wind ten, vol. 679 of American Institute of Physics Conference Series,* Velli M, Bruno R, Malara F, Bucci B (Eds.), AIP: Pisa, pp. 190–193. https://doi.org/10.1063/1.1618574.

Arge CN, Pizzo CN. 2000. Improvement in the prediction of solar wind conditions using near-real time solar magnetic field updates, *J Geophys Res,* **105(A5)**: 10465–10480. https://doi.org/10.1029/1999JA000262.

Badman ST, Bale SD, Martínez Oliveros JC, Panasenco O, Velli M, et al. 2020. Magnetic connectivity of the ecliptic plane within 0.5 au: potential field source surface modeling of the first parker solar probe encounter. *Astrophys J Suppl Ser* **246(2)**: 23. https://doi.org/10.3847/1538-4365/ab4da7.

Barnard L, Owens M. 2022. HUXt – an open source, computationally efficient reduced-physics solar wind model, written in Python. *Front Phys* **10**, 1005621. https://doi.org/10.3389/fphy.2022.1005621.

Berghmans D, Hochedez J, Defise J, Lecat J, Nicula B, et al. 2006. SWAP onboard PROBA 2, a new EUV imager for solar monitoring. *Adv Space Res* **38(8)**: 1807–1811. Magnetospheric dynamics and the international living with a star program. https://doi.org/10.1016/j.asr.2005.03.070.

Fox NJ, Velli MC, Bale SD, Decker R, Driesman A, et al. 2016. The solar probe plus mission: humanity's first visit to our star. *Space Sci Rev* **204(1–4)**: 7–48. https://doi.org/10.1007/s11214-015-0211-6.

Halain JP, Berghmans D, Seaton DB, Nicula B, De Groof A, Mierla M, Mazzoli M, Defise JM, Rochus P. 2013. The SWAP EUV imaging telescope. Part II: in-flight performance and calibration. *Solar Phys* **286(1)**: 67–91. https://doi.org/10.1007/s11207-012-0183-6.

He H, Wang H, Yan Y. 2011. Nonlinear force-free field extrapolation of the coronal magnetic field using the data obtained by the Hinode satellite. *J Geophys Res Space Phys* **116(A1)**:, A01101. https://doi.org/10.1029/2010JA015610.

Hill F. 2018. The global oscillation network group facility – an example of research to operations in space weather, *Space Weather* **16(10)**: 1488–1497. https://doi.org/10.1029/2018SW002001.

Huang Z, Tóth G, Huang J, Sachdeva N, van der Holst B, Manchester WB. 2024. Adjusting the potential field source surface height based on magnetohydrodynamic simulations. *Astrophys J Lett* **965(1)**: L1. https://doi.org/10.3847/2041-8213/ad3547.

Kruse M, Heidrich-Meisner V, Wimmer-Schweingruber RF, Hauptmann M. 2020. An elliptic expansion of the potential field source surface model. *A&A* **638**: A109. https://doi.org/10.1051/0004-6361/202037734.

Kumar S, Paul A, Vaidya B. 2020. A comparison study of extrapolation models and empirical relations in forecasting solar wind. *Front Astron Space Sci,* **7**: 92. https://doi.org/10.3389/fspas.2020.572084.

Kumar S, Srivastava N. 2022. A parametric study of performance of two solar wind velocity forecasting models during 2006–2011. *Space Weather* **20(9)**: e2022SW003069. https://doi.org/10.1029/2022SW003069.

Lee CO, Luhmann JG, Hoeksema JT, Sun X, Arge CN, de Pater I. 2011. Coronal field opens at lower height during the solar cycles 22 and 23 minimum periods: imf comparison suggests the source surface should be lowered. *Solar Phys* **269(2)**: 367–388. https://doi.org/10.1007/s11207-010-9699-9.

Li H, Feng X, Wei F. 2021. Comparison of synoptic maps and PFSS solutions for the declining phase of solar cycle 24. *J Geophys Res Space Phys* **126(3)**: e28870. https://doi.org/10.1029/2020JA028870.

Lowder C, Qiu J, Leamon R. 2017. Coronal holes and open magnetic flux over cycles 23 and 24. *Solar Phys* **292(1)**: 18. https://doi.org/10.1007/s11207-016-1041-8.

Mayank P, Vaidya P, Chakrabarty D. 2022. SWASTi-SW: space weather adaptive simulation framework for solar wind and its relevance to the Aditya-L1 mission. *Astrophys J Suppl Ser,* **262(1)**: 23. https://doi.org/10.3847/1538-4365/ac8551.

Meyer KA, Mackay DH, TalpeanuD-C, Upton LA, West MJ. 2020. Investigation of the middle corona with SWAP and a data-driven non-potential coronal magnetic field model. *Solar Phys* **295(7)**: 101. https://doi.org/10.1007/s11207-020-01668-2.

Narechania NM, Nikolić L, Freret L, De Sterck H, Groth CPT. 2021. An integrated data-driven solar wind – CME numerical framework for space weather forecasting. *J Space Weather and Space Clim* **11**: 8. https://doi.org/10.1051/swsc/2020068.

Nikolić L. 2019. On solutions of the PFSS model with GONG synoptic maps for 2006–2018. *Space Weather* **17(8)**: 1293–1311. https://doi.org/10.1029/2019SW002205.

Odstrcil D, Riley P, Zhao XP. 2004. Numerical simulation of the 12 May 1997 interplanetary CME event. *J Geophys Res Space Phys* **109(A2)**: A02116. https://doi.org/10.1029/2003JA010135.

Perri B, Leitner P, Brchnelova M, Baratashvili T, Kuzma B, Zhang F, Lani A, Poedts S. 2022. COCONUT, a novel fast-converging MHD model for solar corona simulations: I. Benchmarking and optimization of polytropic solutions. *Astrophys J* **936(1)**: 19. https://doi.org/10.3847/1538-4357/ac7237.

Pomoell J, Poedts S. 2018. EUHFORIA: European heliospheric forecasting information asset. *J Space Weather Space Clim* **8**: A35. https://doi.org/10.1051/swsc/2018020.

Reiss MA, MacNeice PJ, Mays LM, Arge CN, Möstl C, Nikolić L, Amerstorfer T. 2019. Forecasting the ambient solar wind with numerical models. I. On the implementation of an operational framework. *Astrophys J Suppl Ser* **240(2)**: 35. https://doi.org/10.3847/1538-4365/aaf8b3.

Riley P, Linker JA, Arge CN. 2015. On the role played by magnetic expansion factor in the prediction of solar wind speed. *Space Weather* **13(3)**: 154–169. https://doi.org/10.1002/2014SW001144.

Riley P, Linker JA, Mikić Z. 2001. An empirically-driven global MHD model of the solar corona and inner heliosphere. *J Geophys Res Space Phys* **106(8)**: 15889–15901. https://doi.org/10.1029/2000JA000121.

Riley P, Lionello R. 2011. Mapping solar wind streams from the sun to 1 au: a comparison of techniques. *Solar Phys* **270(2)**: 575–592. https://doi.org/10.1007/s11207-011-9766-x.

Samara E, Laperre B, Kieokaew R, Temmer M, Verbeke C, Rodriguez L, Magdalenic J, Poedts S. 2022. Dynamic time warping as a means of assessing solar wind time series. *Astrophys J* **927(2)**: 187. https://doi.org/10.3847/1538-4357/ac4af6.

Santandrea S, Gantois K, Strauch K, Teston F, Proba2 Project Team, et al. 2013. PROBA2: Mission and spacecraft overview *Solar Phys* **286(1)**: 5–19. https://doi.org/10.1007/s11207-013-0289-5.

Schatten KH. 1971. Current sheet magnetic model for the solar corona. *Cosmic Electrodyn* **2**: 232–245.

Schatten KH, Wilcox JM, Ness NF. 1969. A model of interplanetary and coronal magnetic fields. *Solar Phys* **6(3)**: 442–455. https://doi.org/10.1007/BF00146478.

Scherrer PH, Bogart RS, Bush RI, Hoeksema JT, Kosovichev AG, et al. 1995. The solar oscillations investigation – Michelson Doppler Imager. *Solar Phys* **162(1–2)**: 129–188. https://doi.org/10.1007/BF00733429.

Scherrer PH, Schou J, Bush RI, Kosovichev AG, Bogart RS, et al. 2012. The Helioseismic and Magnetic Imager (HMI) investigation for the solar dynamics observatory (SDO). *Solar Phys* **275(1–2)**: 207–227. https://doi.org/10.1007/s11207-011-9834-2.

Seaton DB, Berghmans D, Nicula B, Halain JP, De Groof A, et al. 2013. The SWAP EUV imaging telescope part I: instrument overview and pre-flight testing. *Solar Phys* **286(1)**: 43–65. https://doi.org/10.1007/s11207-012-0114-6.

Shiota D, Kataoka R, Miyoshi Y, Hara Y, Tao C, Masunaga K, Futaana Y, Terada N. 2014.Inner heliosphere MHD modeling

system applicable to space weather forecasting for the other planets. *Space Weather* **12(4)**: 187–204. https://doi.org/10.1002/2013SW000989.

Stansby D, Yeates A, Badman ST. 2020. pfsspy: a Python package for potential field source surface modelling. *J Open Source Soft* **5 (54)**: 2732. https://doi.org/10.21105/joss.02732.

The SunPy Community, Barnes WT, Bobra MG, Christe SD, Freij N, et al. 2020. The SunPy Project: open source development and status of the version 1.0 core package. *Astrophys J* **890**: 68. https://doi.org/10.3847/1538-4357/ab4f7a.

van der Holst B, Sokolov IV, Meng X, Jin M, Manchester IV WB, Tóth G, Gombosi TI. 2014. Alfvén Wave Solar Model (AWSoM): coronal heating. *Astrophys J* **782(2)**: 81. https://doi.org/10.1088/0004-637X/782/2/81.

Wang YM, Sheeley Jr NR. 1990. Solar wind speed and coronal flux-tube expansion. *Astrophys J* **355**: 726. https://doi.org/10.1086/168805.

West MJ, Seaton DB, D'Huys E, Mierla M, Laurenza M, Meyer KA, Berghmans D, Rachmeler LR, Rodriguez L, Stegen K. 2022. A review of the extended EUV corona observed by the sun watcher with active pixels and image processing (SWAP) instrument. *Solar Phys* **297(10)**: 136. https://doi.org/10.1007/s11207-022-02063-9.

Wiegelmann T. 2004. Optimization code with weighting function for the reconstruction of coronal magnetic fields. *Solar Phys* **219(1)**: 87–108. https://doi.org/10.1023/B:SOLA.0000021799.39465.36.

Cite this article as: Kumar S, Srivastava N, Talpeanu D, Mierla M, D'Huys E, et al. 2025. On the role of source surface height and magnetograms in solar wind forecast accuracy. *J. Space Weather Space Clim.* **15**, 24. https://doi.org/10.1051/swsc/2025021.

Appendix

Figures A1 and A2 illustrate the MAPE for different CRs with different R_{ss} in the first and second approaches, respectively. It is evident that the average MAPE has increased significantly for the SC25 maximum (rightmost column of both Figures) in the second approach compared to the first.

In contrast, the MAPE values for the SC24 maximum and declining phase did not increase as significantly. Specifically, for ZPC maps in the SC24 declining phase, MAPE increased moderately from 20% to 25%. However, for the SC25 maximum, the increase was much more pronounced, rising from 22% to 114% (average for all three R_{ss} values) in Figure A2 compared to Figure A1.

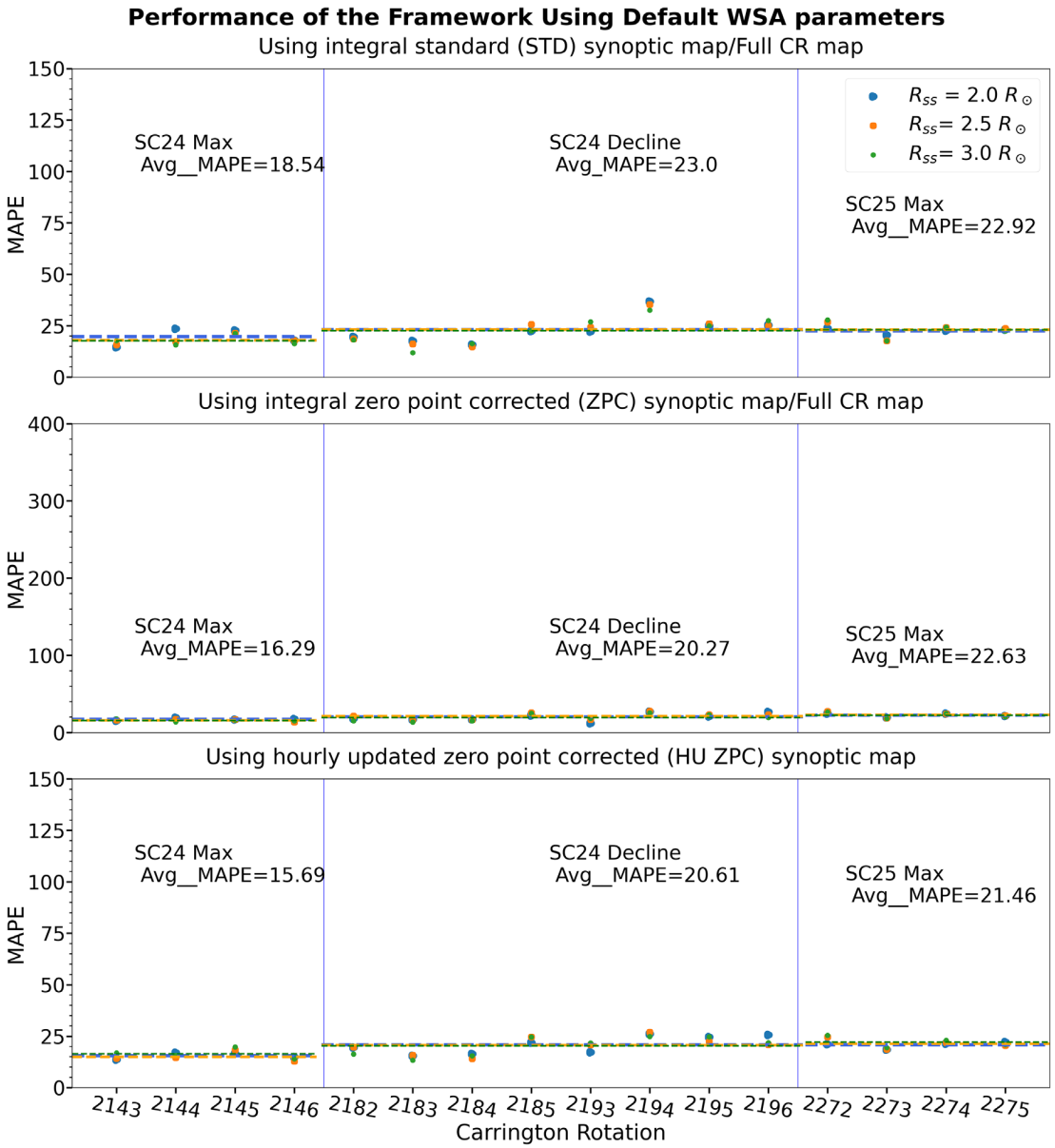

Figure A1. Mean Absolute Percentage Error (MAPE) for different CRs with different R_{ss} based on default WSA parameters. The top panel shows the result using standard Carrington maps (STD), the middle panel is for the zero-point corrected Carrington maps (ZPC), and the bottom panel is for zero-point corrected hourly updated maps (HU ZPC). Blue, orange, and green dots represent the performance of the framework for R_{ss} of 2.0 $R_\odot$, 2.5 $R_\odot$, and 3.0 $R_\odot$, respectively. Horizontal dashed lines show the average performance in the respective phase for each R_{ss} and all CRs. An annotated average MAPE for each phase shows the aggregate average values for all the three R_{ss}.

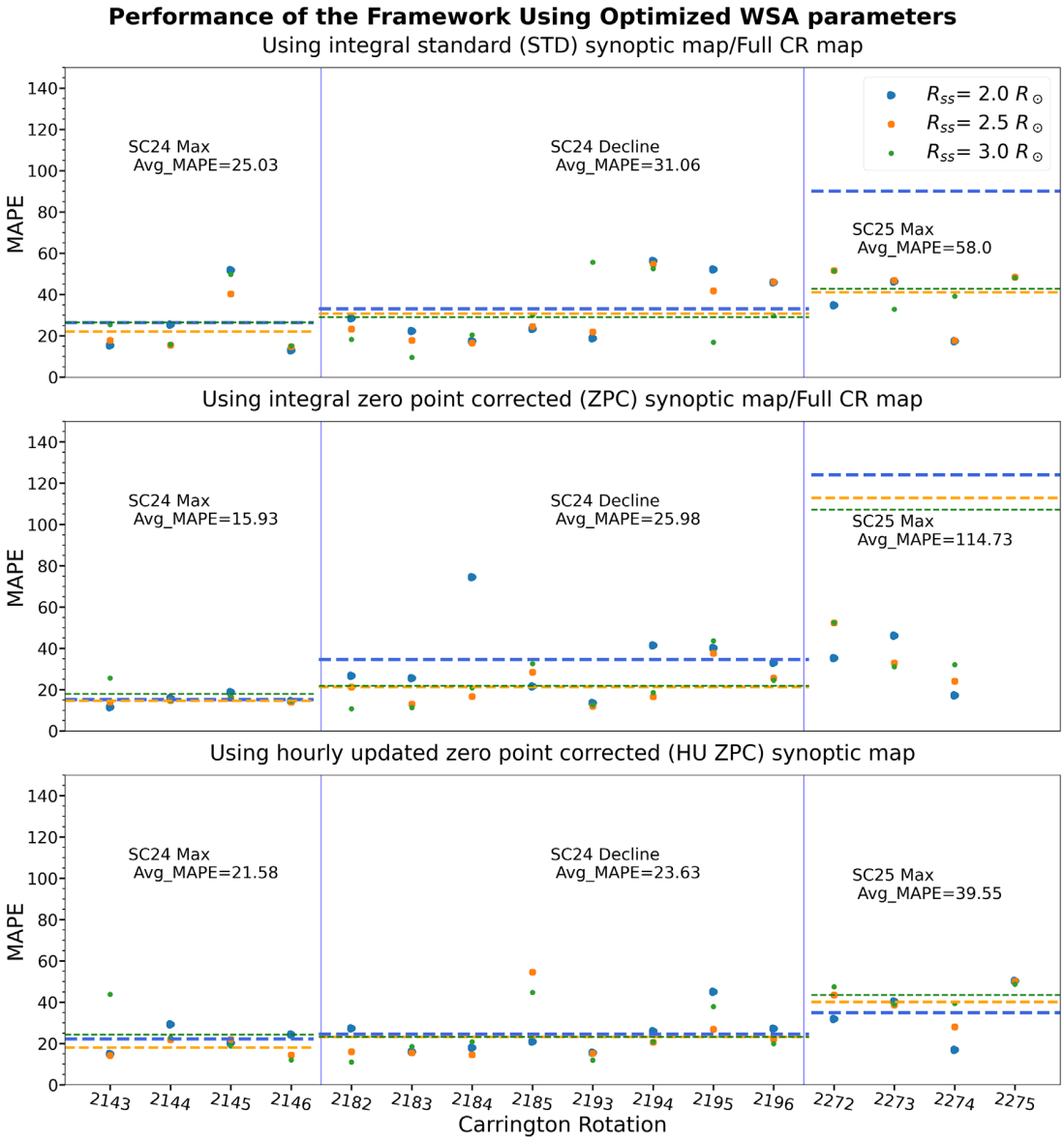

Figure A2. Similar to Figure A1. Corresponding to optimized WSA parameters, i.e., WSA parameters corresponding to highest *cc*. It may be noted that MAPE values for CR2275 using the ZPC map (middle panel) are in the range of 300–400 and, therefore, can not be shown in the selected limit of the *y*-axis.